

This item was submitted to Loughborough University as a PhD thesis by the author and is made available in the Institutional Repository (<https://dspace.lboro.ac.uk/>) under the following Creative Commons Licence conditions.



For the full text of this licence, please go to:
<http://creativecommons.org/licenses/by-nc-nd/2.5/>



Pilkington Library

Author/Filing Title G o H

Vol. No. Class Mark T

**Please note that fines are charged on ALL
overdue items.**

FOR REFERENCE ONLY

0402590864



An Exploding Foil Shockwave Technique for Magnetic Flux Compression and High-Voltage Pulse Generation

By


Swée-Eng Goh, Diplom-Ingenieur (Nachrichtentechnik)

A Doctoral Thesis
submitted in partial fulfilment of the requirements
for the award of
Doctor of Philosophy of Loughborough University

May 2002

LOUGHBOROUGH UNIVERSITY
Department of Electronic and Electrical Engineering

© by Swée-Eng Goh 2002

	Loughborough University Library
Date	Dec 02
Class	
Acc No.	040259086

Abstract

This thesis describes a novel electromagnetic shockwave technique for use in compressing magnetic flux and to serve as the basis for a new approach to producing fast-rising voltage pulses with amplitudes of several hundred kV. The shockwave is produced by an exploding foil driven electric gun that accelerates a Mylar flyer to impact with a sample of aluminium powder. Both Japanese and Russian researchers have previously published experimental results for shockwave magnetic flux compression using an explosive driver. The present research considers replacing the explosive energy of this driver by the electrostatic energy stored in a capacitor bank, thereby enabling experiments to be performed in a laboratory environment. Differences in performance that arise from the use of explosive and electrical driver are examined. A conventional electric gun system in planar geometry is developed to study the insulator-to-metallic transition in shock-compressed aluminium powder. This provides data on the conducting shock front in powder that can be used for flux compression and high-voltage pulse generation. A prototype cylindrical geometry system is described for proof-of-principle experiments, in which an imploding shockwave compresses flux towards the central axis of a system. A high-voltage pulse can then be produced by the rapid time-change in the flux linking a suitably situated coil. Design calculation, constructional details and experimental results for the new system are all presented. The experimental programme is augmented by a detailed study of the fundamental shockwave processes. A new mathematical model for an electric gun is developed, that provides detailed description of the foil explosion and flyer acceleration processes. A hydrodynamic code including an equation of state model for the powder is developed, and is shown to reproduce with reasonable accuracy the shock compression of aluminium powder by flyer impact, including the elastic precursor phenomenon. A magnetohydrodynamic code with an electrical conductivity model for the shock-compressed powder is developed for the study of flux compression and high-voltage pulse generation techniques. This provides a critical insight into the shockwave processes and facilitates a systematic design and performance prediction for future experimentation.

Acknowledgements

I am indebted to my employer at DSO National Laboratories of Singapore for providing the financial support for my research. I would like to thank my Research Supervisor Professor I.R. Smith, and Director of Research Professor R.M. Goodall for the opportunity of research at Loughborough University. Professor Smith gave me invaluable encouragement and editorial assistance. I also wish to acknowledge members of the Pulsed Power Research Group, in particular, Dr B.M. Novac for technical guidance, useful discussions and practical assistance in the fabrication of different probes and sensors. I would like to thank P. Senior for the generous loan of laboratory equipment and helpful advice on experimental techniques, and H.R. Stewardson for important instructions on operating the main capacitor bank at Loughborough and for vital clues on maintaining the Blumlein trigger system. Finally, my deepest thanks and appreciation go to my ever-patient wife, Isabel.

To Isabel and my family

With Love and Gratitude

G.E. Duvall on shockwave: "... there seems to be a tendency for the mind to be paralyzed by the sight and sound of an explosion to such a degree that it fails to recognize it as the orderly physical process it is."

TABLE OF CONTENTS

	Page
Abstract.....	i
Acknowledgements.....	ii
Dedication.....	iii
Table of Contents.....	iv
List of Principal Symbols	xi
1. INTRODUCTION	1
1.1 THESIS OBJECTIVES	2
1.2 THESIS ORGANISATION.....	4
2 SHOCKWAVE MAGNETIC FLUX COMPRESSION	7
2.1 SHOCKWAVES	7
2.1.1 Shock Jump Equations.....	8
2.1.2 Conditions for Strong Shock.....	10
2.2 GENERATION OF SHOCKWAVE FOR DYNAMIC COMPRESSION OF MATERIAL	11
2.2.1 Explosive Driven Technique	11
2.2.2 Gun Techniques	12
2.2.3 Laser and Electron Beam Loading.....	13
2.2.4 Exploding Foil Technique	13
2.3 MAGNETIC FLUX COMPRESSION BY CYLINDRICAL IMPLOSION.....	14
2.3.1 Basic Flux Compression Equation for Cylindrical Implosion.....	15
2.3.2 Flux Diffusion Speed	16
2.3.3 Magnetic Reynolds Number	17
2.4 SHOCKWAVE MAGNETIC FLUX COMPRESSION	18
2.4.1 Principle of Operation.....	18
2.4.2 Material with Variable Electrical Conductivity.....	19
2.5 EXPLODING FOIL SHOCKWAVE DRIVEN MAGNETIC FLUX COMPRESSION.....	21
2.6 CONCLUSIONS.....	24

3	ELECTRIC GUN.....	25
3.1	INTRODUCTION	25
3.2	MODELLING THE FLYER ACCELERATION PROCESS	27
3.2.1	Gurney Equation for Planar Geometry	29
3.2.2	Acceleration Solution using an Ideal Gas Law EOS	31
3.2.3	Adiabatic Constant, γ	35
3.2.4	Prediction of Flyer Velocity.....	35
3.2.5	Estimation of Shock Pressure Generated by the Exploding Foil.....	39
3.3	EMPIRICAL MODELLING OF EXPLODING FOIL	43
3.3.1	Action Integral Method.....	43
3.3.2	Tucker and Toth Model	43
3.3.3	AFWL Model.....	44
3.3.4	LU Model for Electric Gun Applications	45
3.3.5	System Parameters	46
3.3.6	Time of Burst for Exploding Foil	47
3.4	THE INTEGRATED MODEL FOR ELECTRIC GUNS.....	48
3.4.1	Governing Equations	48
3.4.2	Numerical Solution	53
3.4.3	Foil Plasma Properties	53
3.4.4	Explosion Quality Factor	53
3.5	FLYER VELOCITY MEASUREMENTS	54
3.5.1	Fibre-Optic Probes.....	54
3.5.2	Experimental Arrangement.....	55
3.5.3	Experimental Results	56
3.6	CONCLUSIONS.....	66
4	HYDRODYNAMIC MODEL AND EOS	67
4.1	HYDRODYNAMIC MODEL IN ONE DIMENSION	67
4.1.1	Governing Equations	68
4.1.2	Eulerian Description	68
4.1.3	Lagrangian Description.....	69
4.1.4	Artificial Viscosity.....	71

4.1.5	Finite Difference Implementation.....	72
4.1.6	Conducting Shock Front	76
4.1.7	Treatment of Material Interface	77
4.2	EQUATION OF STATE.....	79
4.2.1	Mie-Grüneisen EOS.....	79
4.2.2	Linear $U_s - u_p$ Equation of State.....	81
4.2.3	Equation of State for Porous Material	81
4.2.3.1	Porosity and Theoretical Density.....	82
4.2.3.2	The Snow-Plow Model	83
4.2.3.3	The Mie-Grüneisen Model.....	85
4.2.4	The $P - \alpha$ Model	90
4.2.5	Equation of State for Powder Material	94
4.2.6	Equation of State for Aluminium Powder	96
4.2.6.1	One-dimensional Steady Shock Propagation Test.....	97
4.2.6.2	One dimensional Shock Reflection Test.....	100
4.2.7	EOS for Mylar Polyester.....	103
4.3	ELECTRICAL CONDUCTIVITY FOR SHOCK-LOADED ALUMINIUM POWDER	104
4.3.1	Simple Switch Model.....	104
4.3.2	Almström's Model.....	106
4.4	ELECTRICAL CONDUCTIVITY FOR IONISED GAS.....	107
4.4.1	Spitzer's Equation	107
4.5	CONCLUSION.....	110
5.	SHOCK COMPRESSION OF ALUMINIUM POWDER.....	111
5.1	ALUMINIUM POWDER	111
5.2	SHOCK COMPRESSION EXPERIMENTS.....	112
5.2.1	Small-Scale Electric Gun.....	112
5.2.2	Flyer Plate-Target Stand-off Distance	113
5.2.3	Determination of Flyer Velocity by TOA Measurement.....	114
5.2.3.1	Coaxial Contact-Pin Probe for Single TOA	114
5.2.3.2	Experimental Arrangements	116
5.2.3.3	Experimental Results	116

5.2.4	Determination of Shock Velocity by TOA Measurement	118
5.2.4.1	Coaxial Contact-Pin Probes for Multiple TOAs.....	118
5.2.4.2	Experimental Arrangements	119
5.2.4.3	Experimental Results	119
5.2.5	Continuous Monitoring of Shock Velocity.....	123
5.2.5.1	Spiral Resistance Probe	123
5.2.5.2	Circuit Analysis	124
5.2.5.3	Experimental Arrangement.....	128
5.2.5.4	Measurements Results	129
5.3	NUMERICAL ANALYSIS OF EXPERIMENTAL RESULTS	132
5.3.1	Stimulation Method	132
5.3.2	Simulation Method	133
5.3.3	Solution Approach.....	134
5.3.4	Tuning Factors	135
5.3.5	Numerical Results.....	137
5.3.5.1	Flyer Acceleration and Impact Model	137
5.3.5.2	Shock Propagation Model	140
5.3.5.3	Elastic Precursor	145
5.3.5.4	Three-Dimensional Graphs.....	148
5.3.5.5	Circuit Model for Spiral Probe	151
5.3.6	Comparison with Theory	154
5.3.6.1	Impedance Matching Method	154
5.3.6.2	Pressure and Particle Velocity at Impact	155
5.3.6.3	Shock Velocity at Impact.....	155
5.3.6.4	Shape of Impact Pressure Pulse.....	156
5.4	FLAMMABILITY OF THE ALUMINIUM POWDER.....	158
5.5	CONCLUSIONS.....	159
6	MAGNETOHYDRODYNAMIC MODEL FOR CYLINDRICAL IMPLOSION	160
6.1	MATHEMATICAL MODELLING OF CYLINDRICAL ELECTRIC GUN	160
6.1.1	Gurney Equation for Implosion of Cylindrical Asymmetric Sandwich ...	160
6.1.2	Acceleration Solution using Ideal Gas Law EOS.....	163

6.1.3	Gurney Terminal Velocity	167
6.1.4	Explosive Pressure at Foil Burst.....	169
6.1.5	Integrated Model for the Cylindrical Electric Gun.....	169
6.1.6	Numerical Solution.....	174
6.2	MAGNETOHYDRODYNAMIC MODEL.....	175
6.2.1	MHD Equations.....	176
6.2.2	Computational Domain.....	179
6.2.3	Finite Difference Scheme	181
6.2.4	Finite Difference Equations.....	181
6.2.5	Alfven Velocity and Stability Criteria.....	185
6.3	NUMERICAL ANALYSIS OF NAGAYAMA EXPERIMENT	186
6.3.1	Experimental Conditions	186
6.3.2	Considerations for Numerical Simulations.....	187
6.3.3	Numerical Results.....	188
6.3.4	Initial Powder Density and Magnetic Flux Compression.....	193
6.4	CONCLUSION	194
7	MAGNETIC FLUX COMPRESSION BY A CONVERGING SHOCKWAVE.....	195
7.1	CYLINDRICAL IMPLODER	195
7.1.1	Design Considerations	196
7.1.2	Main Capacitor Bank.....	197
7.1.3	Aluminium Exploding Foil.....	198
7.1.4	High-Voltage Insulator	199
7.1.5	Cylindrical Current Conductor	200
7.2	INITIAL FIELD COIL.....	201
7.2.1	Auxiliary Circuit.....	201
7.2.2	Circuit Analysis	202
7.2.3	Design Calculation.....	205
7.2.4	Construction of Field Coil	208
7.2.5	Magnetic Diffusion through Cylindrical Current Conductor	208
7.2.6	Measured Performance	211
7.3	MAGNETIC FIELD PROBES	213

7.3.1	Initial Field Probe	214
7.3.2	Final Field Probe.....	215
7.3.3	Aluminium Powder Assembly.....	216
7.3.4	Calibration of Magnetic Field Probe	217
7.4	MAGNETIC FLUX COMPRESSION EXPERIMENTS.....	219
7.4.1	Experimental Programme	219
7.4.2	Experimental Arrangements	219
7.4.3	Electric Gun Performances	222
7.4.4	Initial Magnetic Flux Density	227
7.4.5	Final Compressed Flux Density - with Aluminium Powder	228
7.4.6	Final Compressed Flux Density - without Aluminium Powder	230
7.5	NUMERICAL ANALYSIS.....	233
7.5.1	Flux Compression Model	233
7.5.2	MHD Model.....	239
7.6	CONCLUSIONS.....	243
 SHOCKWAVE GENERATION OF HIGH-VOLTAGE PULSES		245
8.1	DYNAMIC POWDER TRANSFORMER	245
8.1.1	Helical Coil with Epoxy Insulation	246
8.1.2	Helical Coil with Powder Assembly.....	248
8.2	EXPERIMENTS WITH DYNAMIC POWDER TRANSFORMER	249
8.2.1	Experimental Arrangements	249
8.2.2	Electric Gun Performance.....	250
8.2.3	Initial Magnetic Flux Density.....	252
8.2.4	Transformer Output Voltage.....	253
8.2.5	Circuit Analysis	254
8.2.5.1	Circuit Model for Dynamic Powder Transformer	254
8.2.5.2	Velocity of the Conducting Shock Front.....	256
8.2.5.3	Effect of Loading on Output Voltage	259
8.2.6	Elastic Precursor	260
8.3	DESIGN OF DYNAMIC POWDER TRANSFORMER	262
8.3.1	Simplified Analysis and Design Method	262
8.3.2	Estimated Pressure at Flyer Impact	263

8.3.3	Design Examples for High-Voltage Pulse Generation	265
8.4	EFFICIENCY OF THE DYNAMIC POWDER TRANSFORMER	272
8.5	CONCLUSIONS.....	272
9	CONCLUSIONS AND FUTURE WORK.....	273
9.1	CONCLUSIONS.....	273
9.2	FUTURE WORK	276
References.....		278
Bibliography		294
Publications		295
APPENDICES.....		297
A.	PHOTOGRAPHS OF SPIRAL RESISTANCE PROBE.....	297
B.	PHOTOGRAPHS OF FIELD COIL.....	300
C.	DRAWINGS AND PHOTOGRAPHS OF IMPLoder.....	303
D.	FLAMMABILITY OF THE ALUMINIUM POWDER.....	313
E.	EFFICIENCY OF THE DYNAMIC POWDER TRANSFORMER.....	316

LIST OF PRINCIPAL SYMBOLS

		Unit
α	porosity, the density ratio of powder to the corresponding solid material	-
α_e	porosity at zero pressure (unshocked, initial condition)	-
α_p	porosity at the transition from elastic to plastic region	-
β	coefficient of volumetric expansion	$1 / K$
\vec{B}	magnetic field vector	T
B_z	magnetic flux density in axial direction	T
B_{z0}	initial magnetic flux density in axial direction	T
c_s	speed of sound in material	m / s
C	explosive mass per unit area (planar)	kg / m^2
	explosive mass per unit length (cylindrical)	kg / m
C_{aux}	capacitance of auxiliary capacitor bank	F
C_b	capacitance of main capacitor bank	F
C_p	specific heat capacity at constant pressure	$J / (kg K)$
C_v	specific heat capacity at constant volume	$J / (kg K)$
δ_f	thickness of metallic exploding foil	m
δ_p	thickness of projectile or flyer plate	m
δ_t	thickness of tamper	m
\vec{D}	electric displacement vector	C / m^2
ε	energy density	J / kg
ε_G	Gurney energy density	J / kg

ε_o	energy density of unreacted explosive	J/kg
e	charge on electron or proton	C
\vec{E}	electric field vector	V/m
E_θ	electric field in azimuthal direction	V/m
Φ	magnetic flux	Wb
γ	adiabatic constant	-
Γ	Mie-Grüneisen parameter	-
Γ_o	Mie-Grüneisen parameter at zero pressure	-
\vec{H}	magnetic intensity vector	AT/m
I_{aux}	electric current in auxiliary capacitor bank circuit	A
I_b	electric current in electric gun circuit	A
I_θ	electric current in azimuthal direction	A
\vec{J}	electric current density vector	A/m^2
J_B	electric current density at point of burst	A/m^2
J_θ	electric current density in azimuthal direction	A/m^2
k	Boltzmann's constant	J/K
k_{corr}	correction factor for foil explosion	-
k_{eff}	flux conservation coefficient	-
κ	adiabatic bulk modulus	Pa
l_f	length of metallic exploding foil	m
L_{aux}	inductance of auxiliary capacitor bank	H
L_b	inductance of main capacitor bank	H
L_i	inductance of tamper	H
L_f	inductance of metallic exploding foil	H
L_i	inductance of exploded foil plasma	H
L_{load}	inductance of load circuit	H
L_p	inductance of primary coil of transformer	H
L_s	inductance of secondary coil of transformer	H

μ_o	permeability of free space	H / m
m_f	mass of metallic exploding foil	kg
m_p	mass of projectile or flyer plate	kg
m_t	mass of tamper	kg
M	projectile mass per unit area (planar)	kg / m^2
	projectile mass per unit length (cylindrical)	kg / m
N	tamper mass per unit area (planar)	kg / m^2
	tamper mass per unit length (cylindrical)	kg / m
P_o	pressure at ambient conditions (ahead of shock front)	Pa
P_B	magnetic pressure	Pa
P_e	pressure at elastic limit	Pa
P_{ex}	explosive pressure	Pa
P_s	pressure at transition from plastic to solid region	Pa
Q	artificial viscosity	Pa
r_m	radial position of projectile or flyer plate	m
r_{mo}	initial radius of projectile or flyer plate	m
r_N	radial position of tamper	m
r_{No}	initial radius of tamper	m
r_s	radial position of shock front	m
R	resistance	Ω
R_{aux}	resistance of auxiliary capacitor bank	Ω
R_b	resistance of main capacitor bank	Ω
R_e	magnetic Reynolds number	-
R_f	resistance of metallic exploding foil	Ω
R_{load}	resistance of load	Ω
R_p	resistance of primary coil of transformer	Ω
R_s	resistance of secondary coil of transformer	Ω

ρ_o	mass density at ambient conditions (ahead of shock front)	kg / m^3
ρ_{el}	electric charge density	C / m^3
ρ_f	mass density of metallic exploding foil	kg / m^3
ρ_{ex}	mass density of explosive	kg / m^3
ρ_{flyer}	mass density of projectile or flyer plate	kg / m^3
ρ_{tamper}	mass density of tamper	kg / m^3
s	Lagrangian co-ordinate	
	mass per unit area (planar)	kg / m^2
	mass per unit length (cylindrical)	kg / m
STP	standard temperature ($0^\circ C$) and pressure ($1.013 \times 10^5 Pa$)	
σ	electrical conductivity	$1 / \Omega m$
τ	time constant of exponential function	s
T	temperature	K
T_e	temperature of ionised gas	eV
t_{burst}	time of foil burst	s
t_{dur}	duration of pressure pulse	s
t_{imp}	time of flyer impact	s
u_o	particle velocity at ambient conditions (ahead of shock front)	m / s
u_p	particle velocity	m / s
U_i	ionisation potential	eV
U_s	shock velocity	m / s
v	velocity in the x- or r-direction	m / s
v_A	Alfven speed	m / s
v_f	flux diffusion speed	m / s
v_G	Gurney terminal projectile velocity	m / s
v_i	implosion speed	m / s
v_m	velocity of projectile or flyer plate	m / s

v_N	velocity of tamper	m / s
v_p	velocity of projectile or flyer plate at impact	m / s
\vec{v}	velocity vector	m / s
V	specific volume	m^3 / kg
V_{aux}	initial voltage of auxiliary capacitor bank	V
V_b	initial voltage of main capacitor bank	V
V_o	specific volume solid material at zero pressure (unshocked, initial condition)	m^3 / kg
V_{oo}	specific volume of powder material at zero pressure (unshocked, initial condition)	m^3 / kg
V_{porous}	specific volume of porous or powder material	m^3 / kg
V_s	specific volume of solid material	m^3 / kg
w_f	width of metallic exploding foil	m
W_B	magnetic energy	J
W_k	kinetic energy	J
x_m	position of projectile or flyer plate	m
x_{mo}	initial position of projectile or flyer plate	m
x_N	position of tamper	m
x_{No}	initial position of tamper	m

Any other symbols are defined as they appear.

INTRODUCTION

Magnetic flux compression is a technique used for the generation of large electromagnetic power pulses, of the order of 100 GW and above. Typical flux compression systems optimised for maximum current or energy output have produced maximum currents in the 1 to 10 MA range and magnetic energies in the 1 to 25 MJ range.

In magnetic flux compression, a closed electrical conductor linking a magnetic flux is compressed by external forces. This thereby converts mechanical energy into magnetic energy, although the transformation is efficient only as long as the flux losses remain limited. A large body of literature on magnetic flux compression has been accumulated over recent years, e.g. [1] – [7]. Generally speaking, a review of this shows that high-current and high-energy pulses can be achieved in a number of different compression geometries (plate, cylindrical, spherical, conical, helical, single-turn coil etc.) and by using different energy sources as the primary driver (chemical energy in explosive, electrostatic energy in capacitor bank, high pressure gas from combustion).

As an alternative to the production of a high-current/high-energy output, a magnetic flux compression system based on the radial implosion [8]-[10] of a cylindrical hollow conductor can produce the magnetic fields of the order of 1000 T and above, in a volume of 1 cm^3 , that are used in a large variety of physics applications.

In most flux compression systems, a metallic conductor in the solid state (i.e. a solid liner) [11] is employed as the working medium that compresses the magnetic field, although electrical conductors in the gaseous state, in the form of plasma armatures [12]-[14] and the gas-puff Z-pinch [15] have also been used. More recently, flux compression by means of a magnetic bubble (or surfactant) in a Z-pinch configuration [16] has also been reported.

In the majority of flux compression systems driven by capacitor banks, the compression is produced either by (1) single-turn coils or (2) by cylindrical implosion devices. Depending on the direction of current flow, two variations in the cylindrical implosion devices are possible. When the electrical current flows around the cylindrical liner that compresses the magnetic field, we have the so-called θ -pinch configuration. When alternatively the electrical current flows along the cylinder, this is termed the Z-pinch configuration.

Significant work on the single-turn coil configuration was carried out by Herlach [17] and early work on θ -pinch implosion by Cnare [18]-[19] and Miura [20]-[21]. Notable work on the Z-pinch configuration by Alikhanov [22] was later repeated at the University of Washington [23]. In the 1980s, Felber and his co-workers reported using a gas-puff Z-pinch to compress a magnetic field. AFWL (presently the Philips Laboratory at Albuquerque, USA) used the world's largest capacitor bank (the Shiva Star, 9.4 MJ, 120 kV) to conduct flux compression experiments using a plasma armature, with important results presented in [12]

In recent years, Loughborough University has conducted extensive research on explosively driven helical flux compression [24] and the conditioning of the pulsed output power using a variety of devices such as plasma erosion opening switches [25] and electrically exploded metallic foils [26]. This expertise has led to an extension of the exploding foil technique to accelerate a dielectric flyer, to the conduct of impact studies on metallic powder and to investigate the application of the results in magnetic flux compression.

1.1 Thesis Objectives

The present research is concerned with a magnetic flux compression and high-voltage generation technique in a cylindrical imploding geometry, with the following unique features

- a) a high-energy capacitor bank is used as the primary energy source to implement electromagnetic flux compression, rather than an explosively driven process,
- b) an exploding metallic foil accelerates an insulator flyer, driving an air shockwave, to impact an aluminium powder sample and compress an initially established magnetic flux, and
- c) a multi-turn helical secondary coil that converts the time-rate-of-change of magnetic flux density into a high-voltage pulse.

The objective of the research is to achieve magnetic flux compression by a conducting shockwave in aluminium powder, and to obtain high-voltage pulses in laboratory-based experiments. Both theoretical and experimental work has been carried out in the following areas, with the experimental work being performed as part of an EPSRC Standard Research Grant (GR/L97056)

- a) the design and development of an 'electric gun' technique using exploding metal foils to generate intense pressure pulses for (1) accelerating a Mylar polyester flyer (or projectile) and (2) conducting studies on the insulator-to-metal phase transition property of aluminium powder under shock compression,
- b) the design and development of a cylindrical imploder device for proof-of-principle experiments on (1) shockwave magnetic flux compression techniques and (2) shockwave high-voltage generation, and
- c) the design and development of analytical and mathematical models to (1) explain and predict the system performance and (2) compare the performance of explosively driven and electromagnetically-driven implosion process.

The present work was undertaken with the intention of outlining the salient features of shockwave magnetic flux compression using a capacitor bank as the driver, in order to identify the main parameters controlling this process and their effect on the magnetic

flux compression and high-voltage pulse generation. An understanding of this process will lead to a better understanding of magnetic flux compression using different types of shockwave generation methods, phase transition material, extensions to the special case of spherical implosion and a combination of methods (e.g. solid liner plus shockwave) to produce hybrid type magnetic flux compression systems.

1.2 Thesis Organisation

Chapter 2 of the thesis describes the fundamental equations for shockwaves, together with different shockwave generation techniques that may have relevance to magnetic flux compression by cylindrical implosion techniques. The principle of explosively driven shockwave magnetic flux compression that utilises the shock compressed conducting front in a material with a variable electrical conductivity is described. This is followed by a brief resume of the research approach used to achieve capacitor-bank driven shockwave magnetic flux compression under laboratory conditions.

Chapter 3 describes the development of a new mathematical model for a planar electric gun that provides a detailed description of both the electrical performance and the flyer acceleration process. Central to the new model is the combination of the Gurney equation with an ideal gas law equation of state (EOS) to obtain the flyer acceleration solution. Realistic predictions of the electrical circuit performance are based on an empirical model for the electrically exploded metallic foil. Beside a detailed description of the electrical current and voltage and the flyer trajectory, the computer model provides information on the foil plasma properties (mass density, pressure, temperature etc.) after explosion. Comparison of the computer prediction with experimental results is given at the end of the chapter.

Chapter 4 describes the development of a hydrodynamic model and EOS for powder material, both of which are necessary for modelling the shock compression of aluminium powder. The governing equations for hydrodynamic flow and the finite-difference computational scheme are described in detail. One-dimensional test cases, in the form of (1) steady shock propagation and (2) shock reflection in aluminium powder are used as functional tests to verify the hydrodynamic computer model. A simple switch model is described, for simulating the insulator-to-conductor phase transition in

shock compressed aluminium powder. The contribution of the imploding foil plasma (driving the Mylar flyer) to the flux compression process is assessed, based on Spitzer's equation for the electrical conductivity of an ionised gas.

Chapter 5 describes the application of the planar electric gun to the shock compression study of aluminium powder. The conducting shockwave thereby generated in the aluminium powder sample is characterised by two types of sensors (1) coaxial contact-pin probes to obtain the Time-Of-Arrival (TOA) of the conducting shock front at discrete distances in the aluminium powder and (2) spiral resistance probes for continuous monitoring of the shockwave velocity. This work is followed by a systematic analysis of the results to validate the hydrodynamic code and EOS models of chapter 4.

In Chapter 6, the mathematical model for the electric gun is extended to the case of a cylindrical implosion (as compared to the planar case of chapter 3). The hydrodynamic model is modified by the inclusion of Maxwell's equations to obtain a magnetohydrodynamic (MHD) model for magnetic flux compression by cylindrical implosion. The performance of the MHD model is demonstrated by a detailed analysis of an explosive driven shockwave flux compression experiment conducted by Nagayama et al [29] using metallic powder.

Chapter 7 describes the detailed design of the major components of the cylindrical imploder and the experimental programme for shockwave flux compression using aluminium powder. The TOA data thereby obtained is analysed, using the new electric gun model of chapter 3 to provide useful insight into the implosion process. To understand this process, the rate of change of magnetic flux density ($B\text{-dot}$) is analysed using (1) a simple model for flux compression and (2) the MHD model of chapter 6. Although the quality of the foil explosion was not ideal, the large stand-off between the exploding foil and the powder assembly nevertheless allowed the flyer to be accelerated to an impact velocity of between 1.1 km/s and 1.5 km/s , thus enabling magnetic flux densities of about 40 T to be obtained from an initial flux density of 6 T .

Chapter 8 details experiments aimed at producing a high-voltage pulse by installing a helical coil (surrounded by a thin layer of aluminium powder) inside the cylindrical

imploder in a dynamic transformer configuration. Although experiment results were obtained for a pulse of only about 10 kV peak voltage and $3\text{ }\mu\text{s}$ duration, the data nevertheless provided a unique insight into the mechanism of high-voltage generation by exploding foil flyer impact. A simplified analysis and design method that combines the shock propagation model with the dynamic transformer model is described to allow a systematic design and performance prediction of such transformer. Performance limits are indicated for the present cylindrical imploder configuration.

Conclusions and suggestions for future work are given in chapter 9.

SHOCKWAVE MAGNETIC FLUX COMPRESSION

This chapter details the fundamental equations for shockwaves, together with different shockwave generation techniques that may have relevance to magnetic flux compression by cylindrical implosion technique. The principle for explosively driven shockwave magnetic flux compression that utilises the shock-compressed conducting front in a material with a variable electrical conductivity is described. This is followed by a brief outline of the research approach adapted to achieve capacitor-bank driven shockwave magnetic flux compression under laboratory conditions.

2.1 Shockwaves

A shockwave is caused by a very high-pressure disturbance moving through a material. The disturbance in a shock is neither smooth nor continuous, but is discontinuous as shown in Fig 2-1. The shock pressure is much higher than that in a sound wave, and may indeed stress it well beyond the elastic limit. The material does not then return to its original state after release of the pressure, and the irreversible work performed on the material may cause plastic (or permanent) deformation.

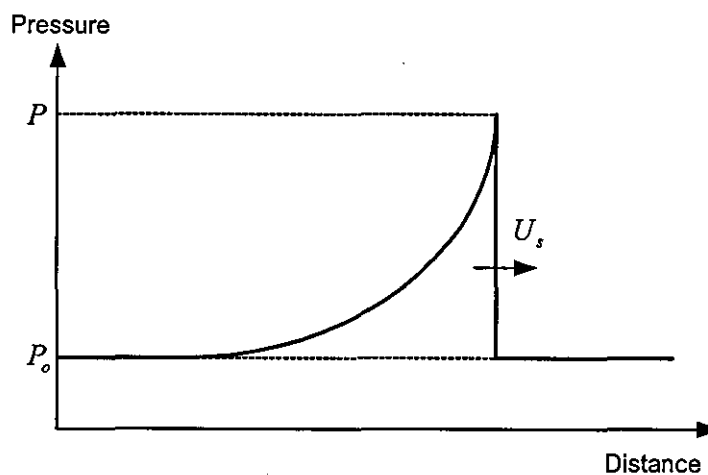


Figure 2-1 Pressure variation in a shockwave.

2.1.1 Shock Jump Equations

As a shockwave moves through a material, the mass, momentum and energy are all conserved across the shock front. The shock process neither creates nor destroys mass or energy. The conservation of the three quantities mentioned above leads to three equations – termed the Rankine-Hugoniot shock-jump equations - that describe the shock process.

material behind shock front		material ahead of shock front	
mass density	ρ	U_s →	ρ_o
pressure	P		P_o
particle velocity	u_p		$u_o = 0$
energy density	ε		ε_o

Figure 2-2 Definition of shockwave parameters.

Using the nomenclature in Fig 2-2, the shock-jump equations can be written as

conservation of mass

$$\rho_o(U_s - u_o) = \rho(U_s - u_p) \quad (2-1)$$

conservation of momentum

$$P - P_o = \rho_o(U_s - u_o)(u_p - u_o) \quad (2-2)$$

and conservation of energy

$$Pu_p - P_o u_o = \rho_o(U_s - u_o) \left[(\varepsilon - \varepsilon_o) + \frac{1}{2}(u_p^2 - u_o^2) \right] \quad (2-3)$$

If the material ahead of the shock front is at rest $u_o = 0$, and if the ambient pressure P_o prior to the arrival of the shock is sufficiently small for it to be considered as zero, equations (2-1) – (2-3) may be simplified to

$$\rho_o U_s = \rho(U_s - u_p) \quad (2-4)$$

$$P = \rho_o U_s u_p \quad (2-5)$$

$$\text{and} \quad \varepsilon - \varepsilon_o = \frac{1}{2} P \left(\frac{1}{\rho_o} - \frac{1}{\rho} \right) \quad (2-6)$$

For the case of a shockwave in air or a gas, the above equations can be combined with the ideal gas EOS to yield expressions for the compressed state (behind the shockwave) as a function of the (usually) known state ahead of the shockwave. The EOS expresses the energy density for both the material ahead of and behind the shock front as a function of pressure and density, so that

$$\varepsilon_o = \frac{P_o}{\rho_o(\gamma - 1)} \quad (2-7)$$

$$\text{and} \quad \varepsilon = \frac{P}{\rho(\gamma - 1)} \quad (2-8)$$

Substituting into the energy equation (2-6) we obtain

$$\frac{P}{P_o} = \frac{1 - \frac{(\gamma + 1)}{(\gamma - 1)} \frac{\rho}{\rho_o}}{\frac{\rho}{\rho_o} - \frac{(\gamma + 1)}{(\gamma - 1)}} \quad (2-9)$$

Equation (2-9) can be combined with the shock velocity from equations (2-1) and (2-2) to give

$$U_s = \sqrt{\left(\frac{\rho}{\rho_o} \right) \frac{P - P_o}{\rho - \rho_o}} \quad (2-10)$$

and with the definition for the local speed of sound

$$c_s = \sqrt{\frac{\gamma P_o}{\rho_o}} \quad (2-11)$$

to yield

$$\frac{U_s}{c_s} = \sqrt{\frac{2}{(\gamma + 1) \frac{\rho_o}{\rho} - (\gamma - 1)}} \quad (2-12)$$

Eliminating the shock velocity U_s from equations (2-1) and (2-2) gives the particle velocity as

$$u_p = \sqrt{(P - P_o) \left(\frac{1}{\rho_o} - \frac{1}{\rho} \right)} \quad (2-13)$$

which when combined with equation (2-9) and the local sound speed yields

$$\frac{u_p}{c_s} = \left(1 - \frac{\rho_o}{\rho} \right) \sqrt{\frac{2}{(\gamma + 1) \frac{\rho_o}{\rho} - (\gamma - 1)}} \quad (2-14)$$

The ratio of pressure $\frac{P}{P_o}$ across the shock front is usually called the *shock strength*, and

the density ratio $\frac{\rho}{\rho_o}$ across the shock front is known as the *compression ratio*. The

shock strength equation (2-9) can be re-arranged to obtain the compression ratio as

$$\frac{\rho}{\rho_o} = \frac{1 + \frac{(\gamma + 1)}{(\gamma - 1)} \frac{P}{P_o}}{\frac{P}{P_o} + \frac{(\gamma + 1)}{(\gamma - 1)}} \quad (2-15)$$

2.1.2 Conditions for Strong Shock

From equation (2-9), it can be seen that as the denominator approaches zero, the pressure behind the shock front will approach infinity. The condition for a strong shock is therefore that

$$\frac{\rho}{\rho_o} = \frac{(\gamma + 1)}{(\gamma - 1)} \quad (2-16)$$

2.2 Generation of Shockwave for Dynamic Compression of Material

2.2.1 Explosive Driven Technique

Explosive driven systems have been developed over many years to generate a plane shockwave in a target sample (see Fig 2-3) for EOS studies [30], [31]. A plane wave generator in the form of a conical explosive lens is commonly used to transform a point detonation (as produced by a detonator), into a plane detonation wave. The pressure obtained by flyer impact is significantly higher than that by an explosive in direct contact.

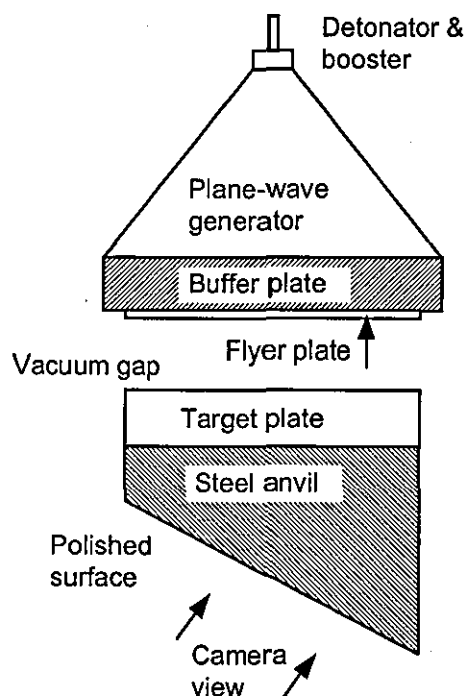


Figure 2-3 Plane shockwave generation technique by explosive.

The generation of cylindrically converging shockwaves by explosives usually requires an array of exploding bridge-wire (EBW) detonators arranged in a ring, to achieve a close to simultaneous release of explosive energy. Innovative solutions involving the use of an array of such wires embedded in explosive have been reported [32]-[33]. As an alternative to using explosives arranged in a cylindrical form, Russian researchers have described the use of a tube of explosive with a rectangular cross section and detonated along the four edges to produce the same effect [34].

Meyers and Wang [35] used a cylindrical imploding flyer configuration (Fig 2-4) for the shock consolidation of hard metal powder. Significant improvements in compaction quality were obtained for nickel-based superalloys, titanium alloys and aluminium-lithium alloys.

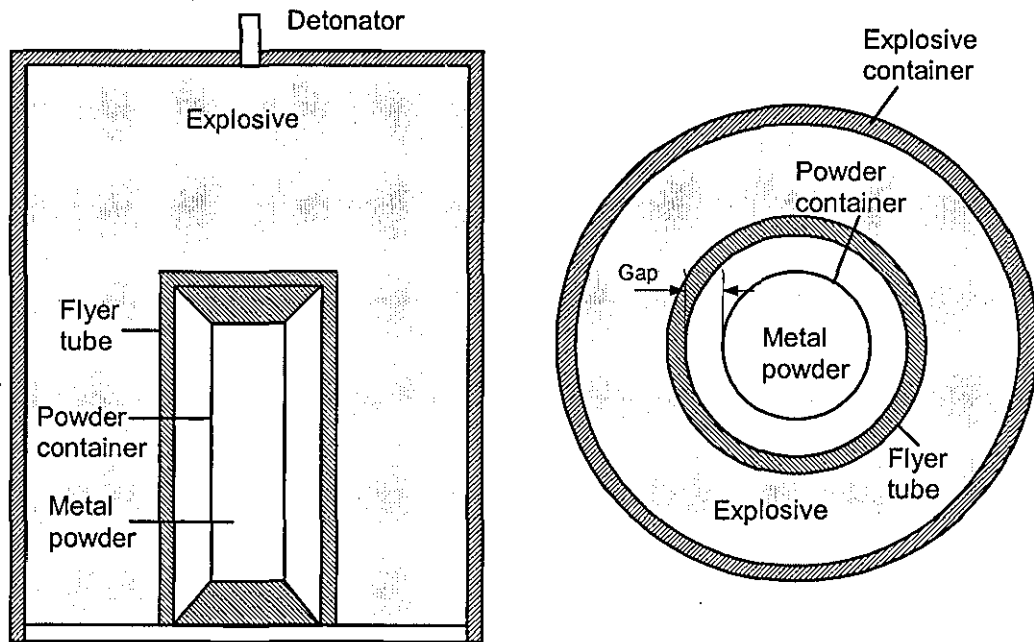


Figure 2-4 Cylindrical flyer implosion technique using explosive.

2.2.2 Gun Techniques

The gun technique uses either a propellant (e.g. a smokeless powder) or compressed gas to accelerate a flat nosed projectile to impact on a target. In general compressed gas guns are preferred, on the basis of their operating convenience and predictability of the impact velocity. To avoid driving a strong air shock ahead of the projectile, it is necessary to evacuate the gun barrel to a pressure of between 2 Pa to 5 Pa (1.5×10^{-2} to $3.0 \times 10^{-2}\text{ Torr}$), with O-ring seals on the projectile isolating the barrel from the expanding gas. The projectile head may be a flyer plate backed by low-impedance foam or honeycomb and the duration of the impact pressure pulse is governed by the thickness and diameter of the flyer plate and the shock and rarefaction wave velocities in both the flyer plate and target materials.

The gun technique has been used in several research laboratories for shockwave studies. Single-stage gas guns can accelerate projectiles with diameters in the range 50 mm to 100 mm to velocities of about 1.5 km/s. The peak pressure and duration for impact on common metals are a few tens of GPa (i.e. a few hundred kbar) and a few microseconds.

The gun technique is not however easily adapted to provide the requirements for generating a cylindrically converging shockwave.

2.2.3 Laser and Electron Beam Loading

In both these techniques a large flash of energy, from either a laser or an electron beam, impacts on the surface of a target, with the consequent rapid expansion of the surface region resulting in a shockwave travelling into the target. The main advantage of these techniques is that the shockwave initiation is essentially simultaneous over the area irradiated, although this is generally limited to less than 10 cm² by the power available. Furthermore, the distribution of energy over the irradiated area is frequently non-uniform, meaning that the peak stress will vary. The stress pulses are of the order of one nanosecond and attenuate rapidly.

In recent years, shockwaves driven by high power lasers have been widely used to study the EOSs of materials in the Megabar pressure range [36].

2.2.4 Exploding Foil Technique

In this technique, a thin metal foil is vaporised or exploded by a high current pulse (see Fig 2-5). This causes a thin dielectric plate adjacent to the foil to be accelerated to a high velocity along a short, evacuated space, usually termed the barrel. After a short free flight the plate impacts on the target, where it produces a short-duration flat-top stress pulse.

Dennen and Wilson [37] generated an imploding shockwave by electrically exploding thin metallic foils on the inner surface of glass cylinders. Measurements of the resulting

shock motion showed close agreement with predictions using a constant energy analysis. However, in contrast to an exploding shockwave, the imploding wave is inherently unstable.

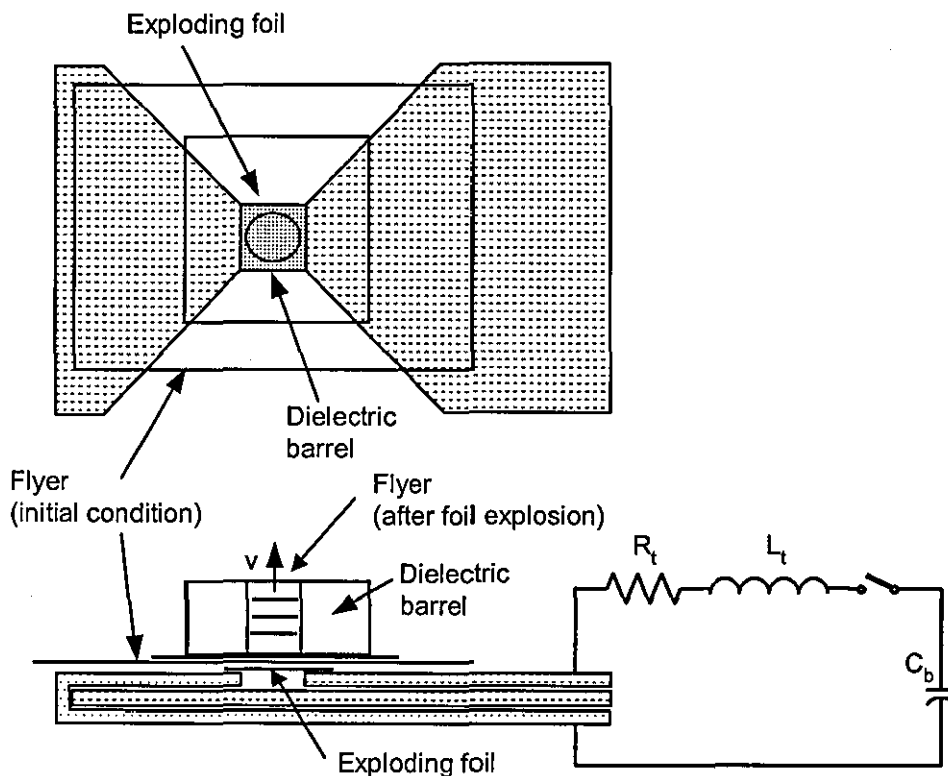


Figure 2-5 Exploding foil technique for acceleration of dielectric flyer.

While the technique of exploding metallic foils in planar geometry has been developed into a well-established technique for conducting research in shockwave physics [38]-[40], their exploitation in cylindrical geometry has not led to the development of a cylindrical version of the electric gun. A coaxial version has been proposed for flux compression [41], but no experimental result has been reported.

2.3 Magnetic Flux Compression by Cylindrical Implosion

An explosively driven implosive device (Fig 2-6) consists essentially of two components; the explosive-liner system that provides sufficient energy for a uniform implosion with a high implosion speed and a coil plus a pulsed-power supply to provide the initial magnetic flux.

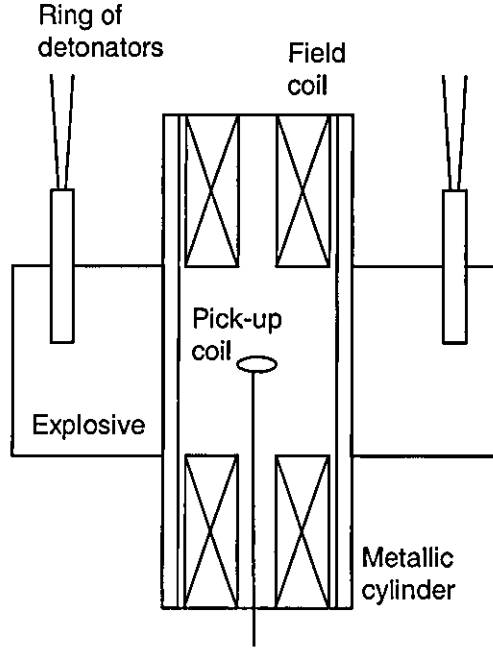


Figure 2-6 Magnetic flux compression by implosion of metallic cylinder.

2.3.1 Basic Flux Compression Equation For Cylindrical Implosion

At the heart of the implosive system is the metallic cylinder, with an initial inner radius r_o , a wall thickness δ and an axial length l , which for analytical purpose will be regarded as much greater than r_o . If the cylinder radius is reduced by the implosion in a time interval that is sufficiently short for flux loss by magnetic diffusion through the cylinder to be small, the magnetic flux is compressed and the magnetic flux density increases according to

$$B_z = B_{zo} k_{eff} \left(\frac{r_o}{r} \right)^2 \quad (2-17)$$

where B_{zo} is the initial magnetic flux density, r is the reduced radius and k_{eff} is the flux conservation coefficient.

2.3.2 Flux Diffusion Speed

A useful concept in developing a simple quantitative description of the magnetic flux diffusion loss in cylindrical implosion is the flux diffusion speed [42], given by

$$v_f = \frac{E_\theta}{B_z} = \frac{J_\theta}{\sigma B_z} = -\frac{1}{\mu_0 \sigma} \frac{1}{B_z} \frac{\partial B_z}{\partial r} \quad (2-18)$$

The magnetic flux in an imploding cylinder with an inner radius r is $\Phi = B_z \pi \cdot r^2$. The time rate of change of the magnetic flux is therefore

$$\frac{d\Phi}{dt} = \frac{d}{dt} (B_z \pi r^2) = -E_\theta \cdot 2\pi r \quad (2-19)$$

$$\text{or} \quad \frac{dB_z}{dt} = -\frac{2}{r} \left(\frac{dr}{dt} + \frac{E_\theta}{B_z} \right) B_z \quad (2-20)$$

which can be re-written by introducing the implosion speed $v_i = -\frac{dr}{dt}$ and the flux diffusion speed v_f as

$$\frac{dB_z}{dt} = \frac{2}{r} (v_i - v_f) B_z \quad (2-21)$$

Equation (2-21) illustrates the basic principle of flux compression by cylindrical implosion, with the implosion speed v_i representing the generation term and the flux diffusion speed v_f the diffusion loss term. The magnetic flux density will clearly increase if v_i is larger than v_f .

Magnetic flux diffusion through a metallic liner is associated with a current density and thus with Joule heating. During the implosion v_f increases as the electrical resistivity increases, before it finally decreases as kinetic energy is transformed into magnetic energy and heat. Flux compression comes to an end when the implosion speed equals

the flux diffusion speed, and the magnetic field reaches a maximum. In the early days of flux compression this was called 'turn-around', because it was assumed that the imploding cylinder would come to a stand-still and reverse its direction of motion. In reality the imploding cylinder continues to move with approximately the flux diffusion speed, until it collides with the probe measuring the magnetic field.

2.3.3 Magnetic Reynolds Number

The relative magnitude of the generation and flux diffusion terms in equation (2-21) is a measure of whether the magnetic field will increase before it has time to diffuse through the metallic cylinder. The commonly used concept is the magnetic Reynolds number R_e , which is the ratio of the diffusion decay time constant τ_{diff} to the compression time constant τ_{comp} .

The compression time constant is given by

$$\tau_{comp} = \frac{r}{v_i} \quad (2-22)$$

where $v_i = -\frac{dr}{dt}$ is the implosion speed.

The loss of magnetic flux through the cylinder is governed by the time constant τ_{diff} , which is the ratio of its inductance L to its resistance R , or with

$$L = \mu_o \frac{\pi r^2}{l} \quad (2-23)$$

$$\text{and } R = \frac{1}{\sigma} \frac{2\pi \left(r + \frac{\delta}{2} \right)}{l\delta} = \frac{1}{\sigma} \frac{2\pi r_{avg}}{l\delta} \quad (2-24)$$

$$\tau_{diff} = \frac{L}{R} = \mu_o \sigma \frac{r_{avg} \delta}{2} \quad (2-25)$$

The magnetic Reynolds number in a cylindrical implosion is thus

$$R_e = \frac{\tau_{diff}}{\tau_{comp}} = \mu_o \sigma \frac{r_{avg} \delta}{2} \frac{v_i}{r} \approx \mu_o \sigma \frac{v_i \delta}{2} \quad (2-26)$$

leading to a condition for an appreciable growth in the magnetic flux density as

$$R_e = \mu_o \sigma \frac{v_i \delta}{2} \gg 1 \quad (2-27)$$

2.4 Shockwave Magnetic Flux Compression

2.4.1 Principle of Operation

K. Nagayama [27] – [29] and Ye. I. Bichenkov [34] were the first to report on magnetic flux compression by means of a cylindrical converging shockwave in a material with variable electrical conductivity. The principle, illustrated by Fig 2-7, is based on the insulator-to-metallic phase transition of semiconductor materials under a very high shock pressure. The metallic phase, advancing inside the dielectric material just behind the shockwave, is used to compress an initially seeded magnetic field. This method of flux compression has the advantage that the implosion speed v_i is now equal to the shock speed U_s in the shock compressed material. For most materials, the shock speed U_s is significantly higher than the speed of the material behind the shock front u_p .

The shockwave method of flux compression is governed by [27]

$$\frac{dB_z}{B_z} = -\frac{2u_p}{U_s} \frac{dr_s}{r_s} \quad (2-28)$$

where r_s denotes the shock front position at time t and the shock speed is defined by

$$U_s = -\frac{dr_s}{dt} \quad (2-29)$$

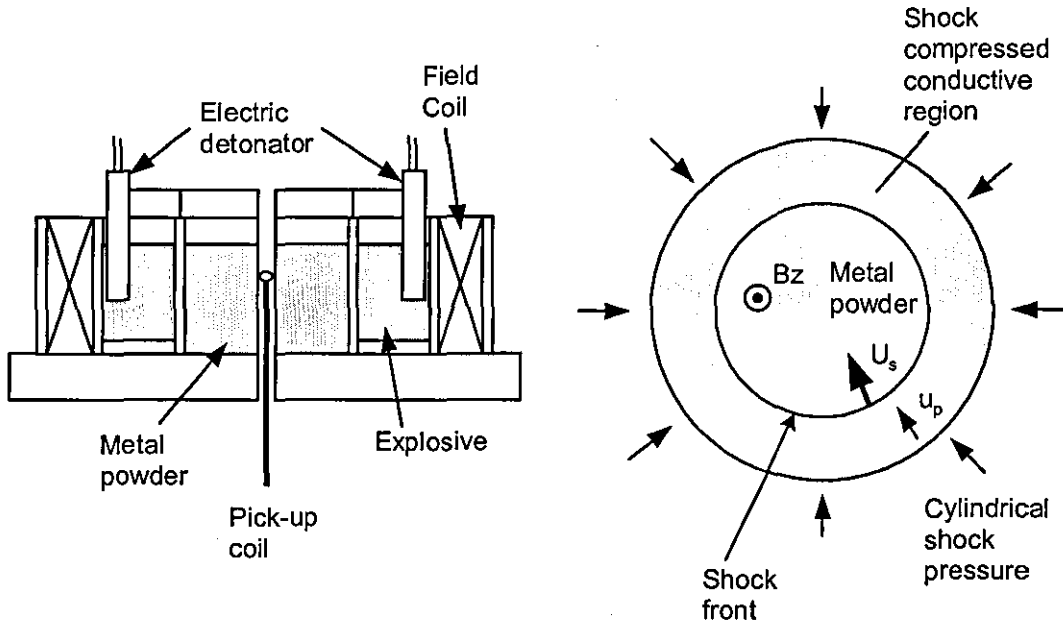


Figure 2-7 Explosively driven shockwave magnetic flux compression.

Equation (2-28) can be re-written as

$$\frac{dB_z}{dt} = \frac{2u_p}{r_s} B_z \quad (2-30)$$

Examination of equations (2-21) and (2-30) reveals that the flux diffusion speed for such a system is

$$u_p = v_i - v_f \quad \text{or} \quad v_f = U_s - u_p \quad (2-31)$$

2.4.2 Material with Variable Electrical Conductivity

a) Semiconductor Crystal

Semiconductors such as germanium and silicon have an electrical conductivity that is sensitive to applied pressure. Minomura and Drickamer [43] found a decrease in electrical resistance of six orders of magnitude in germanium at static high pressure between 12.0 and 12.5 GPa (Fig 2-8), with the large change in resistance indicating

clearly that the transition was to a metallic phase. They also reported a five to six orders of magnitude decrease in the electrical resistance of silicon samples at pressures between 19.5 and 20.0 GPa when the shear stresses are low, but a resistance drop between pressure of 13.5 and 15.0 GPa when the shear stresses are high. Since the transitions are sensitive to shear, the relation between static and shock observations is unclear but certainly one or both of the shock transitions may be to the metallic state. Current estimates for the transition pressure [44] are 19.2 GPa and 14.8 GPa for silicon and germanium respectively. Flux compression experiments using this approach have been reported previously by Nagayama [27]-[28] and Barmin and Prishchenpenko [45].

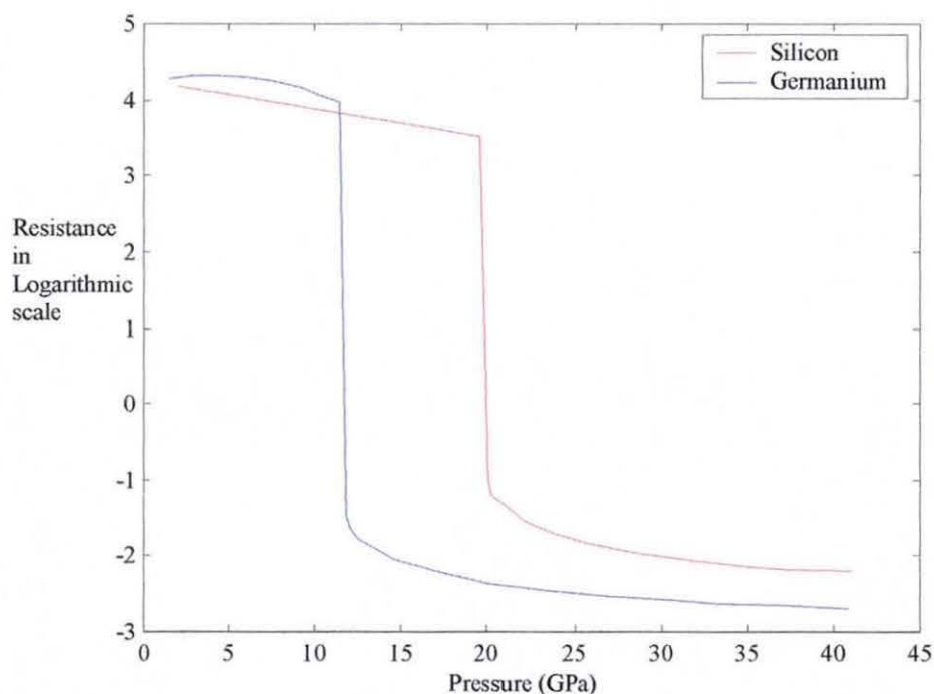


Figure 2-8 Variation with pressure of resistance of silicon and germanium, which both undergo a semiconductor to metallic transition.

Figure from Minomura and Drickhamer [43].

b) Metallic Powder

Besides semiconductor crystals, various types of metallic powder have been investigated for the compression of a magnetic field [29], [34]. Under normal, unstressed conditions, a metallic powder such as aluminium behaves as an insulator, because of the thin oxide layer existing between the grains. When compacted by a

pressure pulse, either by means of a projectile impact or by the explosion of a chemical substance, the aluminium powder changes to a good electrical conductor. The transition process is apparently achieved as a result of the very short duration deposition of high energy in the vicinity of particle surfaces, through rapid plastic deformation and friction between surfaces. The localised heating at the particle interface destroys the thin oxide layer and allows electrical conduction.

2.5 Exploding foil shockwave driven magnetic flux compression

For the proposed technique of using the energy stored in a capacitor bank to replace the explosive energy, the magnetic flux compression process may be divided into the following phases

- (1) resistive heating of the metallic (e.g. aluminium) foil to the point of explosion (Fig 2-9),
- (2) acceleration and free flight of the Mylar flyer by the exploding foil plasma. (Fig 2-10) and
- (3) impact on aluminium powder and generation of a conducting shock front that converges on the axis, thereby compressing the initial magnetic flux (Fig 2-11).

Schenk and Linhart [46] described experiments in which plasma generated by an electrically exploded cylindrical metallic foil may have been responsible for compressing an axial magnetic field to a final magnetic flux density of about $6T$. Since the Mylar flyer is accelerated by the exploding foil plasma as it converges towards the centre, it is possible that phase (2) above may be regarded as a further stage of flux compression. The flux loss during this stage will depend largely on the electrical conductivity of the plasma and the implosion speed of the foil plasma, i.e. the magnetic Reynold number associated with this process. The electrical conductivity of plasma is reviewed briefly in chapter 4.

If the exploding foil shockwave method for compressing magnetic flux proves feasible, a helical coil could be placed at the centre of the imploding device, to couple with the

rapidly changing magnetic flux and so generate high-voltage pulses in an external load (Fig 2-12)

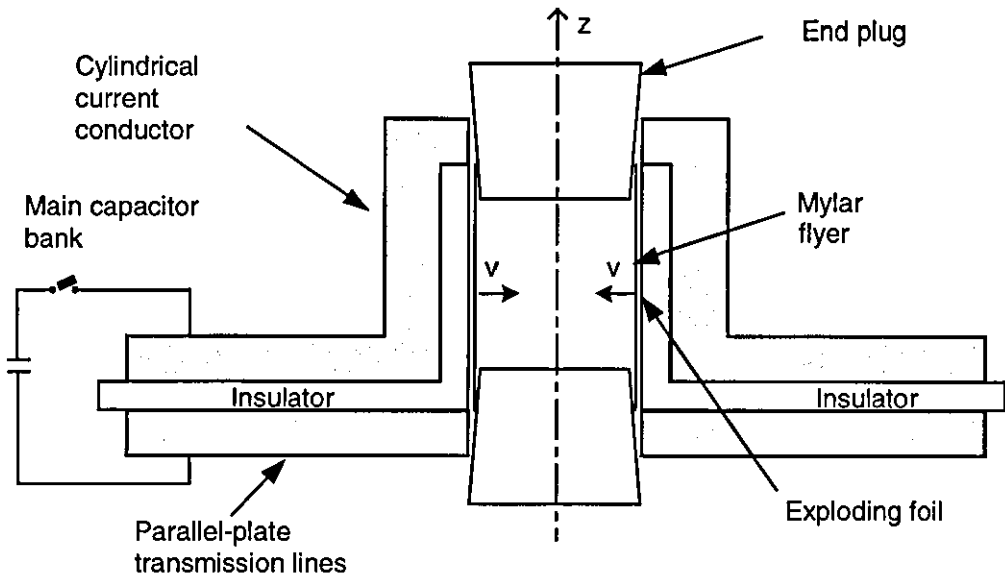


Figure 2-9 Generation of converging shockwave by exploding foil in cylindrical geometry.

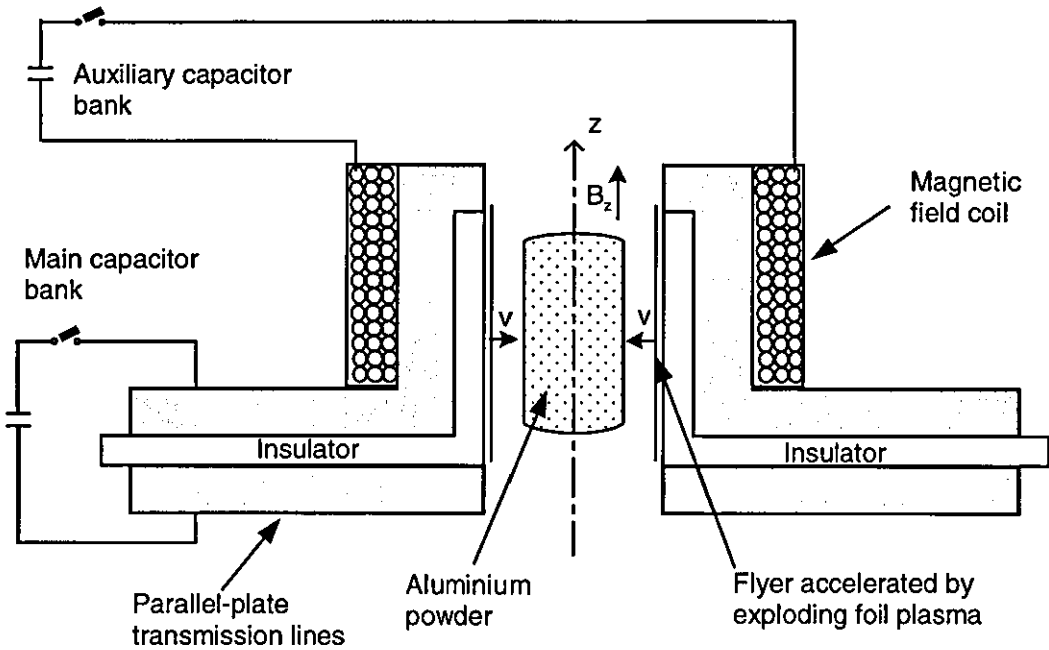


Figure 2-10 Acceleration of Mylar flyer by exploding foil plasma.

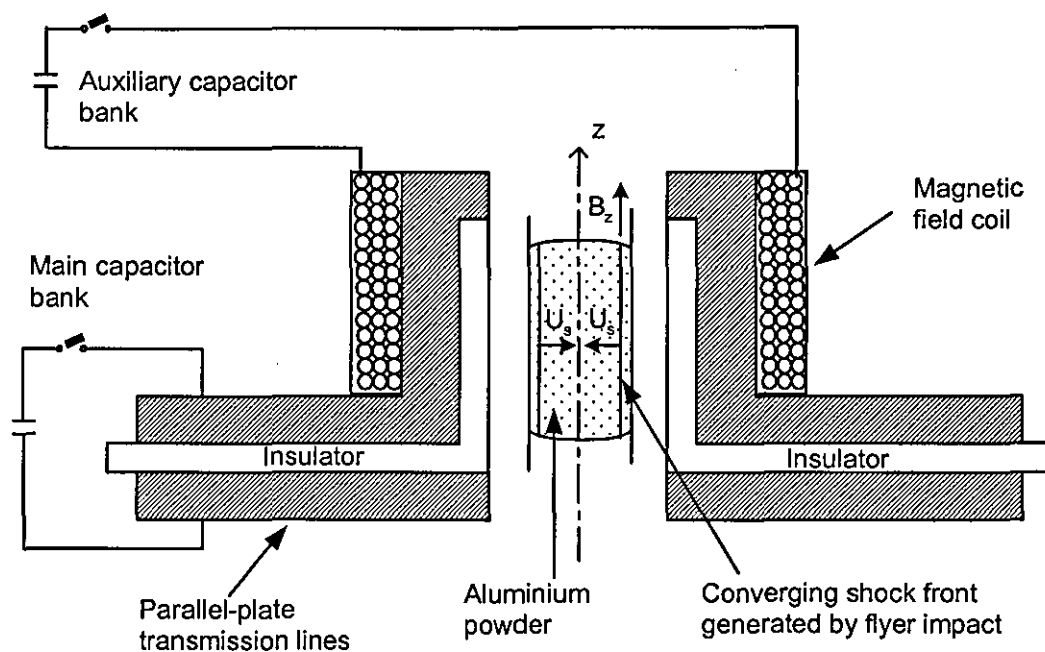


Figure 2-11 Converging conducting shock front inside aluminium powder produced by flyer impact.

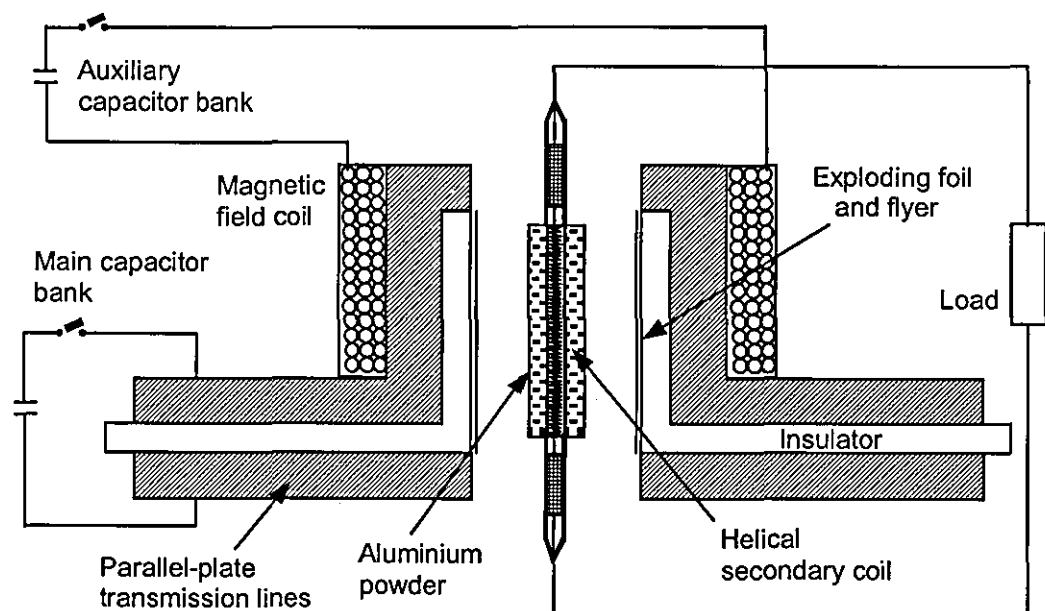


Figure 2-12 Generation of high-voltage pulses using the shockwave magnetic flux compression technique.

2.6 Conclusions

This chapter has introduced the basic principle of flux compression by cylindrical implosion (equation 2-21) and compared it with the governing equation for flux compression by shockwave (equation 2-28). The relation between the flux diffusion speed and the shock and particle speed has been highlighted in equation (2-31). If a simple relationship exists between the shock and particle velocity for a powder material, e.g. if the particle velocity may be expressed as a function of the shock velocity and some properties of the powder material (such as mass density, porosity etc.), then the description of the shockwave flux compression process can be greatly simplified. This is the key towards a complete and detailed understanding of the experimental results presented later in chapters 7 and 8.

ELECTRIC GUN

This chapter describes the development of a new mathematical model for a planar electric gun that provides a detailed description of both the electrical performance and the flyer acceleration process. Central to the new model is the combination of the Gurney equation with an ideal gas law EOS to obtain the flyer acceleration solution. Realistic prediction of the electrical circuit performance is based on an empirical model for the electrically exploded metallic foil. Beside a detailed description of the electrical current and voltage and the flyer trajectory, the computer model provides information on the foil plasma properties (mass density, pressure, temperature etc.) after explosion. Comparison of the computer prediction with experimental results is given at the end of the chapter.

3.1 Introduction

The electrical explosion of conductors has been studied extensively and it has found significant applications in electro-forming and exploding wire detonators. Both of these applications make use of the shockwave produced as the electrical conductor (or wire) explodes. Exploding wires have also been investigated for use as electrical fuses and as fast opening switches for pulse shaping in pulsed power applications.

Keller and Penning [47] and Guenther et al [48] were the first to report on the production of planar shockwaves and the acceleration of thin flyer plates. They both showed how shockwaves can be generated with a much higher pressure than is produced directly by an exploding conductor. When a thin sheet of dielectric material was placed on a metallic foil that was exploded electrically, the sheet was accelerated to several kilometers per second and produced an intense pressure (up to 15 *GPa*) when it was allowed to strike a target. The work led to the invention of the slapper detonator (also commonly known as an electric foil initiator, EFI).

Following this initial work, the Lawrence Livermore National Laboratory (LLNL) developed a general-purpose shockwave generator, which they termed the electric gun. Reports of a 87 kJ , 100 kV electric gun appeared in the 1980s [49]-[51], while in 1993 plans for an even larger 1 MJ , 120 kV gun were reported [52]. The technology involved is fairly reliable and has been applied to the area of shockwave studies to determine the shock sensitivity and threshold initiation-pressure of explosives [53] – [54].

The design of the present system is similar to that adopted previously, and Fig 3-1 shows its construction in planar geometry. The flyer is made from a dielectric material such as Mylar polyester bonded to an aluminium exploding foil (EF). Power for the gun is provided by a simple resistor-inductor-capacitor (RLC) discharge circuit. The transmission line from the capacitor bank is tapered down to the width of the exploding foil and the dielectric barrel is aligned over the exploding foil and bonded to the dielectric flyer. The leading edge of the gun barrel bore serves to cut the flyer out of the dielectric sheet while the barrel limits any sideways expansion during the plasma expansion phase. On the reverse side of the transmission line, a massive plate absorbs the recoil and directs plasma along the barrel. The plate is much heavier than the flyer and serves a purpose similar to that of an anvil, and it is sometimes referred to as the tamper. The bore of the barrel can be round, square or rectangular, and it is normally matched to the square or rectangular shape of the exploding foil.

Operating Characteristics of Exploding Foil Electric Gun

Operation of the electric gun is analysed below in two different ways (1) by considerations of the current waveform in the electrical circuit, subject to the non-linear characteristics of the exploding foil near burst and (2) by investigating the details of the acceleration process of the flyer.

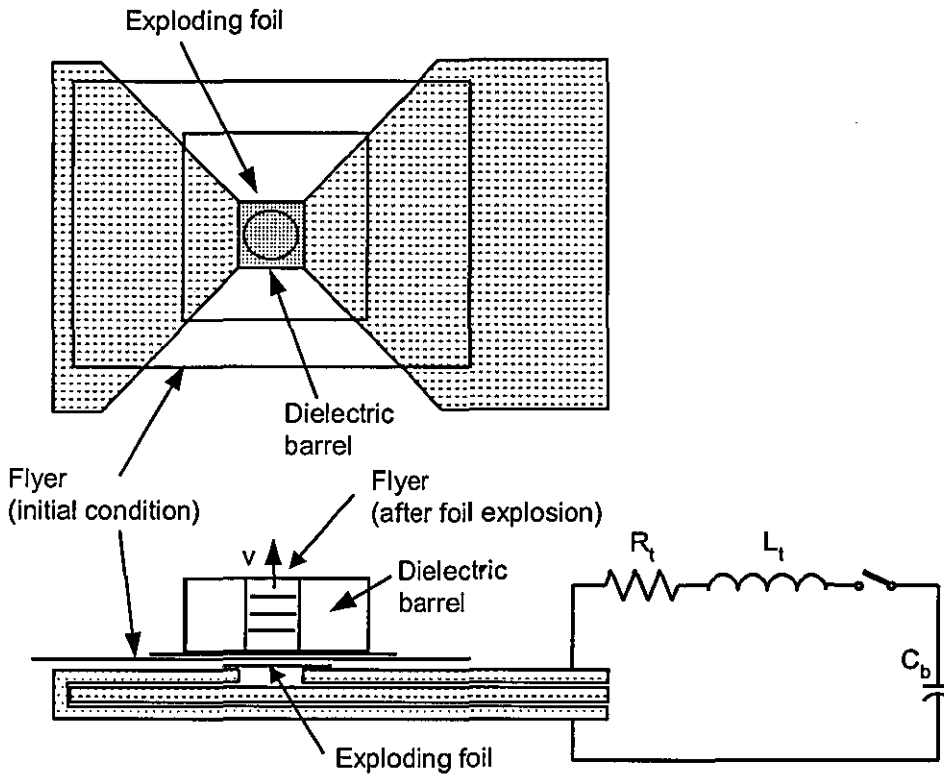


Figure 3-1 Electric gun – planar geometry.

3.2 Modelling the Flyer Acceleration Process

Different mathematical models have been proposed to describe the acceleration process of the flyer. In the following sections, two major models are outlined that are based on an electrical analogue of the Gurney model.

The Gurney model predicts the velocity of a plate accelerated by a high explosive charge having a characteristic energy density ε_G , by relating it to the maximum velocity an explosive material is capable of imparting to the plate. In a one-dimensional system, with a explosive sheet of mass C per unit area backed by a tamper of infinite mass on one side and a metallic plate of mass M per unit area on the other, the final velocity given by the Gurney model is [55]

$$v_G = \sqrt{2\varepsilon_G} \left(\frac{M}{C} + \frac{1}{3} \right)^{-\frac{1}{2}} \quad (3-1)$$

Method of Tucker and Stanton [56]

Tucker and Stanton, [56] were the first to suggest an electrical analogue of the Gurney model. They assumed that the characteristic energy density ε_G associated with the exploding foil depends only on the burst current density J_B , giving the relation

$$v_G = \sqrt{k J_B^b \left(\frac{M}{C} + \frac{1}{3} \right)^{\frac{1}{2}}} \quad (3-2)$$

where k and b are empirically determined constants.

Method of Osher [50]

Osher et al [50] used the energy balance concept, where the energy available after burst is shared between the energy required to heat up and explode the foil material and the kinetic energy of the flyer. This is coupled with an electrical analogue of the Gurney model to predict the terminal velocity of the flyer. The electric gun circuit is assumed to be optimized, so that foil burst occurs at the end of the first quarter period when nearly all the initial capacitor bank energy is available for acceleration purposes. The Gurney equation (3-1) is used to calculate the flyer velocity in terms of the mean velocity of the expanding foil plasma, with the Saha equation [57] used to estimate the degree of ionisation of the foil material. For simplicity in calculating the plasma temperature, the authors assumed that the flyer attains its terminal velocity after the plasma has expanded by 200 times. As a solution to the set of energy balance equation, the Osher model provides (amongst other outputs) an estimate of the terminal velocity of the flyer projectile.

The Osher method has been used extensively as a guide to the design of the present planar electric gun, although the assumption of an optimised gun places severe restrictions on its applicability. However, the lack of an acceleration solution, to provide the flyer velocity as a function of time, was a major motivation towards the present development of a full and detailed mathematical model.

3.2.1 Gurney Equation for Planar Geometry

The Gurney model assumes that the chemical energy of the explosive is fully transformed into kinetic energy in the explosive product and the metal flyer. Two simplifying assumptions are made concerning the behaviour of the gaseous detonation product (1) a linear velocity profile and (2) a uniform mass density as the explosive product expands.

Fig 3-2 shows an asymmetric sandwich, in which a slab of explosive of mass C per unit area is confined between a flyer of mass M per unit area and a tamper of mass N per unit area. The x -axis is normal to the flyer surface and it is assumed that the flyer moves in this direction. The initial location of the tamper and the flyer plate are x_{No} and x_{mo} respectively. Some time after the explosion, v_m is both the terminal speed of the flyer and that of the gaseous explosion product in contact with it. v_N is the terminal speed of the tamper and the gaseous product adjacent to it.

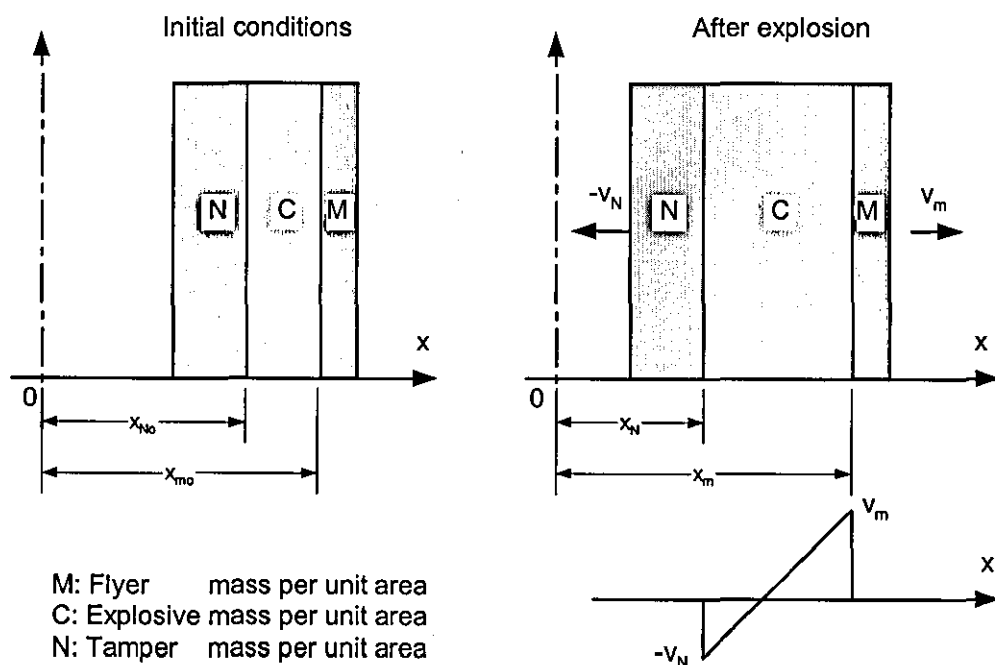


Figure 3-2 Asymmetric sandwich for planar configuration.

With the density of the explosion product assumed to be uniform

$$\rho(x) = \frac{C}{x_m - x_N} \quad (3-3)$$

and with the velocity profile for the explosion product assumed to be linear, so that

$$v(x) = -v_N + \frac{v_m + v_N}{x_m - x_N}(x - x_N) \quad (3-4)$$

the equations for the conservation of momentum and energy are respectively

$$0 = Mv_m - Nv_N + \int_{x_N}^{x_m} \rho(x)v(x)dx \quad (3-5)$$

$$\text{and} \quad C\varepsilon_G = \frac{1}{2}Mv_m^2 + \frac{1}{2}Nv_N^2 + \frac{1}{2} \int_{x_N}^{x_m} \rho(x)[v(x)]^2 dx \quad (3-6)$$

The integral in equation (3-5) can be evaluated by inserting equations (3-3) and (3-4) for the assumptions of uniform density and linear velocity profile, to give the ratio of terminal speeds as

$$A = \frac{v_N}{v_m} = \frac{\left(1 + 2\frac{M}{C}\right)}{\left(1 + 2\frac{N}{C}\right)} \quad (3-7)$$

The integral in the energy equation (3-6) can be evaluated using the assumptions of uniform density and linear velocity profile. After replacing v_N by Av_m , equation (3-6) can be re-written to give the terminal flyer (or projectile) velocity as

$$v_m = \sqrt{2\varepsilon_G} \left[\frac{M}{C} + \frac{N}{C}A^2 + \frac{1+A^3}{3(A+1)} \right]^{-\frac{1}{2}} \quad (3-7)$$

Tamper with Infinite Mass

For the case of a tamper of infinite mass $N \rightarrow \infty$, giving $A = 0$ and

$$v_m = \sqrt{2\varepsilon_G} \left(\frac{M}{C} + \frac{1}{3} \right)^{-\frac{1}{2}} \quad (3-9)$$

Open-faced Sandwich

For the case of an open-face sandwich $N \rightarrow 0$, and

$$A = 1 + \frac{2M}{C} \quad (3-10)$$

$$\text{giving } v_m = \sqrt{2\varepsilon_G} \left[\frac{M}{C} + \frac{1 + \left(1 + 2\frac{M}{C}\right)^3}{6\left(1 + \frac{M}{C}\right)} \right]^{-\frac{1}{2}} \quad (3-11)$$

An alternative expression for the flyer velocity may be obtained as

$$v_m = \sqrt{2\varepsilon_G} \left[\frac{3}{1 + 5\left(\frac{M}{C}\right) + 4\left(\frac{M}{C}\right)^2} \right]^{\frac{1}{2}} \quad (3-12)$$

3.2.2 Acceleration Solution using an Ideal Gas Law EOS

The Gurney equations can be combined with an ideal gas law EOS to yield an acceleration solution for the flyer plate. If ε_o is the chemical energy density of the unreacted explosive and ε is the internal energy density remaining in the explosive, the energy balance equation can be written

$$C\varepsilon_o = C\varepsilon + \frac{1}{2}Mv_m^2 + \frac{1}{2}Nv_N^2 + \frac{1}{2} \int_{x_N}^{x_n} \rho(x) [v(x)]^2 dx \quad (3-13)$$

in which v_m and v_N are instantaneous and not terminal velocities.

Evaluation of the final term of equation (3-13) gives

$$\frac{1}{2} \int_{x_N}^{x_m} \rho(x) [v(x)]^2 dx = \frac{C}{6} \left[\frac{v_m^3 + v_N^3}{v_m + v_N} \right]$$

so that the equation becomes

$$C\varepsilon_o = C\varepsilon + \frac{1}{2} M v_m^2 + \frac{1}{2} N v_N^2 + \frac{C}{6} \left[\frac{v_m^3 + v_N^3}{v_m + v_N} \right] \quad (3-14)$$

The equation for the conservation of momentum is, from equation (3-5),

$$0 = M v_m - N v_N + \int_{x_N}^{x_m} \rho(x) v(x) dx \quad (3-15)$$

and evaluation of the integral yields

$$\int_{x_N}^{x_m} \rho(x) v(x) dx = \frac{C}{2} (v_m - v_N)$$

$$\text{giving } \left(M + \frac{C}{2} \right) v_m = \left(N + \frac{C}{2} \right) v_N \quad (3-16)$$

$$\text{and } A = \frac{v_N}{v_m} = \frac{\left(M + \frac{C}{2} \right)}{\left(N + \frac{C}{2} \right)} \quad (3-17)$$

Replacing v_N with $A v_m$ in equation (3-14) gives

$$C\varepsilon_o = C\varepsilon + \frac{1}{2} M v_m^2 + \frac{1}{2} N (A v_m)^2 + \frac{C}{6} \left[\frac{v_m^3 + (A v_m)^3}{v_m + (A v_m)} \right]$$

$$\text{or } \varepsilon_o = \varepsilon + \frac{1}{2} \left[\frac{M}{C} + \frac{N}{C} A^2 + \frac{1 + A^3}{3(1 + A)} \right] v_m^2 \quad (3-18)$$

When $\varepsilon = 0$, the energy initially in the unreacted explosive has all been converted to kinetic energy and the terminal velocity of

$$v_m(t) = \sqrt{2\varepsilon_o} \left[\frac{M}{C} + \frac{N}{C} A^2 + \frac{1+A^3}{3(1+A)} \right]^{\frac{1}{2}} \quad (3-19)$$

is identical to the form of equation (3-7) except that ε_o is replaced by ε_G . Since the terminal velocity of an explosively driven metal has been used [55] to determine the chemical energy density in explosives, we equate ε_o to ε_G .

By assuming an ideal gas EOS for the explosion product [58]

$$\varepsilon = \frac{P}{\rho(\gamma-1)} \quad (3-20)$$

we obtain from equation (3-18)

$$\varepsilon_G = \frac{P}{\rho(\gamma-1)} + \frac{1}{2} \left[\frac{M}{C} + \frac{N}{C} A^2 + \frac{1+A^3}{3(1+A)} \right] v_m^2 \quad (3-21)$$

For a planar configuration, in which M is the flyer mass per unit area, Newton's equation for motion is

$$P = M \frac{dv_m}{dt} \quad (3-22)$$

Defining a new constant by

$$B = \frac{M}{C} + \frac{N}{C} A^2 + \frac{1+A^3}{3(1+A)} \quad (3-23)$$

we obtain from equation (3-21)

$$\varepsilon_G = \frac{1}{\rho(\gamma-1)} M \frac{dv_m}{dt} + \frac{1}{2} B v_m^2$$

or
$$\frac{dv_m}{dt} = \frac{\rho(\gamma-1)(2\varepsilon_G - B v_m^2)}{2M} \quad (3-24)$$

To obtain an ordinary differential equation with only one unknown, ρ is eliminated using the initial conditions given in Fig 3-2 that at $t = 0$, $x_m = x_{mo}$ and $x_N = x_{No}$. As the motion proceeds to a later time τ , we have

$$x_m = x_{mo} + \int_0^\tau v_m(t) dt \quad (3-25)$$

and
$$x_N = x_{No} - \int_0^\tau v_N(t) dt = x_{No} - A \int_0^\tau v_m(t) dt \quad (3-26)$$

By combining these equations and eliminating the integral, we find that

$$x_N = x_{No} - A(x_m - x_{mo}) \quad (3-27)$$

and from the conservation of mass

$$\rho = \frac{C}{(x_m - x_N)} \quad (3-28)$$

substituting for x_N , from equation (3-27), gives

$$\rho = \frac{C}{x_m(1+A) - Ax_{mo} - x_{No}} \quad (3-29)$$

which allows ρ to be eliminated from equation (3-24), to give

$$\frac{dv_m}{dt} = \frac{C}{2M} \frac{(\gamma-1)(2\varepsilon_G - B v_m^2)}{[x_m(1+A) - Ax_{mo} - x_{No}]} \quad (3-30)$$

which together with

$$\frac{dx_m}{dt} = v_m \quad (3-31)$$

forms a system of coupled first-order differential equations that can be solved numerically. Once the flyer trajectory has been found from the solution of equations (3-30) and (3-31), the shock pressure generated by the exploding foil in equation (3-22) can be re-written as

$$P_{ex} = \frac{C}{2} \frac{(\gamma - 1)(2\varepsilon_G - Bv_m^2)}{[x_m(1 + A) - Ax_{mo} - x_{No}]} \quad (3-32)$$

3.2.3 Adiabatic Constant, γ

For an ideal gas, the adiabatic constant γ is related to the specific heat at constant pressure C_p and the specific heat at constant volume C_v by

$$\gamma = \frac{C_p}{C_v} \quad (3-33)$$

For air and for most diatomic gases (such as oxygen, hydrogen, nitrogen), the value of γ is usually taken as 1.4, while for most explosives it is known to vary between 1.3 and 3.0. However a value for γ of 2.0 [59] provides a good approximation to the plasma state in a uniform magnetic field, and this value will be used in the simulation model for the electric gun that follows.

3.2.4 Prediction of Flyer Velocity

If the electrical explosion of the metallic foil is treated as the electrical analogue of the explosive driven asymmetric sandwich, the foil mass m_f is related to the explosive mass C per unit area by the expression

$$C = \frac{m_f}{l_f w_f} = \rho_f \delta_f \quad (3-34)$$

Similar expressions follow for the tamper and flyer mass per unit area as

$$M = \frac{m_p}{l_f w_f} = \rho_{flyer} \delta_{flyer} \quad (3-35)$$

$$\text{and } N = \frac{m_t}{l_f w_f} = \rho_{temper} \delta_{temper} \quad (3-36)$$

It is common practice to assume for an electric gun that the tamper is massive compared with both the flyer and explosive masses, so that

$$N = \rho_{temper} \delta_{temper} = 10^5 \rightarrow \infty \quad (3-37)$$

and equation (3-9) for infinite tamper may be used to predict the terminal flyer velocity. Since the mass densities of both the exploding foil ρ_f and the flyer ρ_{flyer} are usually known, the terminal flyer velocity can be estimated as a function of the flyer thickness δ_{flyer} and the characteristic Gurney energy density ε_G . This is shown in Fig 3-3 and Table 3-1 for flyer thicknesses between $75 \mu m$ and $300 \mu m$ and for Gurney energy densities between $1 MJ/kg$ and $20 MJ/kg$. For calculation purposes, $25.4 \mu m$ thick aluminium foil has been chosen as the exploding metallic foil.

Fig 3-3 shows that, for example, a $250 \mu m$ thick Mylar flyer at a Gurney energy density of $20 MJ/kg$ can achieve a terminal flyer velocity slightly greater than $3 km/s$, which implies that a burst energy density of about $20 MJ/kg$ is required to achieve a velocity of $3 km/s$ for the $250 \mu m$ thick Mylar flyer used in shock compression study of aluminium powder in chapter 5.

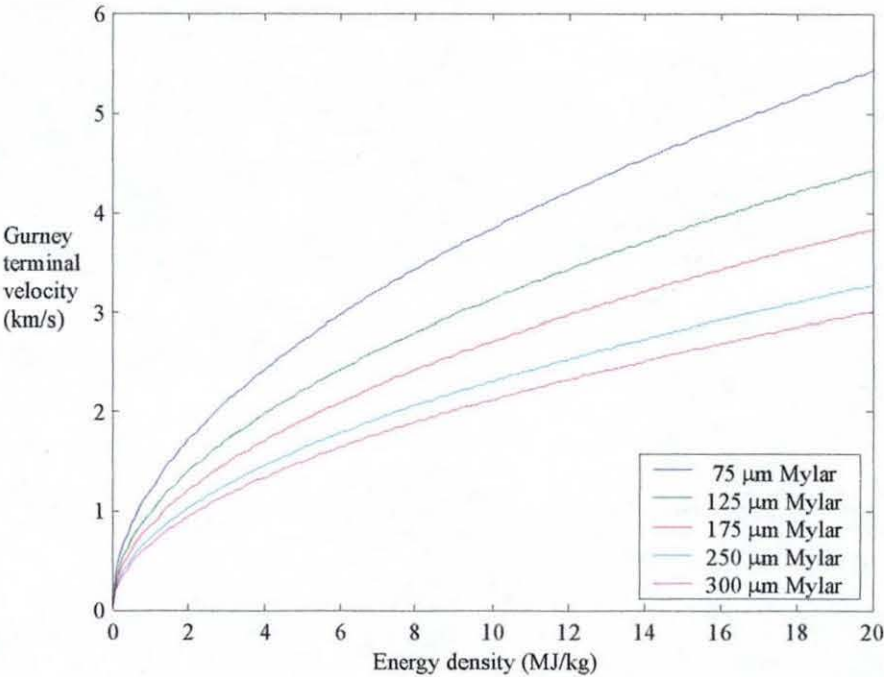


Figure 3-3 Gurney terminal velocity for different flyer thicknesses and energy densities.

Table 3-1 Gurney terminal velocity for Mylar flyer.

ε_G (MJ / kg)	Gurney velocity (km / s)	
	250 μm Mylar flyer	75 μm Mylar flyer
1	0.73	1.21
5	1.65	2.72
10	2.31	3.84
15	2.83	4.70
20	3.27	5.43

The velocity and trajectory of the flyer can be obtained by solving equations (3-30) and (3-31) for different combinations of energy density and flyer thickness, and Fig 3-4 shows that all the flyer velocities have the characteristic shape of a critically damped step response. Normalisation of the result is possible by introduction of the non-dimensional variables $\frac{v(t)}{v_G}$ and $\frac{\sqrt{2\varepsilon_G}}{\delta}t$, giving the result shown in Fig 3-5.

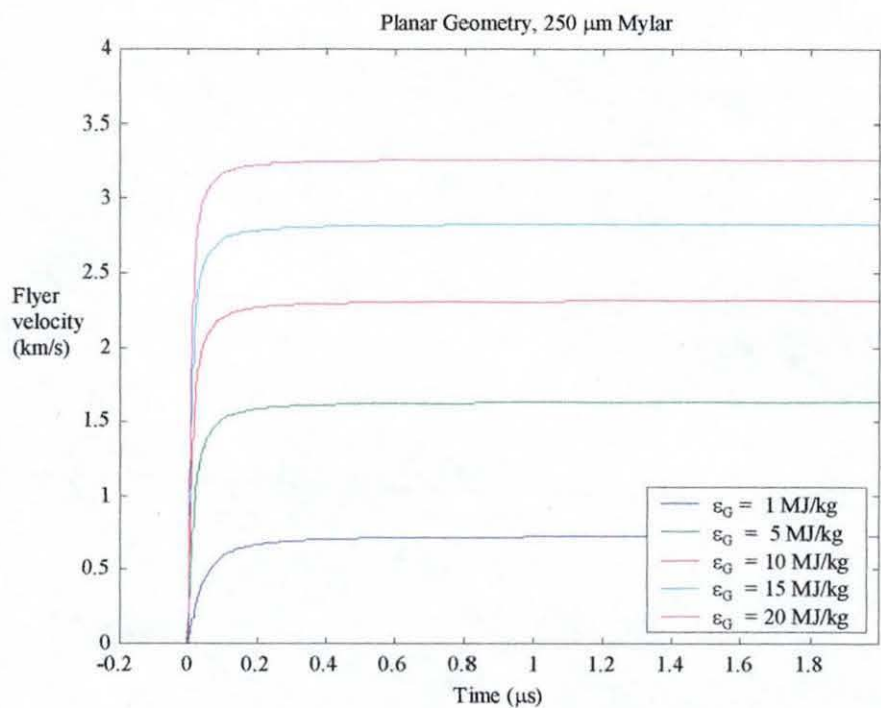


Figure 3-4 Flyer acceleration solution for 250 μm thick Mylar flyer.

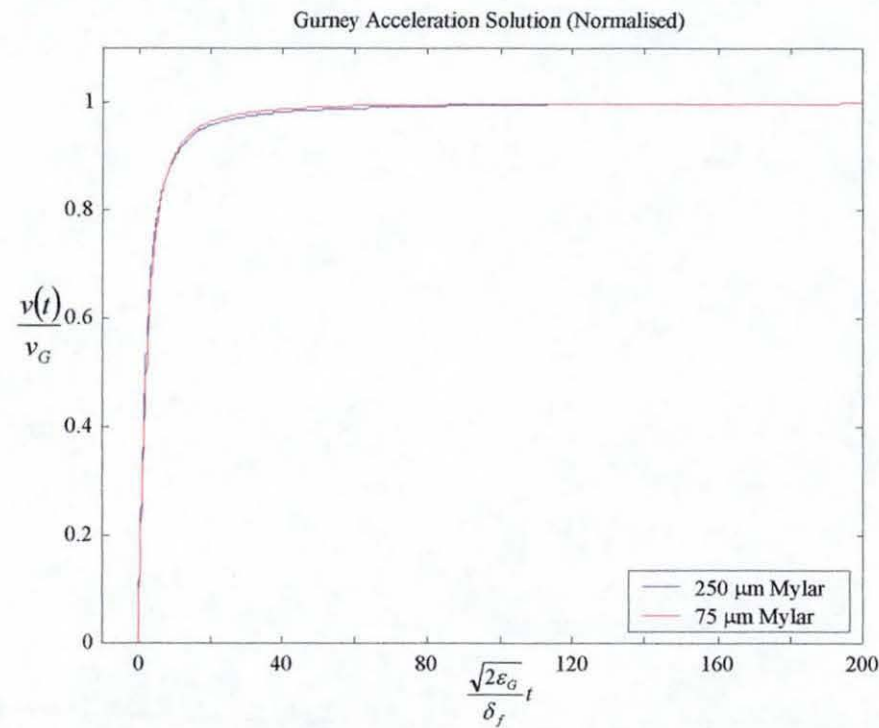


Figure 3-5 Normalised solution for flyer acceleration.

3.2.5 Estimation of Shock Pressure Generated by the Exploding Foil

Figs 3-6 and 3-7 show the shock pressure calculated using equation (3-32) for Mylar flyers of $250\ \mu\text{m}$ and $75\ \mu\text{m}$ thickness. The peak value of the pressure pulse is directly proportional to the Gurney energy density. The longer duration of the pulse for the thicker flyer implies that because it is heavier a longer time is needed for it to reach terminal velocity. After that, the foil pressure behind the Mylar flyer falls to zero. The peak explosion pressure at a particular energy density is independent of the flyer thickness.

Fig 3-8 shows the linear relationship between the peak pressure and the energy density corresponding to the ideal gas law. Essentially, the explosion process is treated as instantaneous. At foil burst, the entire volume is immediately transformed to the gaseous state under a high pressure corresponding to a particular explosive energy ε_o , which is followed by a blast expansion of the volume of this highly compressed hot gas.

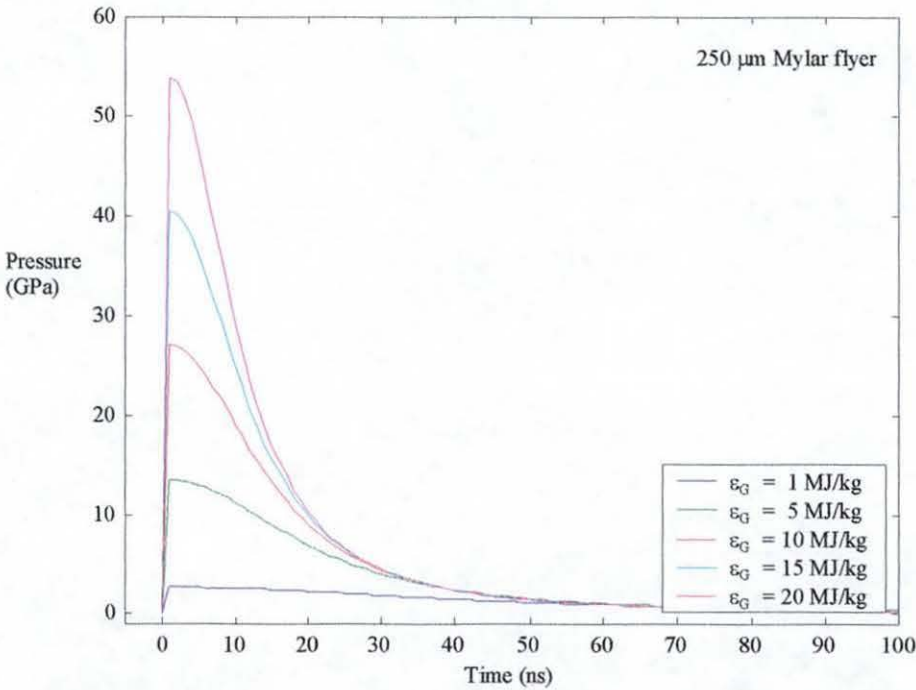


Figure 3-6 Foil explosion pressure for a $250\ \mu\text{m}$ Mylar flyer.

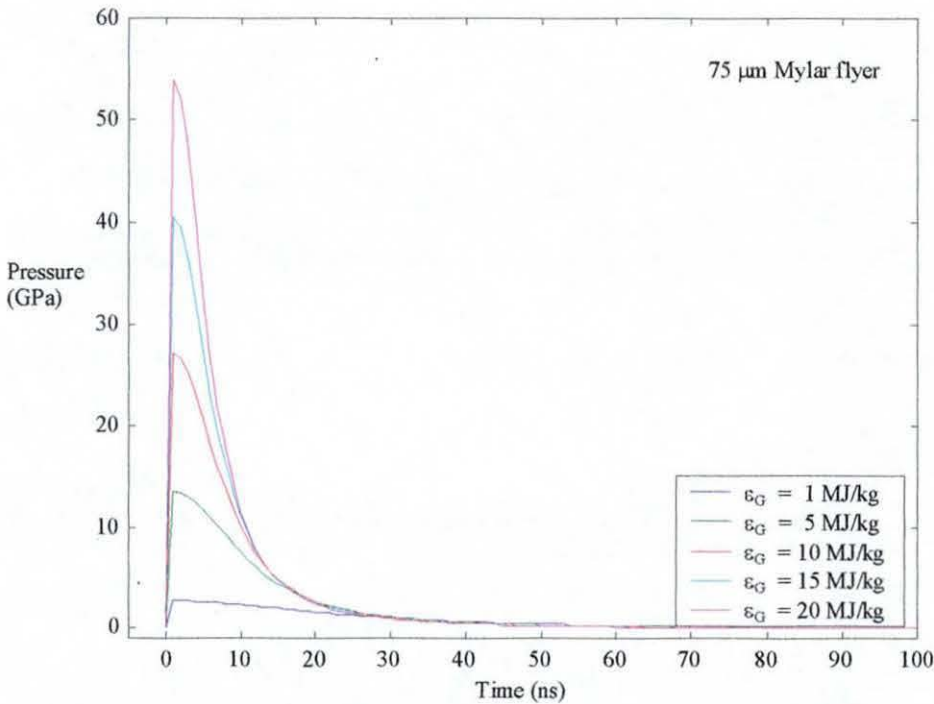


Figure 3-7 Foil explosion pressure for a 75 μm Mylar flyer.

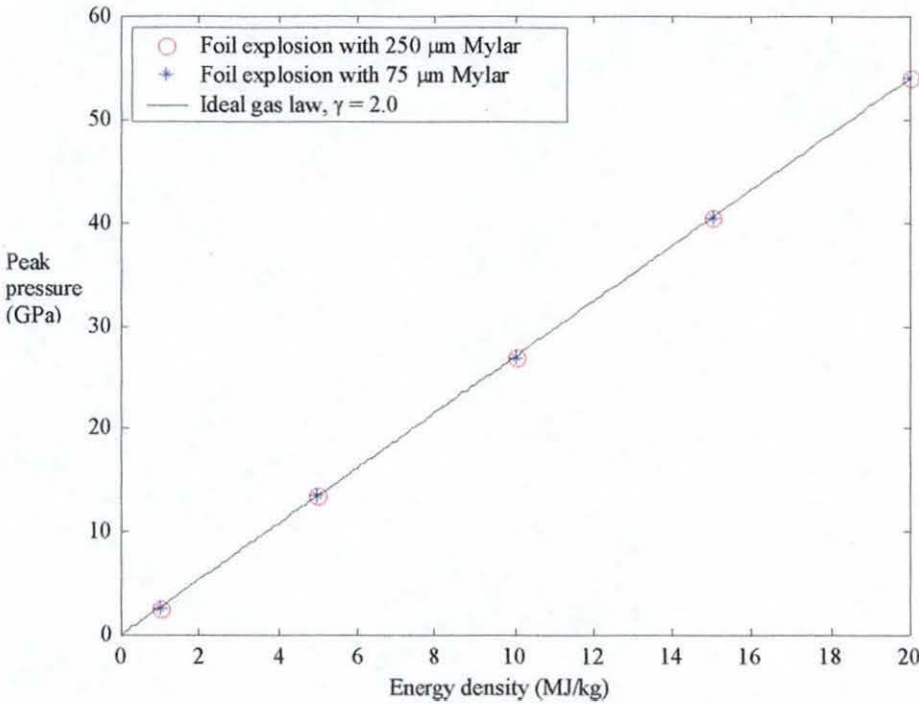


Figure 3-8 Peak pressure at point of explosion as a function of energy density ϵ_0 with adiabatic exponent $\gamma = 2.0$.

The pressure pulse obtained by equation (3-32) may be used to represent the foil burst and flyer acceleration in a hydrodynamic or MHD calculation. Fig 3-9 suggests that the pulse can conveniently be represented by a mathematical function consisting of two parts (1) a linearly decreasing function followed by (2) an exponentially decaying function, or

$$P = \begin{cases} P_{\max} - \left(\frac{P_{\max} - P_1}{t_1} \right) t & \text{if } 0 < t < t_1 \\ P_1 \exp\left(-\frac{t - t_1}{\tau}\right) & \text{if } t \geq t_1 \end{cases} \quad (3-38)$$

where the values of the constants P_{\max} , P_1 , t_1 and τ that give the best fit with the Gurney model results are given in Tables 3-2 and 3-3.

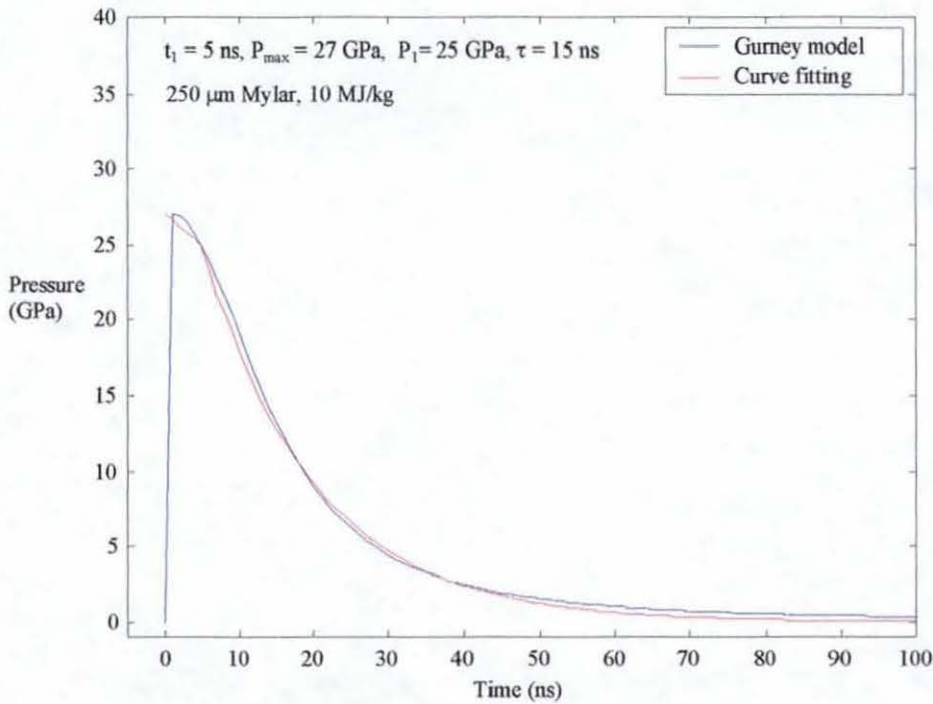


Figure 3-9 Approximate analytical description of explosion pressure.

Table 3-2 Foil explosion pressure for 250 μm Mylar flyer.

Energy density (MJ/kg)	Peak pressure (P_{max} , GPa)	Time delay (t_1 , ns)	Pressure (P_1 , GPa)	Time constant, (τ , ns)
1	2.7	15	2.5	50
5	13.5	8	12	20
10	27	5	25	15
15	40.5	5	36	12
20	54	5	50	10

Table 3-3 Foil explosion pressure for 75 μm Mylar flyer.

Energy density (MJ/kg)	Peak pressure (P_{max} , GPa)	Time delay (t_1 , ns)	Pressure (P_1 , GPa)	Time constant (τ , ns)
1	2.7	8	2.5	25
5	13.5	4	13	10
10	27	3	26	8
15	40.5	3	38	6
20	54	2.5	52	5

The results in Tables 3-2 and 3-3 compare well with those reported by Keller and Penning [47], who determined the shock pressure from the measured free-surface jump-off velocity and a linear $U_s - u_p$ EOS. Their reported result of a square pressure pulse of 8 GPa having a duration of 100 ns for a 125 μm Mylar polyester flyer is within the range of values predicted by the Gurney acceleration solution. Fig 3-8 shows that a peak pressure of 8 GPa corresponds to an instantaneous release of energy at a burst energy density of about 3 MJ/kg .

3.3 Empirical Modelling of Exploding Foil

A metallic exploding foil undergoes a rapid change in resistivity as it passes from a solid to a liquid, on to a weakly ionised vapour or plasma, and finally to a fully ionised plasma. Several empirical models have been proposed to describe the physics of exploding foils in a manner suitable for numerical calculation and the prediction of circuit performance.

3.3.1 Action Integral Method

The earliest model of an exploding foil was based on a control parameter $g(t)$ termed the action integral [60]

$$g(t) = \int_0^t [J(\tau)]^2 d\tau \quad (3-39)$$

where $J(t)$ is the instantaneous current density. Experimentally, the action integral to the time of burst has been shown [60] to be approximately constant for a given material and to be almost independent of the power-supply current waveform.

3.3.2 Tucker and Toth Model

Humphries Jr reported [61] an electrical resistivity model based on a combination of the SESAME [62] electrical conductivity data and the Tucker and Toth model [63] for exploding wires. He replaced the portion of the theoretical electrical conductivity data (in the low temperature and solid density region) in the SESAME EOS database by the empirical data obtained by Tucker and Toth, to obtain an exploding wire model that agrees well with experimental data. The empirical model of Tucker and Toth is reproduced in Fig 3-10.

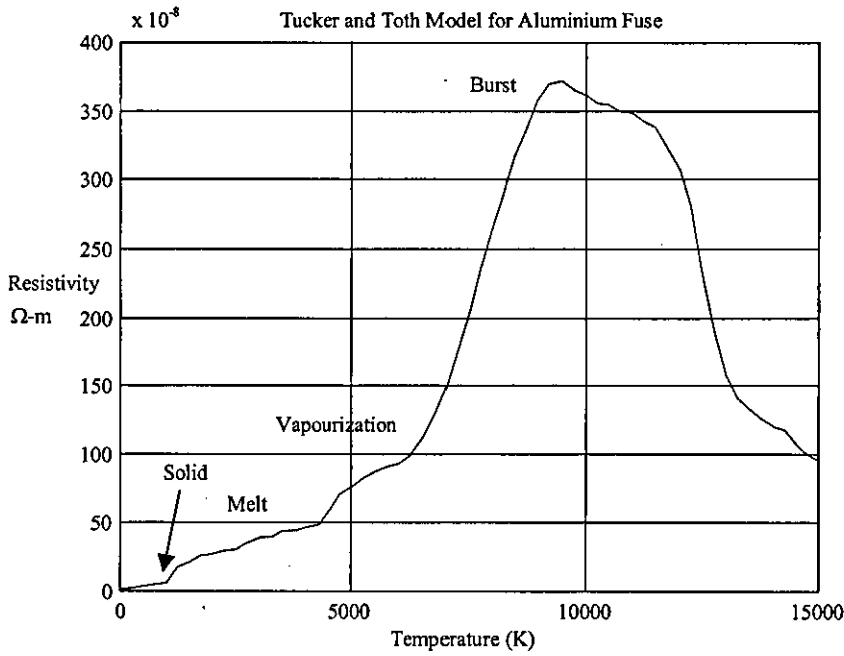


Figure 3-10 Aluminium fuse resistivity due to Tucker and Toth [63].

3.3.3 AFWL Model

The AFWL has formulated an empirical model to describe the fractional increase in resistance of a aluminium foil as a function of the electrical energy deposited per unit mass of the foil. This model, described by Roderick et al [64] and Lindemuth et al [65], has been found to be both simple and reasonably accurate. Empirical models deduced from voltage and current measurements of $17 \mu\text{m}$ and $25.4 \mu\text{m}$ copper foils and used in modelling exploding foil switches have also been reported [26]. The fractional

resistance increase $\frac{R_f}{R_{fo}}$ is obtained by plotting the instantaneous foil resistance R_f against the specific deposited energy ε .

The AFWL model for aluminium foil reproduced in Fig 3-11 shows the monotonic increase in resistance that is characteristic of opening switch (or fuse) applications, while the Tucker and Toth model shows a fall in resistivity after foil burst in the case of exploding bridge-wires (EBWs). This distinction is probably traceable to the medium surrounding the foil at the point of burst, since if it inhibits both arcing and the formation of a spark channel the resistance after foil burst will continue to increase. For electric gun applications, observations from current waveforms at Loughborough

University indicate that current continues to flow after foil burst and may contribute to further acceleration of the flyer by magnetic pressure. An empirical model for the exploding foil in electric gun operations would take a form similar to the Tucker and Toth model.

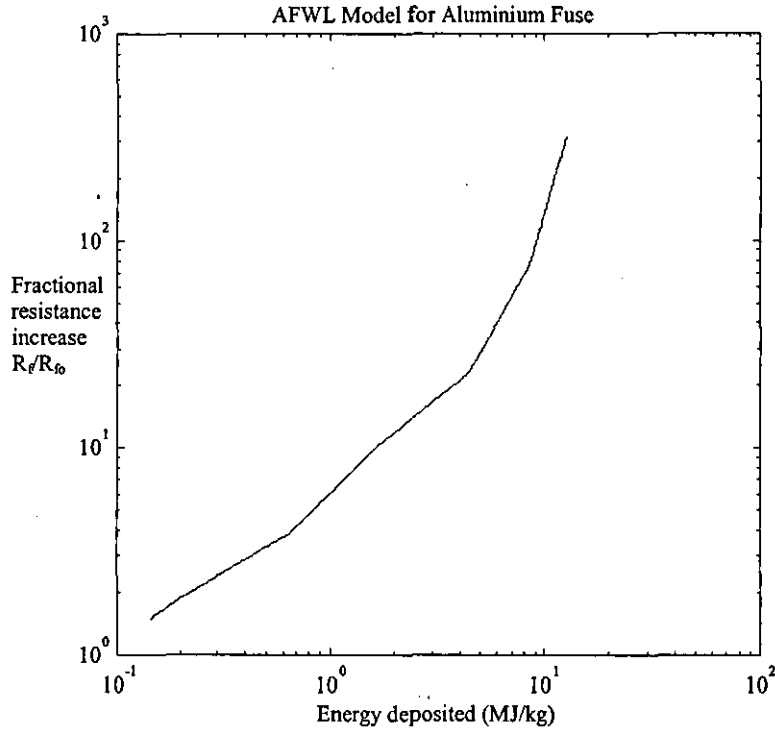


Figure 3-11 Fractional resistance increase of aluminium fuse as a function of energy deposited [65].

3.3.4 LU Model for Electric Gun Applications

Beside the confining medium, the behaviour of an exploding foil also depends on parameters such as the material and its dimensions and the current waveform. An empirical model can be obtained from current and voltage measurements, using the equation for the specific energy density and instantaneous foil resistance [26]

$$\varepsilon = \frac{1}{m_f} \int_0^t I^2(\tau) R_f d\tau = \frac{1}{m_f} \int_0^t I(\tau) V(\tau) d\tau \quad (3-40)$$

where $m_f = \rho_f l_f w_f \delta_f$

$$\text{and } R_f(t) = \frac{V(t)}{I(t)} \quad (3-41)$$

Fig 3-12 shows an empirical model for fractional resistance increase derived for the 15 mm x 15 mm x 25.4 μm aluminium exploding foil used in electric gun experiments. The lower energy portion of the model is taken from the AFWL aluminium model. This will be termed the Loughborough University (LU) model in this thesis.

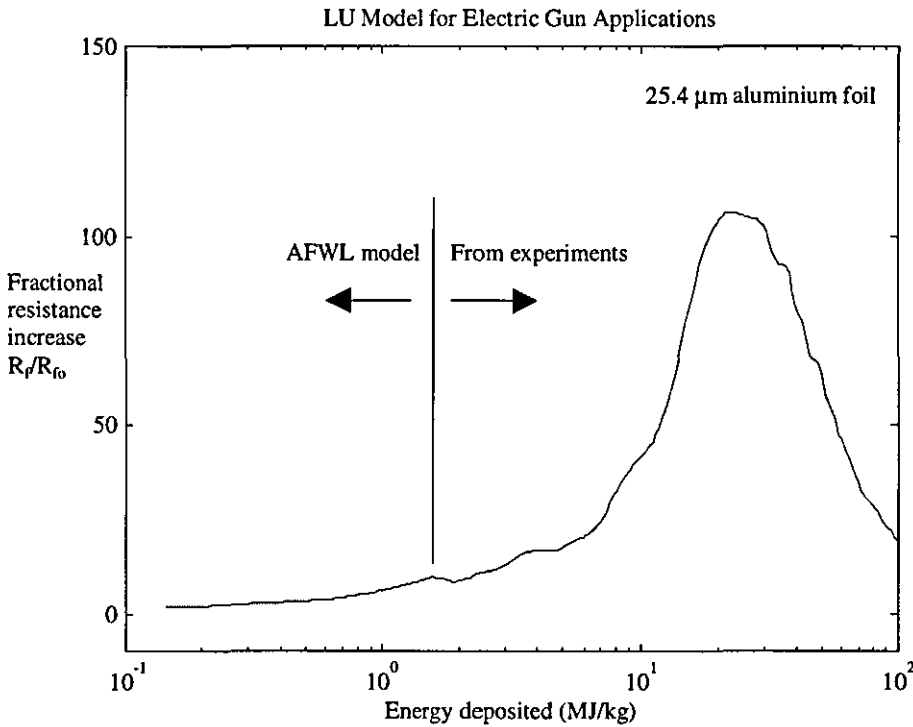


Figure 3-12 Fractional resistance increase of aluminium foil used in mathematical model for electric gun.

3.3.5 System Parameters

The ability of a numerical model to predict with good accuracy the current waveform in a circuit including an exploding foil depends on the correct determination of all the circuit parameters external to the exploding foil, including the inductance and resistance of the parallel-plate transmission line that connects the capacitor bank to the foil. Data for calibration is obtained from current measurements with the thin foil replaced by a

much thicker foil of the same length and width, enabling the system parameters (inductance L_t and resistance R_t) to be determined [66].

3.3.6 Time of Burst for Exploding Foil

In most of the literature, the burst time for exploding foils and wires is defined as that point on the current waveform where the current begins to reverse in direction. Mathematically, it is determined by $\frac{dI}{dt} = 0$ and this definition is adopted in the numerical model for the electric gun that follows. Fig 3-13 shows the typical current waveform obtained in the present electric gun experiments.

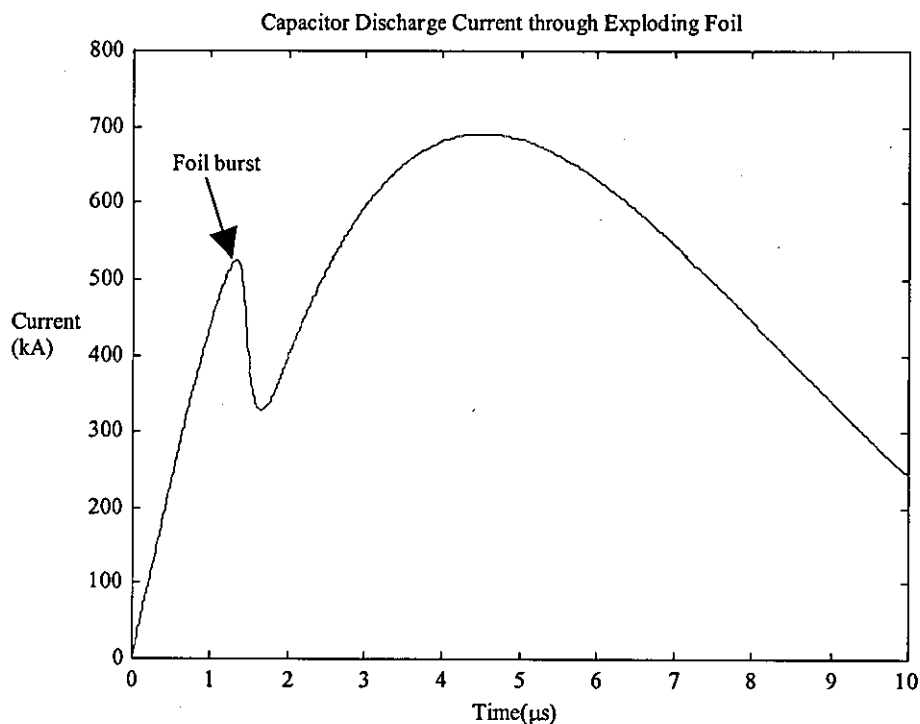


Figure 3-13 Foil burst criterion.

3.4 The Integrated Model for Electric Guns

In this section, the Gurney acceleration solution is combined with the empirical model for the exploding foil to provide a complete description of the electric gun.

3.4.1 Governing Equations

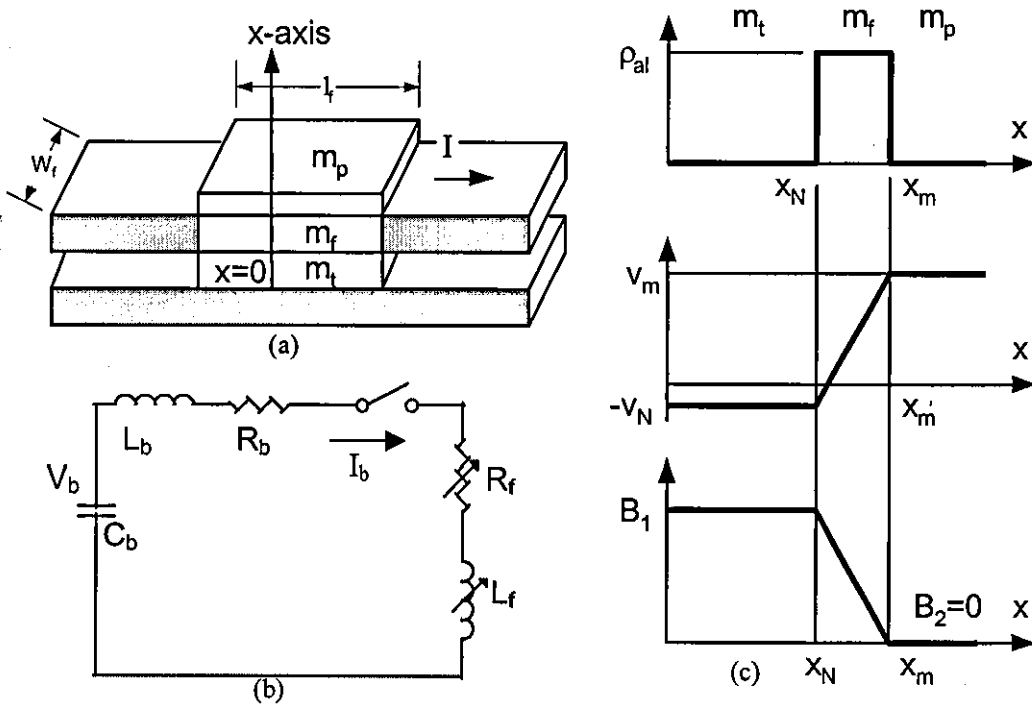


Figure 3-14 Electric gun (a) planar geometry, (b) equivalent electrical circuit and (c) approximations for mass density, velocity distribution and magnetic flux density.

The geometry of the exploding foil driven electric gun is shown in Fig 3-14a. The explosion of the metallic foil and the subsequent acceleration of the dielectric flyer are described by the Gurney acceleration solution. Using the same two fundamental assumptions, the mass density of the foil plasma after the explosion is assumed to be uniform and given by

$$\rho(x) = \frac{C}{x_m - x_N} \quad (3-42)$$

Similarly, the velocity profile for the explosion product is assumed to be linear, such that

$$v(x) = -v_N + \frac{v_m + v_N}{x_m - x_N}(x - x_N) \quad (3-43)$$

The simplification that the thickness of the foil plasma is much less than the magnetic diffusion skin-depth leads to a third approximation, that the magnetic flux density varies linearly across the foil. Then, as shown in Fig 3-14c,

$$B(x) = B_1 - \frac{B_1}{x_m - x_N}(x - x_N) \quad (3-44)$$

If the position of the return conductor at the base of the tamper is taken as the reference $x = 0$, then at time $t = 0$ we have

$$x_{No} = \delta_t \quad \text{and} \quad x_{mo} = x_{No} + \delta_f \quad (3-45)$$

where δ_t and δ_f are the thickness of the tamper and the metallic foil respectively.

The equivalent electrical circuit for the exploding foil driven planar electric gun is given in Fig 3-14b. The initial foil resistance is

$$R_{fo} = \eta \frac{l_f}{w_f \delta_f} \quad (3-46)$$

As the foil plasma may expand rapidly after the explosion, the foil inductance is separated into $L_f = L_1 + L_i$, where L_1 is associated with the tamper and L_i with the foil plasma. These inductances have the following definitions

$$L_1 = \frac{\mu_o l_f}{w_f} x_N \quad (3-47)$$

$$\text{and } L_i = \frac{\mu_o l_f}{w_f} (x_m - x_N) \quad (3-48)$$

The equations for the electrical circuit are now

$$C_b \frac{dV_b}{dt} = I_b \quad (3-49)$$

$$R_b I_b + L_b \frac{dI_b}{dt} + \frac{d}{dt} [(L_1 + L_i) I_b] + R_f I_b = V_b \quad (3-50)$$

$$\text{and } R_f(\varepsilon) = R_{f0} f(\varepsilon) \quad (3-51)$$

where ε is the specific energy density deposited in the metallic foil and $f(\varepsilon)$ is the resistance increase as a function of this energy.

The time of foil burst t_{burst} is determined by the criterion $\frac{dI_b}{dt} = 0$, where the energy density deposited in the foil and defined as

$$\varepsilon_{burst} = \varepsilon(t_{burst}) \quad (3-52)$$

is instantaneously released as explosive pressure to accelerate the flyer.

At a time before burst ($t \leq t_{burst}$), both the flyer and the tamper ideally remain at rest. However, a large magnetic pressure is exerted by the current, which tends to increase their separation. Due to the small thickness of the foil, it can be ruptured by the magnetic pressure P_B even before it has reached the point of explosion. After the foil has burst ($t > t_{burst}$) the flyer is accelerated by both the foil explosion pressure P_{ex} and the magnetic pressure P_B . The equations of the motion for the flyer are

$$\frac{dx_m}{dt} = v_m \quad (3-53)$$

$$\text{and } \frac{dv_m}{dt} = \begin{cases} \frac{1}{M} P_B & \text{if } t \leq t_{burst} \\ \frac{1}{M} (P_{ex} + P_B) & \text{if } t > t_{burst} \end{cases} \quad (3-54)$$

where P_B is the magnetic pressure, given by

$$P_B = \frac{B_1^2}{2\mu_o} = \frac{1}{2\mu_o} \left(\frac{\mu_o I_b}{w_f} \right)^2 = \frac{\mu_o}{2} \left(\frac{I_b}{w_f} \right)^2 \quad (3-55)$$

and P_{ex} is the explosion pressure given by the Gurney acceleration solution as

$$P_{ex} = \frac{C}{2} \frac{(\gamma - 1)(2\mathcal{E}_G - Bv_m^2)}{[x_m(1+A) - Ax_{mo} - x_{No}]} \quad (3-56)$$

$$\text{where } A = \frac{v_N}{v_m} = \frac{\left(M + \frac{C}{2} \right)}{\left(N + \frac{C}{2} \right)} \quad (3-57)$$

$$\text{and } B = \frac{M}{C} + \frac{N}{C} A^2 + \frac{1+A^3}{3(1+A)} \quad (3-58)$$

The equations for the motion of the tamper are

$$\frac{dx_N}{dt} = v_N \quad (3-59)$$

$$\text{and } \frac{dv_N}{dt} = -A \frac{dv_m}{dt} \quad (3-60)$$

By integrating the velocity profile in equation (3-43), the kinetic energy of the foil plasma, tamper and flyer together can be obtained as

$$W_k = \frac{1}{2} m_f \left(\frac{1}{3} (v_m - v_N)^2 + v_m v_N \right) + \frac{1}{2} m_t v_N^2 + \frac{1}{2} m_p v_m^2 \quad (3-61)$$

Similarly, by integrating the magnetic flux density equation (3-44), the magnetic energy within the foil plasma is obtained as

$$W_B = \frac{\mu_o l_f \delta_f}{2w_f} \left(\frac{1}{3} I_b^2 \right) \quad (3-62)$$

The electrical energy deposited in the foil can appear as kinetic energy, magnetic energy or foil internal energy. Conservation of the energy [65] requires that

$$\frac{d}{dt} \left[m_f \varepsilon + W_K + W_B - \frac{1}{2} (L_i I_b^2) \right] = R_f I_b^2 + \frac{1}{2} I_b^2 \left(\frac{dL_1}{dt} + \frac{dL_i}{dt} \right) \quad (3-63)$$

The first term on the right hand side of equation (3-63) represents Ohmic heating and the second term the work done by the magnetic field on the foil. The last term on the left hand side is required because of non-zero current density in the foil [65].

Introducing a new variable, $W_t = m_f \varepsilon + W_B + W_K$ enables equation (3-63) to be simplified as

$$\frac{dW_t}{dt} = R_f I_b^2 + \frac{1}{2} I_b^2 \left(\frac{dL_1}{dt} + \frac{dL_i}{dt} \right) + \frac{1}{2} \frac{d}{dt} (L_i I_b^2) \quad (3-64)$$

Equations (3-49), (3-50), (3-53), (3-54), (3-59), (3-60) and (3-64) together form a set of seven ordinary differential equations, with time as the independent variable. The seven principal dependent variables are V_b , I_b , x_m , v_m , x_N , v_N and W_t , and other quantities of importance include

$$\frac{dL_i}{dt} = \frac{\mu_o l_f}{w_f} v_N \quad (3-65)$$

$$\frac{dL_i}{dt} = \frac{\mu_o l_f}{w_f} (v_m - v_N) \quad (3-66)$$

3.4.2 Numerical Solution

The system of seven equations describes the temporal evolution of the exploding foil plasma, the flyer and the tamper and forms a complete set of highly non-linear coupled ordinary differential equations. The solution cannot be obtained analytically and among the numerical techniques that have been successfully applied [67] is the Newton iterative process. In the present research, a computer program is implemented in *Matlab*© to provide all the information needed for comparison with experimental data.

3.4.3 Foil Plasma Properties

The assumption of a uniformly distributed foil plasma allows the approximate determination of the foil plasma properties after the explosion (e.g. mass density, pressure, temperature). The temporal evolution of the flyer and tamper trajectories can be used to estimate the expansion of the foil plasma volume and when this is combined with the ideal gas law EOS, the foil plasma temperature can be estimated.

3.4.4 Explosion Quality Factor

Ideally, all the energy deposited in the metallic foil is released at the instant of the foil explosion. Numerous experiments have shown however that the quality of the foil explosion varies from shot to shot and that it is dependent on the care and precision taken during preparation of the foil/flyer package. Thus

$$\mathcal{E} = \mathcal{E}_{burst} k_{corr} \quad \text{where } k_{corr} \leq 1.0 \quad (3-67)$$

To account for situations in which the foil explosion is non-ideal, resulting in a lower than predicted flyer velocity, the correction factor k_{corr} is introduced to adjust the amount of energy that is instantaneously released and contributes to the explosive acceleration of the flyer package. The factor can be understood as a explosion quality factor, with $k_{corr} \rightarrow 1.0$ as the experimental processes approach ideal conditions.

Conversely, when the experimental process is non-ideal, k_{corr} takes on a reduced value to enable the model calculations to reproduce the experimental results.

3.5 Flyer Velocity Measurements

3.5.1 Fibre-Optic Probes

Fibre-optics is a useful tool in characterising shockwave and detonation events in hostile environment, because it is inherent safe and unaffected by electromagnetic transients and noise. Lu [68] reports the use of open-ended fibre-optic cables to measure the detonation velocity of shaped charges, and Caird [69] and Benjamin [70] used fibre-optics cables with xenon gas-filled microshell tips (to increase the light-output) for diagnostics purposes in explosive flux compressor research.

The light source for the fibre-optic probe is either the intense light produced by the detonation event itself, or that created externally by the shock compression of xenon gas. Since the flyer in an electric gun is propelled and accompanied by a conductive plasma layer, which radiates an intense flash of light, the high-temperature plasma behind the flyer can be used to as a source of light to determine its TOA.

The fibre-optic probes used in the present experiments are low-cost plastic fibre-optic cables (FOC) and they are placed in the path of the Mylar flyer. The free-ends of the cable are usually sealed with a non-transparent material (blue tac). Passage of the flyer over the cable cuts through the black jacket that protects against stray light and rough handling, and light from the conducting plasma is detected by an opto-electric converter connected to an oscilloscope. The diameter of the fibre core is 1.0 mm , and that of the outside of the black plastic jacket is 2.16 mm .

High-grade glass or quartz fibre was not used because of the difficulty in preparing its ends in the way needed for the present applications. On the other hand, plastic fibre can be cut easily with a heated knife blade to produce a reasonably smooth and flat surface that does not require end polishing. This greatly simplifies the process and reduces the time and cost of fibre-optics preparation or repair, which is necessary after each test.

3.5.2 Experimental Arrangement

Fig 3-15 shows the arrangement in which a fibre-optic probe (with sealed end) is placed 6.0 mm away from the initial location of the exploding foil/Mylar flyer (Fig 3-16) with another open-end probe used to measure the time to foil burst so that the mean velocity can be calculated. Important parameters for the experiment are summarised in Table 3-4.

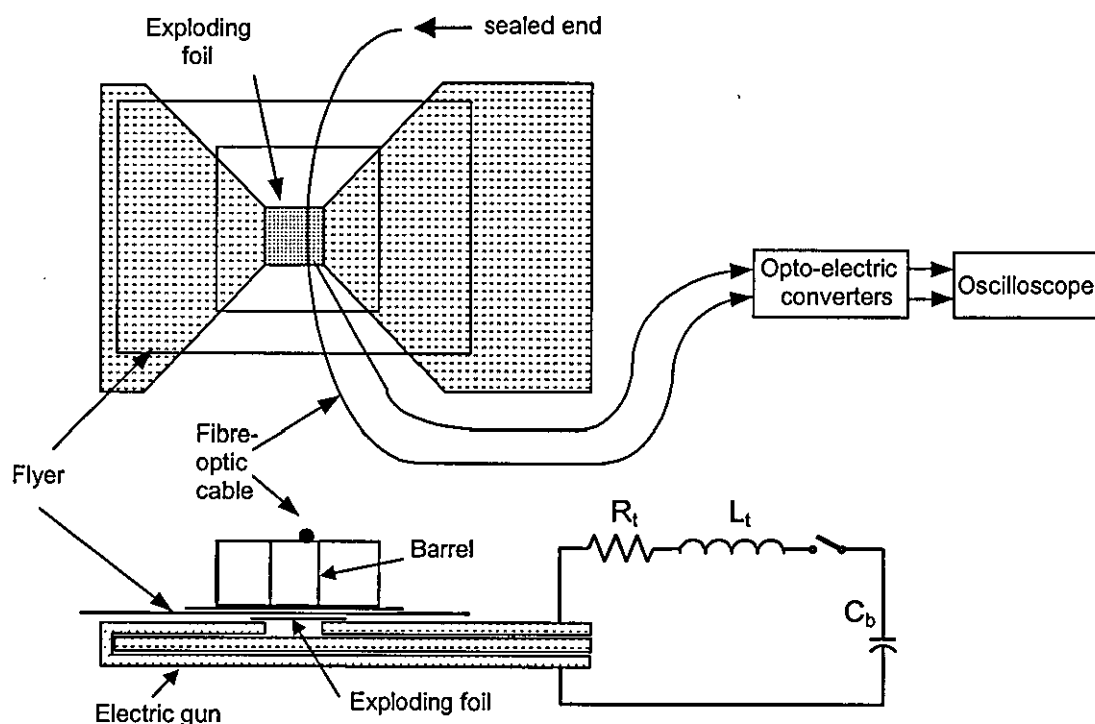


Figure 3-15 Experimental scheme for flyer velocity measurement.

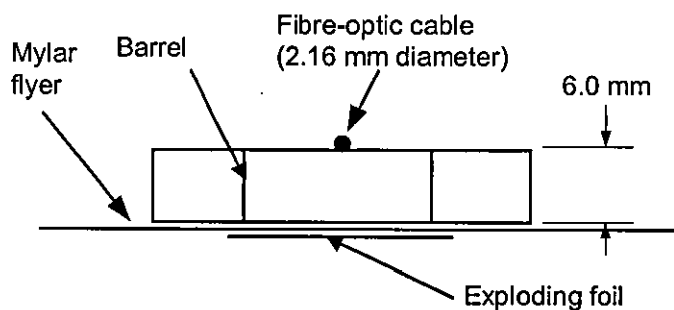


Figure 3-16 Fibre-optic probes for TOA measurement.

Table 3-4 Electric gun parameters for test no. 03.

Capacitor bank	Aluminium exploding foil	Barrel	Mylar flyer
$C_b = 248 \mu F$	$\delta_f = 25.4 \mu m$	length = 55.0 mm	55.0 mm x
$V_b = 20 kV$	$l_f = 60.0 mm$	width = 55.0 mm	55.0 mm x
$L_b = 39 nH$	$w_f = 60.0 mm$	height = 6.0 mm	75 μm
$R_b = 5.5 m\Omega$			

3.5.3 Experimental Results

The measured results in Fig 3-17 show a time interval of about $3 \mu s$ between foil burst and arrival at the second FOC probe. With a distance of 7.08 mm separating these two events, an average flyer speed in excess of 2 km/s was obtained.

Figs 3-18 and 3-19 show reasonable agreement between measured and computed results for the current and the $\frac{dI}{dt}$ signals, although the measured data is slightly corrupted by high-frequency noise after foil burst at $1.23 \mu s$. The current at foil burst was 529.5 kA.

Fig 3-20 shows the flyer trajectory predicted by the computer model, with the corresponding flyer velocity being given in Fig 3-21. The Gurney terminal velocity estimated by the computer model of 1.89 km/s is reached in less than $1 \mu s$ after a travel of less than 2 mm. After reaching the terminal velocity, the Mylar flyer continues to accelerate as a result of magnetic pressure.

Fig 3-22 shows the division of the deposited energy between kinetic, magnetic and Joule heating and Fig 3-23 shows the foil burst pressure estimated by the model to be about 7 GPa.

The properties of the exploded foil plasma calculated by the model in Fig 3-24 indicate that the foil plasma has expanded by about 50 times when the Gurney terminal velocity

is reached. The maximum temperature reached by the foil plasma is in the 3 to 6 eV range.

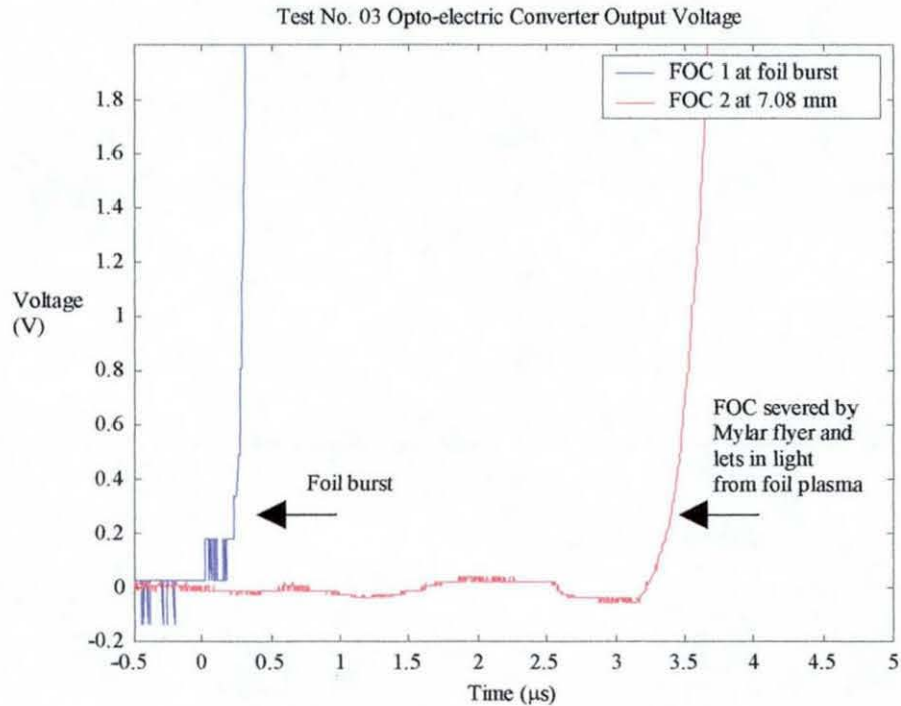


Figure 3-17 Fibre-optic probe data.

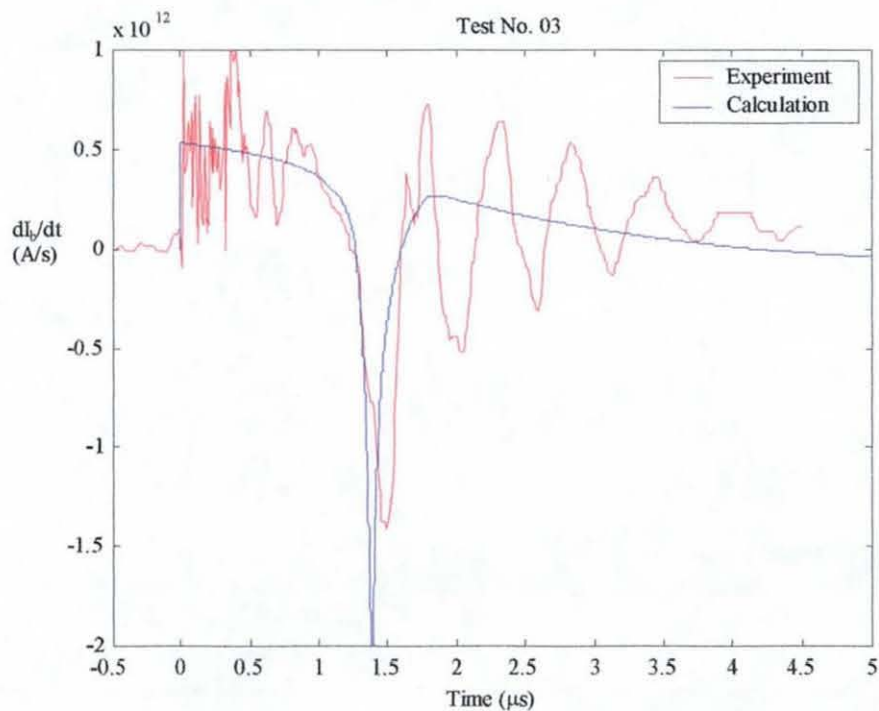


Figure 3-18 Measured $\frac{dl_b}{dt}$ and computed result.

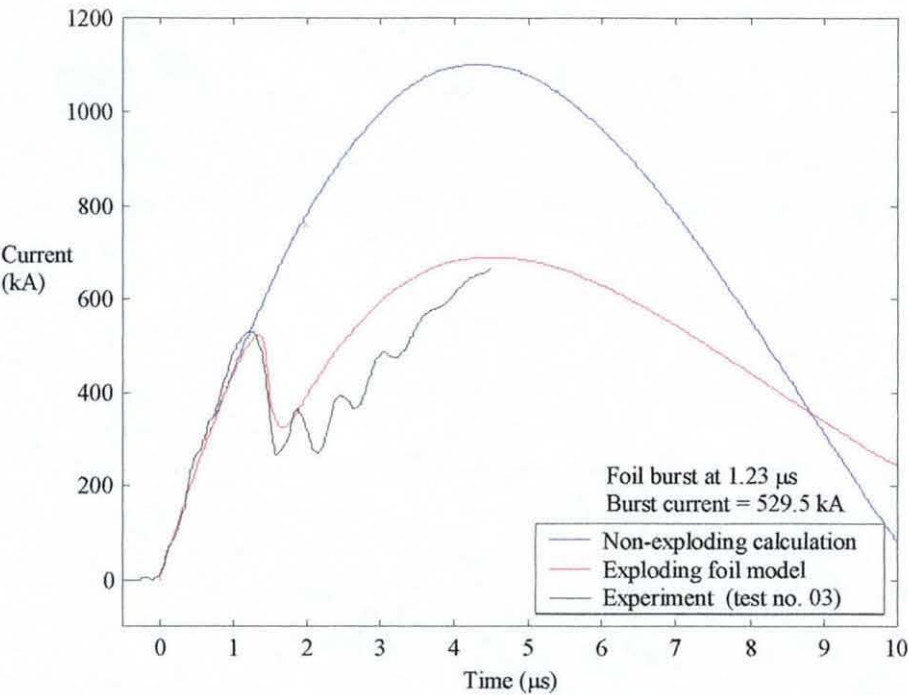


Figure 3-19 Measured current and computed result.

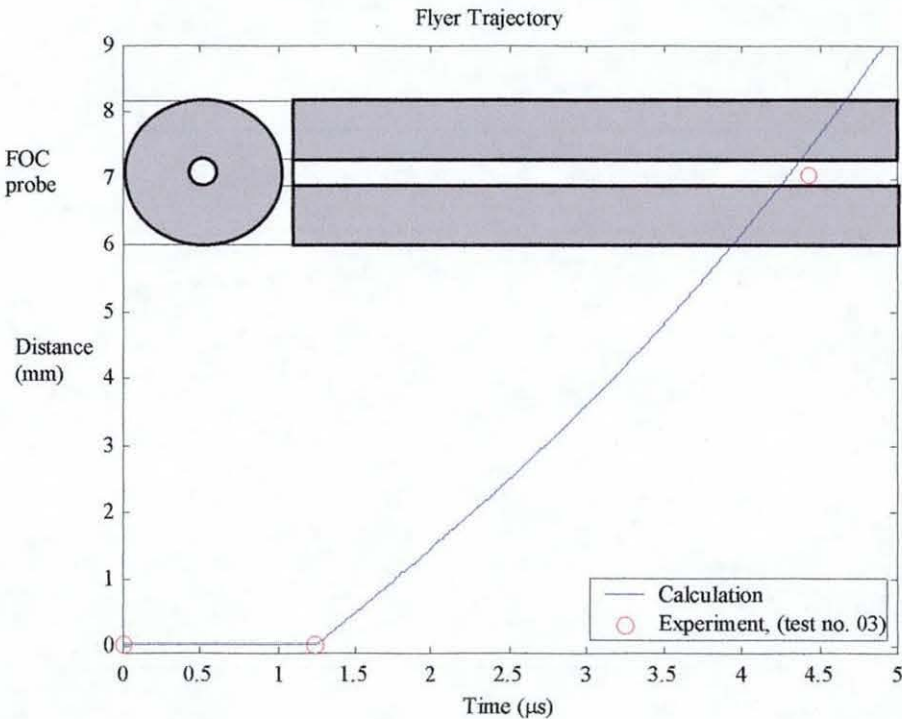


Figure 3-20 Measured TOA data and flyer trajectory.

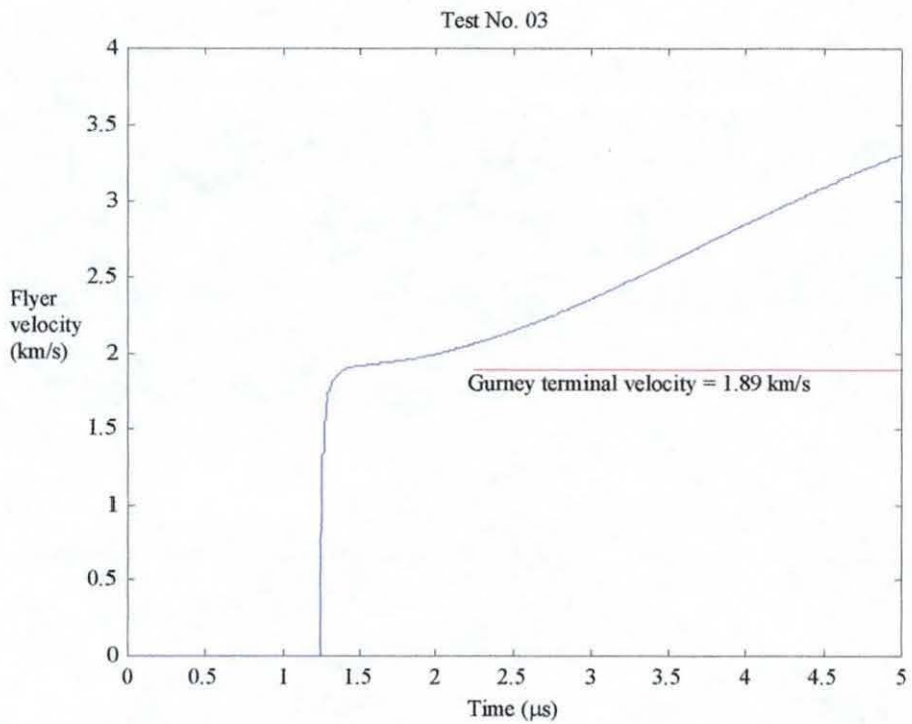


Figure 3-21 Flyer velocity according to computer model.

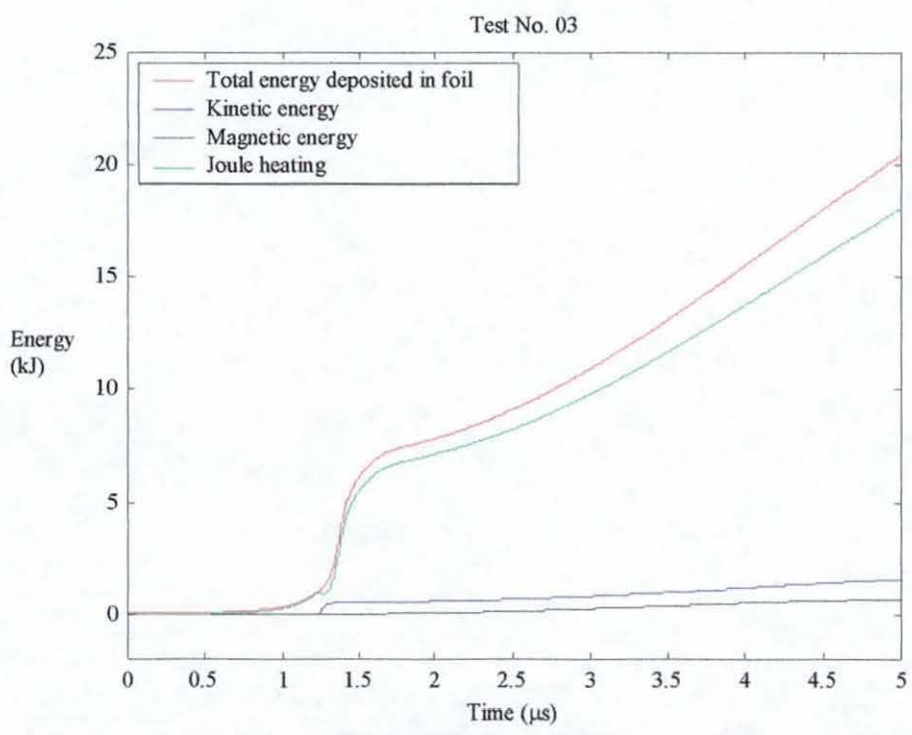


Figure 3-22 Partition of energy between kinetic, magnetic and Joule heating.

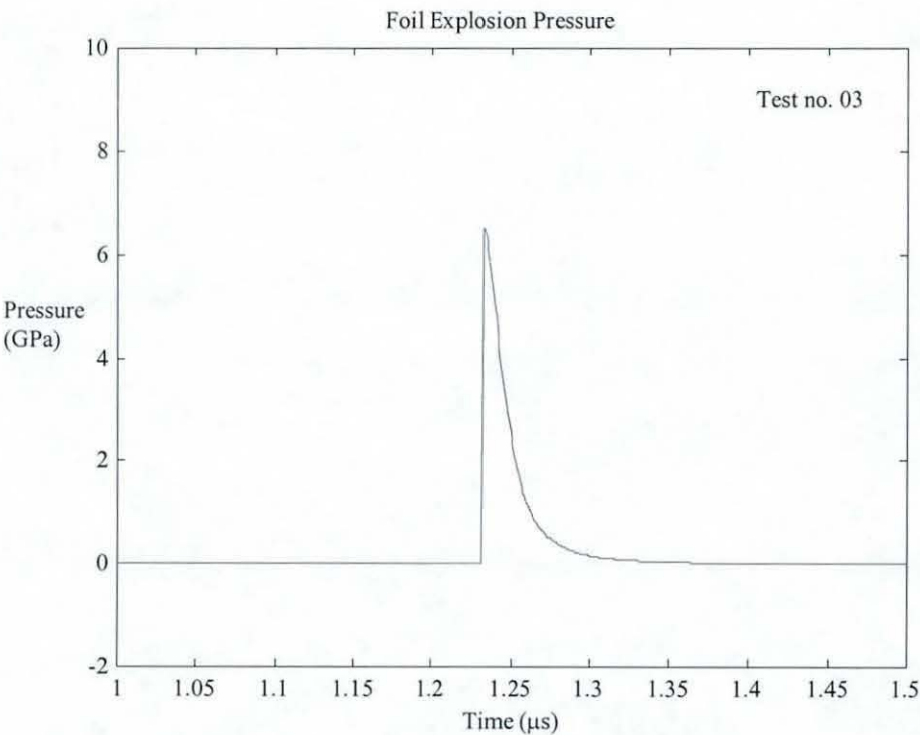


Figure 3-23 Estimated foil explosion pressure according to computer model.

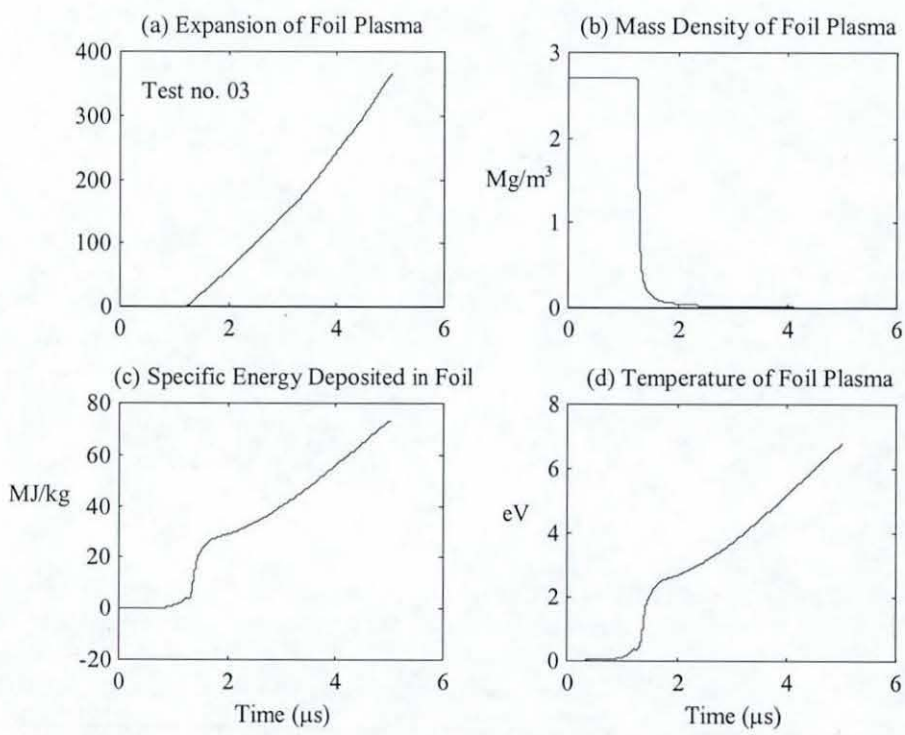


Figure 3-24 Foil plasma properties, (a) plasma expansion, (b) mass density, (c) specific energy deposited in foil and (d) foil plasma temperature.

In other experiments, three fibre-optic probes were placed at increasing distances from the exploding foil (Fig 3-25). The dimensions of the aluminium foil are unchanged but the flyer package now includes a copper foil (Table 3-5). The measured probe outputs in Fig 3-26 suggest that only two out of the three fibre-optic cables were cut by the Mylar flyer, allowing the intense light of the foil plasma to be detected by the opto-electric converter. The shape of the signal in FOC-2 and FOC-3 indicates a weak impact due to a low flyer velocity.

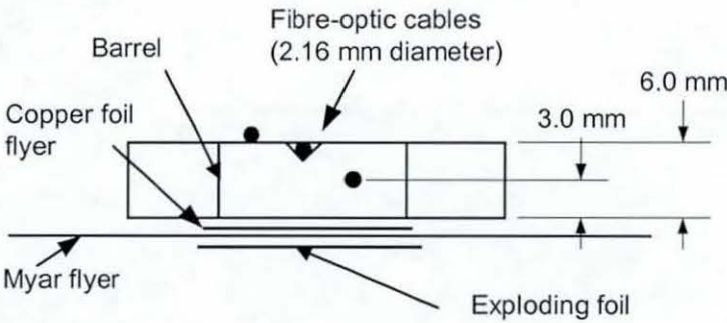


Figure 3-25 Fibre-optic probes for TOA measurement.

Table 3-5 Electric gun parameters for test no. 04.

Capacitor bank	Aluminium exploding foil	Barrel	Flyer
$C_b = 248 \mu F$	$\delta_f = 25.4 \mu m$	length = 55.0 mm	250 μm thick
$V_b = 20 \text{ kV}$	$l_f = 60.0 \text{ mm}$	width = 55.0 mm	Mylar and
$L_b = 39 \text{ nH}$	$w_f = 60.0 \text{ mm}$	height = 6.0 mm	17 μm thick
$R_b = 5.5 \text{ m}\Omega$			copper foil

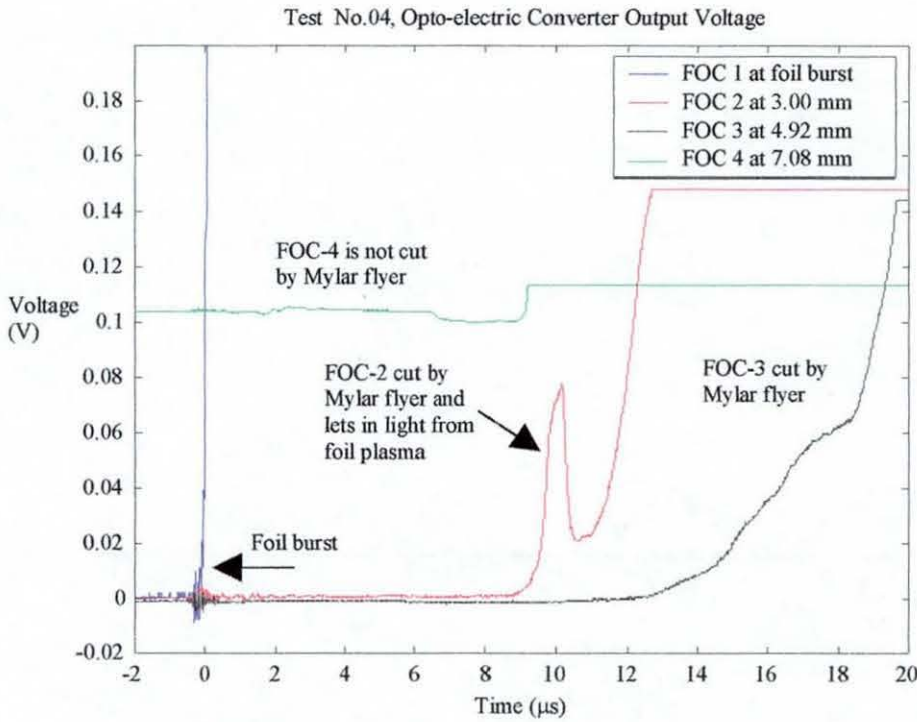


Figure 3-26 Fibre-optic probe data.

Comparison of the measured $\frac{dI}{dt}$ and current with the computed results in Figs 3-27 and 3-28 confirms that the empirical model for the exploding foil is able to reproduce fairly accurately the experimental results. The burst current of 521.9 kA and the burst time of 1.27 μ s (Fig 3-28) are consistent with the previous result in Fig 3-19, which would suggest that roughly the same amount of electrical energy has been deposited in the aluminium foil and that a higher flyer velocity is expected. In contrast to the previous experiment, the measured TOA data in Fig 3-29 agrees reasonably well with a velocity profile that does not include magnetic acceleration (Fig 3-30). The Gurney terminal velocity of about 0.3 km/s indicates a rather low foil burst pressure of only 0.6 GPa (Fig 3-32). Fig 3-31 shows that almost all the energy in the capacitor bank has been deposited in the exploding foil as Joule heating. It is therefore reasonable to conclude, based on the computed results, that the foil may not have exploded properly. The presence of a copper foil in close proximity to the parallel transmission line may have led to electrical breakdown and malfunction of the electric gun.

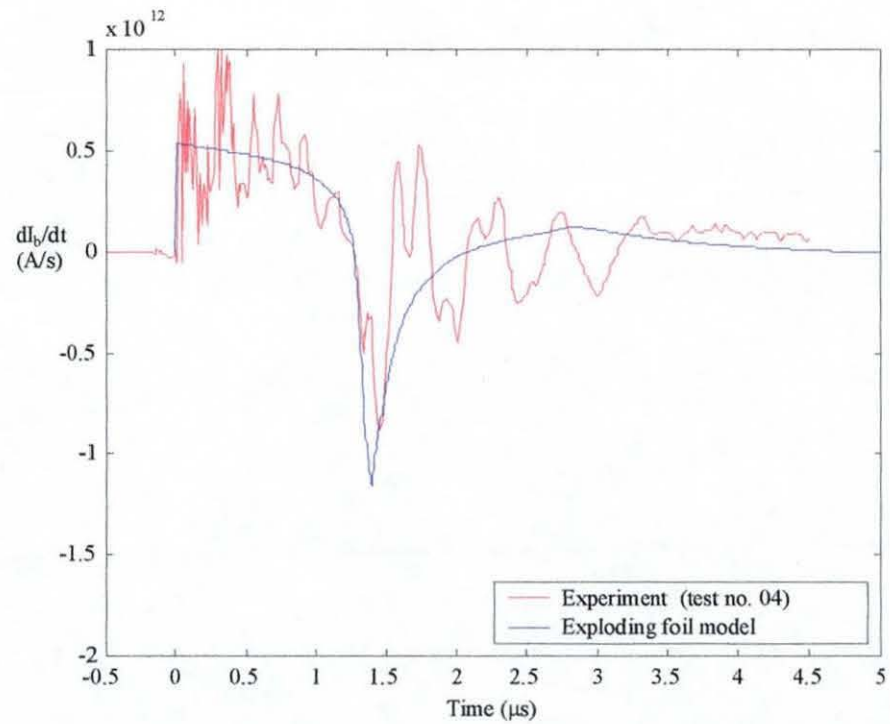


Figure 3-27 Measured $\frac{dI_b}{dt}$ and computed result.

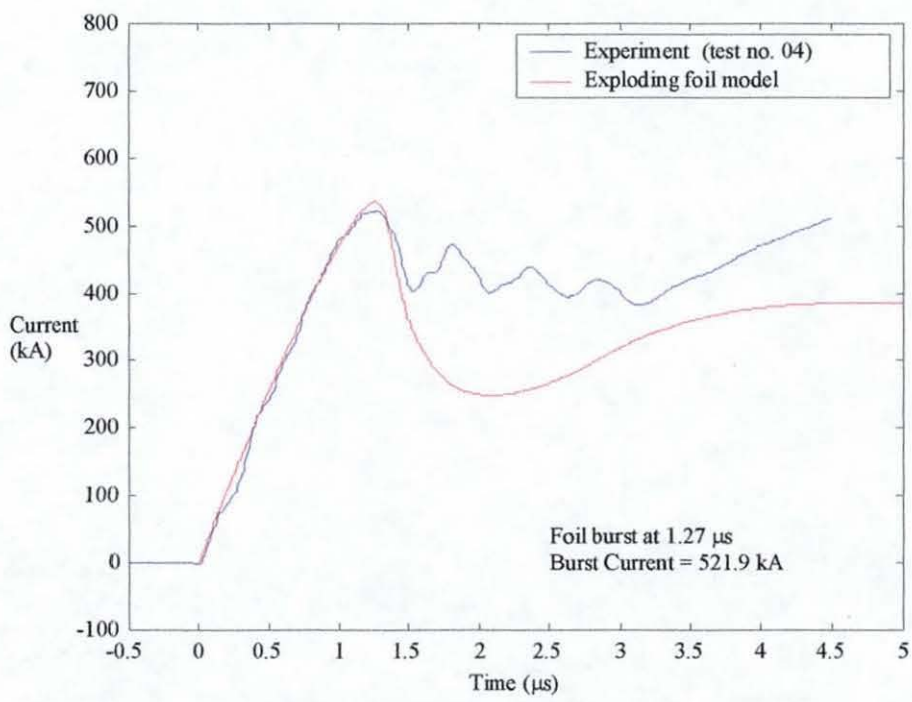


Figure 3-28 Measured current and computed result.

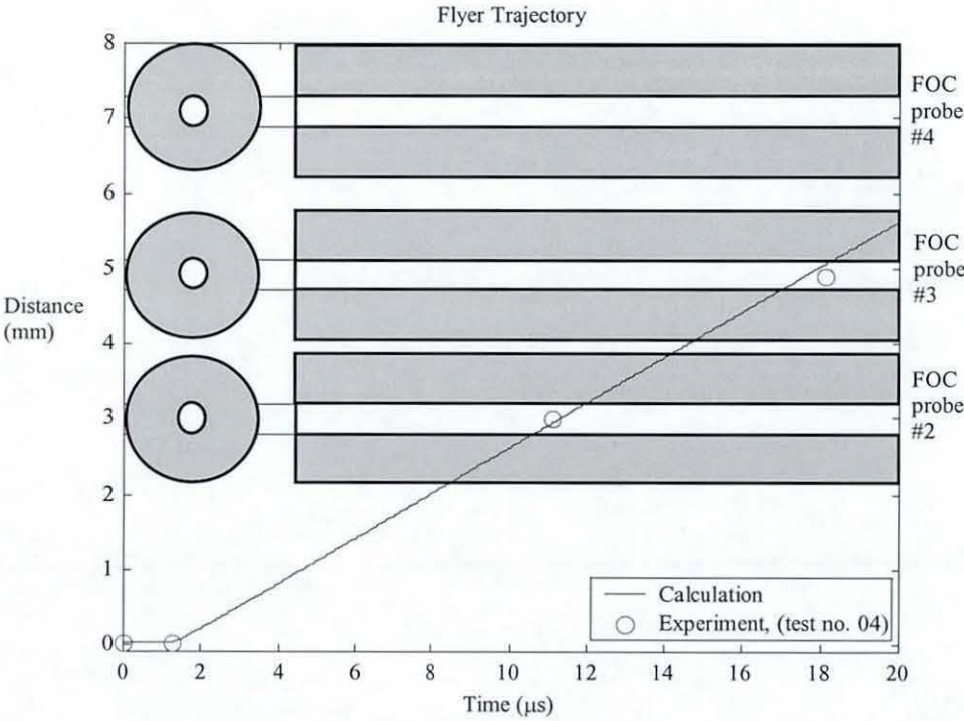


Figure 3-29 Measured TOA data and flyer trajectory.

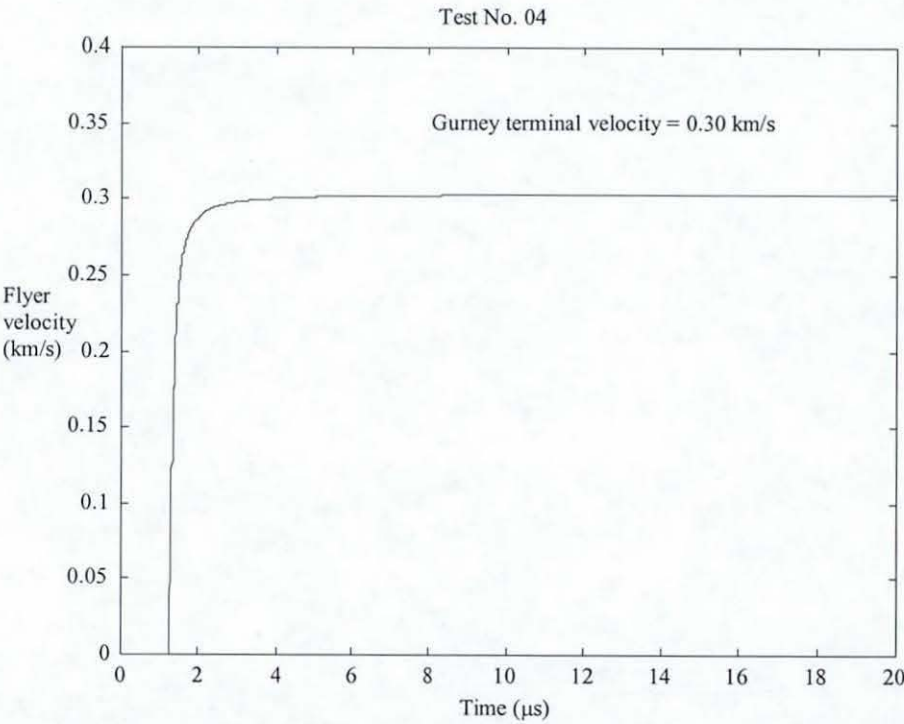


Figure 3-30 Flyer velocity according to computer model.

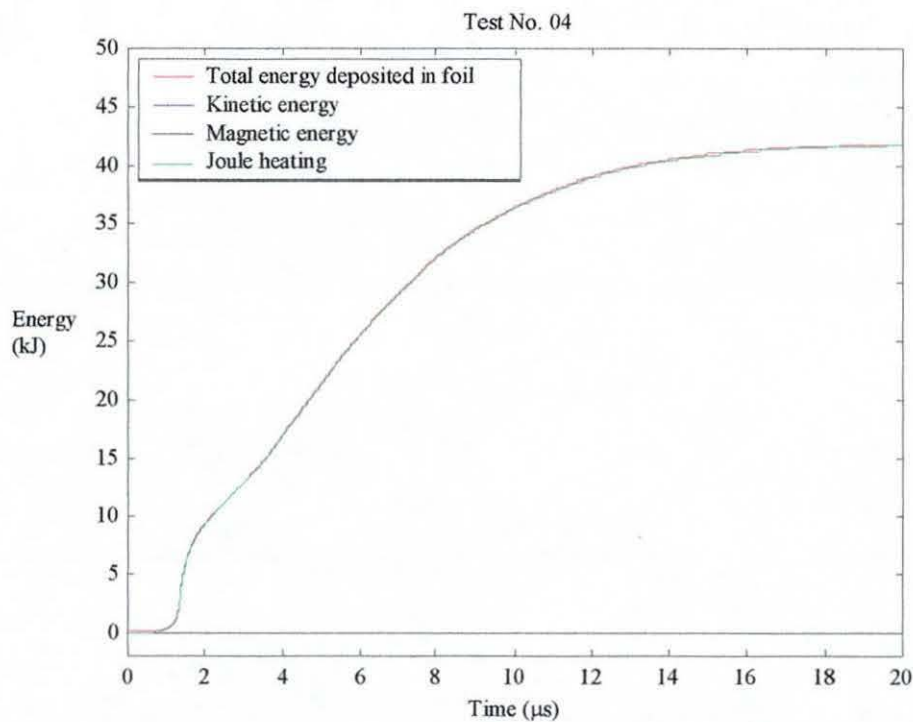


Figure 3-31 Partition of energy between kinetic, magnetic and Joule heating.

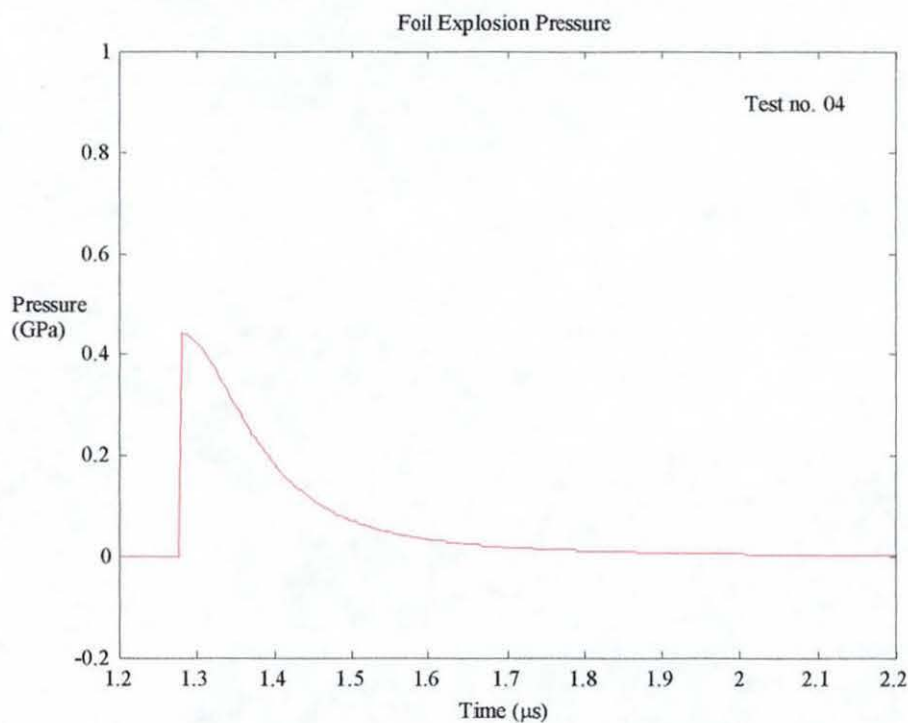


Figure 3-32 Estimated foil explosion pressure.

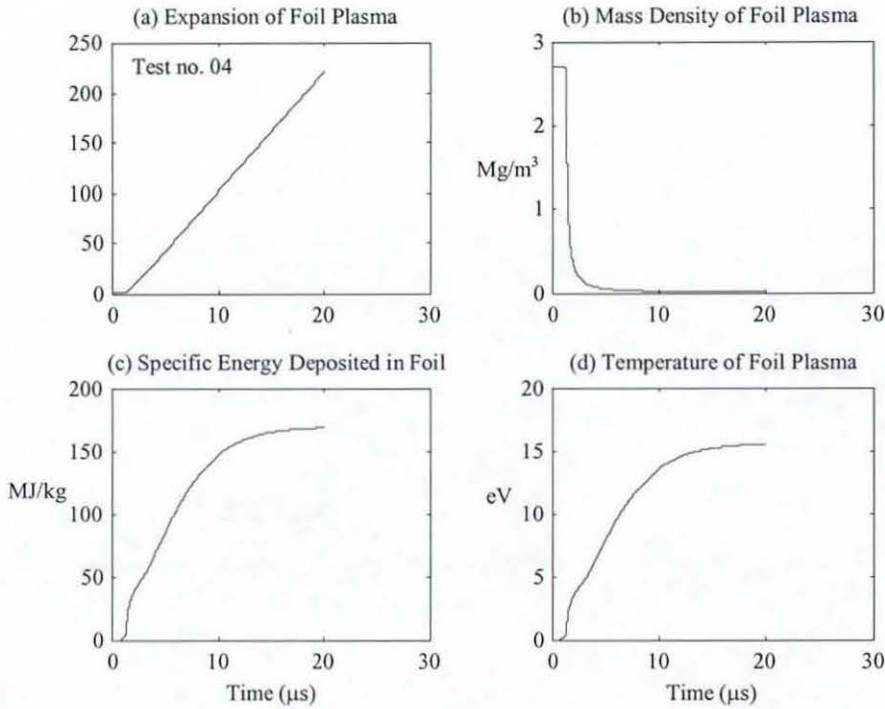


Figure 3-33 Foil plasma properties, (a) plasma expansion, (b) mass density, (c) specific energy deposited in foil and (d) foil plasma temperature.

3.6 Conclusions

In this chapter, a new mathematical model for the planar electric gun has been developed with the flyer acceleration process described by the Gurney model. The combination of an ideal gas law EOS with the Gurney equations makes the new model conceptually much simpler than the CONFUSE code developed by Lindemuth [65] for exploding foil opening switch and adapted for electrical gun applications [50]. In essence, the new model represents a simple extension of the empirical model for exploding foil opening switches already developed at Loughborough University [26], by monitoring the specific energy density and using the burst energy density to provide information on the flyer acceleration process. Dedicated flyer velocity measurements using fibre-optic probes described in this chapter are in good agreement with the computer predictions. The validity of the new model has also been verified using TOA data obtained by other measurement techniques in a series of exploding foil driven experiments that forms part of the present research.

HYDRODYNAMIC MODEL AND EOS

This chapter describes the development of a hydrodynamic model and the EOS for powder material, both of which are necessary for modelling the shock compression of aluminium powder. The governing equations for hydrodynamic flow and the finite-difference computational scheme are described in detail. One-dimensional test cases, in the form of (1) steady shock propagation and (2) shock reflection in aluminium powder are used as functional tests to verify the working of the hydrodynamic computer model. A simple switch model is described to simulate the insulator-to-conductor phase transition in shock compressed aluminium powder. The contribution of the imploding foil plasma (driving the Mylar flyer) to the flux compression process is assessed, based on the Spitzer equation for the electrical conductivity of an ionised gas.

4.1 Hydrodynamic Model in One Dimension

Hydrodynamic codes (or Hydrocodes in short) are computer programs that handle the propagation of shockwaves and compute velocities, strains, stress etc. as a function of time and position. They are essential numerical tools for the study of the dynamic response of material to various impact and penetration phenomena, cracks and fracture formation. Early code formulations did not include material strength effects, and metals were treated as a fluid with no viscosity. This enabled the approximate response of a material object to be calculated, providing that the pressures were sufficiently high and that strength effect could be ignored. Because of this, the expression hydrodynamic calculation was commonly used to refer to a calculation that did not include material strength effects. However, over time, modern hydrodynamic codes have become very much more complex, with the inclusion of better constitutive equations for material modelling.

4.1.1 Governing Equations

The behaviour of fluid flow is governed by three basic conservation equations. If

$\vec{x} = \begin{bmatrix} x \\ y \\ z \end{bmatrix}$ denotes a position vector in a Cartesian co-ordinate system, the properties of

the fluid medium are characterised by the density $\rho = \rho(\vec{x}, t)$, the pressure $P = P(\vec{x}, t)$,

the internal energy density per unit mass $\varepsilon = \varepsilon(\vec{x}, t)$ and the fluid velocity

vector $\vec{v} = \begin{bmatrix} v_x \\ v_y \\ v_z \end{bmatrix}$. If it is assumed that viscous forces, body forces (like gravity), heat

conduction and energy sources are all absent, the equation for the conservation of mass (sometimes called the equation of continuity) is

$$\frac{\partial \rho}{\partial t} + (\vec{v} \cdot \nabla) \rho = -\rho \nabla \cdot \vec{v} \quad (4-1)$$

the equation for the conservation of momentum (sometimes called the equation of motion) is

$$\rho \left[\frac{\partial \vec{v}}{\partial t} + (\vec{v} \cdot \nabla) \vec{v} \right] = -\nabla \cdot P \quad (4-2)$$

and the equation for the conservation of energy is

$$\rho \left[\frac{\partial \varepsilon}{\partial t} + (\vec{v} \cdot \nabla) \varepsilon \right] = -P \nabla \cdot \vec{v} \quad (4-3)$$

4.1.2 Eulerian Description

The above equations may be expressed in either Eulerian and Lagrangian form. The Eulerian equations describe conditions at a point fixed in space and the variation with time t of these conditions and the Eulerian co-ordinate of the particle becomes one of

the dependent variables. The Lagrangian form describes the motion of individual particles of the fluid and the Lagrangian co-ordinate system is fixed in the fluid and moves with it. The two forms of the differential equations are formally equivalent.

Using the simplification for one-dimensional symmetry that $\vec{v} = \begin{bmatrix} v_x \\ v_y \\ v_z \end{bmatrix} = \begin{bmatrix} v \\ 0 \\ 0 \end{bmatrix}$ and noting

that $\frac{\partial}{\partial y} = \frac{\partial}{\partial z} = 0$, because all variables depend only on the x-co-ordinate and on time,

leads to the Euler equations

$$\frac{\partial \rho}{\partial t} + v \frac{\partial \rho}{\partial x} = -\rho \frac{\partial v}{\partial x} \quad (4-4)$$

$$\frac{\partial v}{\partial t} + v \frac{\partial v}{\partial x} = -\frac{1}{\rho} \frac{\partial P}{\partial x} \quad (4-5)$$

$$\frac{\partial \varepsilon}{\partial t} + v \frac{\partial \varepsilon}{\partial x} = -\frac{P}{\rho} \frac{\partial v}{\partial x} \quad (4-6)$$

4.1.3 Lagrangian Description

The corresponding equations in Lagrangian form depend on the definition of the Lagrangian variable s . The initial position of the particle at time zero has been used for this, but it is physically more intuitive to associate the Lagrangian co-ordinate with a mass rather than a length. Thus

$$s = \int_0^x \rho(x,t) dx, \quad \partial s = \rho \partial x, \quad (4-7)$$

the specific volume V is equal to $\frac{1}{\rho}$, and the total derivative is

$$\frac{d}{dt} = \frac{\partial}{\partial t} + v \frac{\partial}{\partial x}, \quad (4-8)$$

The equations corresponding to (4-4)-(4-6) now take the form

$$\frac{dV}{dt} = \frac{\partial v}{\partial s} \quad (4-9)$$

$$\frac{dv}{dt} = -\frac{\partial P}{\partial s} \quad (4-10)$$

$$\frac{d\varepsilon}{dt} = -P \frac{\partial v}{\partial s} \quad (4-11)$$

which are used together with

$$\frac{dx}{dt} = v \quad (4-12)$$

and the EOS

$$P = P(\rho, \varepsilon) \quad (4-13)$$

In the Lagrangian description, the grid points are attached to the material and move with its local velocity. Velocity, pressure, density, temperature, etc. are all computed as time progresses, for each discrete point in the continuum. Adjacent points can be stretched or moved closer together, depending upon the forces (or pressures) applied. Mass, momentum and energy are transported by material flow, so that the grid points move relative to a fixed spatial co-ordinate system. In this formulation the mass in a cell is invariant, although its volume may change with time because of expansion or compression of the material.

In Lagrangian calculations, the mesh is generated to approximate to the material of interest by points placed along exterior boundaries (free surfaces) and material boundaries. The boundary conditions at free surfaces and contact surfaces between different materials are straight-forward, with the positions of these surfaces being automatically determined in the computation.

An important feature of the Lagrangian description is its ability to follow the history of a material particle, so that a material whose properties depend upon its previous history can be modelled. Thus the Lagrangian description allows treatment of material strength,

work hardening, yield and other effects using constitutive equations. However, because each cell in a Lagrangian description is of one material only, and any flow across cell boundaries is not allowed, diffusion and mixing problem cannot be analyzed by a Lagrangian code.

In Lagrangian calculations, the grid mesh is required whenever there is a material, but the mesh may be placed such that maximum resolution is obtained for a specific number of zones. A Lagrangian mesh can be severely compressed and distorted, which causes the time step to become extremely small and effectively terminates the problem. In areas of severe mesh distortion, the Lagrangian mesh can be rezoned.

In view of the above considerations, the Lagrangian description was used in the development of the present hydrodynamic code.

4.1.4 Artificial Viscosity

Von Neumann and Richtmyer [71] were the first to devise a method for handling shocks by the introduction of an artificial dissipative mechanism that causes the shock to be spread smoothly over several mesh intervals. The mechanism used is viscosity, which has the dissipative effect required and appears to be more appropriate than a heat conduction term. In the original formulation the authors were concerned that the thickness of the shock should be independent of the shock strength, and the form of artificial viscosity term chosen was

$$Q = \frac{(c_1 \Delta x)^2}{V} \left| \frac{\partial v}{\partial x} \right| \frac{\partial v}{\partial x} \quad (4-14)$$

where Δx is the mesh size, v is the particle velocity, V is the volume and c_1 is an integer constant greater than one. It was later found [72] that a more appropriate expression was

$$Q = \begin{cases} \frac{(c_1 \Delta x)^2}{V} \left(\frac{\partial v}{\partial x} \right)^2 & \frac{\partial v}{\partial x} < 0 \\ 0 & \frac{\partial v}{\partial x} > 0 \end{cases} \quad (4-15)$$

implying that the artificial viscosity term needs only to be present during material compression. The artificial viscosity term is extremely small, except at the shock front.

Landshoff [73] added a linear term to the artificial viscosity, to give a further form of artificial viscosity for one-dimensional hydrocodes

$$Q = \frac{c_1}{V} (\Delta v)^2 + \frac{c_2}{V} c_s (\Delta v) \quad (4-16)$$

where Δv is the difference in particle velocity across the mesh, c_1 and c_2 are integer constants greater than one and c_s is the local speed of sound. The linear term in the artificial viscosity is effective in damping out non-physical oscillations as the shock propagates through the medium, and for this reason it is an improvement over the Von-Neumann type (or quadratic form) artificial viscosity.

4.1.5 Finite Difference Implementation

Computational Grid

From Fig 4-1, the mesh points x_j^{n+1} are seen to be the boundaries between elements and the particle velocities are defined at the cell-boundaries as v_j^{n+1} . The index j denotes the spatial position of the elements, and integer superscripts n and $n+1$ are element properties at integer multiples of the time step, e.g. $v_j^n \equiv v_j(n\Delta t)$, $v_j^{n+1} \equiv v_j((n+1)\Delta t)$. For time-centering, the average values (over time) of the cell boundaries and particle velocities are denoted by superscript $n+0.5$, e.g. $x_j^{n+0.5} = 0.5(x_j^n + x_j^{n+1})$ and $v_j^{n+0.5} = 0.5(v_j^n + v_j^{n+1})$

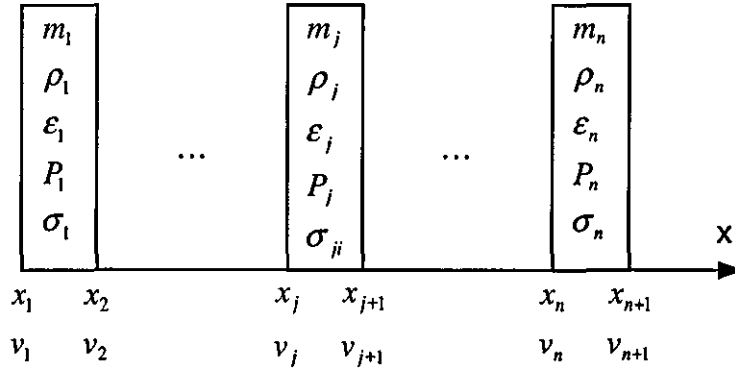


Figure 4-1 Computational domain.

The cell boundaries divide the material into mass element defined as cell-centred values. Using the definition of the Lagrangian co-ordinate for a one-dimensional slab, we get

$$m_j \equiv \partial s = \rho \partial x = \rho_o (x_{j+1}^0 - x_j^0) \quad (4-17)$$

In the momentum equation, ∂s is replaced by the average value of the two adjacent mass elements $0.5(m_j + m_{j-1})$. In the energy equation, which by definition is already cell-centred, ∂s is replaced simply by the corresponding mass element m_j .

Finite Difference Equations

The finite difference equations implemented using *Matlab*© in the present hydrodynamic code are listed below in the order of their computation, which follows a form similar to that adopted by Wilkins [74].

a) Momentum Equation

$$\frac{v_j^{n+1} - v_j^n}{\Delta t} = -\frac{1}{0.5(m_j + m_{j-1})} [P_j^{n+0.5} - P_{j-1}^{n+0.5}]$$

$$\text{or } v_j^{n+1} = v_j^n - \frac{\Delta t}{0.5(m_j + m_{j-1})} (P_j^{n+0.5} - P_{j-1}^{n+0.5}) \quad (4-18)$$

$$v_j^{n+0.5} = 0.5(v_j^n + v_j^{n+1}) \quad (4-19)$$

Boundary conditions v_1^{n+1} and v_{N+1}^{n+1} are considered in the solution of the equation of motion. Once these are determined, the new cell boundaries and mass densities can be updated.

$$\frac{x_j^{n+1} - x_j^n}{\Delta t} = v_j^{n+0.5} \quad \text{or} \quad x_j^{n+1} = x_j^n + v_j^{n+0.5} \Delta t \quad (4-20)$$

$$x_j^{n+0.5} = 0.5(x_j^n + x_j^{n+1}) \quad (4-21)$$

b) Continuity (or conservation of mass) Equation

The mass within a cell is invariant, but its volume may change with time because of expansion or compression of the material.

$$V_j^{n+1} = \frac{x_{j+1}^{n+1} - x_j^{n+1}}{m_j} \quad (4-22)$$

$$\rho_j^{n+1} = \frac{1}{V_j^{n+1}} \quad (4-23)$$

c) Electrical Conductivity Model

If a density-dependent model is available to describe the insulator-to-conductor transition of shock-loaded metallic powder, a new value of electrical conductivity for each mass element is calculated using the updated mass density

$$\sigma_j^{n+1} = \sigma(\rho_j^{n+1}) \quad (4-24)$$

d) Energy Equation

The change in internal energy is determined from the work performed by the pressure

$$\frac{\varepsilon_j^{n+1} - \varepsilon_j^n}{\Delta t} = -P_j^{n+0.5} \frac{x_{j+1}^{n+0.5} v_{j+1}^{n+0.5} - x_j^{n+0.5} v_j^{n+0.5}}{m_j}$$

$$\text{or } \varepsilon_j^{n+1} = \varepsilon_j^n - \Delta t \left(P_j^{n+0.5} \frac{x_{j+1}^{n+0.5} v_{j+1}^{n+0.5} - x_j^{n+0.5} v_j^{n+0.5}}{m_j} \right) \quad (4-25)$$

e) Equation of State

The internal energy and mass density give new values for the pressure through the EOS

$$P_j^{n+1} = P(\rho_j^{n+1}, \varepsilon_j^{n+1}) \quad (4-26)$$

f) Artificial Viscosity

The new velocity flow field is inspected for the calculation of artificial viscosity

$$\text{if } v_j^{n+1} \leq v_{j+1}^{n+1} \quad Q_j^{n+1} = 0 \quad (4-27)$$

but if $v_j^{n+1} > v_{j+1}^{n+1}$, then in quadratic form

$$Q_j^{n+1} = \frac{c_1^2}{V_j^{n+1}} \left| v_{j+1}^{n+1} + v_j^{n+1} \right| (v_{j+1}^{n+1} - v_j^{n+1}) \quad (4-28)$$

or in linear form

$$Q_j^{n+1} = \frac{c_2}{V_j^{n+1}} c_s (v_{j+1}^{n+1} - v_j^{n+1}) \quad (4-29)$$

where c_1 and c_2 are constants and c_s is the local speed of sound.

g) Hydrodynamic Pressure

A modified two-step method [75] is used to update the pressure field and is used in the solution of the equation of motion in the next iteration

$$P_j^{n+0.5} = 0.5(P_j^n + Q_j^n + P_j^{n+1} + Q_j^{n+1}) \quad (4-30)$$

h) Stability Criterion

The Courant-Friedrichs-Levy (CFL) stability criterion [72] is used to determine the next time step dt

$$dt \leq \frac{\min(\Delta x_j^{n+1})}{\max(v_j^{n+1})} \quad (4-31)$$

where $\Delta x_j^{n+1} = x_j^{n+1} - x_{j-1}^{n+1}$

4.1.6 Conducting Shock Front

The boundary separating the elements ahead of the shock front (characterised by low mass density and low electrical conductivity) from those behind the front (characterised by compression to near solid density and high electrical conductivity) is taken as the location of the shock front. Due to the discrete nature of the computational grid, the motion of the conducting shock front is necessarily 'jerky' and follows the 'stair-case' form seen in Fig 4-2.

The speed at which the conducting shock front advances with the shockwave is calculated using a simple algorithm, by noting the time and location at which each successive step jump occurs.

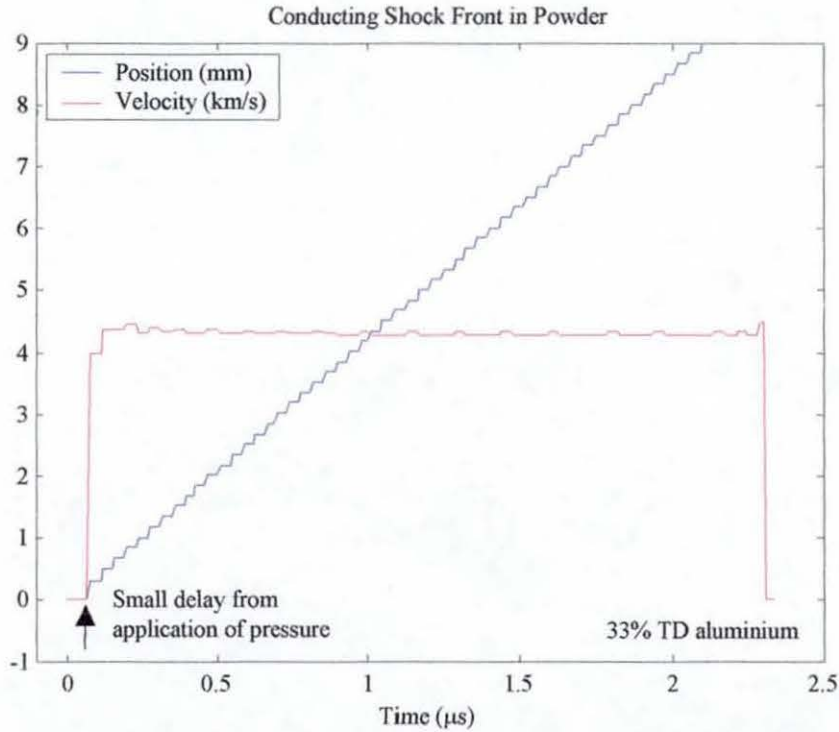


Figure 4-2 Trajectory and velocity of conducting shock front.

4.1.7 Treatment of Material Interface

To facilitate the calculation of flow involving multiple materials, an algorithm adapted from one described by Richtmyer and Morton [72] is included in the one-dimensional hydrodynamic model.

In a computational domain, where an interface exists at the index $j = J + 1$ between two material, the set of finite difference equations in section 4.1.5 may be used as they are, with the appropriate EOS on each side of the interface. However, a special method of treating the material interface is needed to avoid any large computational error that may lead to computational instability. In essence, the method works by ensuring continuity of the pressure gradient $\frac{\partial P}{\partial s}$ across the interface.

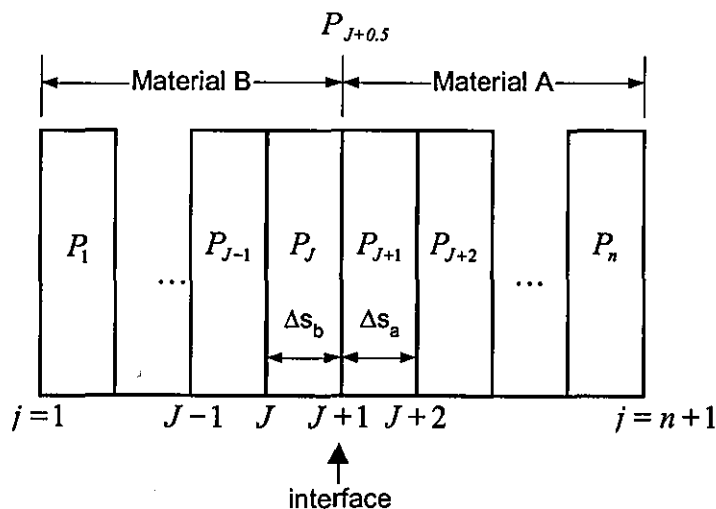


Figure 4-3 Treatment of material interface.

In Fig 4-3, all the elements to the left of the interface (material B) have the same mass Δs_b , although different cell widths are possible due to compression and expansion. Similarly, all the elements in material A have the same mass Δs_a . Since pressure has been defined as cell-centred, the pressure at the material interface (a cell boundary in Fig 4-3) is denoted by $P_{J+0.5}^n$.

For material B, we have

$$\left. \frac{\partial P}{\partial s} \right|_J \approx \frac{P_J^n - P_{J-1}^n}{\Delta s_b} \quad (4-32)$$

$$\left. \frac{\partial P}{\partial s} \right|_{J+0.5} \approx \frac{P_{J+0.5}^n - P_J^n}{0.5\Delta s_b} \quad (4-33)$$

where $P_{J+0.5}^n$ is the pressure at the material interface.

By extrapolation,

$$\left. \frac{\partial P}{\partial s} \right|_{J+1} \approx \frac{4}{3} \left. \frac{\partial P}{\partial s} \right|_{J+0.5} - \frac{1}{3} \left. \frac{\partial P}{\partial s} \right|_J \quad (4-34)$$

$$\left. \frac{\partial P}{\partial s} \right|_{J+1} \approx \frac{4}{3} \frac{P_{J+0.5}^n - P_J^n}{0.5\Delta s_b} - \frac{1}{3} \frac{P_J^n - P_{J-1}^n}{\Delta s_b} \quad (4-35)$$

Similarly for material A, we have

$$\left. \frac{\partial P}{\partial s} \right|_{J+2} \approx \frac{P_{J+2}^n - P_{J+1}^n}{\Delta s_a} \quad (4-36)$$

$$\left. \frac{\partial P}{\partial s} \right|_{J+1.5} \approx \frac{P_{J+1}^n - P_{J+0.5}^n}{0.5\Delta s_a} \quad (4-37)$$

$$\left. \frac{\partial P}{\partial s} \right|_{J+1} \approx \frac{4}{3} \frac{P_{J+1}^n - P_{J+0.5}^n}{0.5\Delta s_a} - \frac{1}{3} \frac{P_{J+2}^n - P_{J+1}^n}{\Delta s_a} \quad (4-38)$$

Eliminating $P_{J+0.5}^n$, gives

$$\left. \frac{\partial P}{\partial s} \right|_{J+1} = \frac{3(P_{J+1}^n - P_J^n) - \frac{1}{3}(P_{J+2}^n - P_{J-1}^n)}{(\Delta s_a + \Delta s_b)} \quad (4-39)$$

which at the material interface ($j = J + 1$) is used in the momentum equation to obtain new values for the boundary velocity and the new location of the interface.

4.2 Equation of State

4.2.1 Mie-Grüneisen EOS

Solution of the partial differential equations (4-9) to (4-12) is usually treated as an initial-value problem, with the solutions calculated in response to a set of initial excitation functions and boundary conditions. It is apparent that specific material properties govern the response of the material, and will result in different behaviours for nominally the same initial conditions. For the set of flow equations to be solvable, an expression is required for the EOS relationship between pressure, volume and internal energy. Thermodynamic theory allows a material description to be given by three thermodynamic variables, such that one of these can be expressed in terms of the other two, e.g. the pressure in terms of the internal energy density ε , and specific volume

$V \left(\rho = \frac{1}{V} \right)$. Thus

$$P = P(\varepsilon, V) \quad \text{or} \quad P = P(\varepsilon, \rho) \quad (4-40)$$

Equation (4-40) can be thought of as a surface in pressure-energy-volume space. As such, a change in the pressure dP can be written in terms of the changes in the other two variables by

$$dP = \left(\frac{\partial P}{\partial V} \right)_{\varepsilon} dV + \left(\frac{\partial P}{\partial \varepsilon} \right)_V d\varepsilon \quad (4-41)$$

where subscripts ε and V refer to the derivative being obtained for one variable while the other is held constant. Integration of this equation allows the pressure to be expressed in terms of the volume and energy relative to the pressure at a reference volume and energy V_R and ε_R .

The Mie-Grüneisen parameter is defined as [30]

$$\Gamma = V \left(\frac{\partial P}{\partial \varepsilon} \right)_V \quad (4-42)$$

and if it is assumed that Γ is pressure independent, integration of equation (4-41) gives the Mie-Grüneisen EOS [30], [31]

$$P(V) = P_h(V) + \frac{\Gamma}{V} (\varepsilon - \varepsilon_h) \quad (4-43)$$

where the reference state is taken as the Hugoniot. The Hugoniot of a material is a locus of the final pressure-volume-energy states that can be attained by shock compression, and it is neither an isotherm nor an isotope. The actual thermodynamic path followed is a straight line from the initial state to the final state, called the Rayleigh line.

The Mie-Grüneisen parameter is found by evaluating equation (4-43) using various thermodynamic identities [76]

$$\Gamma = \frac{\beta \kappa}{\rho C_p} \quad (4-44)$$

where β is the coefficient of volumetric expansion, κ is the adiabatic bulk modulus, ρ is the density and C_p is the specific heat at constant pressure. Normally the Mie-Grüneisen parameter is determined from

$$\Gamma = V \frac{\Gamma_o}{V_o} \quad (4-45)$$

where the subscript refers to the room temperature, ambient pressure values [31].

The Mie-Grüneisen EOS has been shown to be valid for solids, and in particular metals, as well as liquids. But at very high pressures or distended states (e.g. vaporisation), it must be replaced by other formulae.

4.2.2 Linear $U_s - u_p$ Equation of State

Beside the Mie-Grüneisen EOS, an empirically determined relationship between the particle and shock velocity has been used in conjunction with the Rankine Hugoniot shock-jump equations of section 2.1.1 to obtain solutions to shockwave problems. In this the relationship between U_s and u_p is described initially by a polynomial equation with parameters $c_s, S_1, S_2, S_3 \dots$

$$U_s = c_s + S_1 u_p + S_2 u_p^2 + S_3 u_p^3 + \dots \quad (4-46)$$

However, for most solid materials, the relationship between particle and shock velocities has been found [77] to be adequately described by a linear function, thus giving the linear $U_s - u_p$ EOS

$$U_s = c_s + S u_p \quad (4-47)$$

where c_s is the speed of sound in the material at ambient pressure and S is a dimensionless constant. Values of c_s and S are tabulated in the literature [77].

4.2.3 Equation of State for Porous Material

Solids in a distended or porous state require special handling in a hydrodynamic code, since they absorb energy upon impact and mitigate the consequences of shock loading. This usually results in compaction to a partially or fully compacted state, with heating associated with pore compaction. In describing the dynamic response of porous materials, it is generally necessary to describe both the compaction behaviour at low pressure and the effect of heating at high pressure.

4.2.3.1 Porosity and Theoretical Density

For a porous or powder material, the definition of porosity due to Hermann [78] is

$$\alpha = \frac{V_{porous}}{V_s} \quad (4-48)$$

where V_{porous} is the specific volume of the porous material and V_s is that of the corresponding solid material at the same pressure and temperature. α is of course unity when the material becomes solid.

For porous and powder materials, the Hugoniot depends on an additional parameter, namely the initial porosity α_e , where

$$\alpha_e = \frac{V_{oo}}{V_o} = \frac{\rho_o}{\rho_{oo}} \quad (4-49)$$

in which ρ_{oo} is the initial powder density and ρ_o is the solid density at ambient pressure (sometimes termed zero pressure).

It is common practice to use the solid density (equivalent to full compaction) at zero pressure as the reference, called the theoretical density (TD). An 80% TD sample would have an initial density equivalent to 80% of the solid density at zero pressure.

Since it would be impractical to generate experimental data for every possible porosity, various methods have been proposed [78], [83], [88], [92], [96] - [98] to calculate the Hugoniot curves for porous or powder material.

4.2.3.2 The Snow-Plow Model

Historically, the development of theoretical models for the shock compaction of porous material evolved from the assumption of particle re-arrangement, pore collapse and compression to solid density. This model is usually referred to as the snow-plow model, and the material is assumed to collapse to solid density at infinitesimally small loading pressure [76], [31] and thereafter to remain incompressible.

The model may be illustrated by applying a triangular shock pressure (Fig 4-4a) to a porous material to bring it to a pressure P and velocity u_p (Fig 4-4b). Both of these quantities will be assumed to be uniform throughout the compacted material.

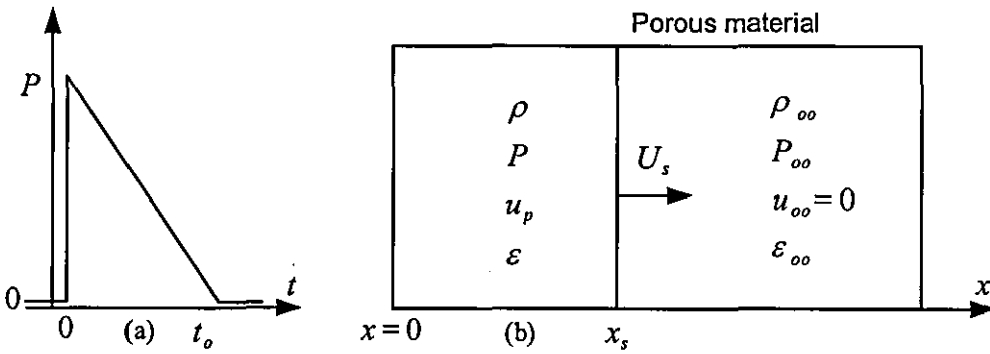


Figure 4-4 Shock pressure pulse (a) and geometry (b).

If at time t , the shock (Fig 4-4b) at location x_s is related to the shock velocity U_s by

$$x_s = \int U_s(t) dt \quad (4-50)$$

the conservation of momentum requires that

$$P - P_{oo} = \rho_{oo} U_s u_p \quad \text{or} \quad P = \rho_{oo} U_s u_p \quad (4-51)$$

by assuming negligible ambient pressure $P_{oo} = 0$.

The shock velocity U_s may be eliminated from equation (4-51) by using the equation for the conservation of mass

$$\rho_{oo}U_s = \rho(U_s - u_p) \quad \text{or} \quad U_s = \frac{V_{oo}}{V_{oo} - V} u_p \quad (4-52)$$

By integrating the pressure to get the initial impulse as

$$I_o = \int P(t)dt = \int \rho_{oo}u_p U_s(t)dt = \rho_{oo}u_p x_s = \frac{u_p x_s}{V_{oo}}, \quad (4-53)$$

the particle velocity behind the shock front can be written as

$$u_p = \frac{I_o}{x_s} V_{oo} \quad (4-54)$$

Substituting equations (4-52) and (4-54) into equation (4-51), and using the assumption that the density in the compressed state behind the shock equals the solid density, the pressure P may be related to the shock position x_s by

$$P(x_s) = \frac{I_o^2}{x_s^2} \frac{\alpha_e^2}{(\alpha_e - 1)} V_o \quad (4-55)$$

The results for a 25 GPa triangular pressure pulse with a base duration of $t_o = 0.5 \mu s$ are shown in Fig 4-5, which indicates that equation (4-55) over-estimates the peak pressure in the first 1.5 mm of shock travel. Thus the snow-plow theory is clearly ineffective for the prediction of shock pressure near the impact surface, although it describes the pressure decay reasonably well further into the powder.

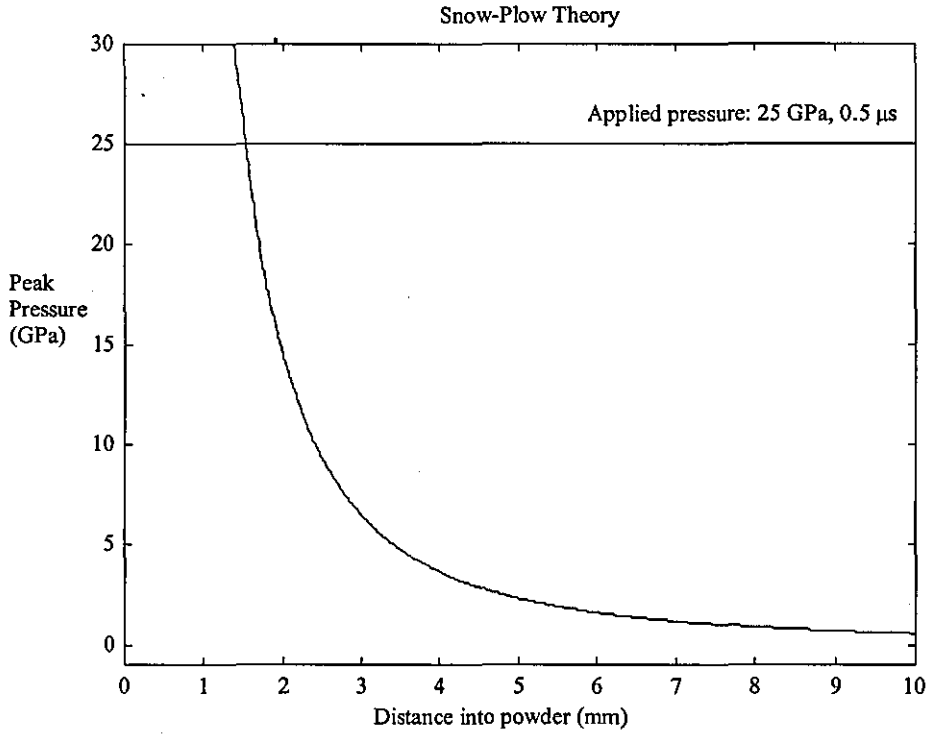


Figure 4-5 Attenuation of pressure in porous or powder material according to snow-plow theory.

4.2.3.3 The Mie-Grüneisen Model

The Mie-Grüneisen theory has traditionally been used to describe the Hugoniot response of porous material at high shock pressure (above a few tens of GPa), since it uses the known Hugoniot for the fully dense material.

The procedure for calculating the Hugoniot of porous material [35] is based on the Mie-Grüneisen equation, given by

$$P = P_h(V) + \frac{\Gamma}{V}(\varepsilon - \varepsilon_h) \quad (4-56)$$

where P_h and ε_h are the pressure and specific internal energy along the solid Hugoniot curve in thermodynamic space, and are functions of the specific volume. Γ is the Mie-Grüneisen parameter previously defined in section 4.2.1.

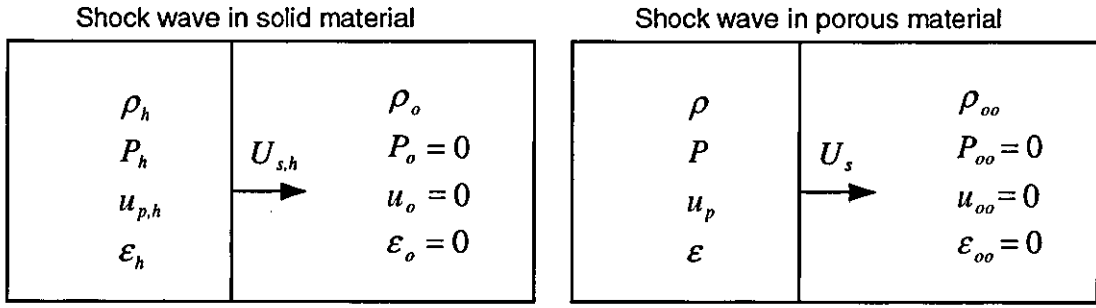


Figure 4-6 Shockwave parameters for (a) solid material with subscript h and (b) porous material with subscript oo .

If the solid material is described by the linear $U_s - u_p$ EOS of section 4.2.2, its particle velocity u_{ph} is linearly related to the shock velocity U_{sh} by

$$U_{sh} = c_s + S u_{ph} \quad (4-57)$$

where subscript h denotes a solid material and S is a dimensionless constant.

Applying the Rankine-Hugoniot shock-jump equations (see section 2.1.1) for the conservation of mass, momentum and energy to the solid material of Fig 4-6a gives

$$\rho_h (U_{sh} - u_{ph}) = \rho_o U_{sh} \quad (4-58)$$

$$P_h = \rho_o U_{sh} u_{ph} \quad (4-59)$$

$$\varepsilon_h = \frac{1}{2} (P_h + P_o) (V_o - V_h) \quad (4-60)$$

Similarly for the porous material denoted by the subscript oo in Fig 4-6b, the Rankine-Hugoniot shock-jump equations are

$$\rho (U_s - u_p) = \rho_{oo} U_s \quad (4-61)$$

$$P = \rho_{oo} U_s u_p \quad (4-62)$$

$$\varepsilon = \frac{1}{2} (P + P_{oo}) (V_{oo} - V) \quad (4-63)$$

For the solid, equation (4-57) can be combined with equations (4-58) to (4-59) to yield the relationship between pressure and specific volume as

$$P_h(V) = \frac{c_s^2 (V_0 - V)}{(V_0 - (V_0 - V)S)^2} \quad (4-64)$$

Inserting equations (4-64) and (4-60) into equation (4-56) leads to a relationship between pressure and specific volume for the porous material

$$P(V) = \frac{2V - \Gamma(V_o - V)}{2V - \Gamma(V_{oo} - V)} P_h(V) \quad (4-65)$$

To obtain the relationship between shock and particle velocity for the powder, the simplest procedure is to solve equation (4-65) to find $P-V$ pairs, and then to apply the following relationships [35]

$$U_s = V_{oo} \sqrt{\frac{P}{(V_{oo} - V)}} \quad (4-66)$$

$$u_p = \sqrt{P(V_{oo} - V)} \quad (4-67)$$

which are obtained by combining equations (4-61) and (4-62) for the porous material.

a) Empirical Data for Porous Aluminium

Experimental shockwave data for porous aluminium [31] has been used to verify the theoretical EOS in equations (4-65) to (4-67). The experimental data given in Appendix B [31] is for porous aluminium with a relatively high initial powder density at 91%, 80%, 70% and 59% TD . Material constants for the linear $U_s - u_p$ EOS for solid aluminium are [77] $\rho_o = 2.79 \times 10^3 \text{ kg/m}^3$, $c_s = 5.33 \text{ km/s}$ and $S = 1.34$. Figs 4-7 to 4-9 show good agreement between the calculation procedure and McQueen's data [31], and confirm that the Mie-Grüneisen model is accurate for porous material with an initial density greater than 60% TD .

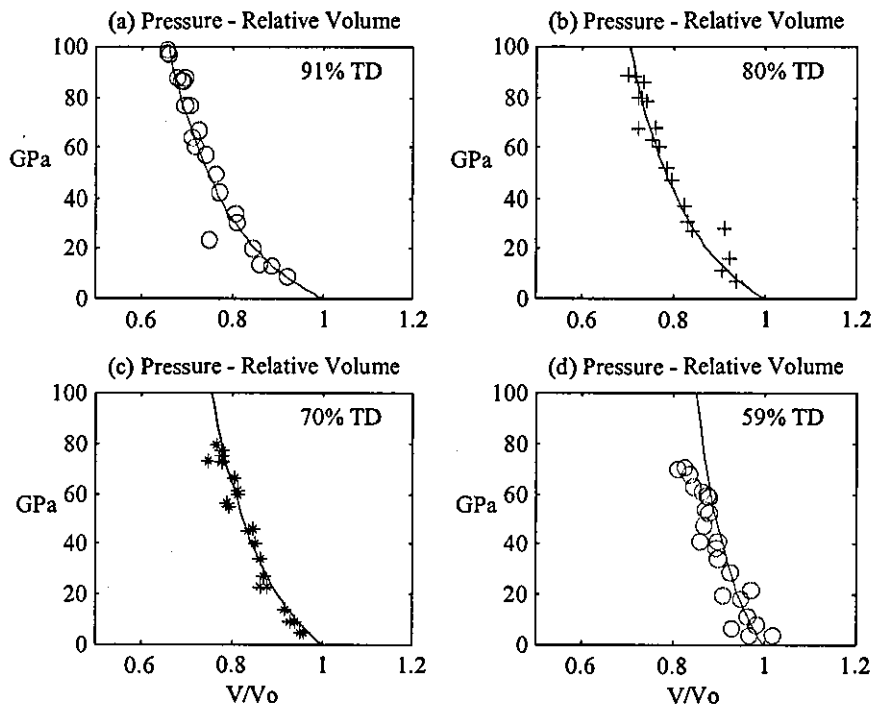


Figure 4-7 Pressure - relative volume relationship for porous aluminium
(a) 91% TD , (b) 80% TD , (c) 70% TD and (d) 59% TD .

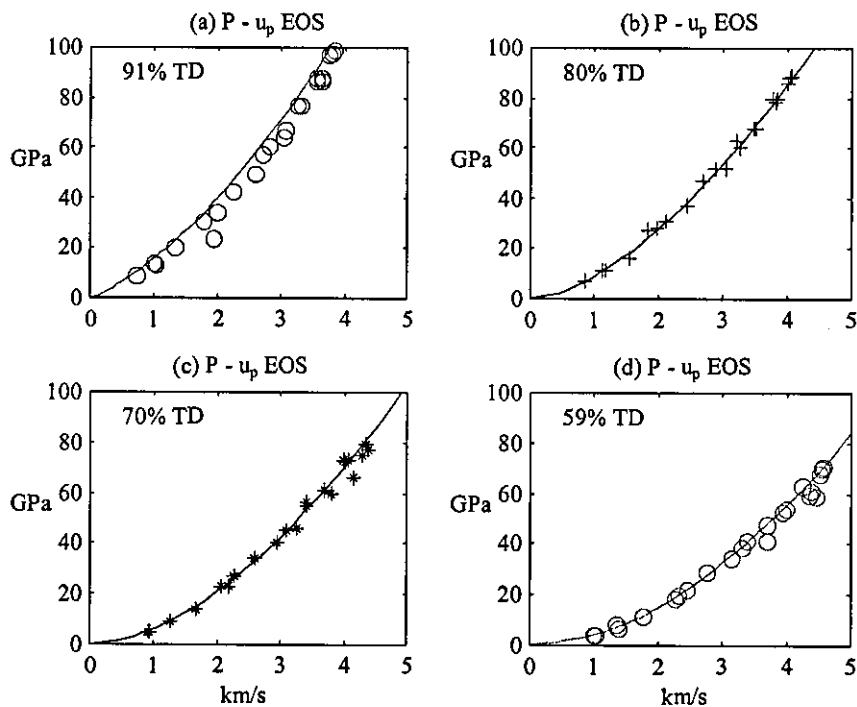


Figure 4-8 $P - u_p$ relationship for porous aluminium
(a) 91% TD , (b) 80% TD , (c) 70% TD and (d) 59% TD .

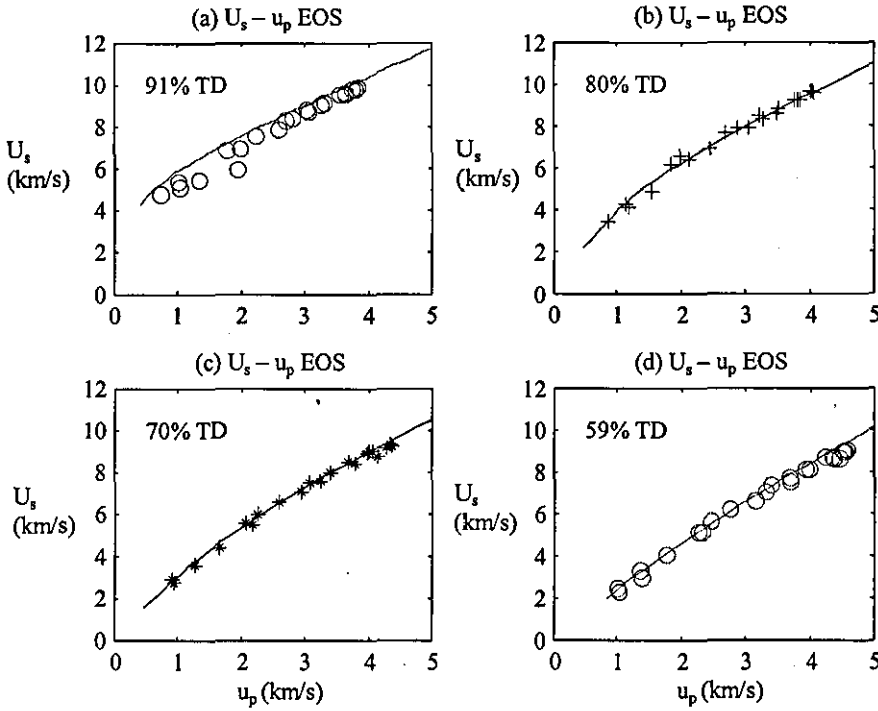


Figure 4-9 $U_s - u_p$ relationship for porous aluminium

(a) 91% TD , (b) 80% TD , (c) 70% TD and (d) 59% TD .

b) Anomalous Compression

The strong heating caused by shock compression of highly porous or powder material can lead to anomalous behaviour in the $P-V$ Hugoniot, where the volume increases instead of decreasing with increasing pressure (see Fig 4-10). This anomalous compressibility was experimentally observed first in the 1960s [76]. Most material models fail to give a realistic representation of experimental data when the compression leads to anomalous behaviour. An analysis of the Mie-Grüneisen EOS for porous material in equation (4-65) reveals that anomalous compression occurs when the initial porous density is less than

$$TD < \frac{\Gamma}{2 + \Gamma} \quad (4-68)$$

Given that the Mie-Grüneisen parameter Γ for most metals lies between 1.8 and 2.0 [77], anomalous compression occurs when the initial porous or powder density is less than 50% TD .

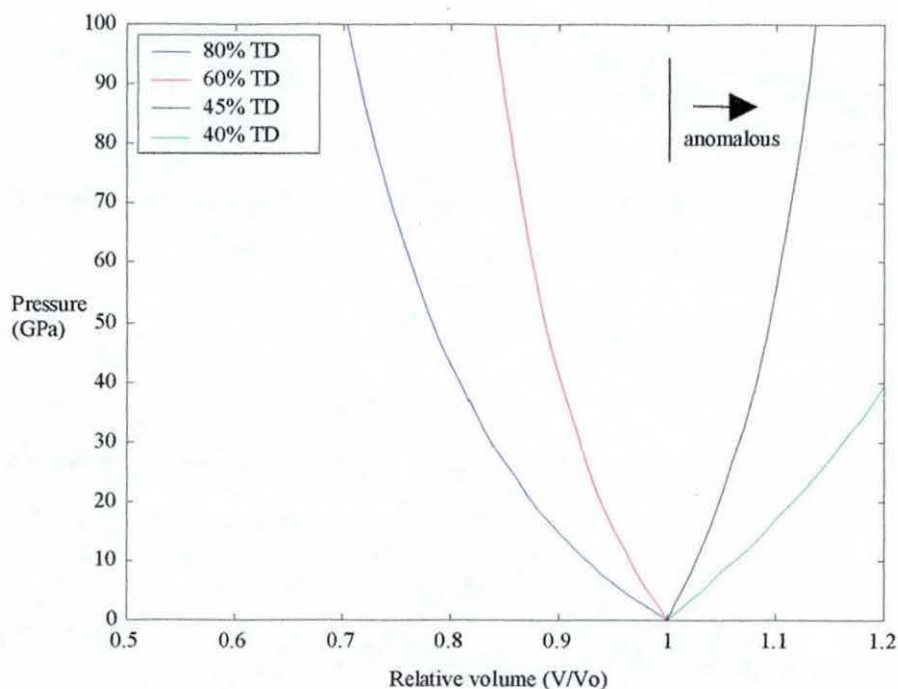


Figure 4-10 Anomalous compression.

4.2.4 The $P-\alpha$ Model

To overcome the limitation of the Mie-Grüneisen and snow-plow models, Hermann [78] developed a set of constitutive equations. These are commonly referred to as the $P-\alpha$ model and accurately reproduce the experimentally observed low-pressure compaction behaviour of porous materials. The $P-\alpha$ model requires, in addition to the Hugoniot of the solid, a specification of the initial response in the porous state, as a function that describes the compaction behaviour and the pressure at which full compaction occurs.

The central assumption in Hermann's $P-\alpha$ model is that the specific internal energy is the same for both the porous material and the solid material under identical conditions of pressure and temperature. Thus, if the EOS for a solid material of volume V_s is

$$P = f(V_s, \epsilon), \quad (4-69)$$

that for the porous material of volume V_{porous} is

$$P = f\left(\frac{V_{porous}}{\alpha}, \varepsilon\right) \quad (4-70)$$

where f is the same function in both equations

In order to complete the description of the porous material, α must be specified as a function of the thermodynamic state

$$\alpha = g(P, \varepsilon) \quad (4-71)$$

Hermann made the further assumption that along the Hugoniot from normal ambient conditions, equation(4-71) can be simplified and expressed as

$$\alpha = g(P) \quad (4-72)$$

Equations (4-70) and (4-72) completely specify the EOS of the material. In essence, the introduction of α allows a very convenient separation of the volume change of the material due to compression from that due to pore collapse.

If experimental data are available for partially compacted states, consisting of pressure, specific volume and internal energy, then α and the function $\alpha = g(P)$ can be calculated directly from the definition of porosity in equation (4-48) and the EOS for the solid material in equation (4-69).

The constitutive equation in the $P-\alpha$ model is divided into (1) the elastic region (2) the plastic region and (3) the solid region (see Fig 4-11).

In the initial elastic region, defined by $0 \leq P \leq P_e$ and $\alpha_p \leq \alpha \leq \alpha_e$, compression of the porous material may be expected to be elastic. Here α_e is the initial porosity and α_p is

the porosity at which plastic flow begins. Elastic behaviour is described mathematically as a constant gradient connecting the initial porosity $(\alpha_e, 0)$ and the elastic limit (α_p, P_e)

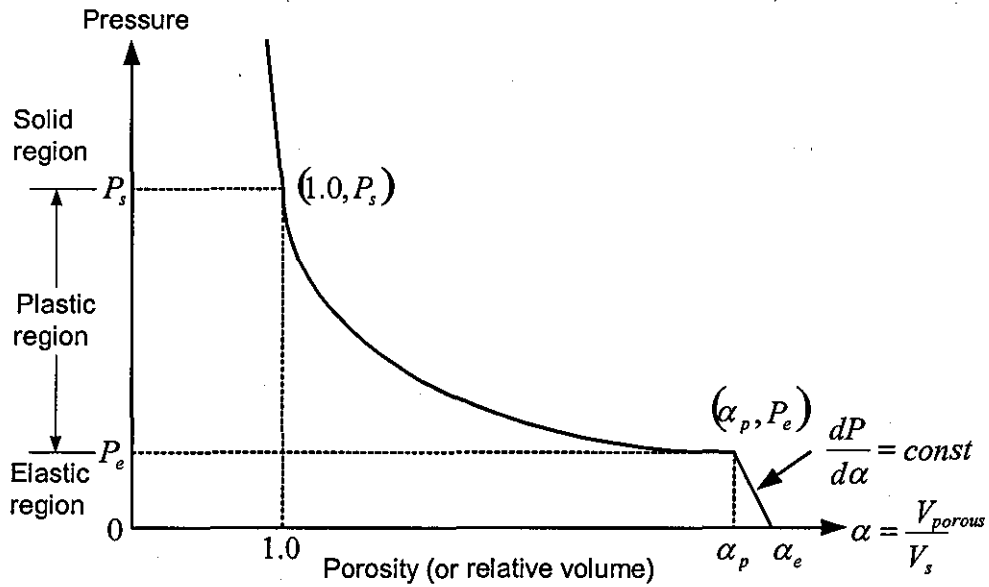


Figure 4-11 Theoretical $P-\alpha$ relationship.

In the plastic region defined by $P_e < P \leq P_s$ and $1.0 < \alpha \leq \alpha_p$, the permanent volume change arising from plastic deformation is described by the general polynomial function

$$\alpha(P) = \alpha_o + \alpha_1 P + \alpha_2 P^2 + \alpha_3 P^3 + \dots \quad (4-73)$$

Butcher and Karnes [80] found that it is adequate to use a quadratic function for $\alpha(P)$ to obtain good agreement with experimental data for porous iron. In the case of porous aluminium, Butcher, Carroll and Holt [81] also used a quadratic function to describe the compression function.

The $P-\alpha$ model is completely defined when the constants α_e , α_p , P_e , P_s and the function $\alpha(P)$ describing the compression process in the plastic region are available. For the case of a quadratic function for the plastic region, the $P-\alpha$ model may be expressed as

$$P(\alpha) = \left(\frac{\alpha_e - \alpha}{\alpha_e - \alpha_p} \right) P_e \quad \text{if } \alpha_p \leq \alpha \leq \alpha_e \quad (4-74)$$

$$P(\alpha) = P_s + (P_e - P_s) \sqrt{\left(\frac{\alpha - 1}{\alpha_p - 1} \right)} \quad \text{if } 1.0 \leq \alpha \leq \alpha_p \quad (4-75)$$

$$\text{and } P(\alpha) = \text{Hugoniot of solid material if } \alpha > 1.0 \quad (4-76)$$

which is shown in Fig 4-12 using $P_e = 0.08 \text{ GPa}$, $\alpha_p = 1.275$ and $P_s = 0.7 \text{ GPa}$ [81].

The Hugoniot for the solid region uses the linear $U_s - u_p$ relation of section 4.2.1.

In this model, plastic deformation occurs in the aluminium powder when it is compressed to a density above 78.43% TD (equivalent to $\alpha_p = 1.275$) at a low pressure of about 0.08 GPa (or 0.8 kbar). It is reasonable to assume that the transition from insulator-to-conductor in aluminium powder is preceeded by the onset of plastic deformation. This would suggest that phase transition takes place either at a pressure greater than 1.0 kbar or a density greater than 80% TD.

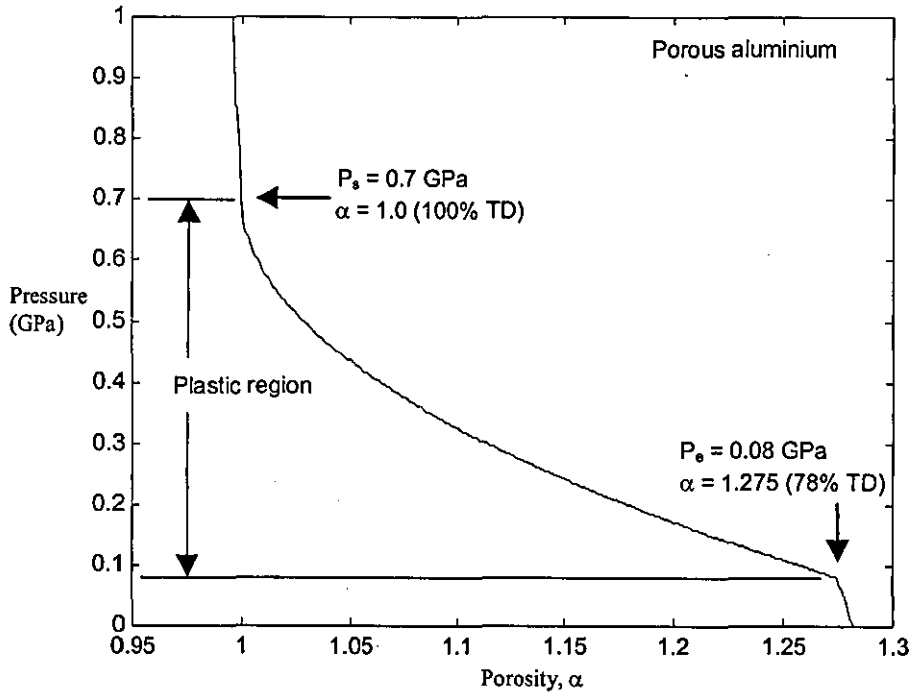


Figure 4-12 $P - \alpha$ model for porous aluminium defined by equations (4-74) to (4-76).

4.2.5 Equation of State for Powder Material

The complexity of the micro-mechanical behaviour of highly porous material (or low-density powder) has led to a wide variety of semi-empirical and analytical approaches to model the EOS for these materials.

In contrast to porous materials, only a few models have been developed specifically to describe powdered materials. The most notable is due to Kawakita [82] - [84], which has found widespread application in the fields of powder metallurgy [85] - [89] and pharmaceuticals. It is an empirical model based on observations of the experimental relationship between pressure and volume, and the form in most common usage is

$$\frac{\rho}{\rho_{oo}} = \frac{1 + bP_c}{1 + abP_c} \quad (4-77)$$

where ρ_{oo} , a and b are experimentally determined constants and P_c is the compression pressure.

The Kawakita model suffers from the disadvantage of not having a sound physical basis, since no clear relationship exists between a and b and the physical properties of the powder. In fact, values for a and b determined by one set of experiments may not be directly relevant for experiments under different experimental conditions. For aluminium powders with particle sizes between $53 \mu m$ and $75 \mu m$, Page and Warpenus reported [90] different values of the constants for dynamic and quasi-static compaction.

More recently, Boshoff-Mostert and Viljoen [91] carried out a comparative study of analytical methods for Hugoniot curves of porous materials, and compared five EOSs developed by Dijken and De Hosson [92] - [94], Oh and Persson [95] - [96], Simon and Legner [97], Wu and Jing [98] and a new method proposed by Viljoen [91].

Dijken and De Hosson [93] proposed a simple model for predicting the shock compaction of low-density powder (or porosity $\alpha > 2.0$), which assumed that the specific volume (or density) behind the shockwave is equal to the zero-pressure solid specific volume (or density). Thus

$$U_s = \frac{V_{oo}}{V_{oo} - V} u_p = \frac{1}{1 - TD} u_p \quad (4-78)$$

$$P = \frac{U_s u_p}{V_{oo}} = \frac{TD}{1 - TD} \rho_o u_p^2 \quad (4-79)$$

where $TD = \frac{1}{\alpha_e} = \frac{V_o}{V_{oo}}$ is theoretical density and α_e is the initial porosity.

Oh and Persson [95] showed that the derivation of Hugoniot curves for porous material using the Mie-Grüneisen EOS is highly sensitive to any error in the Mie-Grüneisen parameter, and they proposed an alternative empirical EOS for extrapolation from the solid Hugoniot.

Simon and Legner [97] extended the Mie-Grüneisen approach to allow for initial porosity. Their method gives good agreement with experiments at high shock strength and relatively low initial porosity, but is less accurate at low shock strength and high initial porosities.

Wu and Jing [98] derived an alternate EOS having the same form as the Mie-Grüneisen model, and the method due to Viljoen [91] is an extension of their work.

Boshoff-Mostert and Viljoen concluded that, while all the methods compare well when the material has a low porosity (i.e. a high initial density), only three methods (Dijken and De Hosson, Wu and Jing, Viljoen) have the ability to predict accurately the Hugoniot when the material has a high porosity. The method of Simon and Legner overestimates the shock velocity U_s at higher values of particle velocity u_p , as is illustrated in Fig 4-13 for the case of 33% TD ($\alpha = 3$) porous copper. The method of Oh and

Persson is not included in their comparison, probably due to a lack of the material data required by it.

It is evident from Fig 4-13 that the $U_s - u_p$ relationship for low-density powder is a straight line passing through the origin. This is in contrast to the linear $U_s - u_p$ relationship for a solid material, which usually intersects the U_s axis at the value of the local speed of sound. This unique feature can be used as a guide (or benchmark) to check different models for low-density powder.

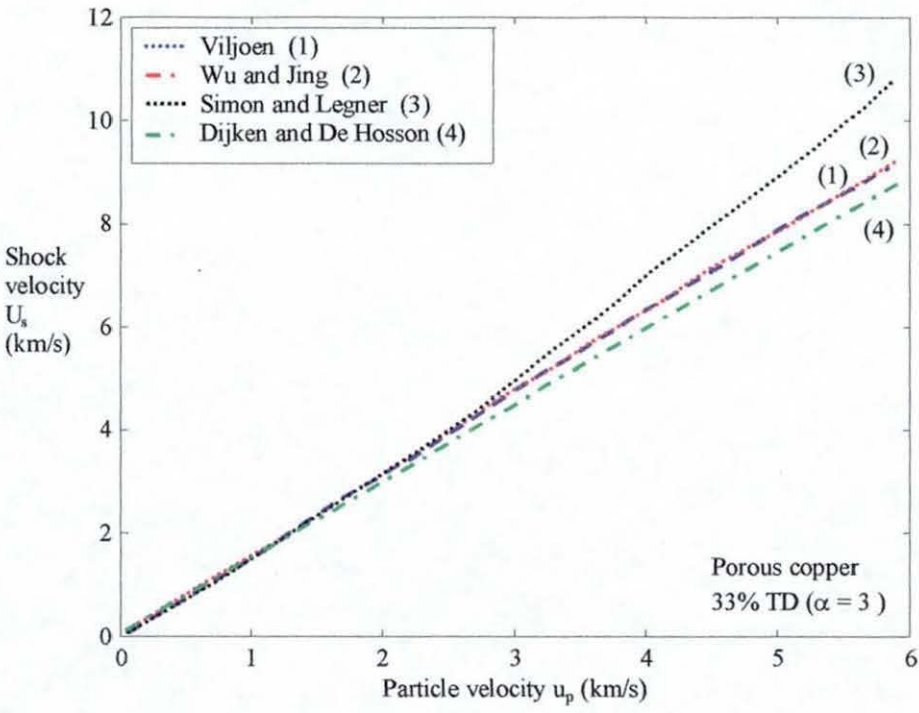


Figure 4-13 $U_s - u_p$ data for 33% TD ($\alpha = 3$) porous copper adapted from Fig 11 of [91].

4.2.6 Equation of State for Aluminium Powder

After careful evaluation, the $P - \alpha$ model was selected to model the aluminium powder in the present hydrodynamic code, primarily because it is a physical model based on the sound fundamental assumptions in the elastic-plastic model of material while explicitly allowing for porosity α . It has also been used successfully to provide accurate

prediction for many different powder materials [79] - [81] covering the range of material response from very weak to very strong shocks.

In [78], Hermann verified his $P-\alpha$ model by generating theoretical Hugoniots ($U_s - u_p$, $P - u_p$ and $P - V$ relationships) for a number of porous material with porosities in the range from $\alpha = 1.0$ (a solid) to $\alpha = 2.0$ (equivalent to 50% TD). He showed that there is excellent agreement between prediction by the $P-\alpha$ model and the available experimental data. No comparison was made for high porosity material with $\alpha > 2.0$, perhaps due to the unavailability of experimental data for low-density powder.

A series of numerical tests were carried out at Loughborough to verify the behaviour of the $P-\alpha$ model in predicting the shock response in low-density powder. It is known [91] that for low-density powder material, the relationship between U_s and u_p is linear with zero intercept, and that the simple model for low-density powder proposed by Dijken and De Hosson [93] gives a linear relationship between U_s and u_p . For simplicity, the model equations given by Dijken and De Hosson are used as a reference.

4.2.6.1 One-dimensional Steady Shock Propagation Test

As a test of the $P-\alpha$ model, the hydrodynamic code was used to model a steady shock ($U_s = \text{const}$) propagating inside aluminium powder, as shown in Fig 4-14.

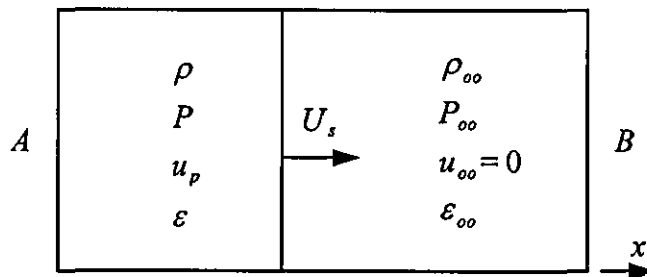


Figure 4-14 Steady shock propagation test case.

The aluminium powder is initially at rest $u_{oo} = 0$ and under ambient condition $P_{oo} = 0$. Initial powder densities of 33% and 50% *TD* (corresponding to porosities of $\alpha = 3.0$ and $\alpha = 2.0$) were tested.

The boundary condition at *A* in Fig 4-14 is set at a constant shock strength, to cause a steady shock to propagate into the aluminium powder. Shock pressures between 5 *GPa* and 25 *GPa* were used in the test.

For each computer run, the state (ρ , P and u_p) behind the steady shock front is noted and tabulated in a form similar to an actual shockwave experiment. In essence, each computer run produces one data point for the shock Hugoniot. Finally, all the data points collected by the numerical shock studies are compared with the theoretical model of Dijken and De Hosson.

Fig 4-15 provides a snap-shot of the detailed shock structure after the shock has travelled some distance into the aluminium powder. The $U_s - u_p$ and $P - u_p$ relationships shown in Figs 4-16 and 4-17 are in fairly good agreement with the Dijken and De Hosson model.

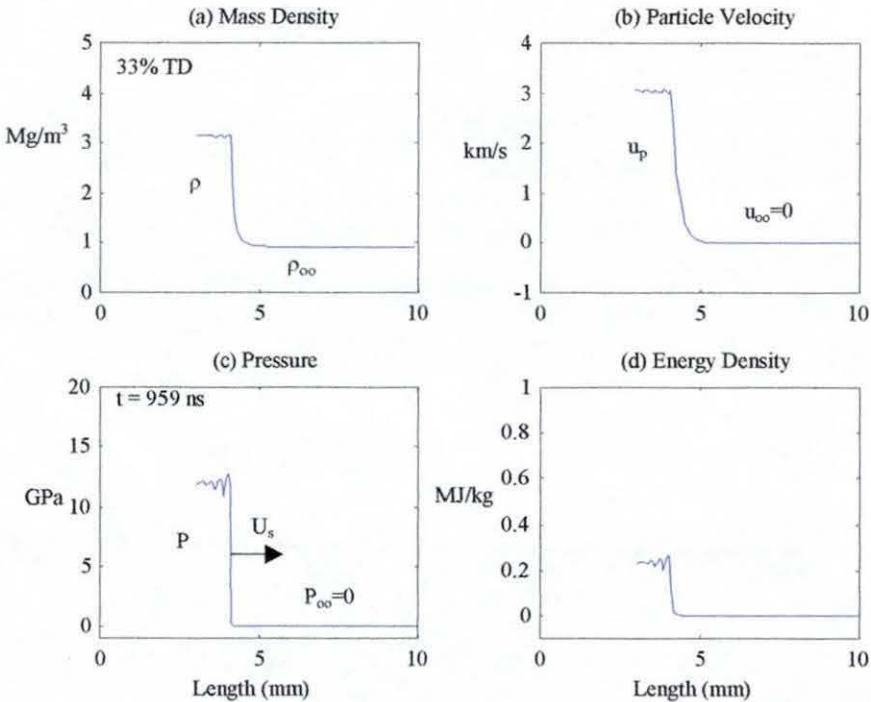


Figure 4-15 Typical computed results for steady shock propagation test.

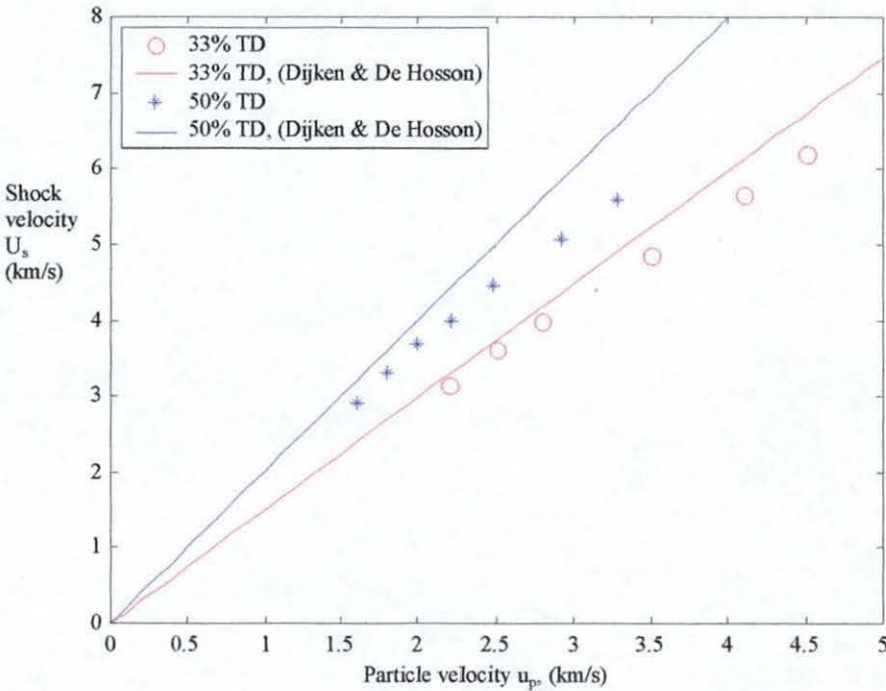


Figure 4-16 $U_s - u_p$ relationship for aluminium powder.

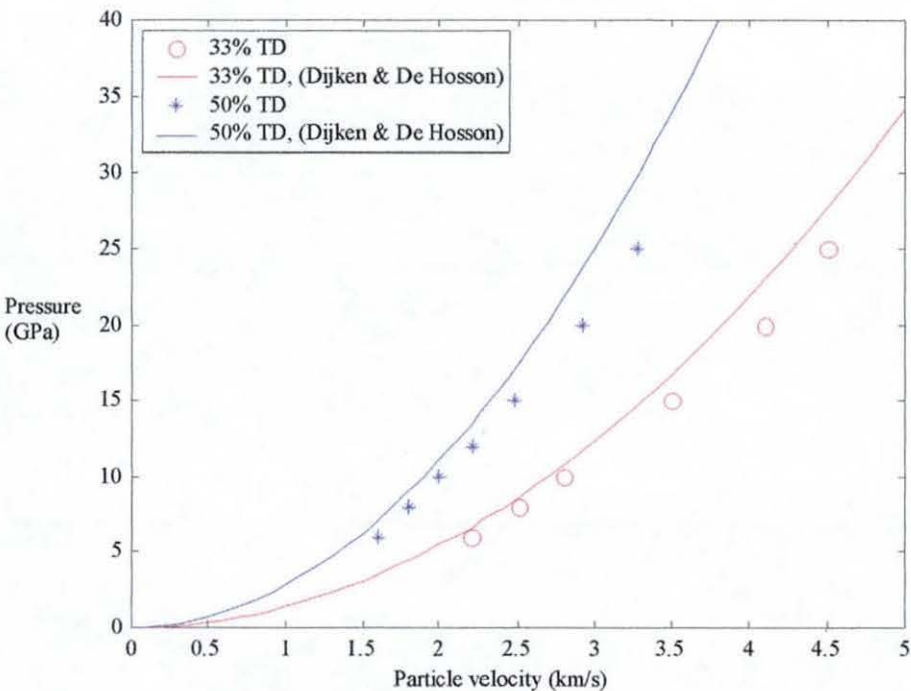


Figure 4-17 $P - u_p$ relationship for aluminium powder.

4.2.6.2 One dimensional Shock Reflection Test

The $P - \alpha$ model has also been verified in a one-dimensional shock reflection test problem (Fig 4-18). Aluminium powder with no porosity was tested (Figs 4-19 to 4-20) and compared with computation using the SESAME EOS for aluminium (Figs 4-21 to 4-22). The results are in good agreement.

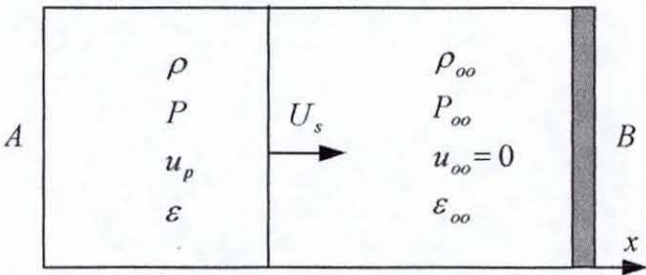


Figure 4-18 Shock reflection test case.

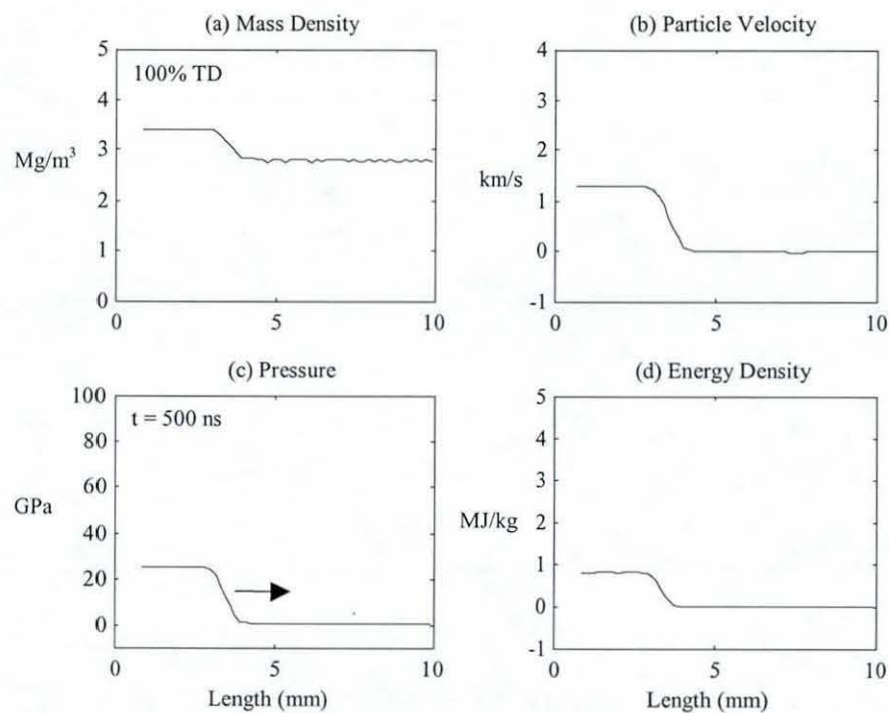


Figure 4-19 Right-going shock using $P-\alpha$ model with $TD = 100\%$.

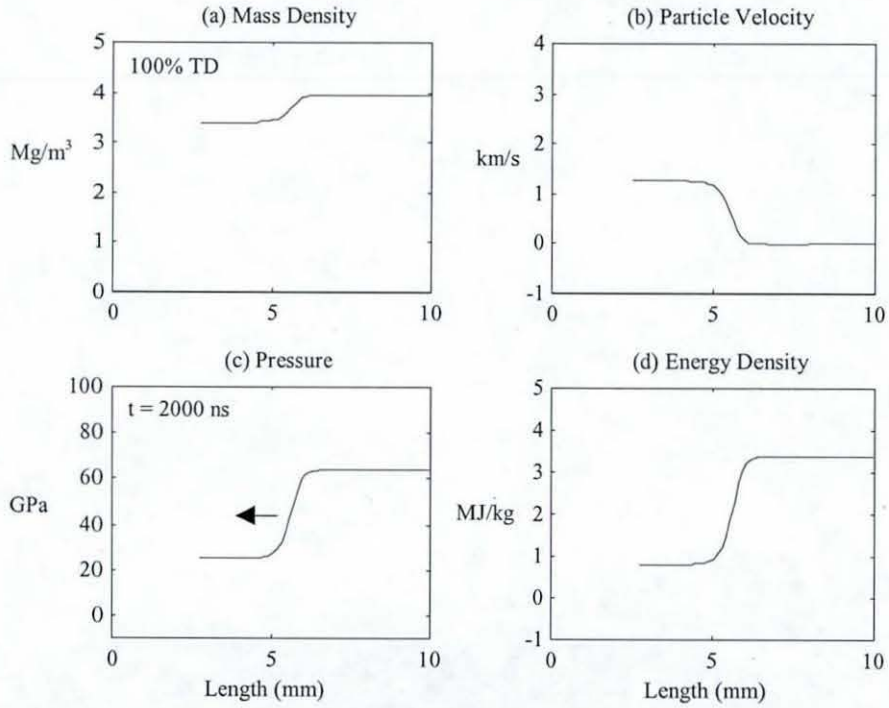


Figure 4-20 Left-going shock after reflection, using $P-\alpha$ model with $TD = 100\%$.

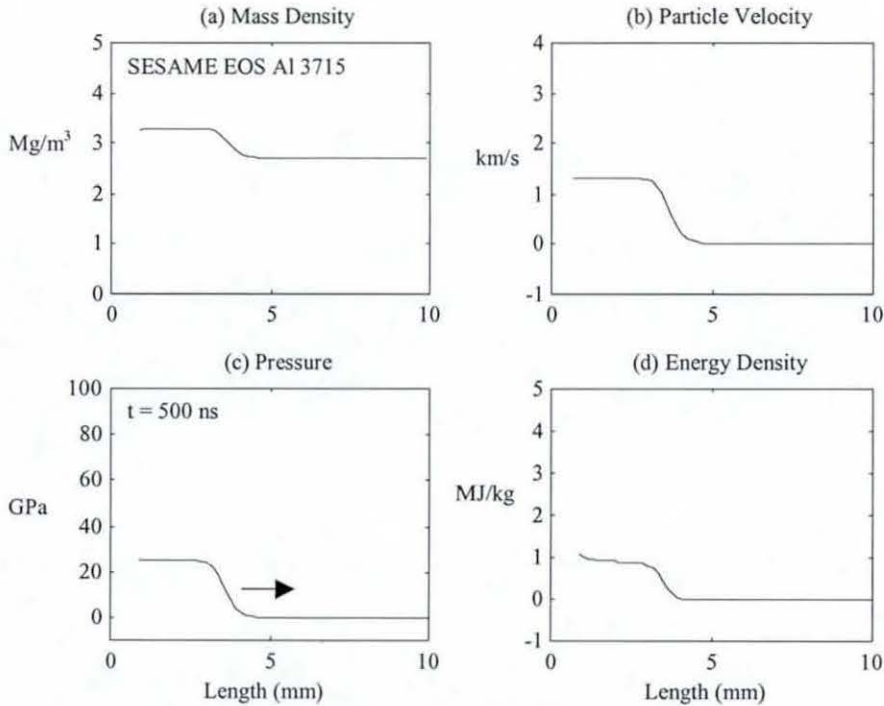


Figure 4-21 Right-going shock using SESAME table AL3715.

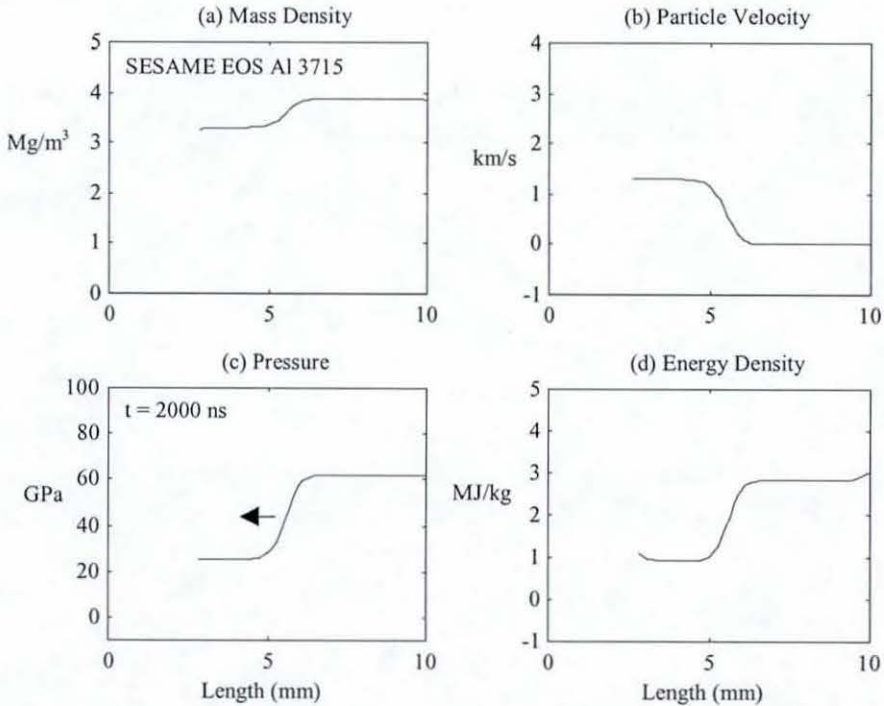


Figure 4-22 Left-going shock after reflection, using SESAME table AL3715.

4.2.7 EOS for Mylar Polyester

The shockwave properties for Mylar polyester film is available in tabular form [99] and has been processed by a linear least square fit to obtain the linear $U_s - u_p$ relationship (see section 4.2.2) shown in Fig 4-23. The speed of sound c_s for Mylar is found to be 2.75 km/s and the constant S has the value 1.29.

Using the linear $U_s - u_p$ relationship and the equation for the conservation of momentum $P = \rho_o U_s u_p$, the $P - u_p$ relationship can be expressed as

$$P = \rho_o (u_p c_s + S u_p^2) \quad (4-80)$$

which is plotted in Fig 4-24. This will be used with the impedance matching method to calculate the impact pressure and particle velocity in chapter 5. It is evident that the linear $U_s - u_p$ relationship is in good agreement with the empirical data provided in [99].

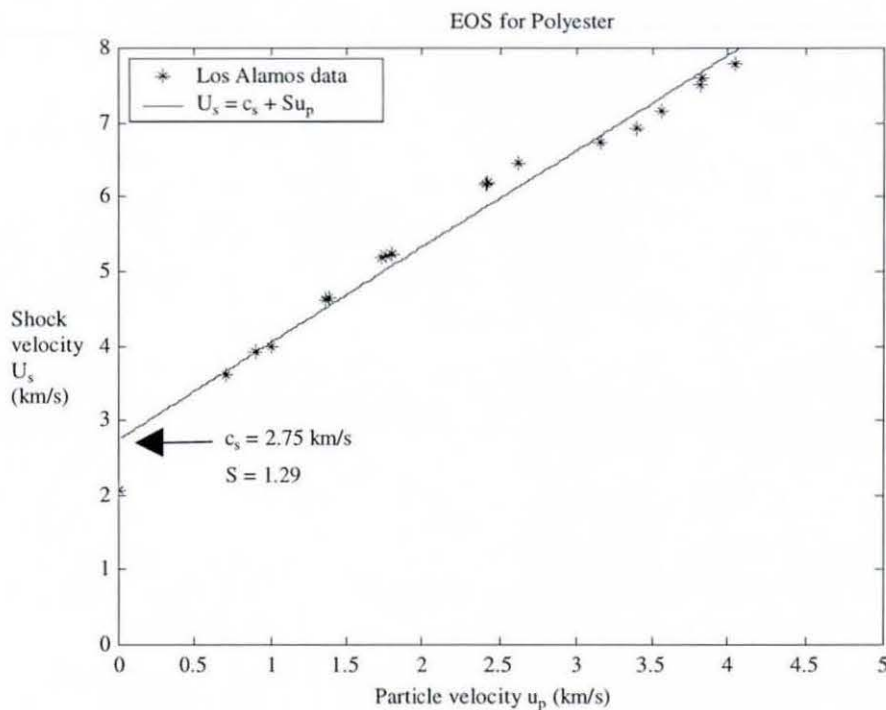


Figure 4-23 $U_s - u_p$ relationship for polyester [99].

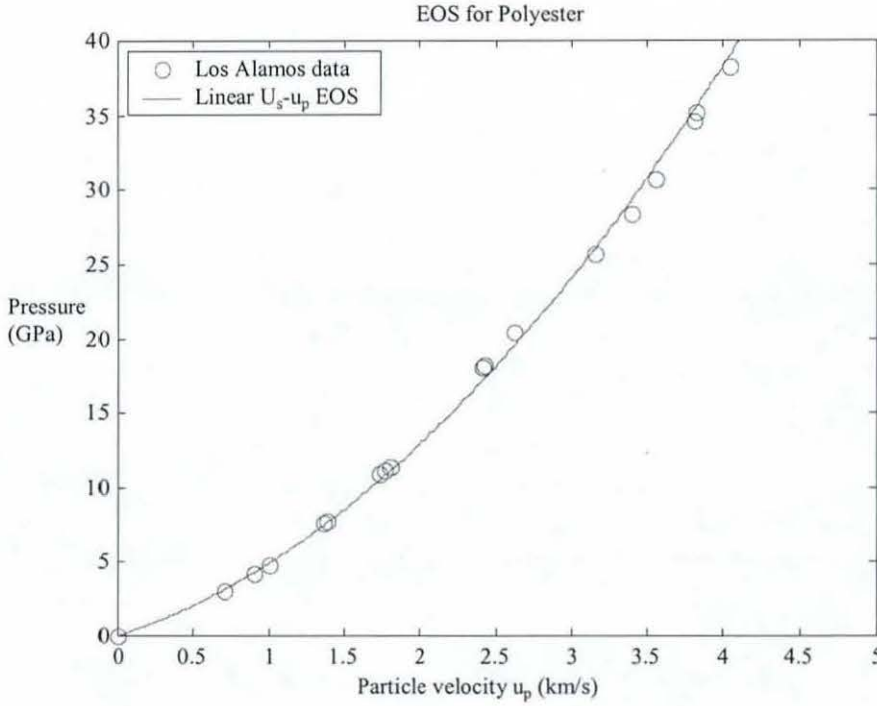


Figure 4-24 $P-u_p$ relationship for polyester [99].

4.3 Electrical Conductivity for Shock-loaded Aluminium Powder

4.3.1 Simple Switch Model

The increase in electrical conductivity in shock-loaded aluminium powder is modelled as the density-dependent function

$$\sigma(\rho) = \begin{cases} 10^{-6} \times \sigma_{al} & \text{if } \rho < \rho_{th} \\ k \times \sigma_{al} & \text{if } \rho \geq \rho_{th} \end{cases} \quad (4-81)$$

where $k \leq 1.0$ is a constant, σ_{al} is the electrical conductivity of solid aluminium and ρ_{th} is the threshold density at which the powder changes from an electrical insulator to an electrical conductor (see Fig 4-25).

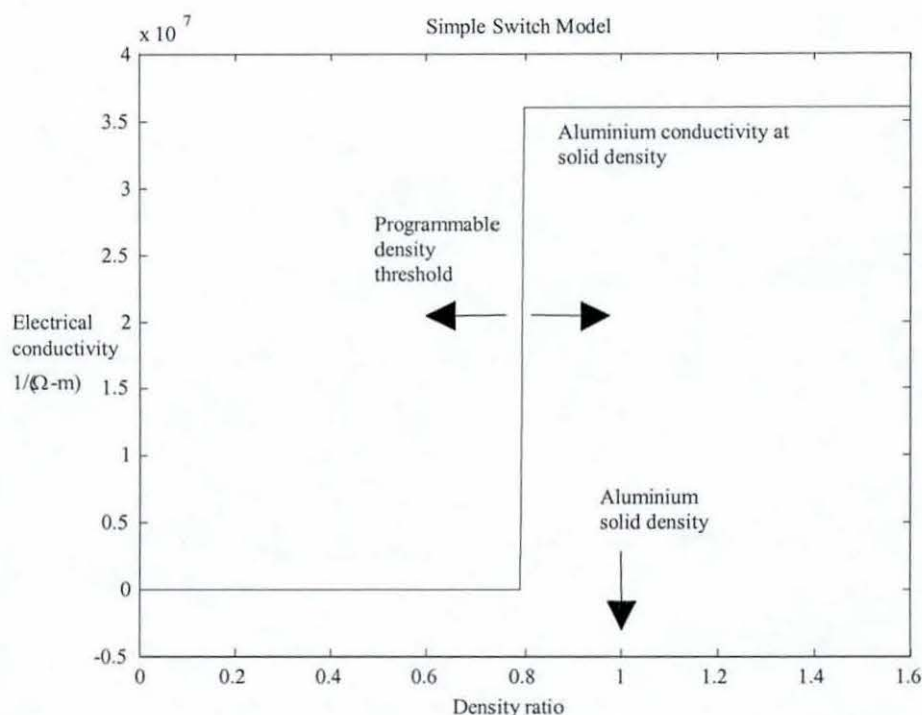


Figure 4-25 Electrical conductivity for aluminium powder - simple switch model.

While simple, this model is nevertheless consistent with the actual transition behaviour of the aluminium powder, which indicates that the thin insulating oxide layer between individual particles of the aluminium powder is destroyed under the action of shock pressure. In this model, the transition is assumed to be instantaneous when the shock compressed powder reaches a threshold density near the theoretical solid density. In the model calculation, the threshold density ρ_{th} is set at a value of 80% TD ($\alpha = 1.25$) corresponding to the onset of plastic deformation in the $P - \alpha$ model of section (4.3.2) and a threshold pressure of about 1 $kbar$. Computer calculations using this value of threshold density have consistently produced results that agree better with experimental data than those calculated using $\rho_{th} = 100\% TD$.

This simple model has the effect of dividing the computational domain into regions of high and low electrical conductivity, with the material behind the conducting shock front having a uniform but high electrical conductivity. Any spatial variation of electrical conductivity within the shock-compressed material is avoided, leading to a simplification of the computational algorithm.

4.3.2 Almström's Model

Almström et al [100] used a similar density-dependent conductivity model for a material with variable conductivity in their MHD calculations. The model has a complicated functional form that gives a smoother transition between the insulating and the conducting phases

$$\sigma(\rho) = \sigma_{\max} \frac{\left(\frac{\rho}{\rho_o} - \rho_{\sigma} \right)^{N_{\sigma}}}{\sigma_i + \left(\frac{\rho}{\rho_o} - \rho_{\sigma} \right)^{N_{\sigma}}} \quad (4-82)$$

where σ_{\max} , σ_i , ρ_{σ} , N_{σ} are constants

In this model, σ_i is the electrical conductivity in the insulation phase and σ_{\max} is the maximum electrical conductivity that the shock-loaded powder can attain in the conductor phase. ρ_{σ} controls the density ratio at the phase transition and N_{σ} the slope of the transition (Fig 4-26). Almström et al reportedly used $N_{\sigma} = 16$ and $\sigma_i = 10^{-5} (\Omega m)^{-1}$ in most of their calculation.

By using typical values for solid aluminium of $\rho_o = 2.77 \times 10^3 \text{ kg/m}^3$ and

$\sigma_{\max} = \sigma_{al} = \frac{1}{2.77 \times 10^{-8} \Omega m}$, the calculated form of the variable conductivity as a

function of the free parameter is shown in Fig 4-26.

While this model undoubtedly gives a smoother transition between the insulating and the conducting phases, it is, in essence, similar to the present simple model in defining two conductivity limits. The difference in the smoothness of the transition is not expected to have any major effect on the computational accuracy.

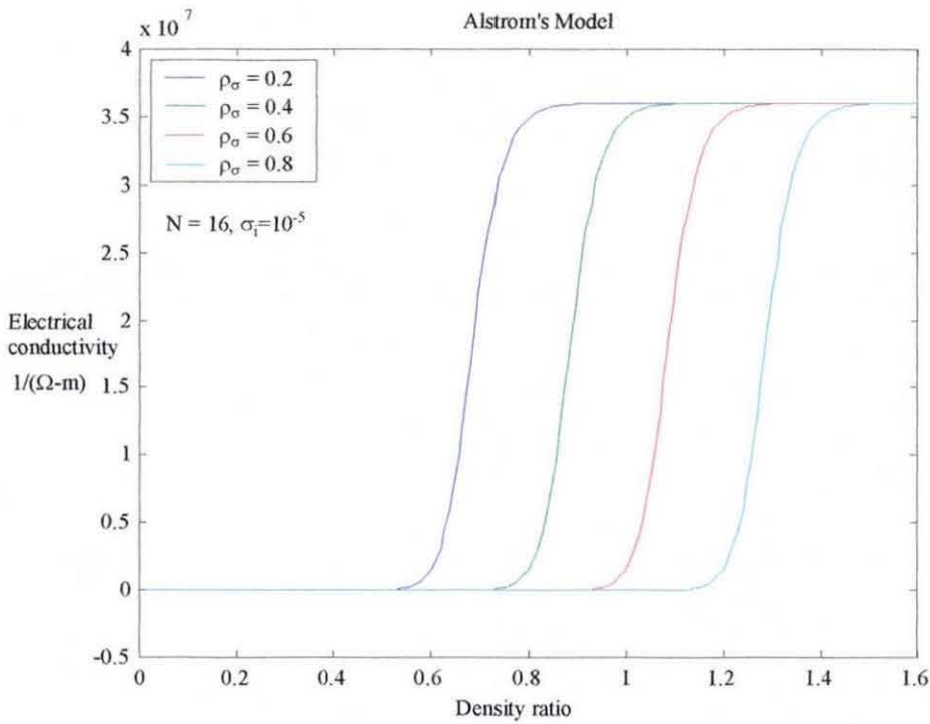


Figure 4-26 Electrical conductivity - Almström's model.

4.4 Electrical Conductivity for Ionised Gas

4.4.1 Spitzer's Equation

The Spitzer equation for the electrical conductivity of fully ionised gases [101], [102] is widely recognised and sufficiently simple for use as a basis for estimating the electrical conductivities of fully ionised plasma. Although a number of papers have appeared in the literature for the calculation of conductivities of non-ideal plasma [103] - [106], the plasma produced by the exploding foil will for simplicity be treated here as a fully ionised gas.

The Spitzer equation for the conductivity of a fully ionised ideal plasma in SI units without a magnetic field can be written [101]

$$\sigma = \frac{\gamma_E}{3.80} \frac{(T)^{\frac{3}{2}}}{Z \ln \Lambda} \quad (\Omega m)^{-1} \quad (4-83)$$

where T is the absolute temperature in K and Z is the mean ionic charge. γ_E is a factor that takes into account electron-electron scattering and has the values given in Table 8-1.

Table 8-1 Values of γ_E

Ionic Charge, Z	1	2	4	16	∞
γ_E	0.582	0.683	0.785	0.923	1.000

$\ln \Lambda$ in equation (4-83) is the Coulomb logarithmic term, which can be written [107]

$$\ln \Lambda = \ln \left[\frac{12\pi}{\sqrt{n_e}} \left(\frac{\epsilon_o kT}{e^2} \right)^{\frac{3}{2}} \right] \quad \text{or} \quad \ln \Lambda = \ln \left(1.24 \times 10^7 \frac{T^{\frac{3}{2}}}{\sqrt{n_e}} \right) \quad (4-84)$$

where n_e is the charge density per unit volume, $\epsilon_o = 8.854 \times 10^{-12} \text{ F/m}$ is the permittivity of free-space, k is Boltzmann's constant and e is the charge of an electron.

Fig 4-27 compares the electrical conductivity for a hydrogen plasma, calculated using equations (4-83) - (4-84) and $Z = 1$, with that for solid copper and aluminium at STP.

From equation (4-83), it can be seen that the conductivity is directly proportional to the three-half power of temperature for a fully ionised gas. Fig 4-27 shows that the conductivity rising rapidly with temperature with, for example, the conductivity of fully ionised hydrogen becoming equal to that of copper at a temperature of about $10^7 K$ ($\approx 1 \text{ keV}$). Calculations using different values for n_e show that the conductivity is practically independent of the charge density.

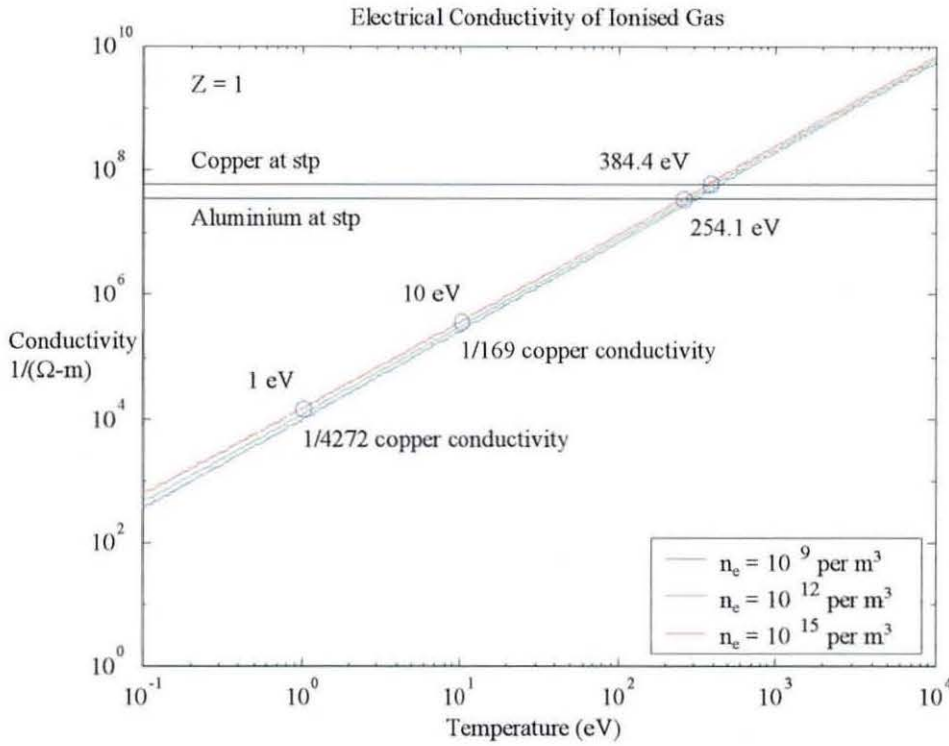


Figure 4-27 Electrical conductivity of ionised gas according to Spitzer's equation

The most significant results from a brief review of the Spitzer equations are

- (1) the electrical conductivity for plasma approaches that of a solid metal conductor (e.g. copper or aluminium) at a temperature of about $10^7 K$ and
- (2) at the temperature attained by the exploding foil plasma (between 1 eV to 10 eV, chapter 3), the electrical conductivity is several orders of magnitude less than that of a solid metal conductor (see Fig 4-27).

It follows from (1) and (2) that, in the initial phase of the flyer acceleration, the aluminium plasma behind the Mylar flyer will need to converge towards the axis at a speed faster than the rate at which magnetic flux diffuses through it, in order to provide significant contribution to the magnetic flux compression process.

4.5 Conclusion

In this chapter, the basic conservation equations for fluid flow, the hydrodynamic equations for flow calculation including shockwave and the description of material properties through the use of EOS have all been introduced. Numerical studies at Loughborough University have shown that the $P-\alpha$ model can represent fairly accurately materials with high porosity, such as the low-density aluminium powder which will be used in a shock compression experiment. The shock Hugoniot produced by numerical impact studies using the $P-\alpha$ model are in reasonable agreement with published results obtained from theoretical studies of porous and low-density powder material, in particular, with the novel EOS for low-density powder due to Dijken and De Hosson that provides an important link between material porosity and shockwave properties. A simple density-dependent model that is consistent with actual transition behaviour has been developed to represent the transition from insulator to conductor in a shock-loaded aluminium powder.

SHOCK COMPRESSION OF ALUMINIUM POWDER

This chapter describes application of the planar electric gun to the shock compression study of aluminium powder. The conducting shockwave thereby generated in the aluminium powder sample is characterised by two types of sensors (1) coaxial contact-pin probes to obtain the TOA data of the conducting shock front at discrete distances in the aluminium powder and (2) spiral resistance probes for continuous monitoring of the shockwave velocity. The experimental programme is followed by a systematic analysis of the results to validate the hydrodynamic code and EOS models of chapter 4.

5.1 Aluminium Powder

The aluminium powder selected for this study has a maximum particle size of $25\ \mu\text{m}$ with a purity of 99% and is supplied by Goodfellow Cambridge Ltd (UK).

For the experimental programme an initial powder density was required as low as is practically possible. However, when the initial powder density is small, it is extremely difficult to determine accurately the initial powder density, and accordingly this was measured by means of a high-precision scale when the powder was (1) loosely packed (2) normally packed and (3) tightly packed. The values obtained were $510\ \text{kg/m}^3$, $740\ \text{kg/m}^3$ and $970\ \text{kg/m}^3$ respectively. Using the theoretical density (TD) for aluminium of $2770\ \text{kg/m}^3$, these results correspond to initial power densities of 18%, 25% and 33% TD. The loosely packed configuration at 18% TD is found to contain numerous air gaps, and since these could cause problems during the compression process the initial density of the powder samples that were used experimentally all lie within the 25% to 33% TD range.

5.2 Shock Compression Experiments

5.2.1 Small-Scale Electric Gun

A small-scale electric gun based on a single, low-inductance capacitor ($26.9\mu F$, $8 kJ$) was developed specifically for use in the shock compression study of aluminium powder, because of the ease it provided for frequent experimentation. Discharge of the capacitor is initiated by a simple nail-switch, operated by an electromagnetically-controlled striker and which punches a hole through the Mylar-insulated parallel-strip transmission line. After each experiment the transmission line is repaired and a new Mylar sheet is inserted between the conductors. The arrangement is similar to that used in other exploding foil opening-switch experiments, but with the addition of a massive tamper plate under the transmission line and directly below the exploding foil, to absorb pressure from the foil explosion.

At the start of the experimental programme, the gun model described in chapter 3 was still undeveloped, so that the design, and in particular the dimensions of the exploding foil, was guided by the empirical model for aluminium foil published by Lindemuth et al [65] and the flyer velocity was estimated by Osher's method of energy balance [50]. Thus dimensions of $15\text{ mm} \times 15\text{ mm} \times 25.4\text{ }\mu\text{m}$ (see Fig 5-1) were chosen with the aim of achieving an estimated flyer velocity of about 3 km/s .

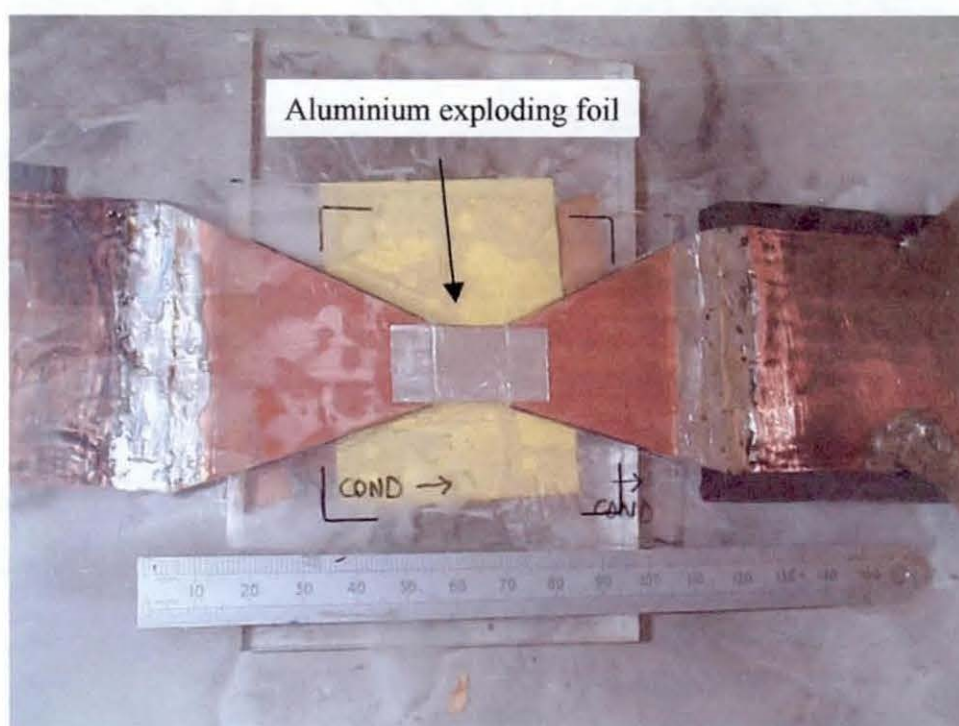


Figure 5-1 Aluminium exploding foil (EF).

5.2.2 Flyer Plate-Target Stand-off Distance

Due to an initial lack of information on the flyer acceleration process, a flyer stand-off distance (or air gap) of 3.0 mm was used to allow sufficient time ($1.0\text{ }\mu\text{s}$ at 3 km/s) for the Mylar flyer to reach terminal velocity. The gap was maintained at 3.0 mm for all experiments with TOA measurement, for ease of data analysis.

With the development of the new gun model in chapter 3, it became possible to obtain a more accurate estimate of the necessary flyer stand-off distance, by integrating the flyer velocity function from burst to the time when the Gurney terminal velocity is reached. Mathematically, the exact Gurney terminal velocity is reached only asymptotically at an infinite time after foil burst, and it is therefore common to use 95% of the terminal velocity when calculating the acceleration time and acceleration distance. The velocity profiles of Fig 3-4 was used in producing the values given in Table 5-1.

Table 5-1 Acceleration time and Stand-off distance

ε_G (MJ/kg)	250 μm Mylar flyer	
	Acceleration time (ns)	Acceleration distance (μm)
1	318	208.07
5	142	207.74
10	101	209.04
15	82	207.78
20	71	207.74

It is clear from the table that the acceleration time decreases as a higher energy density is released at burst, but that the corresponding distance is fairly insensitive to changes in the energy density. A similar calculation for a 75 μm Mylar flyer produced identical values of acceleration time and distance for the same energy density, which indicated that the stand-off distance is independent of the flyer thickness.

The table above shows that similar experiments with exploding foils can be conducted at a stand-off distance as small as 0.2 mm. However, for practical reasons a minimum stand-off distance of 1.0 mm is chosen for the design calculations in chapter 8, where a small stand-off distance is necessary to optimise system performance.

5.2.3 Determination of Flyer Velocity by TOA Measurement

The velocity of the flyer was determined by measuring the time taken for it to impact on an electrical contact-pin probe situated a known distance from the exploding foil.

5.2.3.1 Coaxial Contact-Pin Probe for Single TOA

The electrical contact-pin probes of Fig 5-2 were made by modifying coaxial BNC connectors, as their diameters are close to the size of the exploding foil. They can be used to determine the flyer velocity when the internal volume is left empty or that of the conducting shock front when it is filled with aluminium powder. The distance of the

contact-pin from the exploding foil can be determined precisely, by measuring the distance between the base of the PVC holder (see Fig 5-2) and the contact-pin, and adding the length of the barrel. Different probe position can be obtained by using PVC holder of a different thickness, since a constant air gap (defined by the length of the barrel) is desired.

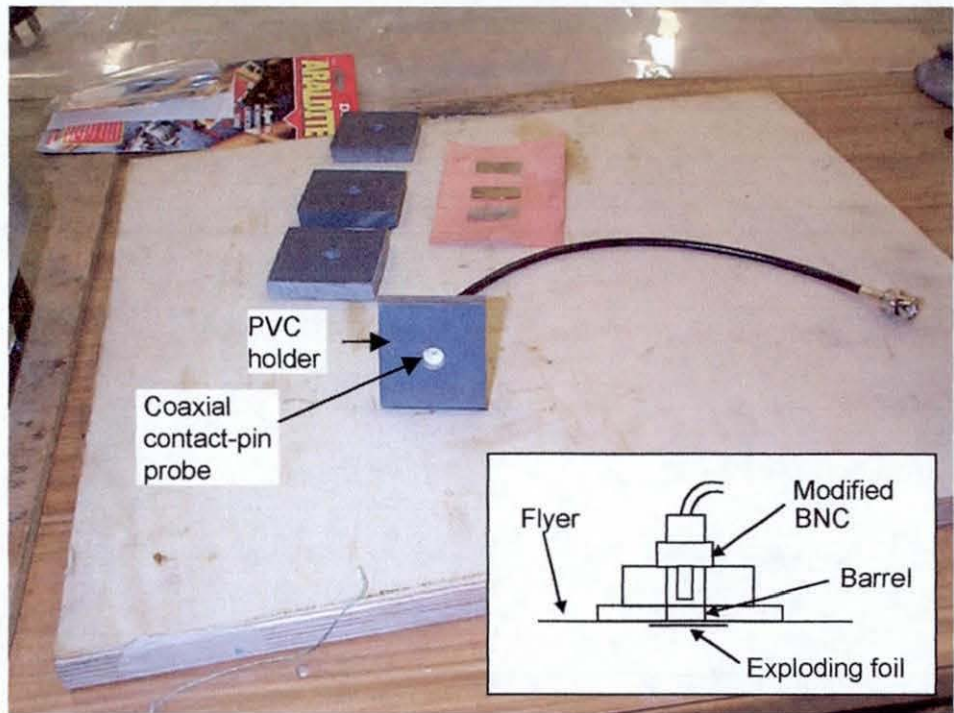


Figure 5-2 Coaxial contact-pin probe for single TOA.

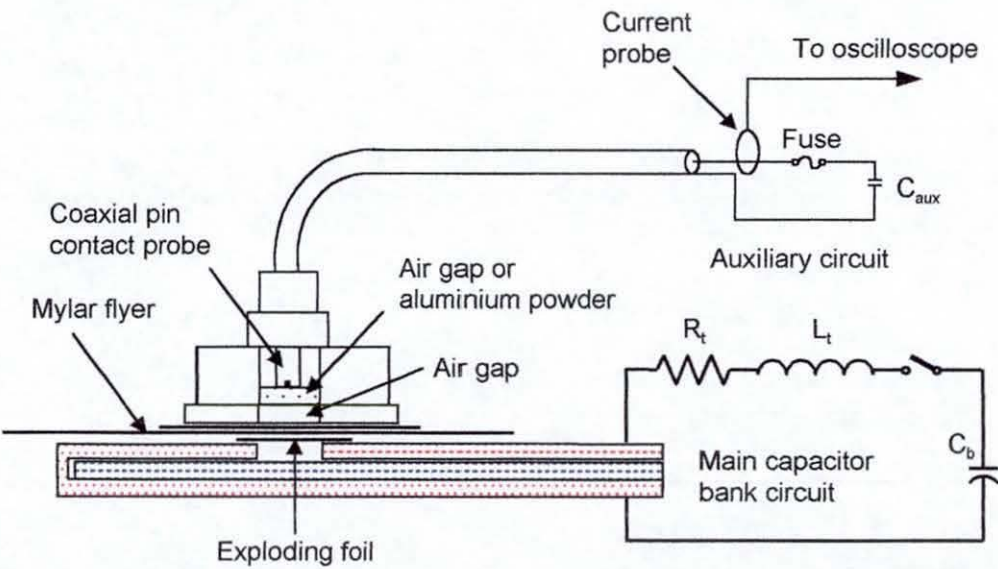


Figure 5-3 TOA measurement scheme with single coaxial contact-pin probe.

5.2.3.2 Experimental Arrangements

In the experimental arrangement of Fig 5-3 the probe is connected to an auxiliary circuit containing a capacitor charged to about 1.0 kV . Arrival of the conducting shock front causes the probe to act as a closing switch that discharges the auxiliary capacitor, with the current probe detecting the discharge to give the TOA of the conducting shock front. The nickel-chrome resistance wire fuse in the auxiliary circuit prevents reverse voltage damage to the high-voltage capacitor.

The arrangement of Fig 5-3, while simple, is immune to any electromagnetic noise generated by the exploding foil, as the high pulsed current from the capacitor produces a signal significantly higher than the electrical transients from the exploding foil. Maintenance of the 1.0 kV voltage at the tip of the contact-pin probe serves also to confirm that under normal unstressed conditions the aluminium powder remains an insulating medium. The high-precision digital oscilloscope used to record the output from the current probe is electrically isolated from the auxiliary circuit and it is therefore immune to damage from the high pulsed current in the main capacitor bank circuit.

5.2.3.3 Experimental Results

Figs 5-4 and 5-5 compare results from one of the many experiments undertaken, together with corresponding results from the new electric gun model described in chapter 3. In this particular experiment, the contact-pin probe was 5.29 mm (Fig 5-5b) from the exploding foil and the time to probe impact by the flyer was $1.68\text{ }\mu\text{s}$ ($2.87\text{ }\mu\text{s} - 1.19\text{ }\mu\text{s}$), leading to an average flyer velocity of 3.15 km/s .

Figs 5-4a and 5-4b show that the computer model is able to reproduce with reasonable accuracy the current and $\frac{dI_b}{dt}$ in the gun circuit, which is an indication of the quality of the empirical model used for the exploding foil in the calculation. The energy density at burst is calculated at 15.02 MJ/kg (Fig 5-4c), giving an explosion pressure of 14 GPa

(Fig 5-5a), while the magnetic pressure exerted by the current in the gun circuit on the Mylar flyer has a maximum of 0.1 GPa (Fig 5-5c).

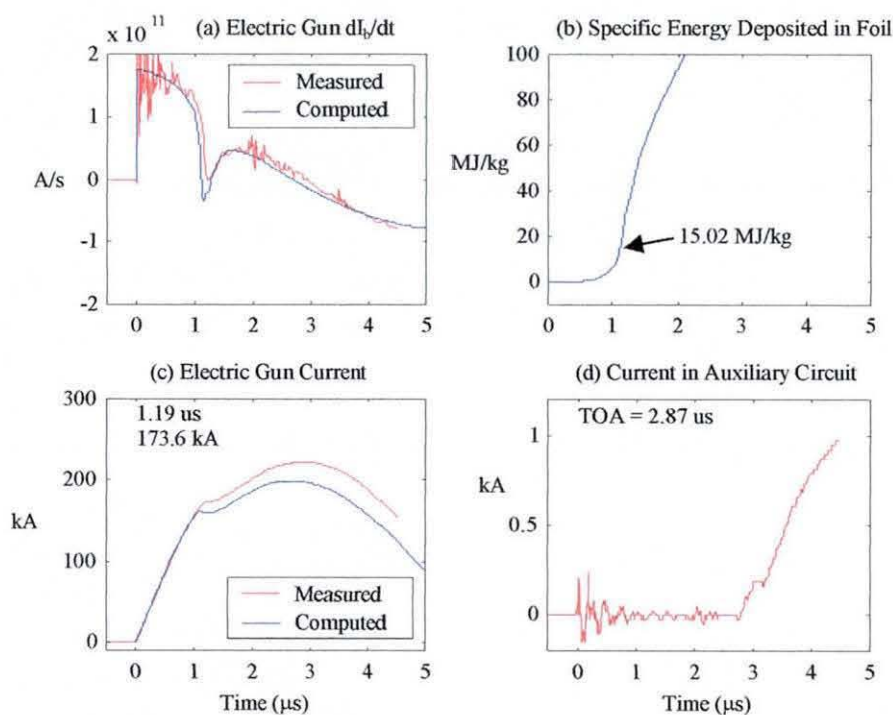


Figure 5-4 Experimental results (test no. 08).

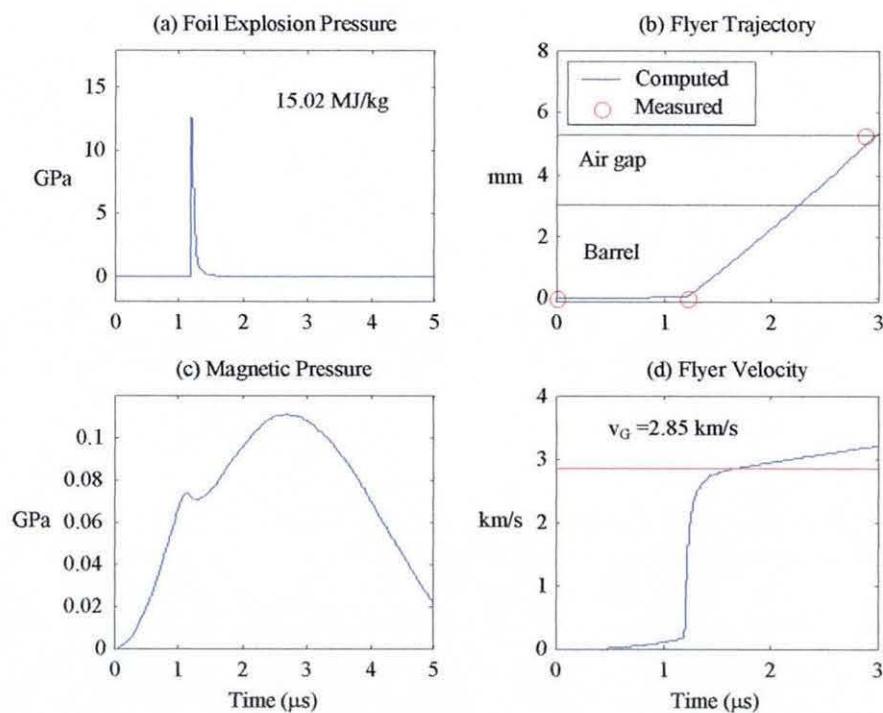


Figure 5-5 Experimental results (test no. 08).

5.2.4 Determination of Shock Velocity by TOA Measurement

5.2.4.1 Coaxial Contact-Pin Probes for Multiple TOAs

Although the coaxial contact-pin probe only provides one data point from each test, the size of the exploding foil in Fig 5-1 allows up to three chambers to be bored in a PVC holder (Fig 5-6) to provide multiple TOA measurement of the conducting shock front. To achieve this, the modified BNC contact-pin probe is replaced by miniature coaxial cables, with their open end placed in the aluminium powder.



Figure 5-6 Coaxial contact-pin probes for multiple TOA measurements.

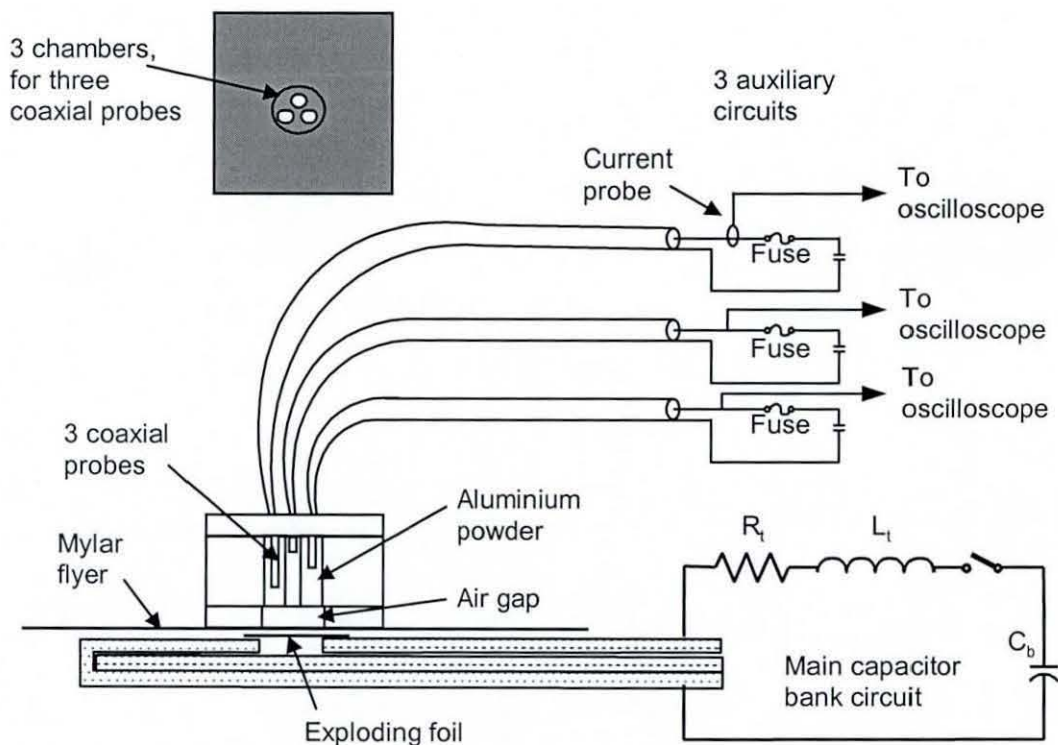


Figure 5-7 TOA measurement scheme with multiple coaxial contact-pin probes.

5.2.4.2 Experimental Arrangements

The experimental arrangement of Fig 5-7 is similar to that of Fig 5-3, except for the multiple auxiliary circuits.

5.2.4.3 Experimental Results

Results from a series of measurements using both types of probes to detect the TOA of the conducting shock front in the aluminium powder are tabulated in Table 5-2.

From the foil burst data in the table, it can be seen that the performance of the electric gun is reasonably repeatable, although there is a small time jitter of about $1.0 \mu\text{s}$. Within experimental tolerance, the test data can be plotted as in Fig 5-8, together with the flyer trajectory obtained from the previous flyer velocity measurement.

Table 5.2 TOA data for electrically conducting shock front in aluminium powder.

Test no.	Probe type	Probe no.	Foil burst time (μs)	Probe location in aluminium powder (mm)	Capacitor discharge time (μs)
10	single	--	1.18	2.29	2.94
11	single	--	1.24	10.5	12.76
17	multiple	I	1.20	1.30	noisy (discarded)
		II		2.03	noisy (discarded)
		III		3.40	3.95
39	multiple	I	1.13	3.58	4.81
		II		5.90	6.23

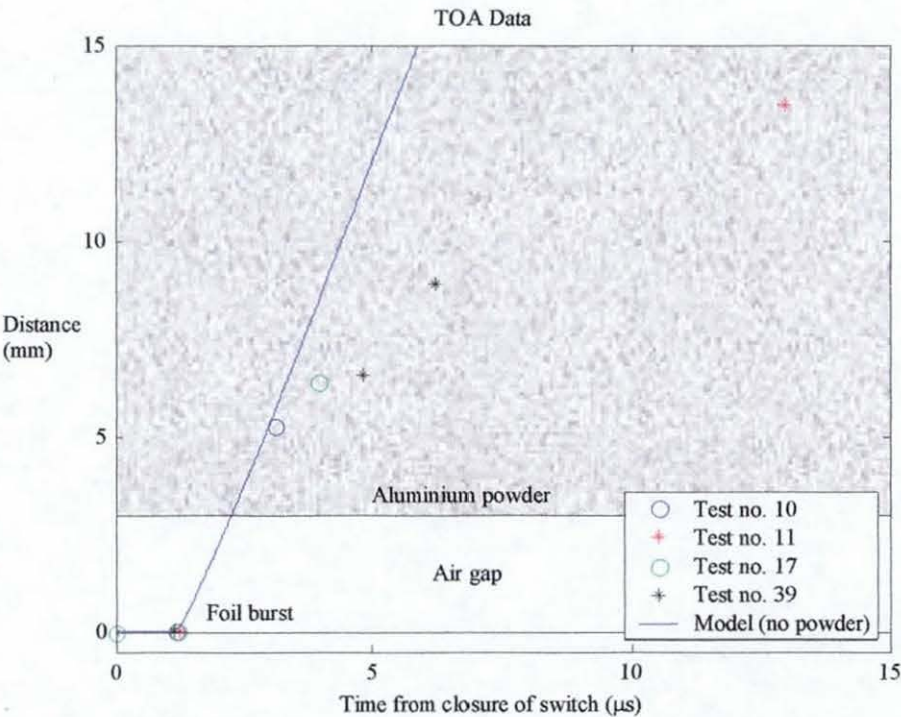


Figure 5-8 Measured TOA data and Mylar flyer trajectory (no aluminium powder).

It is apparent from Fig 5-8 that the velocity of the conducting shock front is rapidly attenuated as it moves further into the aluminium powder. The time to impact t_{imp} can be estimated by noting the intercept of the flyer trajectory with the boundary of the the aluminium at 3.0 mm, and it is possible to fit a curve through these data points (including the time of impact t_{imp}) to obtain a mathematical description of the shock velocity in the powder.

Fig 5-9 shows a second-order polynomial function fitted to the data points while Fig 5-10 shows the same for a third-order function. The shock velocities obtained by differentiating the shock trajectories provide the linear and a quadratic velocity functions seen in Fig 5-11. Despite the small number of data points and possibly a large amount of scatter in the data, it is still possible to conclude that experimental evidence exists for the rapid attenuation of the shock velocity (and with it the shock pressure) within the powder.

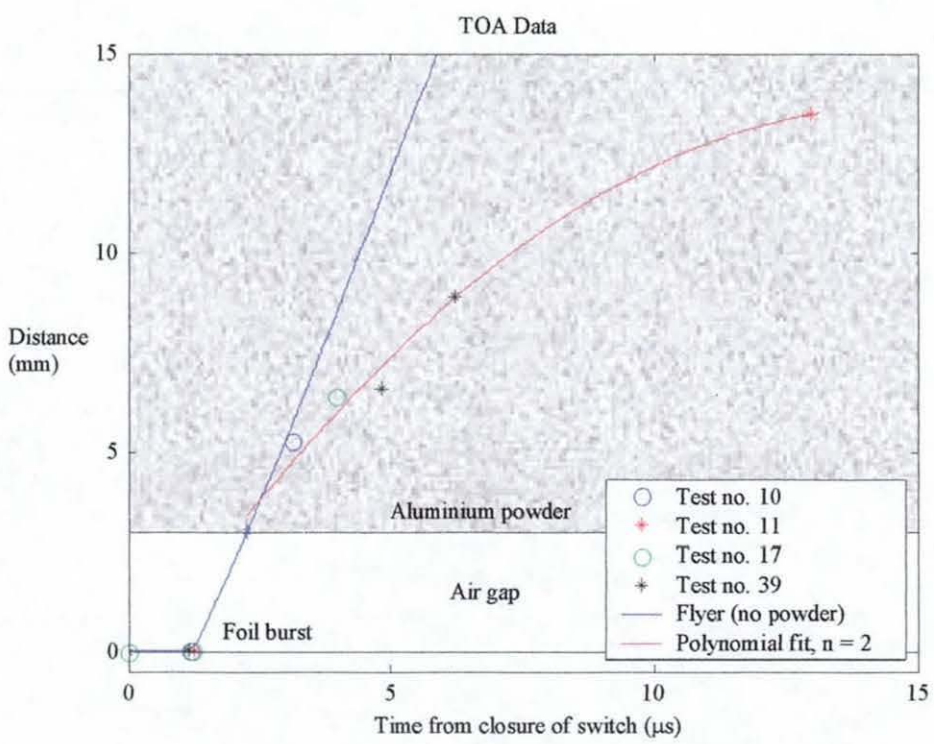


Figure 5-9 Shock trajectory obtained by fitting a second-order polynomial function to the measured TOA data.

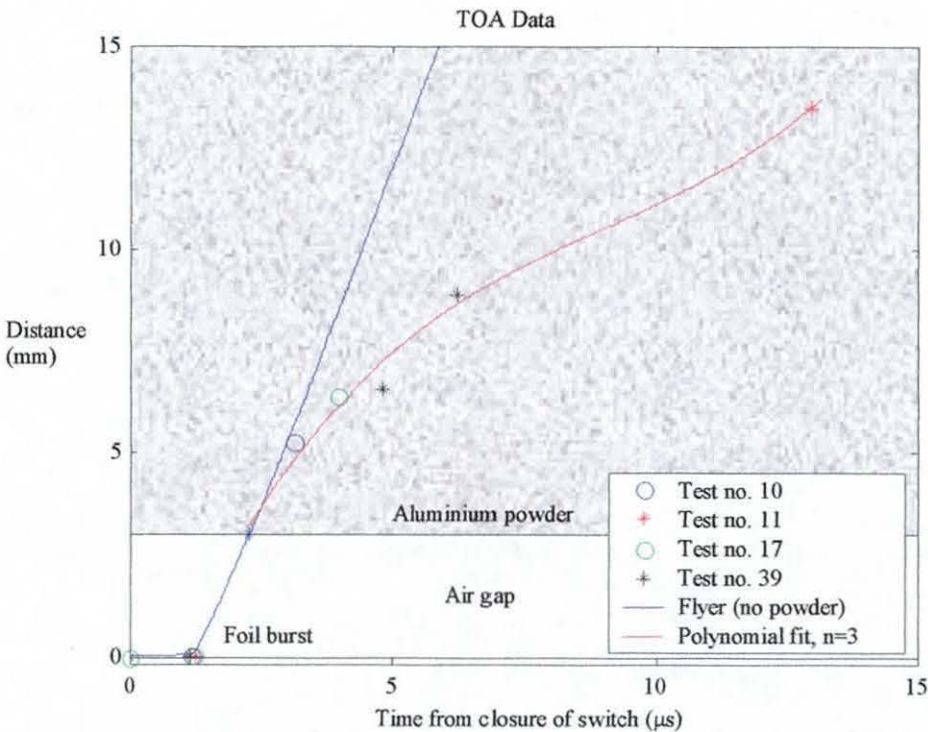


Figure 5-10 Shock trajectory obtained by fitting a third-order polynomial function to the measured TOA data.

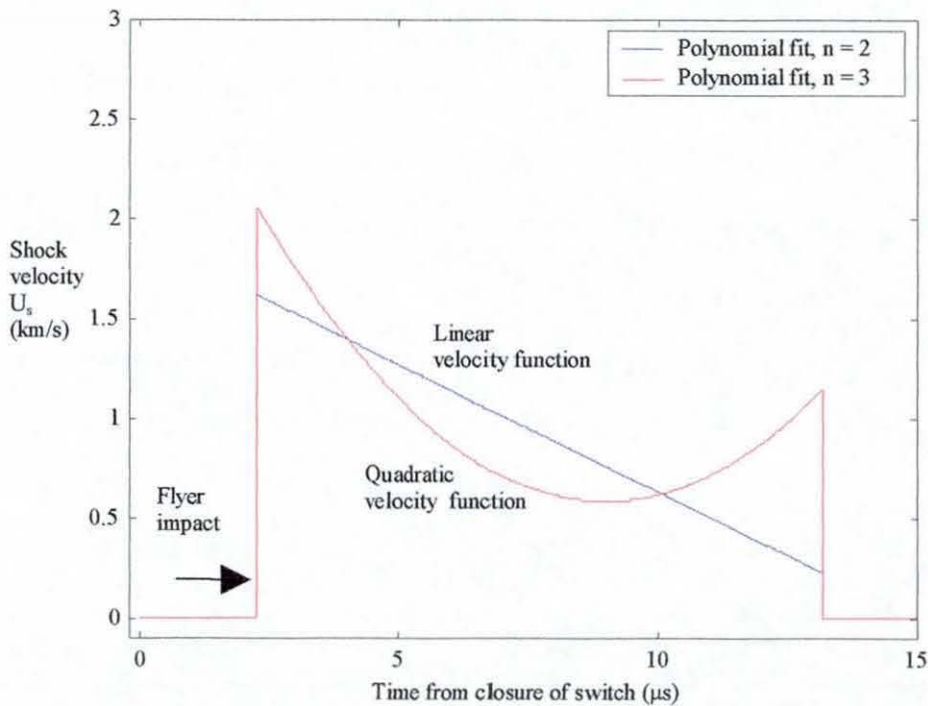


Figure 5-11 Shock velocity profiles from composite TOA measurement.

5.2.5 Continuous Monitoring of Shock Velocity

Although a series of TOA measurements can be combined to provide information on the shock velocity, confidence in the results is low due to variations in the foil burst time and the powder density from test to test. It is desirable therefore to have a method of measurement that provides continuous monitoring of the shock velocity in the aluminium powder in a single experiment.

In methods for continuous monitoring of the shock velocity in solid cast explosives [108] and [109], a resistance probe with a constant resistance per unit length is cast within the explosive and the continuous removal of resistance by the ionising shock or detonation front provides time-resolved shock velocity information. The probe is either a straight wire resistance element or a spiral coil wound on an insulator support, to achieve constant resistance per unit length.

5.2.5.1 Spiral Resistance Probe

Fig 5-12 shows the spiral resistance probe used in the present experiments. Nickel-Chrome resistance wire is coiled around an insulator support and situated in the aluminium powder along the direction of the flyer impact. The coil is progressively shorted as the shock front destroys the thin insulation on the aluminium powder and produce a good connection to the coil. The continuous shorting of the coil (between turns) behind the shock front is illustrated in Figs 5-13a and 5-13b. Photographs for the probe construction and test preparation are given in Appendix A.

A spiral wound probe was chosen rather than a straight wire resistance probe, primarily because of the greater resistance per unit length that can be achieved. This provides a greater voltage variation (and consequently a better signal-to-noise ratio) than is obtained in a linear probe circuit. A bifilar winding is also used to minimise any coupling of electrical noise from the exploding foil into the probe circuit.

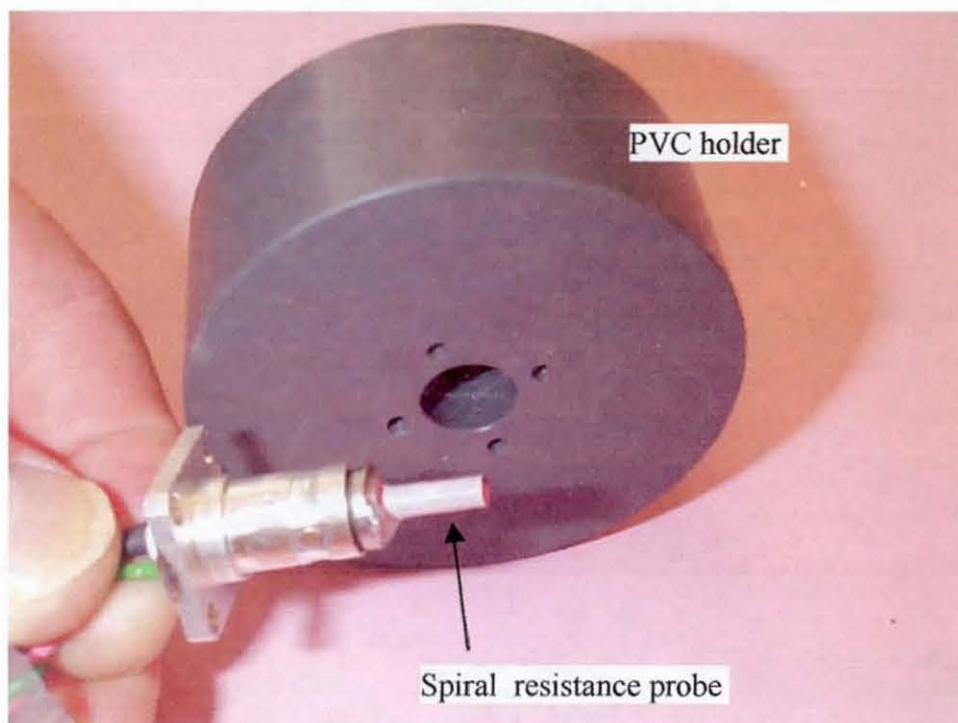


Figure 5-12 Spiral resistance probe before assembly in PVC holder.

5.2.5.2 Circuit Analysis

Normally, a constant-current source is used with the probe and the voltage across the time-varying resistance provides velocity information. Alternatively, batteries could also be assumed to provide a constant-voltage source, if the duration of the shock compaction event is only about $10 \mu\text{s}$. Monitoring of the battery voltage during experimentation justified this assumption and the use of batteries provided a convenient and low-cost source for quick and repeated experimentation.

In the equivalent circuit of Fig 5-13a, the spiral probe is represented by a variable resistor whose resistance is determined by the location of the conducting shock front. The tip of the probe positioned at the boundary of the aluminium powder provides the reference plane, x_o is the initial length of the probe and $x(t)$ is the length behind the conducting shock front and removed from the circuit. The length of the probe that remains in the unshocked powder is therefore

$$x_o - x(t) = x_o - \int_0^t U_s(\tau) d\tau \quad (5-1)$$

where $U_s(t)$ is the shock velocity to be measured.

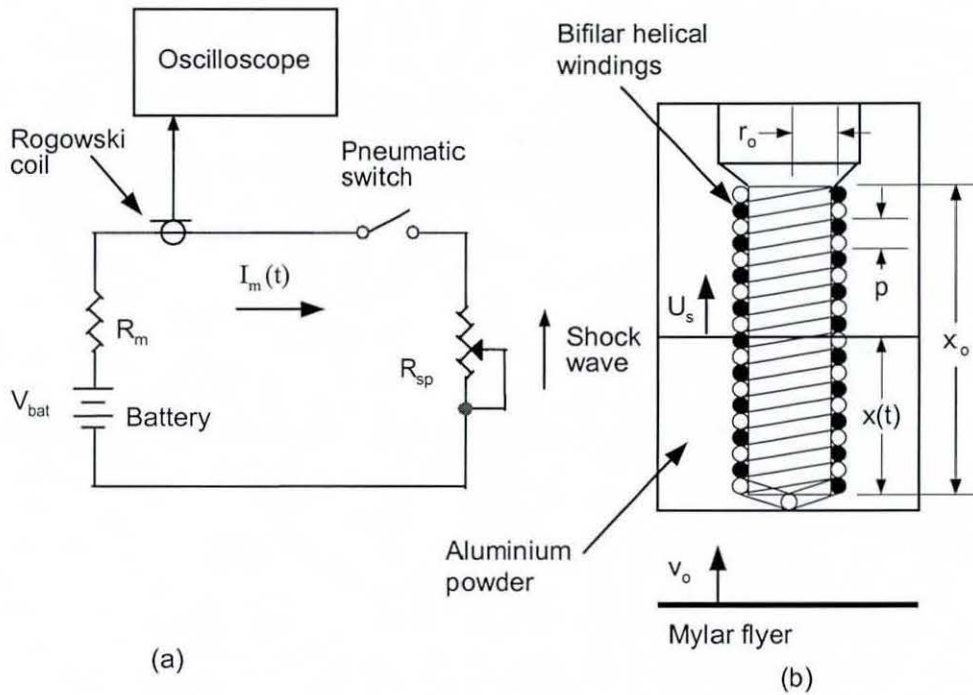


Figure 5-13 Spiral resistance probe, (a) measuring circuit and (b) impact geometry.

If r_o is the radius of the helix, p is the pitch of the bifilar spiral, A is the cross sectional area of the resistance wire and $\eta = \frac{1}{\sigma}$ is the electrical resistivity of the wire, the probe resistance before impact by the Mylar flyer is

$$R_{sp}(0) = \eta \frac{2\sqrt{(2\pi r_o)^2 + p^2}}{pA} x_o \quad (5-2)$$

The resistance R_m in Fig 5-13a is the sum of the resistances due to the pneumatic switch and the connecting wires and is assumed to be negligibly small. A pneumatic switch is used to minimise electromagnetic interference and it is closed very shortly before experimentation to prevent excessive heating of the spiral probe.

After impact, the instantaneous resistance of the probe is

$$R_{sp}(t) = \eta \frac{2\sqrt{(2\pi r_o)^2 + p^2}}{pA} \left[x_o - \int_0^t U_s(\tau) d\tau \right] \quad (5-3)$$

If V_{bat} is the battery voltage and $R_{sp}(t)$ is the instantaneous resistance of the spiral probe, the instantaneous current in the probe circuit is

$$I_m(t) = \frac{V_{bat}(t)}{R_{sp}(t)} = \frac{pA}{2\eta\sqrt{(2\pi r_o)^2 + p^2}} \left[x_o - \int_0^t U_s(\tau) d\tau \right] V_{bat}(t) \quad (5-4)$$

The velocity of the conducting shock front can be obtained from the derivative of this current and since $\frac{dV_{bat}}{dt} = 0$ it follows that

$$U_s(t) = \left(\frac{pA}{2\eta\sqrt{(2\pi r_o)^2 + p^2}} \right) \frac{V_{bat}}{I_m^2} \frac{dI_m}{dt} \quad (5-5)$$

The rather complicated relationship between the shock velocity and the measured current in equation (5-5) is the main drawback to using a constant-voltage rather than a constant-current source. To understand how the shock velocity affects the current in the probe circuit, it is necessary to develop a computer solution for equations (5-1) to (5-5).

Fig 5-14 shows the current in the probe circuit provided by such a solution, and calculated for a constant shock velocity of $U_s = 3 \text{ km/s}$. The current shows an exponential increase similar to that produced by magnetic flux compression devices.

A similar calculation for a shock velocity that begins with $U_s = 5 \text{ km/s}$ and decays exponentially with a time constant of $1.465 \mu\text{s}$ is shown in Fig 5-15. Despite the increased initial velocity, the current has a slower rate of growth and settles at a steady value when the shock velocity falls to zero and the shock front fails to reach the end of the spiral probe. From the numerical analysis, it is clear that the shock front has to travel to the end of the probe in order to produce an exponentially increasing current waveform.

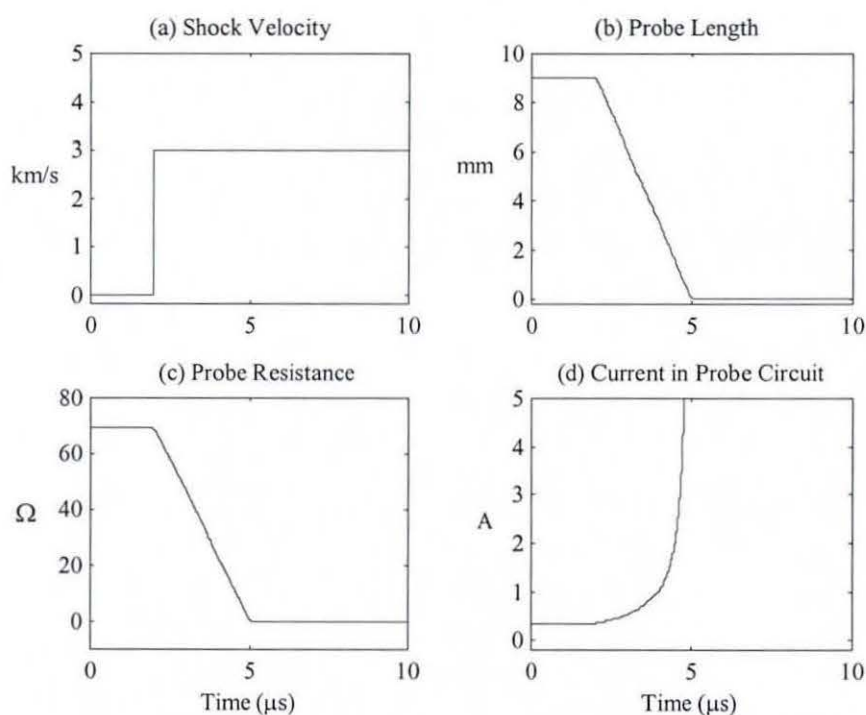


Figure 5-14 Results from computer model for constant shock velocity of 3 km/s .

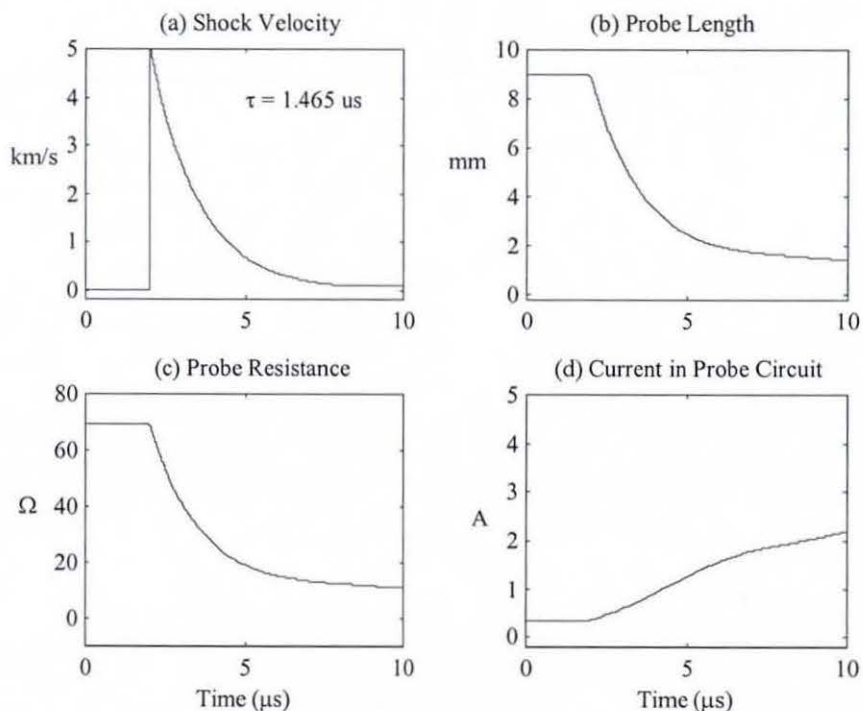


Figure 5-15 Results from computer model for 5 km/s shock velocity decaying exponentially with $1.465 \text{ }\mu\text{s}$ time constant.

5.2.5.3 Experimental Arrangement

Fig 5-16 shows the experimental arrangement, with a Rogowski coil used to measure the current variation for monitoring the shock velocity as the probe resistance is removed. The arrangement shown protects the high-speed digital oscilloscope used for recording purposes, by decoupling the auxiliary and main capacitor bank circuits. The pneumatically controlled switch closes the circuit very shortly before discharge of the capacitor for the electric gun.

The low-voltage probe circuit is extremely sensitive to electromagnetic transients from the exploding foil, and numerous experiments were performed to quantify and remove this noise. The final solution adopted was to shield and screen the auxiliary circuit inside a metallic box and to place all measurement cables inside metallic conduits.

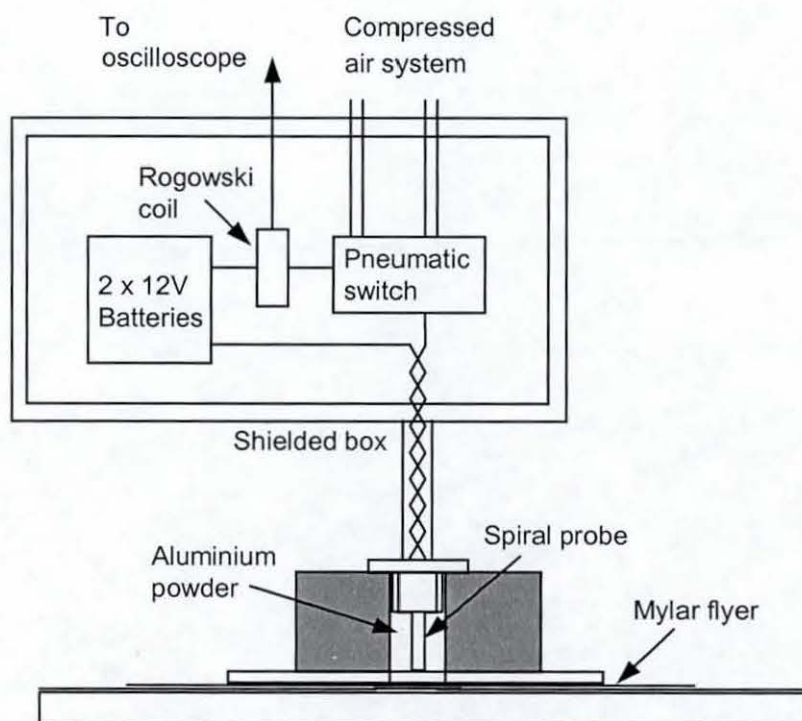


Figure 5-16 Experimental arrangement for continuous monitoring of shock velocity in shock-compressed aluminium powder.

5.2.5.4 Measurements Results

Several spiral resistance probes were constructed for use in the experiments. Two of the best results from a series of experiments are shown in Figs 5-17 and 5-18. The measured battery voltages and the rate of change of current in the gun circuit are almost identical in these tests, which is an indication of reliable and repeatable gun operation. The measured currents show distinctive oscillations at the point of impact, which are believed to be caused by the initial shorting of the spiral probe and ringing in the circuit due to stray inductance and capacitance. This effect in a charged coaxial cable has been previously exploited by Ingram [110] to determine the time when the projectile impacts with a stationary sample in a compressed gas gun. While the effect was not initially anticipated, it has the benefit of indicating the time of impact of the flyer on the aluminium powder. In the absence of this noise (see Figs 5-17d and 5-18d), it would be difficult to determine accurately the impact time, due to the small initial current variation.

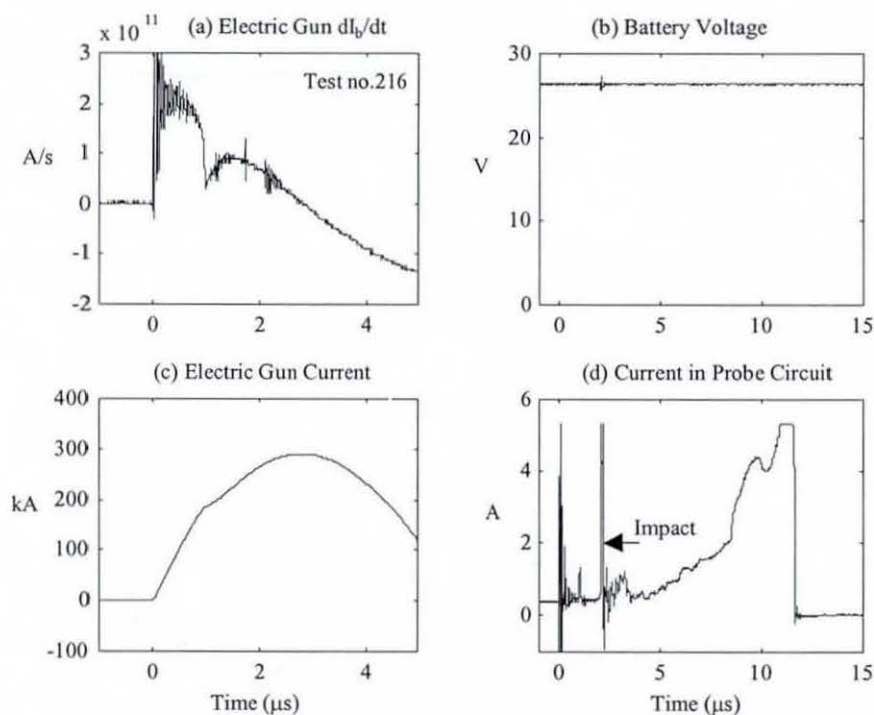


Figure 5-17 Experimental results, (a) electric gun $\frac{dI_b}{dt}$, (b) battery voltage V_{bat} , (c) electric gun current I_b and (d) current I_m in probe circuit.

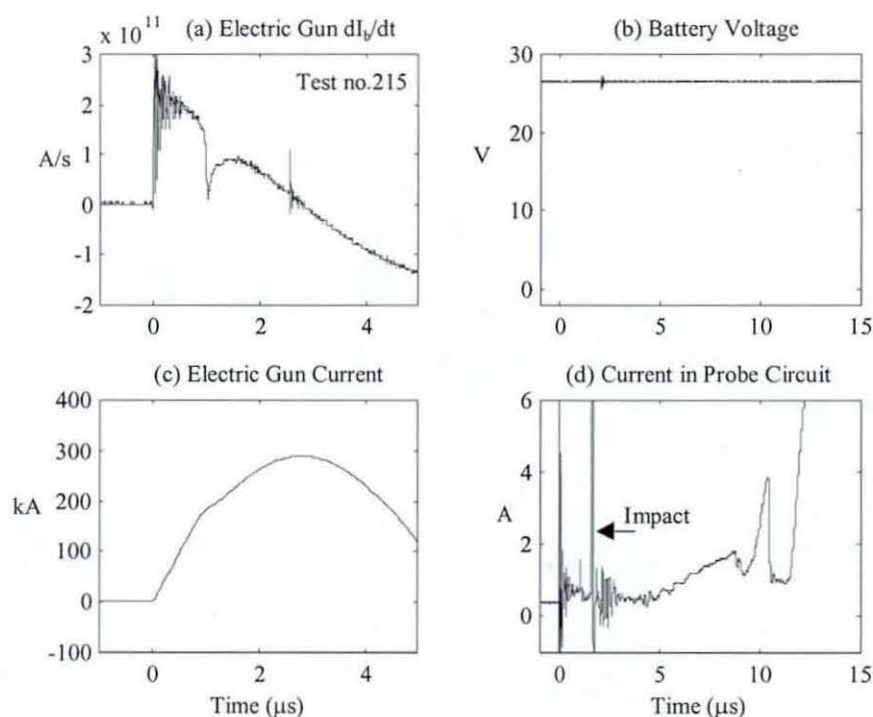


Figure 5-18 Experimental results, (a) electric gun $\frac{dI_b}{dt}$, (b) battery voltage V_{bat} , (c) electric gun current I_b and (d) current I_m in probe circuit.

However, application of equation (5-5) to determine the shock velocity function from the measured current is severely limited by the presence of the noise, which tends to be amplified in any mathematical procedure used to calculate $\frac{dI_m}{dt}$. As an alternative, the shock trajectories (and velocities) obtained by previous TOA measurements could be used as trial input functions for the computer program to calculate the probe current. Fig 5-19 shows that the quadratic velocity function gives a better fit to the experimental data than the linear velocity function. The comparison with the second set of experimental data in Fig 5-20 using the quadratic velocity function shows a reasonable match with experiment, until instability sets in. These preliminary results indicate that the shock velocity did not fall completely to zero and that the shock front did not slow to a stand-still but continued to move into the powder with a slow but steady speed.

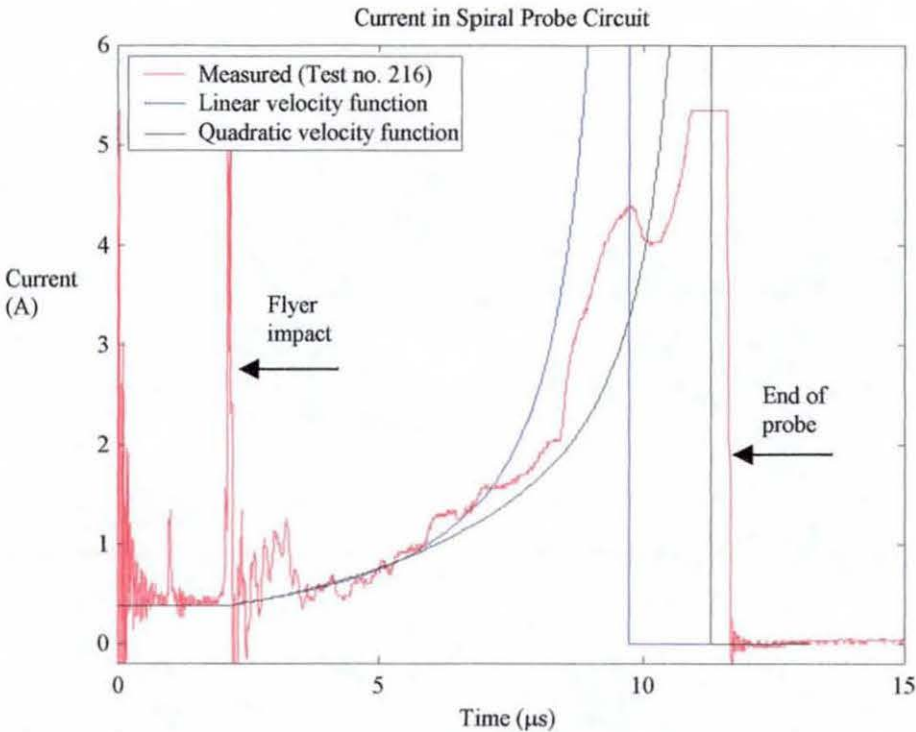


Figure 5-19 Comparison of experimental data with computer model using shock velocity profiles of Fig 5-11.

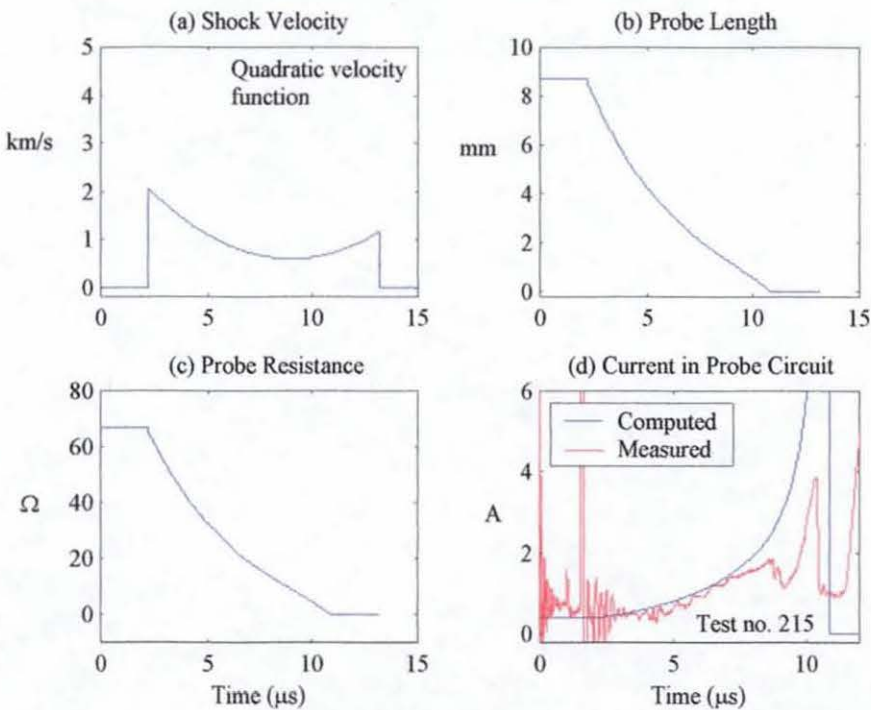


Figure 5-20 Results from computer model using quadratic shock velocity profile of Fig 5-11.

5.3 Numerical Analysis of Experimental Results

Continuous monitoring of the shock velocity in a single experiment provided by the spiral probe data makes it suitable for validating the hydrodynamic code and the EOS for the powder material described in chapter 4. For a complex system in which a chain of physical events separates the initial conditions from the measured data, two methods are available to aid development and validation of mathematical models, namely the stimulation and simulation methods, which are explained in the following sections.

5.3.1 Stimulation Method

In the stimulation method, inputs functions are normally available (e.g. in the form of initial conditions) that can be provided to a mathematical model to calculate and predict the output response.

If the exploding foil flyer impact experiment is to be analysed by the stimulation method, it is necessary to partition the physical processes into the four major parts shown in Fig 5-21, with a separate mathematical model being required for each of the individual processes.

In Fig 5-21, the electric gun model produces the foil burst pressure $P_{burst}(t)$ for the flyer acceleration and impact model, which then calculates the impact pressure $P_{impact}(t)$. The shock propagation model, in turn, takes $P_{impact}(t)$ as an input function and calculates the shock velocity function $U_s(t)$. This is integrated by the circuit model for the spiral probe to obtain the shock position, and to calculate the variation of the current $I_m(t)$ due to the continuous removal of probe resistance. Comparison of the predicted with the measured current will then provide information on the quality of the mathematical model.

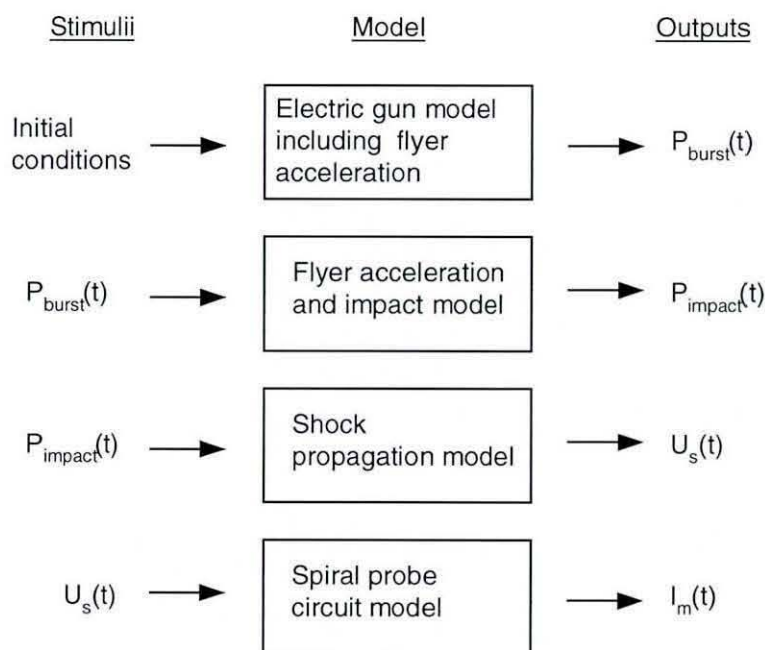


Figure 5-21 Stimulation method.

5.3.2 Simulation Method

In the simulation method, the focus is on estimation of the unknown input function that causes a physical process to produce a particular set of measured outputs. Taking the same four models as for the shock compression experiment, the analysis of Fig 5-22 starts with the measured current $I_m(t)$ to find the shock velocity function that has caused it. Additional inputs, e.g. the velocity function $U_s(t)$ derived by the set of TOA measurements, provide important clues that narrow the search to find the impact pressure $P_{impact}(t)$ that has generated the particular velocity function. Information on the characteristics of the impact pressure from previous explosive driven experiments could be used to guide the search for $P_{impact}(t)$. The process continues until the burst pressure $P_{burst}(t)$ obtained by the flyer acceleration model is comparable with that produced by the electric gun model. One advantage of the simulation method is the identification of key parameters in the input functions that directly affect the measured output response, while ignoring fine detail that does not affect the output response in any significant way.

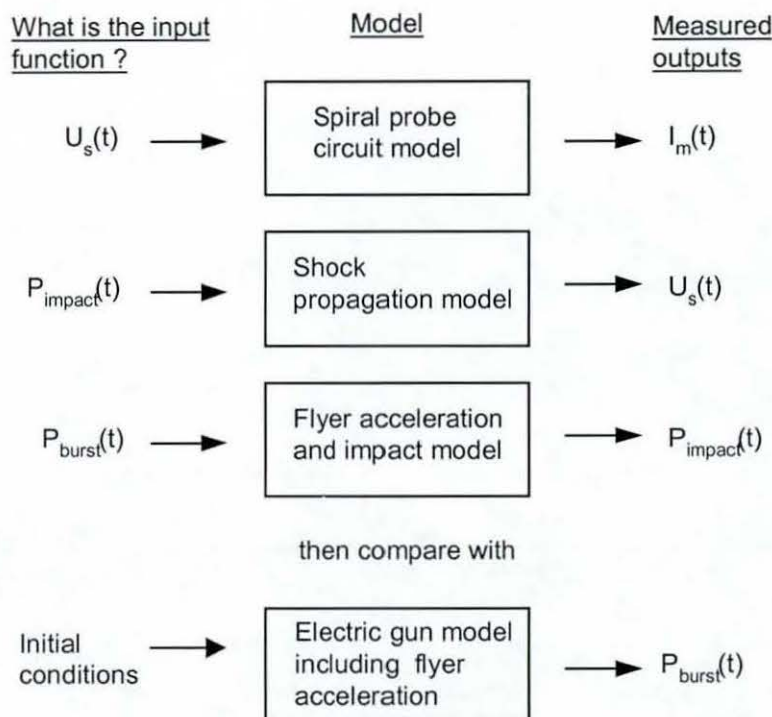


Figure 5-22 Simulation method.

5.3.3 Solution Approach

Analysis of data produced by a chain of physical processes by either the stimulation or the simulation method poses no difficulty, if validated models are available in each case. In the present research however, the circuit model for the spiral probe is the only well-defined model, while in order to gain insight into the physical process, the other three models have to be developed from data collected during the experimental programme.

A systematic divide-and-conquer approach was taken to validating the hydrodynamic code and obtaining an estimate for the impact pressure. The new electric gun model of chapter 3 and the circuit model for the spiral probe were used to limit the problem areas to the hydrodynamic code and the EOS for the powder, allowing the problem to be tackled from two directions. Extensive functional tests were carried out to validate the hydrodynamic code and the EOS for the powder, as previously described in chapter 4. When the hydrodynamic code was developed, a combination of both the stimulation and the simulation method was used over numerous iterations to gain useful insight into the

relationship between the important parameters connecting the models and the limitations of the hydrodynamic model.

The inability of a Lagrangian description to handle mixing of the mesh elements for air and aluminium powder after flyer impact is solved by dividing the hydrodynamic model into two parts, namely the flyer acceleration and impact model and the shock propagation model. This arrangement implies that the calculation has to be carried out in two passes, with the impact pressure estimated in the first pass. In the second pass, the mesh elements for the air are removed from the calculation upon impact, and the impact pressure calculated in the first pass is used to continue the shock propagation calculation. The removal of the elements for the air is used to simulate the penetration of air into and mixing with the powder elements, and to avoid any small time-step problem associated with the severely distorted grid for the air. This method of solution achieves the effect of preventing the air, which is highly compressed and at a high pressure on impact, from further expansion after impact. Finally, this solution has been found to be effective in overcoming the limitation of a Lagrangian description, by producing results consistent with that from experiments.

5.3.4 Tuning Factors

The set of models contains a small number of tuning factor that are chosen to match experimental conditions, both in terms of the shape of the output functions and the TOA data of important events that can be deduced from the measured output. The foil burst time, the time of flyer impact on the powder and the time at which the conducting shock front reaches the end of the spiral probe must all be reproduced faithfully by the set of models.

In the new electric gun model of chapter 3, the correction factor k_{corr} acts as a tuning factor to produce a flyer trajectory that is a good match with the measured TOA data for foil burst and flyer impact. The main purpose of this factor is to account for any uncertainty in the quality of the foil explosions, and its use has been demonstrated in chapter 3.

The hydrodynamic code for the flyer acceleration and impact model does not contain any tuning factor. Agreement with the measured TOA data is achieved by adjusting the amplitude and shape of the foil burst pressure, with the resulting pressure pulse compared with that provided by the Gurney solution of the electric gun model. Fairly good agreement between these two calculated values will be illustrated in the next section. The constant for the artificial viscosity is set at 3 in all calculations, to spread the shock front over a maximum of three cell elements.

In the shock propagation model, fine-tuning of the hydrodynamic code is achieved by setting the density threshold ρ_{th} in the electrical conductivity model. Setting the density threshold at $\rho_{th} = 80\%TD$, at which the insulator-to-conductor phase change takes place, is consistent with the onset of plastic deformation as defined by the plastic compression function $\alpha(P)$ in the $P-\alpha$ model of chapter 4. Because of the physical basis for the $P-\alpha$ model, the parameters needed to define it are viewed as material constants, rather than as empirically determined constants (or tuning factors). Due to the uncertainty in the determination of the initial powder density in the experimental programme, the initial porosity α_e is set at an average value of $33\%TD$ in all calculations, primarily to minimise the number of free parameters and to allow comparison of one set of computer results with several sets of experimental data.

The circuit model for the spiral probe is simple and does not contain any tuning factor. A small value of $R_m = 0.1\Omega$ is included in the computer program to avoid any singularity problems when the shockwave reaches the end of the probe and its resistance is removed from the circuit. This value represents fairly accurately the resistance due to the pneumatic switch and the connecting wires, and it does not influence the circuit calculation until the length of the spiral probe has fallen to $0.1mm$. Another requirement for the computer program is of course that the length of the remaining spiral probe should always be greater than zero.

5.3.5 Numerical Results

In this section, a numerical calculation is described in phases from the flyer acceleration and impact model to the shock propagation and then to the circuit model for the spiral probe, to demonstrate the salient features of the physical processes in the shock compression experiments.

5.3.5.1 Flyer Acceleration and Impact Model

As mentioned earlier, the flyer acceleration and impact model is designed with the aim of providing the pressure upon impact with the aluminium powder. Since the presence of air is included in the model, its effect on the flyer acceleration and impact process can also be assessed using this code.

The calculation is started by specifying the foil burst pressure, consisting of the foil explosion pressure of Fig 5-5a and the magnetic pressure of Fig 5-5c, as initial values as shown in Fig 5-23. The foil explosion pressure is a short duration impulse while the magnetic pressure takes the form of a low-pressure pulse acting over a longer period of time, including after the flyer impact with the aluminium powder.

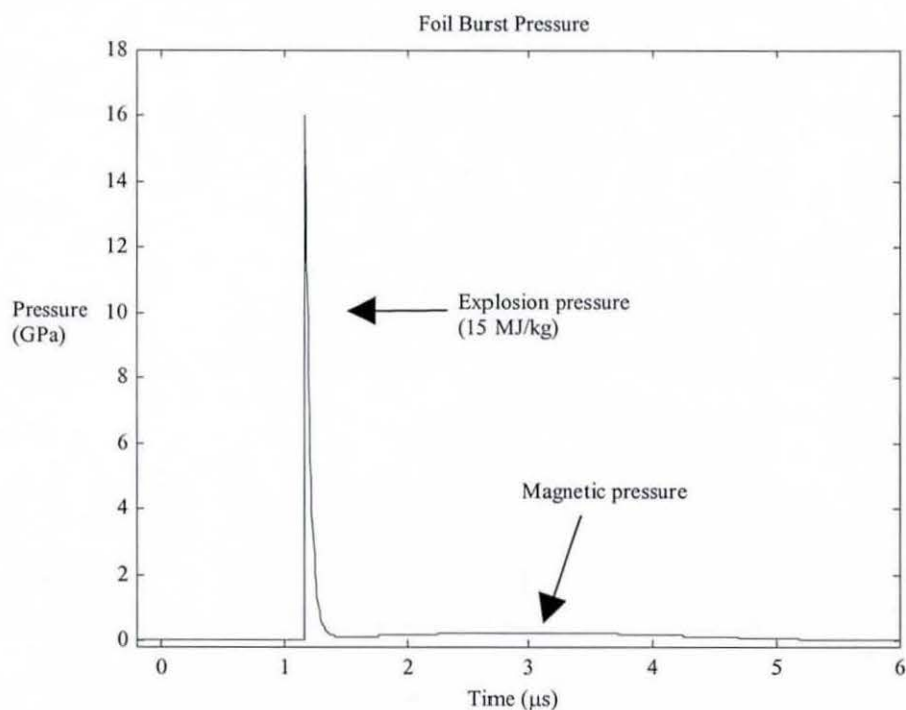


Figure 5-23 Foil burst pressure used in flyer acceleration and impact model.

The trajectory of the Mylar flyer shown as the Lagrangian computational grid of Fig 5-24 is similar to that produced by the electric gun model (see Figs 5-8 to 5-10). The pressure acting at the back of the Mylar flyer causes elements at the back surface to be compressed while those on the front surface show a slight expansion. Compression of the air elements ahead of the Mylar flyer is evident in Fig 5-25

Fig 5-26 shows the impact pressure at the aluminium powder calculated by the flyer acceleration and impact model for the first element of aluminium powder at the air gap boundary. The main pressure pulse has a 'double-spike' structure due to the complex interaction between the shockwave and multiple reflection from the back of the Mylar flyer. The effect of the air shockwave appears in Fig 5-26 as a small pressure pulse of about 0.1 GPa before the main impact. The effect of the magnetic pressure defined in Fig 5-23 appears in Fig 5-26 as a low-pressure with an average value 0.2 GPa.

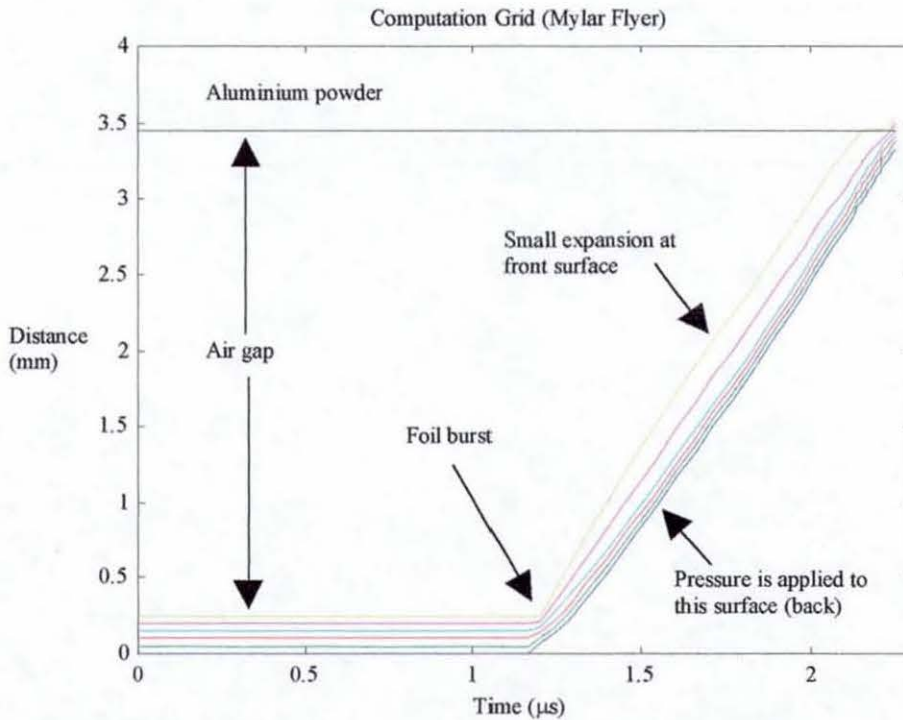


Figure 5-24 Computation grid for Mylar flyer showing acceleration after foil burst and impact with aluminium powder.

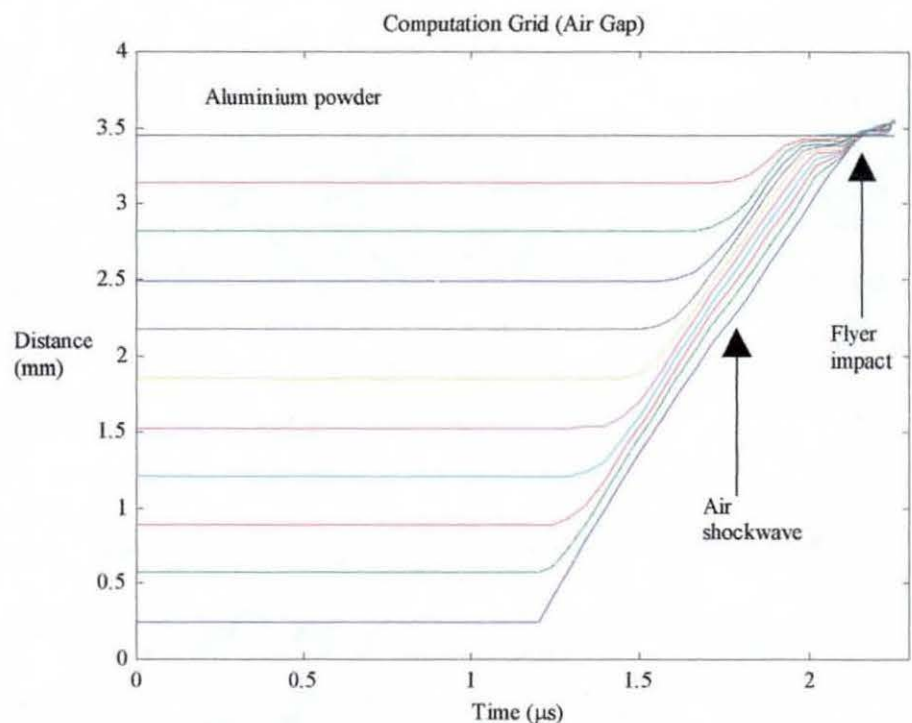


Figure 5-25 Computational grid for air gap showing the air shockwave ahead of the Mylar flyer and impact with aluminium powder.

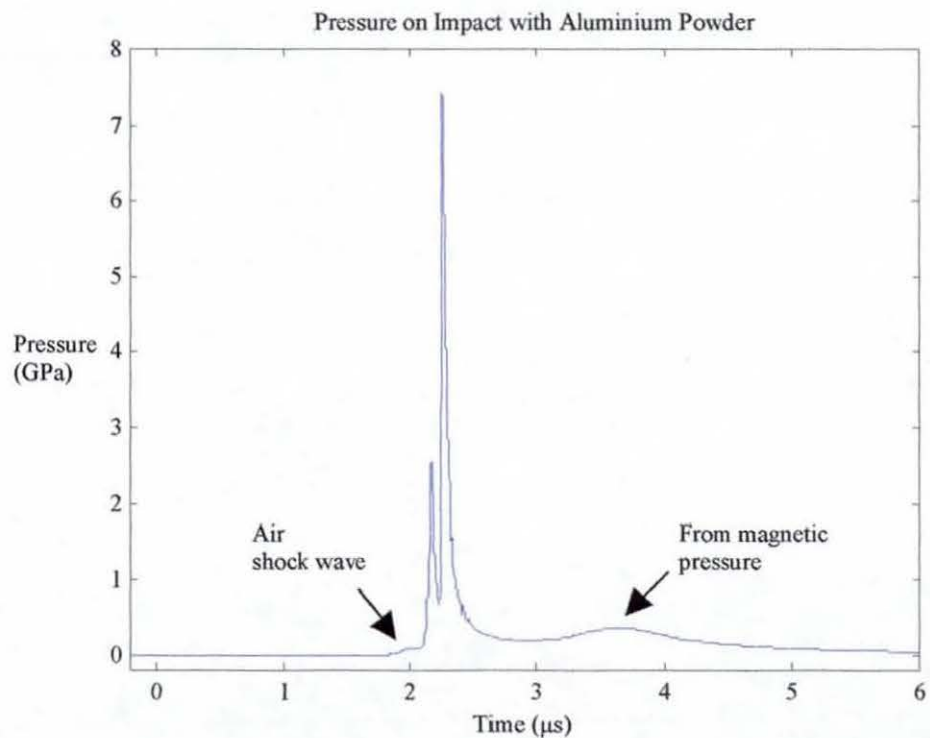


Figure 5-26 Pressure on impact with aluminium powder calculated by the flyer acceleration and impact model.

5.3.5.2 Shock Propagation Model

The shock propagation model takes the impact pressure pulse as an input and calculates the propagation and attenuation of the shock pressure in the powder to provide information on the location and velocity of the conducting shock front. The impact pressure of Fig 5-26 may be approximated by

$$P = \begin{cases} 2.5 \text{ GPa} \times \exp\left(-\frac{t - t_{imp}}{60 \text{ ns}}\right) & t_{imp} < t \leq t_{imp} + 100 \text{ ns} \\ 7.5 \text{ GPa} & t_{imp} + 100 \text{ ns} < t \leq t_{imp} + 130 \text{ ns} \\ 0.2 \text{ GPa} + 7.3 \text{ GPa} \times \exp\left(-\frac{t - t_{imp} - 130 \text{ ns}}{60 \text{ ns}}\right) & t > t_{imp} + 130 \text{ ns} \end{cases} \quad (5-6)$$

which is combined in Fig 5-27 with the original pressure pulse of Fig 5-26.

A functional description is not only computationally convenient, but it also helps to uncover the salient feature of the physical process by temporarily removing some fine details in the input function and determining the sensitivity of the mathematical model to these variations. It was found computationally that a separation of the main pressure into a constant term and an exponentially decaying term does not significantly alter the results, as long as the impulse defined as the area under the pressure-time curve given by

$$I_o = \int_0^t P(\tau) d\tau \quad (5-7)$$

remains unaltered.

Fig 5-28 shows the Lagrangian computational grid for the Mylar flyer, air gap and aluminium powder. The motion of the Mylar flyer in Fig 5-28a is a continuation of Fig 5-23. After impact, the computational grid for the air gap in Fig 5-28c remains as a single line, implying that the air elements are no longer present to interact with the other computational elements. The distortion of the computational grid for the powder in Fig 5-28b is a clear and intuitive representation of the shock compression of the aluminium powder. The trajectory of the conducting front is displayed in Fig 5-28d and a summary of the main physical processes is shown in Fig 5-29.

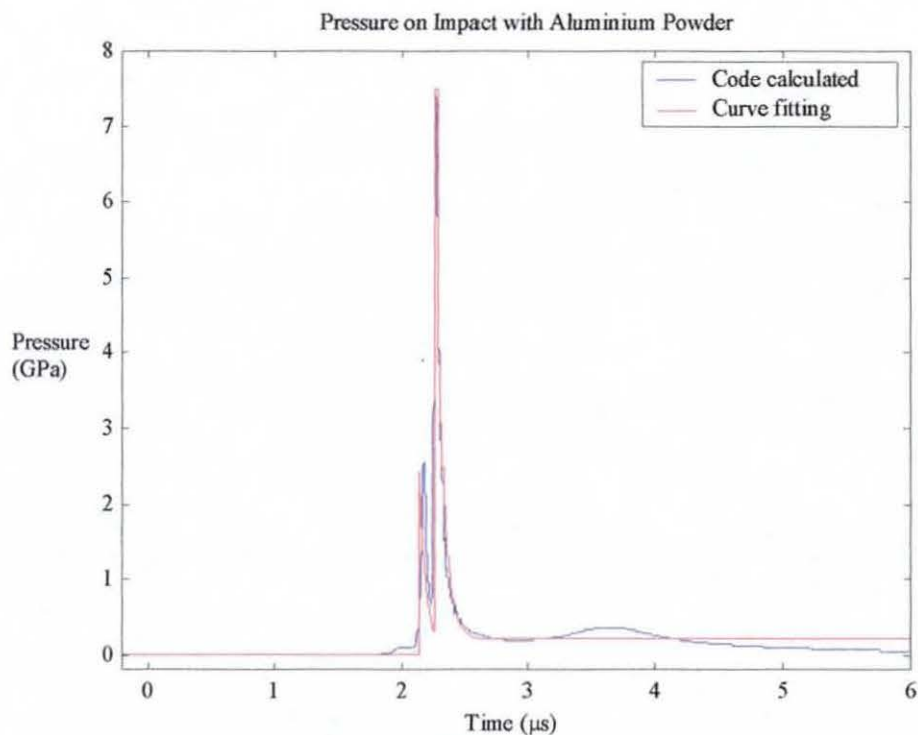


Figure 5-27 Approximate analytic pressure pulse used in the shock propagation model.

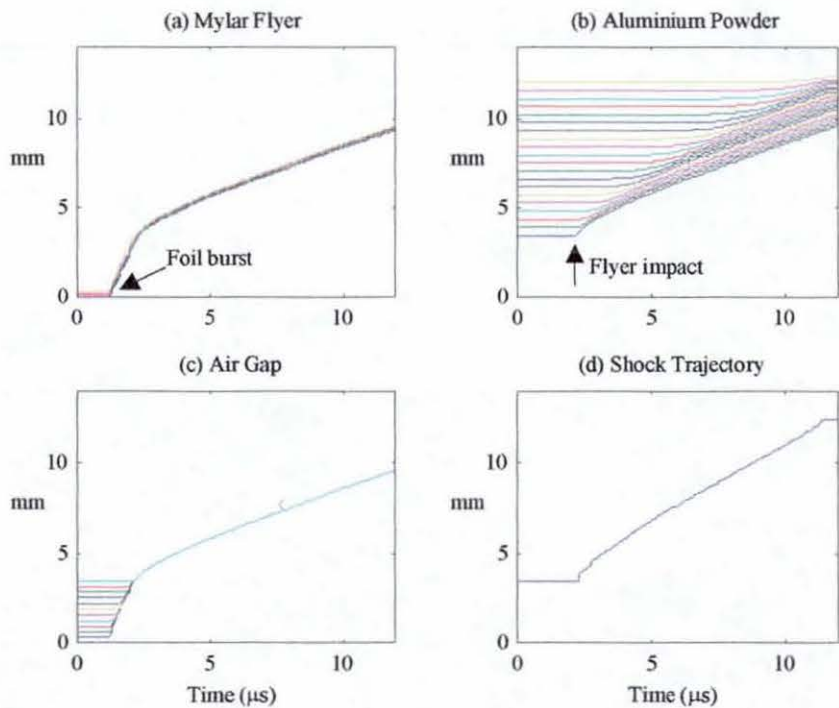


Figure 5-28 Results for the computational grids and shock trajectory obtained by the shock propagation model.

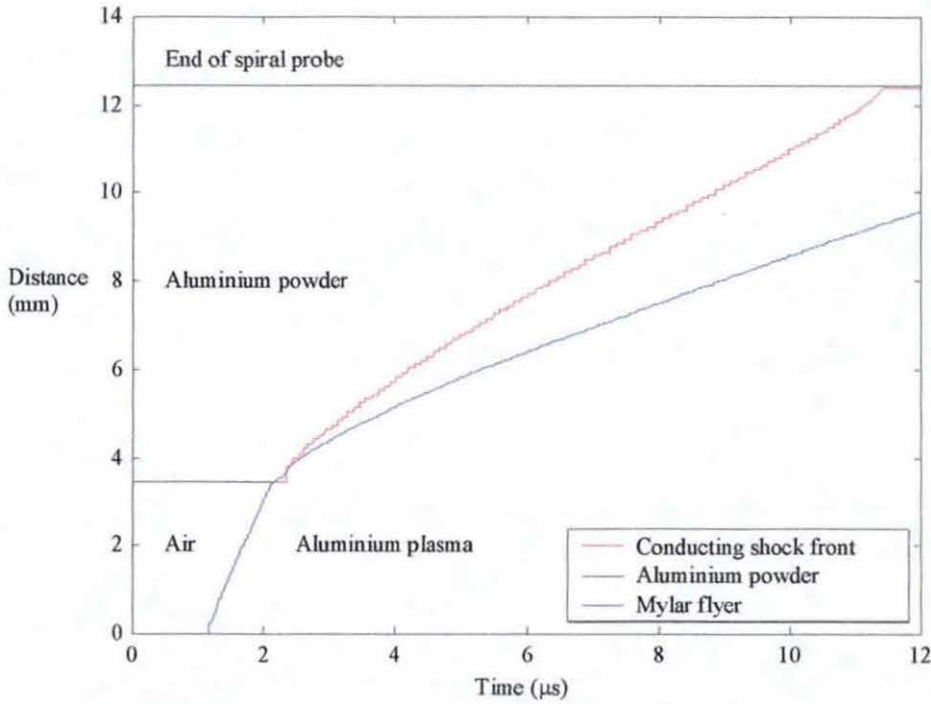


Figure 5-29 Summary of results from shock propagation model.

Fig 5-30 shows the characteristics of the shock velocity in the powder, which is in some ways similar to the quadratic velocity function found from multiple TOA measurements. The shock velocity starts at a peak of 2.5 km/s , decays rapidly to a steady velocity of about 0.6 km/s and rises again at the end of the spiral probe to a second peak of 2.5 km/s . The steady velocity is associated with the small but steady magnetic pressure in the input function of Fig 5-27, and the increase in the shock velocity near the end of the spiral probe with an elastic precursor travelling ahead of the shock front. A more thorough discussion of this precursor is given in the next section.

It is clear from Fig 5-30 that a general form of the shock velocity function, which contains the key parameters associated with actual physical processes, can be written as

$$U_s(t) = U_{s1} + U_{s2} \exp\left(-\frac{t - t_{imp}}{\tau_1}\right) + U_{s3} \exp\left(\frac{t - t_{dur} - t_{imp}}{\tau_2}\right) \quad (5-8)$$

where the constants U_{s1} , U_{s2} and U_{s3} have the dimension of speed. τ_1 and τ_2 are time constants for the exponential functions. t_{imp} is the time of impact and t_{dur} is the time

taken by the shock front to travel the length of the spiral probe. The definition for these parameters is shown in the graph of Fig 5-31.

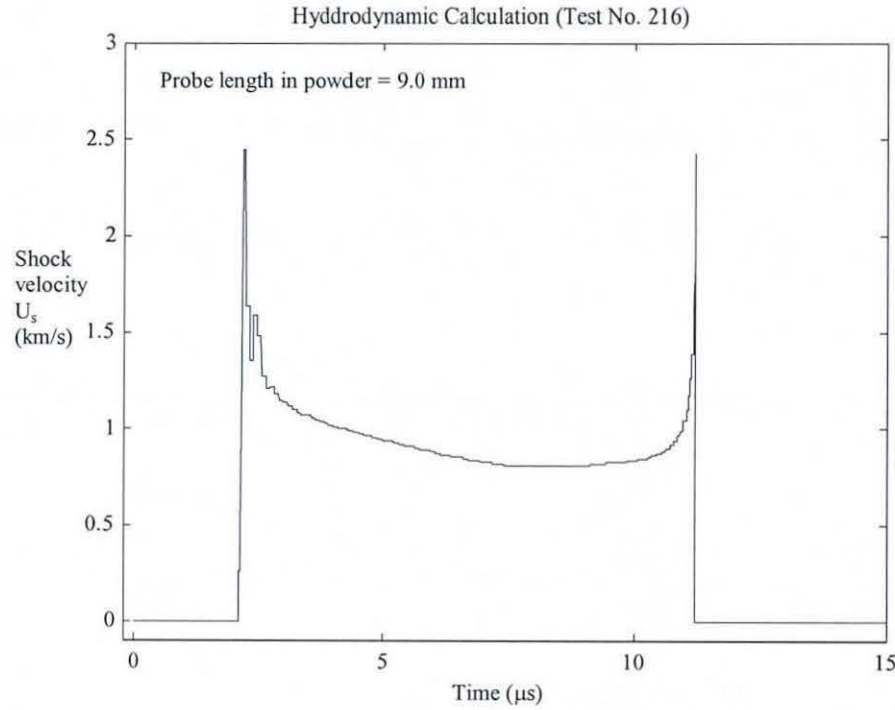


Figure 5-30 Shock velocity in aluminium powder obtained by the shock propagation model.

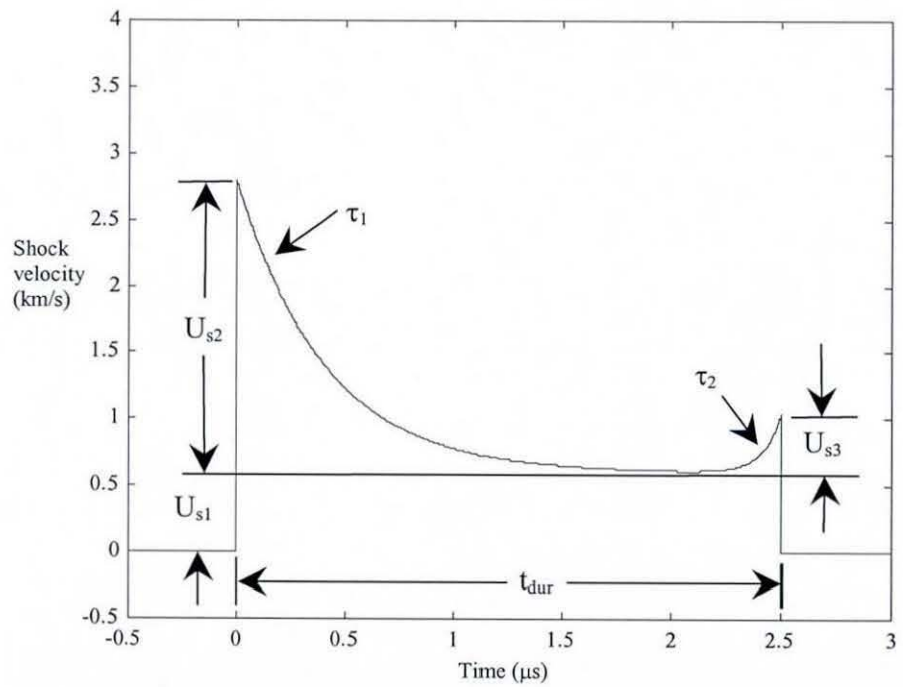


Figure 5-31 Shock velocity function of equation (5-8).

The constant term U_{s1} in equation (5-8) represents that part of the shock velocity arising from the magnetic pressure behind the Mylar flyer which continues to act on the powder sample, even after flyer impact.

The second term represents the exponentially decaying shock velocity imparted to the powder by the shock pressure produced by the Mylar flyer impact.

The final term represents the exponentially growing shock velocity due to the effect of the elastic precursor at a rigid wall.

Fig 5-32 shows a best fit to the hydrodynamic calculation, obtained using the parameters $t_{dur} = 2.13 \mu s$, $U_{s1} = 0.8 \text{ km/s}$, $U_{s2} = 1.7 \text{ km/s}$, $\tau_1 = 0.5 \mu s$, $U_{s3} = 0.85 \text{ km/s}$ and $\tau_2 = 0.2 \mu s$. The importance of a simplified mathematical description is demonstrated in section 5.3.5.4 for a simulation calculation and again in chapter 8 for the analysis and design of dynamic powder transformers.

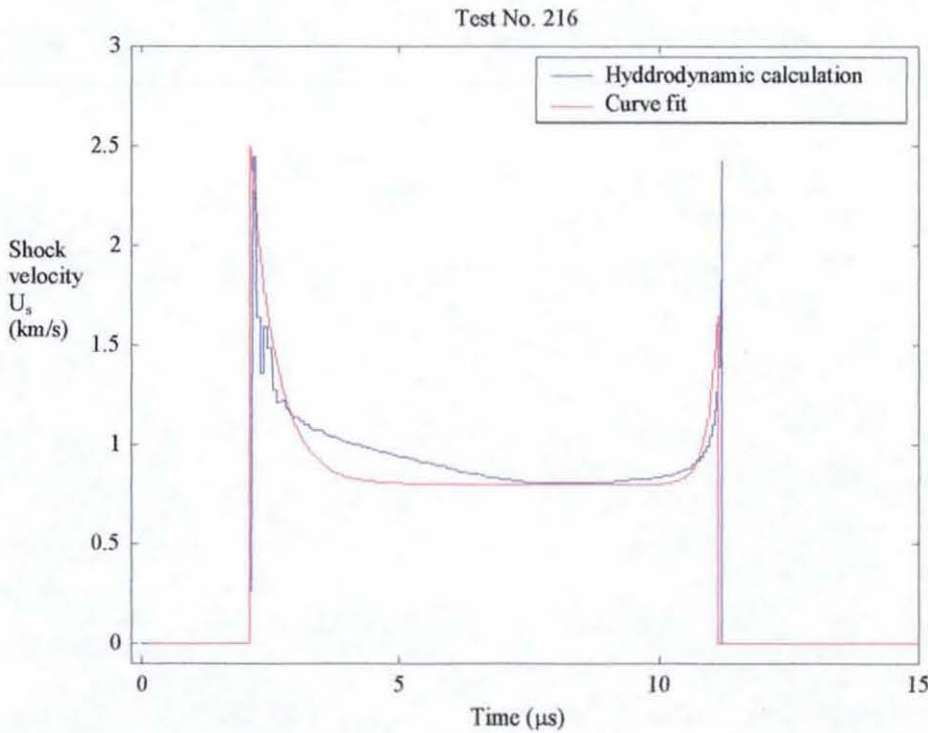


Figure 5-32 Best-fit analytic velocity function for used with the circuit model for spiral probe.

5.3.5.3 Elastic Precursor

The existence of a precursor (see Fig 5-33) travelling faster and appearing ahead of the shock front at the free-surface in powder compression experiments has been observed and reported by McQueen et al [31] and Butcher and Karnes [80]. The free-surface velocity in Fig 5-33 is usually the measured quantity in shockwave experiments and it is manipulated to produce information on the shock pressure. Thus the existence of a precursor is also manifested in a pressure profile of a similar shape.

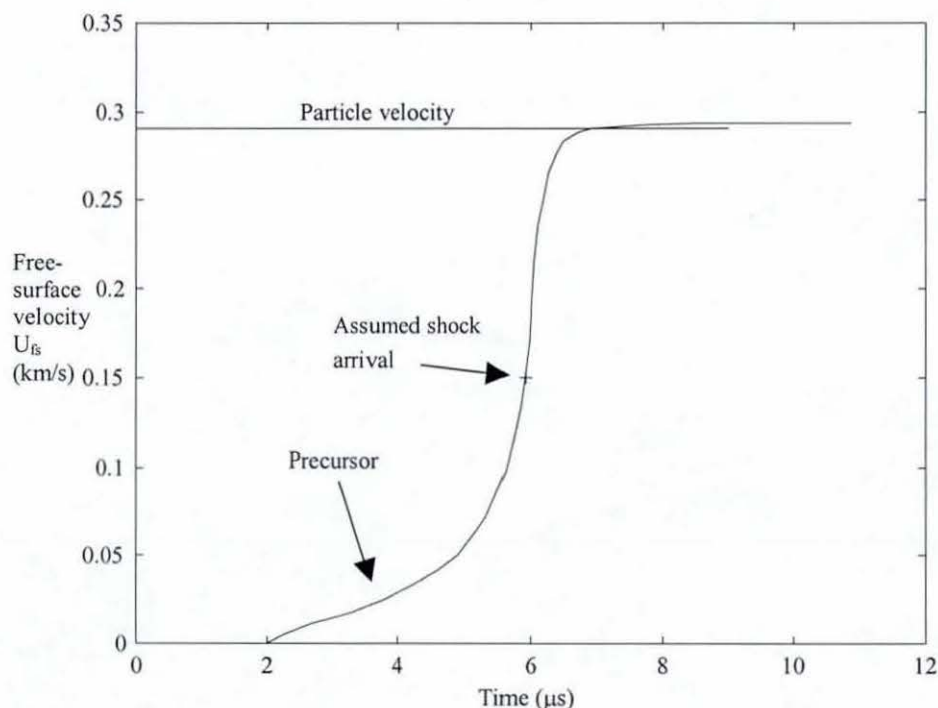


Figure 5-33 Free-surface velocity reproduced from Fig 26 of [31].

Due to its physical existence, the reproduction of the precursor (because of its occurrence in the low-pressure elastic region the term *elastic precursor* is sometimes used) in a hydrodynamic calculation for a powder material would be a desirable feature.

Partitioning of the $P - \alpha$ model in section 4.2.3 into (1) elastic (2) plastic and (3) solid (or fully compacted) regions, each with a separate functional definition, suggests that the dynamic behaviour of the powder material in all three regions should be calculated.

Figs 5-34 shows the material states throughout the powder, when the conducting shock front has travelled about 3.0 mm from the impact surface (The conducting region in the powder is shown in red in all the plots, to indicate the position of the shock front). Fig 5-34b shows that the powder elements less than about 2.0 mm ahead of the shock front are moving with a velocity smaller than the particle velocity in the shock-compressed region. Since the introduction of artificial viscosity (see equations 4-14 to 4-16) is only expected to spread the shock front across the number of cells defined by the constant (in this case $c_1 = 3$), smearing of the pressure front in Fig 5-34c over more than 2.0 mm (corresponding to more than 20 cell elements) is therefore not due to artificial viscosity but to the elastic response calculated by the $P - \alpha$ model.

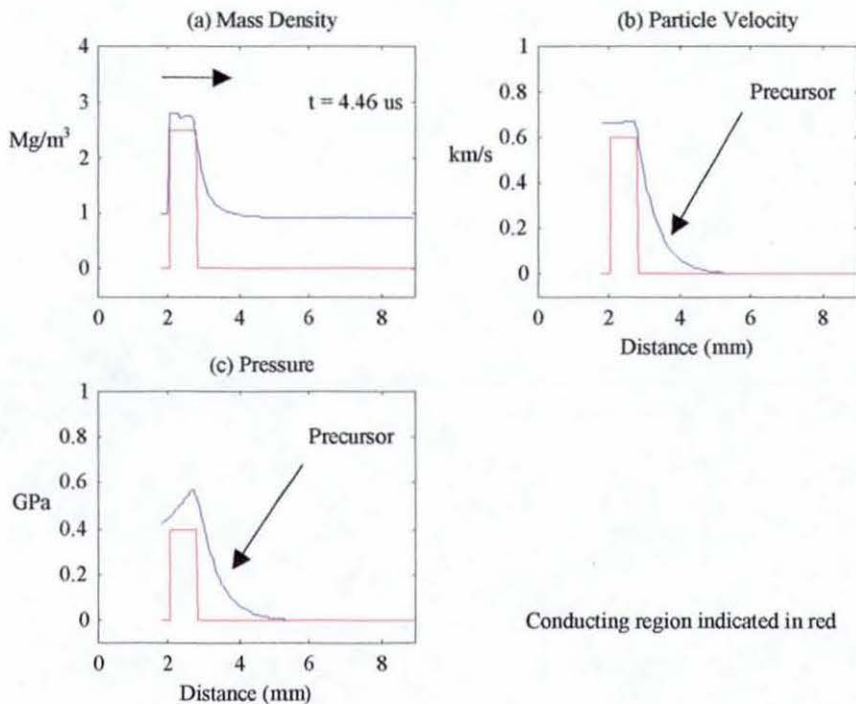


Figure 5-34 States of powder material at time $t = 4.46\text{ }\mu\text{s}$ showing precursor ahead of shock front.

Fig 5-35 shows the material state when the conducting shock front is near the end of the probe, which is modelled as a rigid wall boundary. It is clear from Fig 5-35 that the precursor (which is in the material preceding the shock front) is responsible for a sharp increase in particle velocity due to a phenomenon akin to the snow-plow effect. Finally the elastic precursor is evident in Fig 5-36, which shows the pressure in a powder element at the end of the spiral probe.

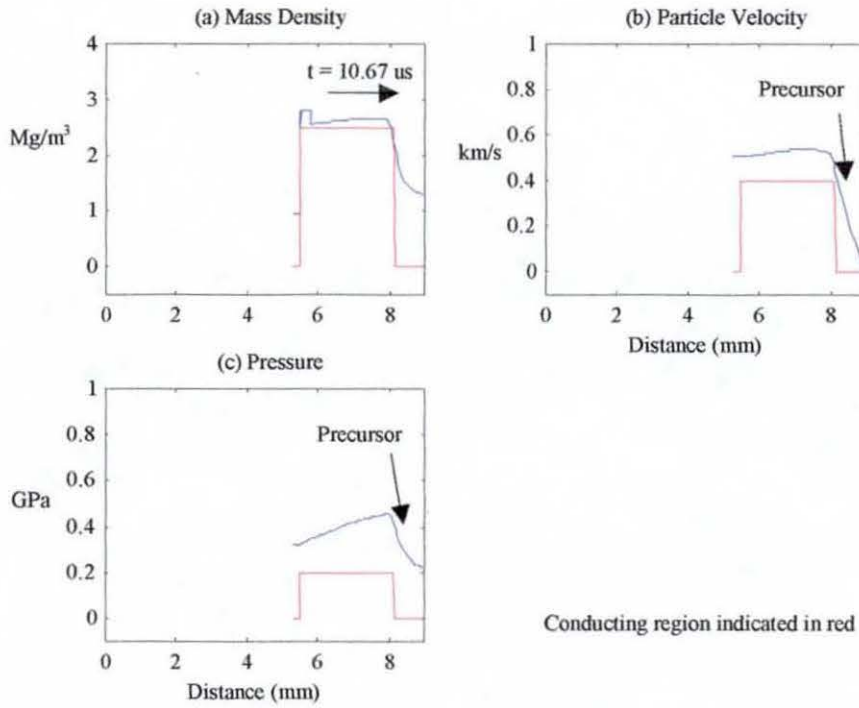


Figure 5-35 States of powder material at time $t = 10.67 \mu\text{s}$ showing precursor before shock reflection from a rigid wall boundary.

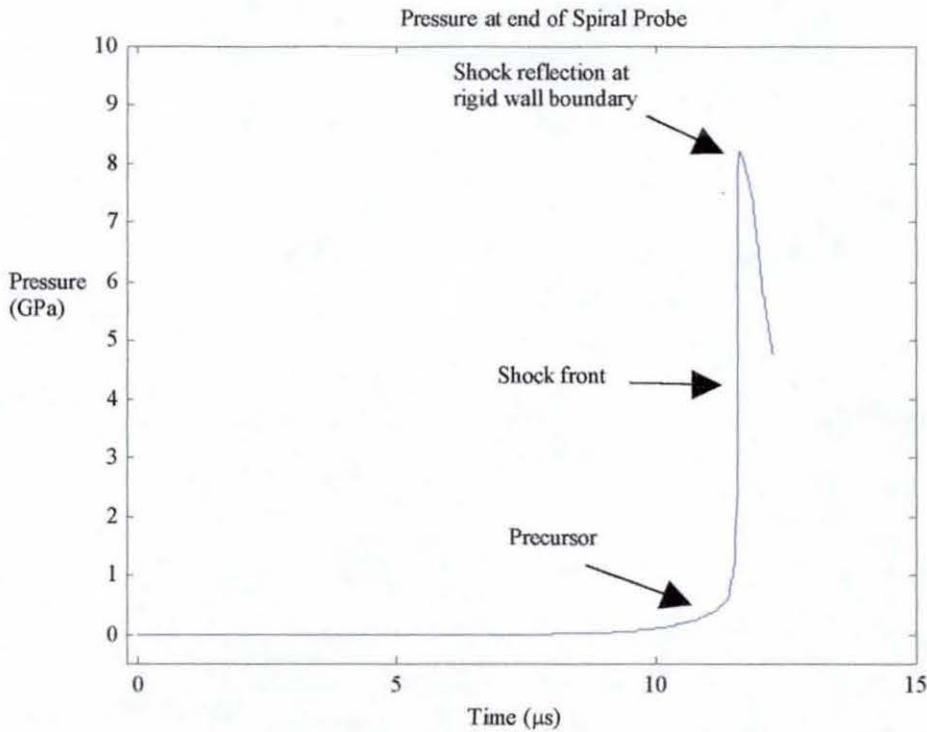


Figure 5-36 Variation of pressure in powder element at end of spiral probe (rigid wall boundary).

5.3.5.4 Three-Dimensional Graphs

The three-dimensional plots in Figs 5-37 to 5-40 provide an overview of the entire powder compression process. Initial conditions for the calculation are displayed along the space axis at time $t = 0$. In Fig 5-37, the Mylar flyer next to the origin (0,0) is separated from the aluminium powder (of about 1 g/cc density) by an air gap (with near zero density). In Fig 5-38, a burst pressure of about 15 GPa representing the foil burst is shown at the origin (0,0), while the air gap and aluminium powder are initially at low ambient pressure. In Fig 5-39, the Mylar flyer starts to move at a velocity of about 3 km/s while the air gap and aluminium powder are initially at rest. In Fig 5-40, the electrical conductivity everywhere (including the aluminium powder) is initially zero.

Computation is stopped very shortly after the shockwave reaches the end of the spiral resistance probe, with the resulting increase in mass density (Fig 5-37), pressure (Fig 5-38) and change in direction for the particle velocity (Fig 5-39) all being due to reflection at the rigid wall boundary. The electrical conductivity in Fig 5-40 does not show any changes at the reflection, because the powder is now in a highly compressed state corresponding to a high electrical conductivity.

The insulator-to-conductor phase change indicated in Fig 5-40 corresponds to locations along the yellow band in Fig 5-37 where the threshold density is exceeded. Comparison with the pressure profile in Fig 5-38 shows that the phase transition occurred along the edge of a low-pressure plateau of the same shape. The particle velocity plot in Fig 5-39 shows a low-velocity plateau with a slightly different shape, which is indicative of the elastic precursor moving faster and ahead of the shock front.

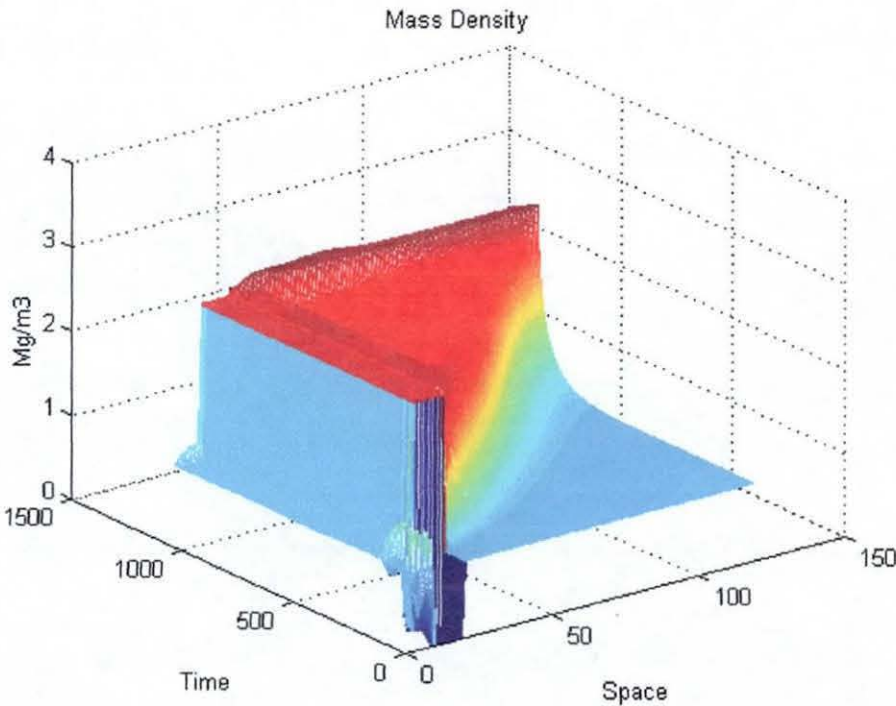


Figure 5-37 Mass density.

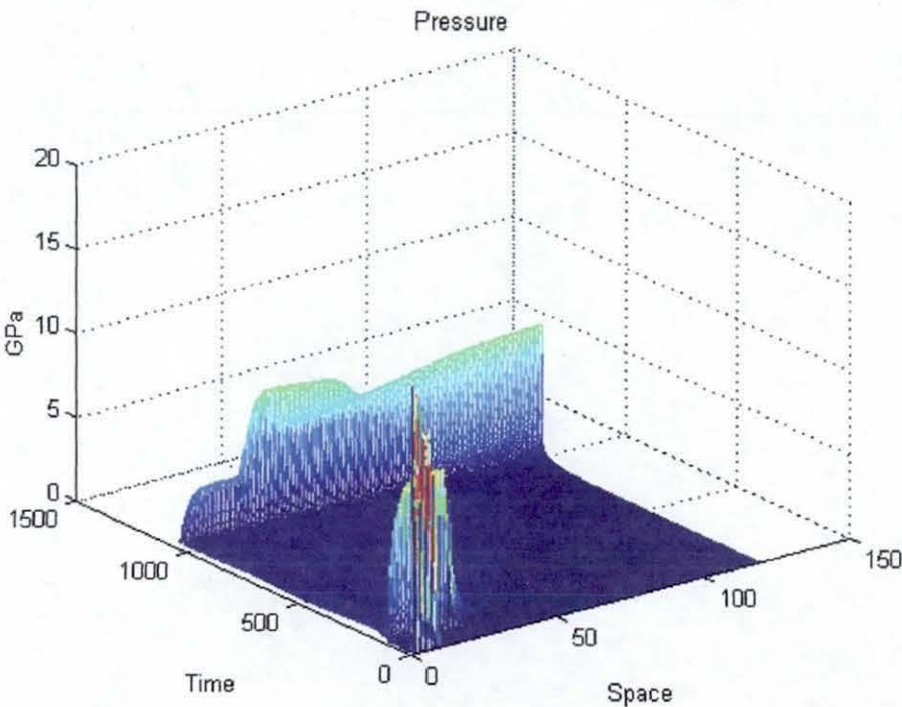


Figure 5-38 Pressure.

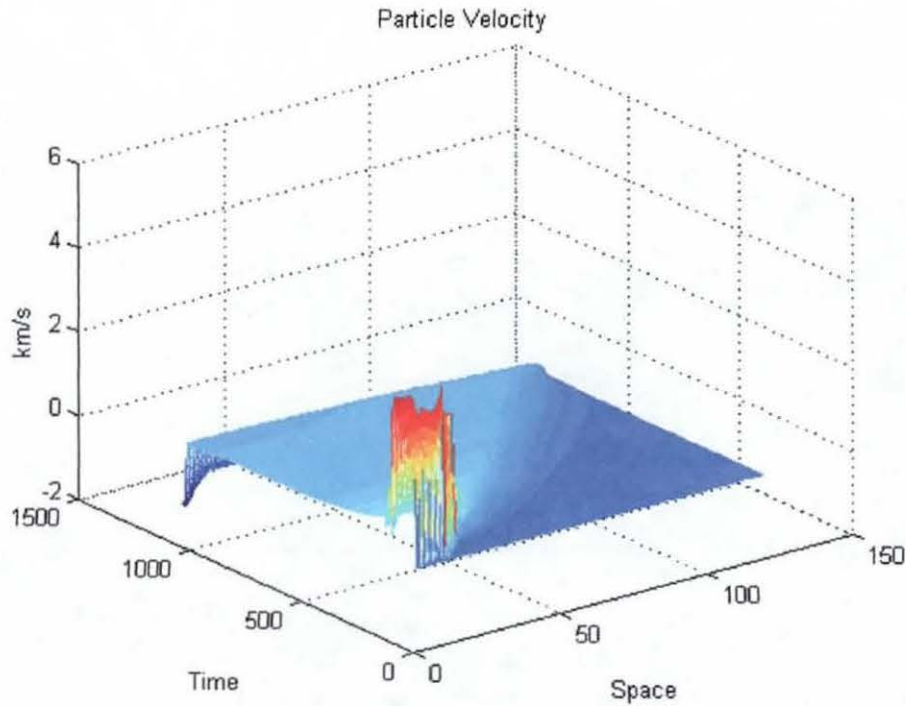


Figure 5-39 Particle velocity.

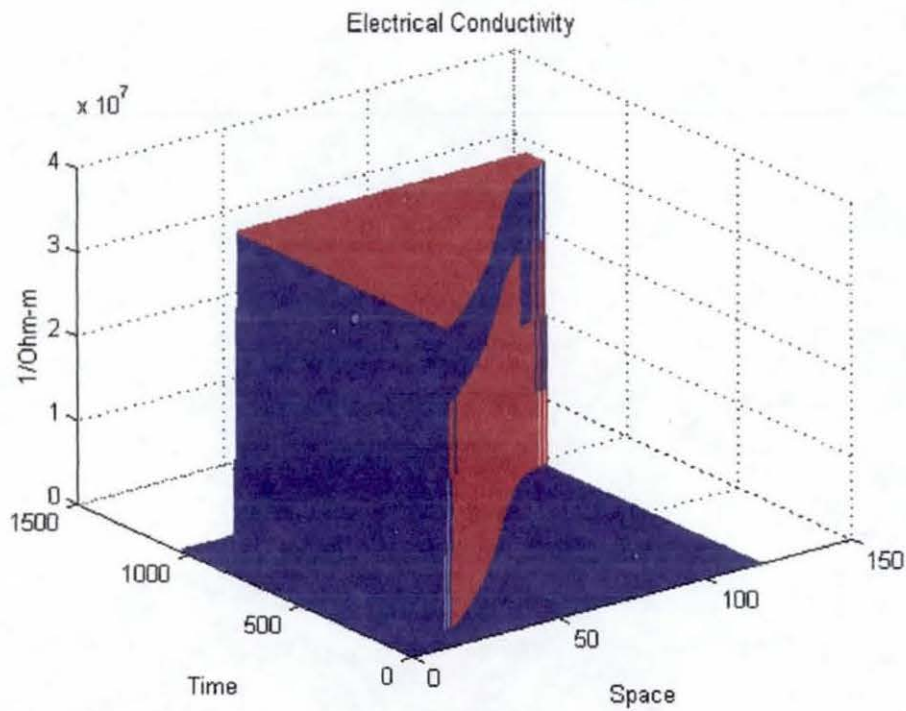


Figure 5-40 Electrical conductivity.

5.3.5.5 Circuit Model for Spiral Probe

When the shock velocity provided by the hydrodynamic code and shown in Fig 5-30 was used as an input to the circuit model for the spiral probe of section 5.2.5.2, the results in Figs 5-41 and 5-42 were obtained. Comparison of computed and measured results shows fairly good agreement, especially in the initial $5 \mu s$ of shock travel.

The poorer match with the later part of the experimental data is traceable to the constant term (0.2 GPa) used in equation (5-6) to represent the magnetic pressure. A better match can be obtained by using a smaller value for magnetic pressure in equation (5-6).

Alternatively, equation (5-8) for the characteristic velocity could be used as the starting point in a calculation to find a shock velocity function that agrees better with the experimental data, in particular with the TOA at the end of the spiral probe. Such a calculation can also test the existence of the elastic precursor at the end of the spiral probe, as suggested by the hydrodynamic calculation.

Figs 5-34 and 5-35 show calculations giving the best fit with the experimental data using the parameter values of Table 5-3 in equation (5-8), to simulate a velocity function with and without the precursor at the end of the spiral probe.

Table 5-3 Parameters for shock velocity equation

	U_{s1}	U_{s2}	τ_1	U_{s3}	τ_2	t_{dur}
Case I without precursor	0.5 km/s	2.5 km/s	$1.53 \mu s$	--	--	--
Case II with precursor	0.5 km/s	2.5 km/s	$1.53 \mu s$	1.25 km/s	$0.153 \mu s$	$12.0 \mu s$

Due to the nature of the spiral probe data, which becomes inaccurate towards the end of the probe, the existence of the elastic precursor predicted by the hydrodynamic code could not be confirmed experimentally by the present shock compression experiments. However, the presence of the elastic precursor is more evident in the dynamic powder transformer experiments described in chapter 8.

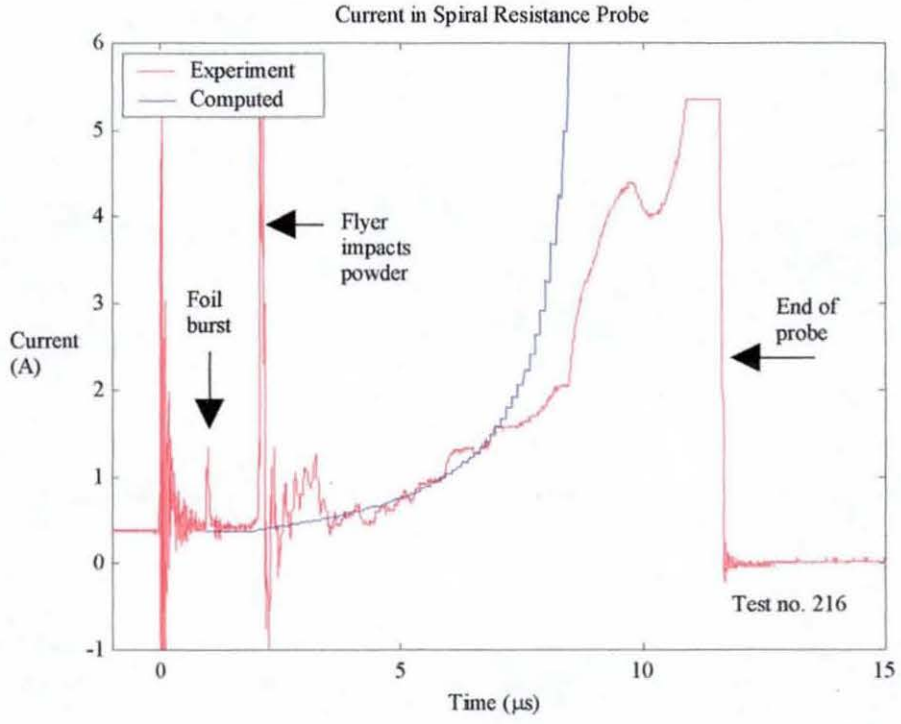


Figure 5-41 Comparison of experimental data with result from computer model using impact pressure of equation (5-6).

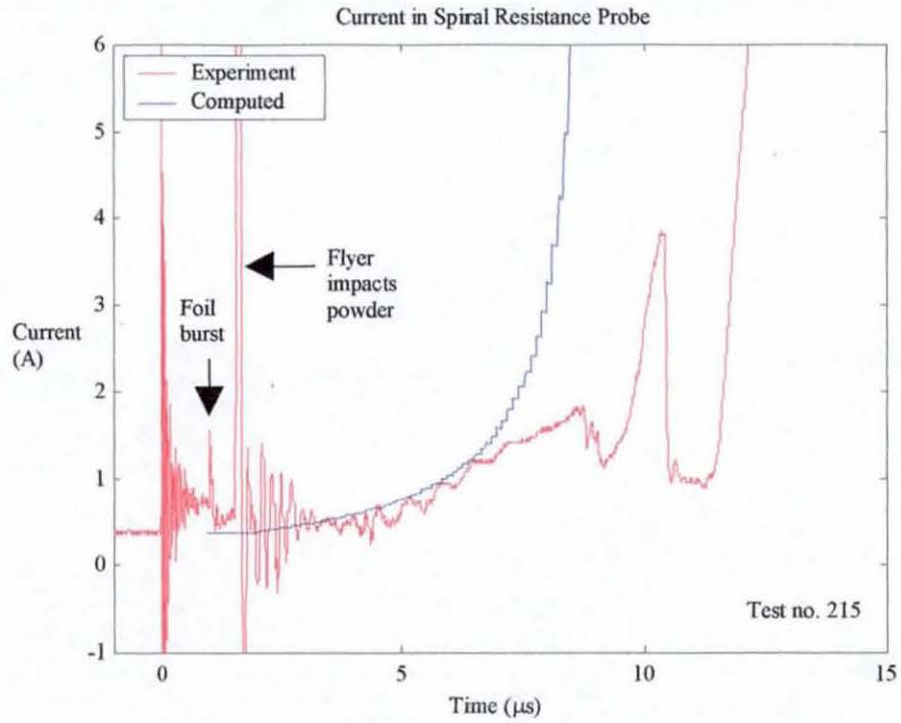


Figure 5-42 Comparison of experimental data with result from computer model using impact pressure of equation (5-6).

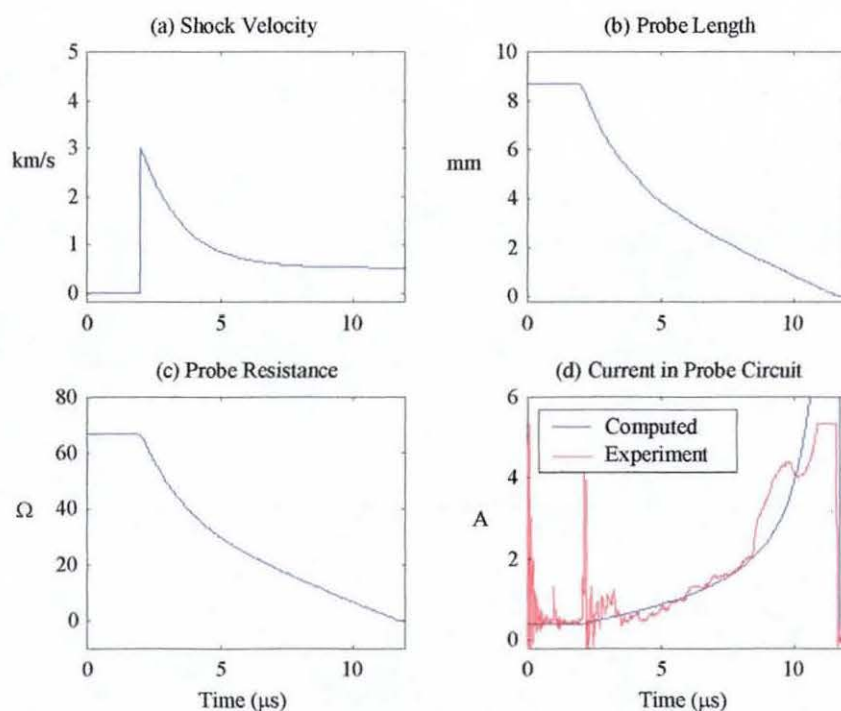


Figure 5-43 Results from circuit model for spiral probe for velocity profile without precursor (Case I in Table 5-3)

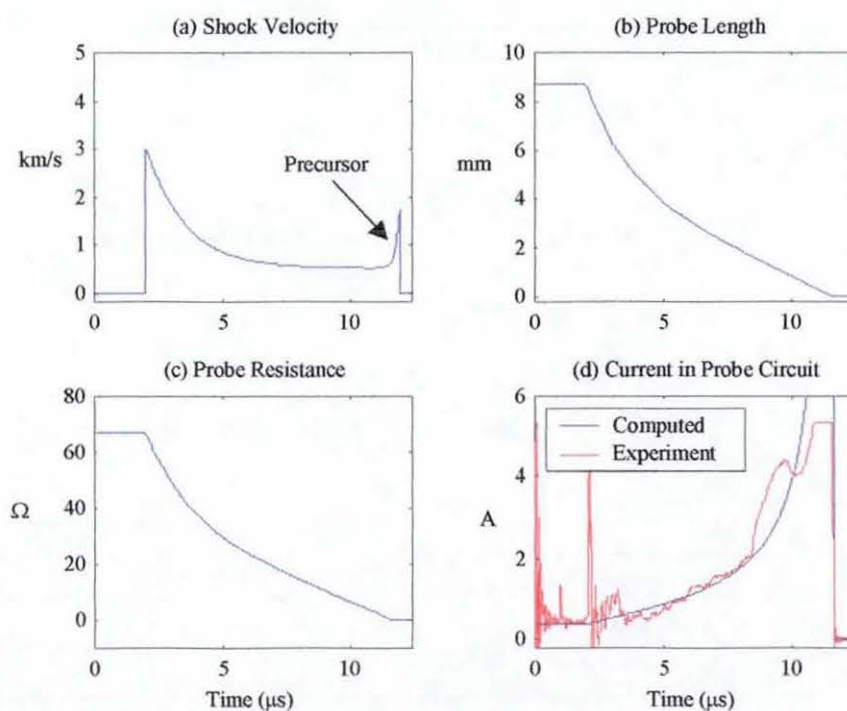


Figure 5-44 Results from circuit model for spiral probe for velocity profile with precursor (Case II in Table 5-3).

5.3.6 Comparison with Theory

5.3.6.1 Impedance Matching Method

In flyer-impact studies, the impedance matching method is normally used to calculate the pressure generated in the target material by the impact of a flyer plate at a velocity v_p . The physical basis for the technique is the requirement that the particle velocity and pressure should be continuous across the impact interface, and it uses the simple graphical solution shown in Fig 5-45. Curves relating the pressure P to the particle velocity u_p are shown starting at the origin for both target and flyer. If the curve for the flyer plate is rotated through 180° and passed through the coordinates $(v_p, 0)$, the reflection curve is obtained. This will intersect the target curve at (u_p, P) , at which point the continuity conditions

$$P_{target} = P_{flyer} \quad (5-9)$$

$$u_{p,target} + u_{p,flyer} = v_p \quad (5-10)$$

are satisfied.

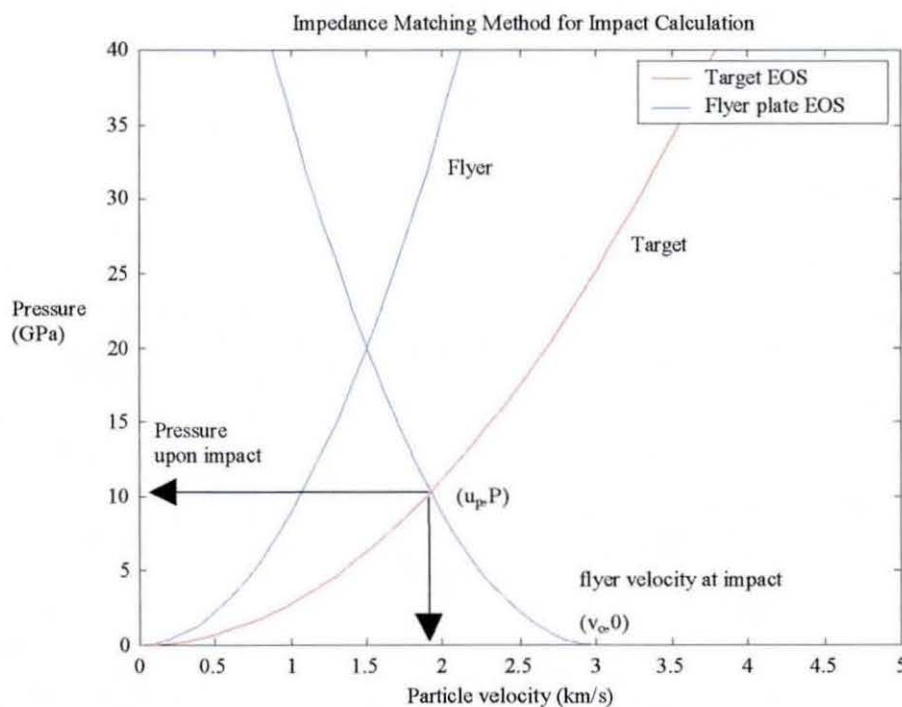


Figure 5-45 Impedance matching method.

5.3.6.2 Pressure and Particle Velocity at Impact

The impact pressure calculated by the impedance matching method using the $P-u_p$ curve for aluminium powder with 33% TD (see Fig 4-17) and that for Mylar polyester (see Fig 4-24) is shown in Fig 5-46 for impact velocities in the range of 1 to 8 km/s. Fig 5-47 shows the corresponding particle velocities obtained by the same method. It is interesting to note that the impact pressure predicted by this method is about 5 GPa for an impact at a velocity of 3 km/s, while the hydrodynamic code predicted a pressure pulse with two 'spikes' of 2.5 GPa and 7.5 GPa in Fig 5-26.

5.3.6.3 Shock Velocity at Impact

Fig 5-47 shows the shock velocity at impact calculated by equation (4-78) for the EOS of aluminium powder with 33% TD. For an impact at a velocity of 3 km/s, similar to the conditions in the present shock compression experiments, a shock velocity of 3 km/s is predicted by this method, which is consistent with the simulation calculation of Figs 5-43 and 5-44 but is slightly higher than the 2.5 km/s predicted by the shock propagation model in Fig 5-30.

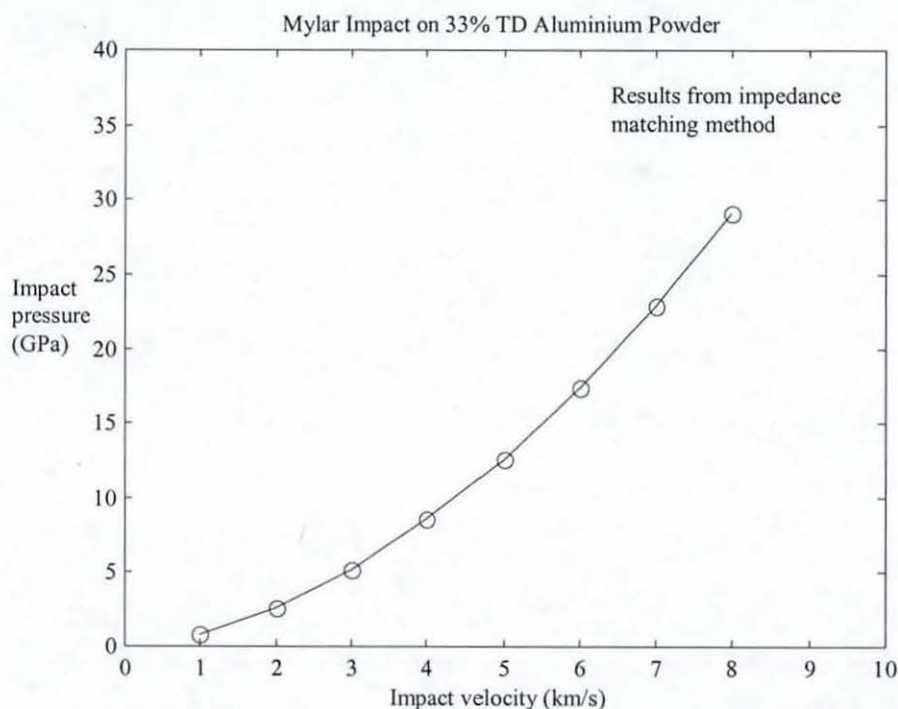


Figure 5-46 Variation of impact pressure with impact velocity.

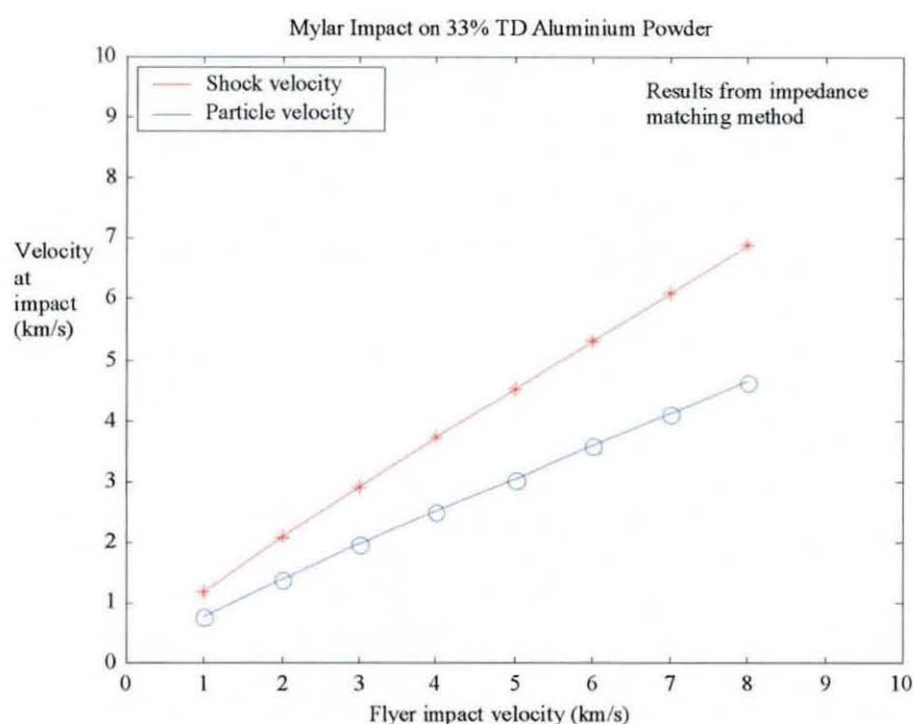


Figure 5-47 Variation of particle and shock velocity with impact velocity.

5.3.6.4 Shape of Impact Pressure Pulse

It is known from explosive driven shockwave studies [111]-[113] that the normal impact of a flyer on a target generates a pressure pulse characterised by a sharp pressure rise, a region in which the pressure is constant and finally an exponential decay of the pressure to zero, as shown in Fig 5-48.

The initial duration (flat top portion) of the pressure pulse travelling through the target material is usually determined by the flyer-plate thickness, although when this exceeds that of the target, the lesser thickness of the target can determine the pulse duration. When a flyer plate of thickness δ and an impact velocity of v_p collides with a target plate, particles in the target are accelerated in the direction of the impact and produce a shockwave moving away from the collision interface. Conversely, particles are decelerated in the flyer plate, producing a shockwave travelling back into the plate. The

time taken by the shock to reach the rear surface of the plate is $t_1 = \frac{\delta}{U_s}$, where it is reflected as a rarefaction wave and returns towards the interface at the speed of sound c_s in compressed material of thickness $\frac{\rho}{\rho_o} \delta$ in a time $t_2 = \frac{\rho}{\rho_o} \frac{\delta}{c_s}$.

Effectively, the initial duration of the pressure pulse at the front face of the target is therefore

$$t_{dur} = t_1 + t_2 = \frac{\delta}{U_s} + \frac{\rho}{\rho_o} \frac{\delta}{c_s} \quad (5-11)$$

A simpler and less rigorous equation for the initial duration of the pressure pulse is of course

$$t_{dur} = \frac{2\delta}{U_s} \quad (5-12)$$

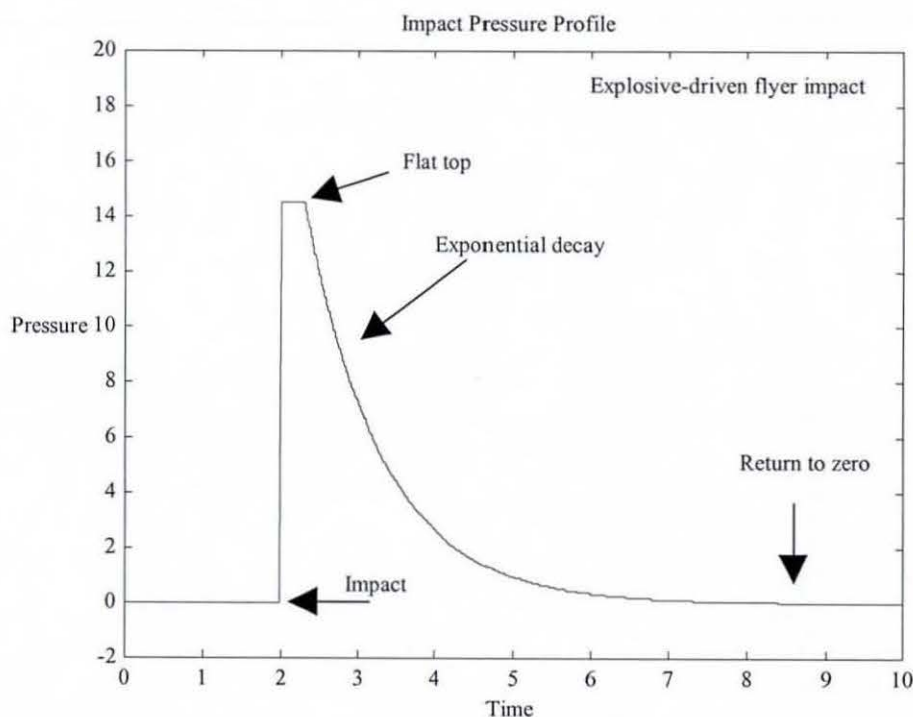


Figure 5-48 Typical shock pressure by explosive driven flyer impact.

The initial duration of the pressure pulse is predicted as $t_{dur} = 224.8 \text{ ns}$ from equation (5-11) and as $t_{dur} = 166.7 \text{ ns}$ from equation (5-12) for the conditions of the present experiments, with a flyer of $250 \mu\text{m}$ thickness impacting an aluminium powder with 33% TD and generating a shock velocity of 3.0 km/s . The powder is assumed to be fully compacted by the shockwave so that $\frac{\rho}{\rho_o} = 3$, with the speed of sound in the solid aluminium used in the calculation being $c_s = 5.3 \text{ km/s}$.

It is clear from the calculations above that the initial duration of the pressure pulse is almost negligible, due to the small thickness of the Mylar flyer, and that the shock velocity begins its exponential decay almost immediately upon impact, as shown in Fig 5-30.

Another distinguishing feature of the shape of the pressure pulse generated by an exploding foil driven flyer impact is the presence of a small-magnitude but long-duration magnetic pressure exerted by the current in the gun circuit. Since the main impact pressure does not have any significant duration, the presence of a magnetic pressure becomes the crucial part of the pressure that helps to sustain the velocity of the conducting shock front in the powder.

5.4 Flammability of the Aluminium Powder

The aluminium powder used in the present shock compression experiments has a relatively high initial density ($>500 \text{ kg/m}^3$) as compared with the typical upper flammability limit ($5-10 \text{ kg/m}^3$) of combustible metal powder or dusts (see Appendix D). The condition for combustion and explosion does not therefore exist. Furthermore, it was observed while preparing the experiments that the $25 \mu\text{m}$ aluminium powder tended to form larger agglomerates with a higher effective particle size, leading to a further reduction in any combustion or explosion hazard. It can therefore be reasonably concluded that the possibility of igniting the aluminium powder used in the present shock compression experiments is virtually non-existent.

5.5 Conclusions

In this chapter, the conducting shock front produced by a Mylar flyer impact on aluminium powder has been measured using TOA measurement and continuous velocity monitoring. Detailed analysis of the numerical results, and comparison with the impedance matching method, confirmed that the flyer acceleration and impact model and the shock propagation model are independently capable of reproducing experimental results reasonably well. The results of the hydrodynamic calculation have revealed the salient features of the shock velocity in the powder, which were used in a simulation calculation to obtain the best estimates of the shock velocity from data provided by a spiral resistance probe. The $P - \alpha$ model used in the hydrodynamic code is shown to be capable of reproducing the elastic precursor phenomenon known to appear in shock compression experiments, although it is not supported by experimental data from the present shock compression study of aluminium powder. A further discussion of the elastic precursor is given in chapter 8.

MAGNETOHYDRODYNAMIC MODEL FOR CYLINDRICAL IMPLOSION

In this chapter, the mathematical model for the electric gun is extended to the case of cylindrical implosion (as compared to the planar case of chapter 3), with the hydrodynamic model being modified by the inclusion of Maxwell's equations to obtain a MHD model for magnetic flux compression under these conditions. The performance of the model is demonstrated by a detailed analysis of an explosive driven shockwave flux compression experiment conducted by Nagayama et al [29] using metallic powder.

6.1 Mathematical Modelling of Cylindrical Electric Gun

For purposes of readability and clarity, the development of the cylindrical model is described in the way used in chapter 3, with a small number of equations repeated where necessary. It is hoped that this will allow the chapter to be read without excessive reference to earlier parts of the thesis.

The most significant difference for the cylindrical case is that the Gurney calculation is carried out using mass per unit length, rather than mass per unit area as in the planar case.

6.1.1 Gurney Equation for Implosion of Cylindrical Asymmetric Sandwich

In the asymmetric arrangement of Fig 6.1 a thin cylindrical sheet of explosive material of mass C per unit length is confined by a flyer and tamper of mass M and N per unit length on the side. r_{mo} and r_{No} denote the initial positions of the flyer and the tamper.

At some time after an explosion, $-v_m$ is both the terminal velocity of the imploding flyer and that of the gaseous explosion product in contact with it. v_N is the terminal velocity of the tamper and the gaseous product adjacent to it.

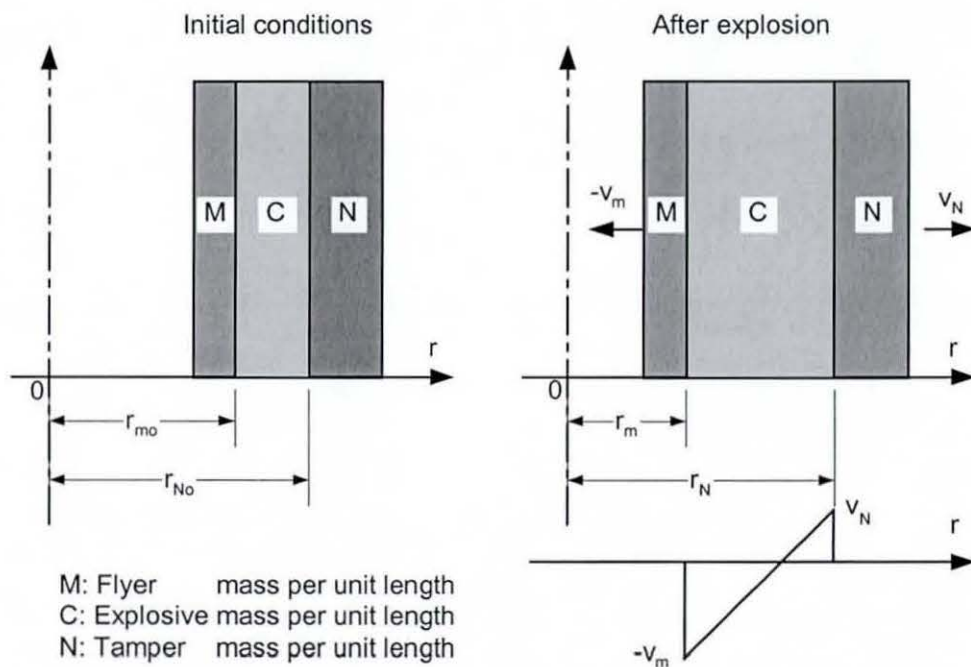


Figure 6-1 Asymmetric arrangement for cylindrical implosion.

It follows from Gurney's assumptions for a uniformly distributed density of the explosion product and a liner velocity profile that

$$\rho(r) = \frac{C}{\pi(r_N^2 - r_m^2)} \quad (6-1)$$

$$\text{and } v(r) = -v_m + \left(\frac{v_N + v_m}{r_N - r_m} \right) (r - r_m) \quad (6-2)$$

The equation for the conservation of momentum is

$$0 = M(-v_m) + Nv_N + \int_{r_m}^{r_N} \rho(r)v(r)2\pi r dr \quad (6-3)$$

and evaluation of the integral under the assumptions for density and velocity distribution gives

$$A = \frac{v_N}{v_m} = \frac{\left[\frac{M}{C} + \frac{r_N + 2r_m}{3(r_N + r_m)} \right]}{\left[\frac{N}{C} + \frac{2r_N + r_m}{3(r_N + r_m)} \right]} \quad (6-4)$$

The equation for the conservation of energy is

$$C\varepsilon = \frac{1}{2} M v_m^2 + \frac{1}{2} N v_N^2 + \frac{1}{2} \int_{r_m}^{r_N} \rho(r) [v(r)]^2 2\pi r dr \quad (6-5)$$

and evaluation of the integral in equation (6-5) leads to

$$\frac{1}{2} \int_{r_m}^{r_N} \rho(r) [v(r)]^2 2\pi r dr = \frac{C}{2} \left[\frac{1}{6} \left(\frac{r_N + 3r_m}{r_N + r_m} \right) v_m^2 - \frac{1}{3} v_m v_N + \frac{1}{6} \left(\frac{3r_N + r_m}{r_N + r_m} \right) v_N^2 \right] \quad (6-6)$$

By substituting equations (6-4) and (6-6) into equation (6-5) to eliminate the tamper velocity v_N , the terminal speed of the flyer (or projectile) may be found as

$$v_m = \sqrt{2\varepsilon_G} \left[\frac{M}{C} + \frac{1}{6} \left(\frac{r_N + 3r_m}{r_N + r_m} \right) - \frac{1}{3} A + \left[\frac{N}{C} + \frac{1}{6} \left(\frac{3r_N + r_m}{r_N + r_m} \right) \right] A^2 \right]^{\frac{1}{2}} \quad (6-7)$$

As previously defined, the terminal velocity of the imploding flyer is $-v_m$.

a) Tamper with Infinite Mass

For the case of an infinite mass tamper $N \rightarrow \infty$, such that $A = 0$ and

$$v_m = \sqrt{2\varepsilon_G} \left[\frac{M}{C} + \frac{1}{6} \left(\frac{r_N + 3r_m}{r_N + r_m} \right) \right]^{\frac{1}{2}} \quad (6-8)$$

If the diameter (or radius) is large compared to the explosive thickness, i.e. $r_N \approx r_m$, equation (6-8) reduces to that previously obtained for a planar configuration of

$$v_m = \sqrt{2\varepsilon_G} \left(\frac{M}{C} + \frac{1}{3} \right)^{-\frac{1}{2}} \quad (6-9)$$

b) Open-faced Sandwich

For the case of open-face sandwich $N \rightarrow 0$, so that

$$A = \frac{v_N}{v_m} = \left[3 \left(\frac{r_N + r_m}{2r_N + r_m} \right) \frac{M}{C} + \left(\frac{r_N + 2r_m}{2r_N + r_m} \right) \right] \quad (6-10)$$

$$\text{and } v_m = \sqrt{2\varepsilon_G} \left[\frac{M}{C} + \frac{1}{6} \left(\frac{r_N + 3r_m}{r_N + r_m} \right) - \frac{1}{3} A + \frac{1}{6} \left(\frac{3r_N + r_m}{r_N + r_m} \right) A^2 \right]^{-\frac{1}{2}} \quad (6-11)$$

If the diameter (or radius) is large compared to the explosive thickness, i.e. $r_N \approx r_m$, equations (6-10) and (6-11) again reduce to those for a planar configuration

$$A = 1 + \frac{2M}{C} \quad (6-12)$$

$$\text{and } v_m = \sqrt{2\varepsilon_G} \left[\frac{M}{C} + \frac{1 + \left(1 + 2\frac{M}{C} \right)^3}{6 \left(1 + \frac{M}{C} \right)} \right]^{-\frac{1}{2}} \quad (6-13)$$

6.1.2 Acceleration Solution using Ideal Gas Law EOS

The procedure for obtaining the Gurney acceleration solution is identical to that previously outlined in chapter 3.

If ε_o is the chemical energy density of the unreacted explosive and ε is the internal energy density remaining in the explosive, the energy balance equation can be written as

$$C\varepsilon_o = C\varepsilon + \frac{1}{2}Mv_m^2 + \frac{1}{2}Nv_N^2 + \frac{1}{2} \int_{r_N}^{r_m} \rho(r)[v(r)]^2 2\pi r dr \quad (6-14)$$

in which v_m and v_N are instantaneous and not terminal velocities.

Evaluation of the final term of equation (6-14) gives

$$\frac{1}{2} \int_{r_m}^{r_N} \rho(r)[v(r)]^2 2\pi r dr = \frac{C}{2} \left[\frac{1}{6} \left(\frac{r_N + 3r_m}{r_N + r_m} \right) v_m^2 - \frac{1}{3} v_m v_N + \frac{1}{6} \left(\frac{3r_N + r_m}{r_N + r_m} \right) v_N^2 \right] \quad (6-15)$$

so that the equation becomes

$$C\varepsilon_o = C\varepsilon + \frac{1}{2}Mv_m^2 + \frac{1}{2}Nv_N^2 + \frac{C}{2} \left[\frac{1}{6} \left(\frac{r_N + 3r_m}{r_N + r_m} \right) v_m^2 - \frac{1}{3} v_m v_N + \frac{1}{6} \left(\frac{3r_N + r_m}{r_N + r_m} \right) v_N^2 \right] \quad (6-16)$$

The equation for the conservation of momentum is

$$0 = M(-v_m) + Nv_N + \int_{r_m}^{r_N} \rho(r)v(r)2\pi r dr \quad (6-17)$$

and evaluation of the integral under the assumptions for density and velocity distribution gives

$$A = \frac{v_N}{v_m} = \frac{\left[\frac{M}{C} + \frac{r_N + 2r_m}{3(r_N + r_m)} \right]}{\left[\frac{N}{C} + \frac{2r_N + r_m}{3(r_N + r_m)} \right]} \quad (6-18)$$

Replacing v_N by Av_m in equation (6-16) gives

$$C\varepsilon_o = C\varepsilon + \frac{1}{2}Mv_m^2 + \frac{1}{2}N(Av_m)^2 + \frac{C}{2}\left[\frac{1}{6}\left(\frac{r_N + 3r_m}{r_N + r_m}\right)v_m^2 - \frac{1}{3}v_m(Av_m) + \frac{1}{6}\left(\frac{3r_N + r_m}{r_N + r_m}\right)(Av_m)^2\right]$$

$$\text{or } \varepsilon_o = \varepsilon + \frac{1}{2}\left[\frac{M}{C} + \frac{1}{6}\left(\frac{r_N + 3r_m}{r_N + r_m}\right) - \frac{1}{3}A + \left[\frac{N}{C} + \frac{1}{6}\left(\frac{3r_N + r_m}{r_N + r_m}\right)\right]A^2\right]v_m^2 \quad (6-19)$$

When $\varepsilon = 0$, the energy initially in the unreacted explosive has all been converted to kinetic energy and the terminal velocity is

$$v_m(t) = \sqrt{2\varepsilon_G}\left[\frac{M}{C} + \frac{1}{6}\left(\frac{r_N + 3r_m}{r_N + r_m}\right) - \frac{1}{3}A + \left[\frac{N}{C} + \frac{1}{6}\left(\frac{3r_N + r_m}{r_N + r_m}\right)\right]A^2\right]^{\frac{1}{2}} \quad (6-20)$$

By equating ε_o to the Gurney energy density ε_G and assuming an ideal gas EOS for the explosion product

$$\varepsilon = \frac{P}{\rho(\gamma - 1)} \quad (6-21)$$

we obtain from equation (6-19)

$$\varepsilon_G = \frac{P}{\rho(\gamma - 1)} + \frac{1}{2}\left[\frac{M}{C} + \frac{1}{6}\left(\frac{r_N + 3r_m}{r_N + r_m}\right) - \frac{1}{3}A + \left[\frac{N}{C} + \frac{1}{6}\left(\frac{3r_N + r_m}{r_N + r_m}\right)\right]A^2\right]v_m^2 \quad (6-22)$$

For a cylindrical configuration, in which M is the flyer mass per unit length, Newton's equation for motion is

$$P2\pi r_m = -M \frac{dv_m}{dt} \quad (6-23)$$

Defining a new variable by

$$B = \frac{M}{C} + \frac{1}{6} \left(\frac{r_N + 3r_m}{r_N + r_m} \right) - \frac{1}{3} A + \left[\frac{N}{C} + \frac{1}{6} \left(\frac{3r_N + r_m}{r_N + r_m} \right) \right] A^2 \quad (6-24)$$

we obtain from equation (6-22)

$$\varepsilon_G = \frac{1}{\rho(\gamma-1)} \left(-\frac{M}{2\pi r_m} \frac{dv_m}{dt} \right) + \frac{1}{2} B v_m^2$$

or

$$\frac{dv_m}{dt} = -\frac{\rho(\gamma-1)}{2} (2\varepsilon_G - B v_m^2) \frac{2\pi r_m}{M} \quad (6-25)$$

To obtain an ordinary differential equation with only one unknown, ρ is eliminated using the initial conditions given in Fig 6-1 that at $t = 0$, $r_m = r_{mo}$ and $r_N = r_{No}$. As the motion proceeds to a later time τ we have

$$r_m = r_{mo} - \int_0^\tau v_m(t) dt \quad (6-26)$$

$$\text{and } r_N = r_{No} + \int_0^\tau v_N(t) dt = r_{No} + A \int_0^\tau v_m(t) dt \quad (6-27)$$

By combining these equations and eliminating the integral, we find that

$$r_N = r_{No} + A(r_{mo} - r_m) \quad (6-28)$$

and from the conservation of mass

$$\rho = \frac{C}{\pi(r_N^2 - r_m^2)} \quad (6-29)$$

Substituting for r_N from equation (6-28), gives

$$\rho = \frac{C}{\pi \left[(A^2 - 1)r_m^2 - 2A(Ar_{mo} + r_{No})r_m + (Ar_{mo} + r_{No})^2 \right]} \quad (6-30)$$

which allows ρ to be eliminated from equation (6-25), to give

$$\frac{dv_m}{dt} = -\frac{C(\gamma-1)(2\varepsilon_G - Bv_m^2)}{2\pi[(A^2-1)r_m^2 - 2A(Ar_{mo} + r_{No})r_m + (Ar_{mo} + r_{No})^2]} \left(\frac{2\pi r_m}{M} \right)$$

or

$$\frac{dv_m}{dt} = -\frac{C}{M} \frac{(\gamma-1)(2\varepsilon_G - Bv_m^2)r_m}{[(A^2-1)r_m^2 - 2A(Ar_{mo} + r_{No})r_m + (Ar_{mo} + r_{No})^2]} \quad (6-31)$$

which together with

$$\frac{dr_m}{dt} = v_m \quad (6-32)$$

form a system of coupled first-order differential equations that can be solved numerically to obtain the trajectory and velocity of the flyer.

Once the flyer trajectory has been found from the solution of equations (6-31) and (6-32), the shock pressure generated by the exploding foil in equation (6-23) can be rewritten as

$$P_{ex} = \frac{C(\gamma-1)(2\varepsilon_G - Bv_m^2)}{2\pi[(A^2-1)r_m^2 - 2A(Ar_{mo} + r_{No})r_m + (Ar_{mo} + r_{No})^2]} \quad (6-33)$$

6.1.3 Gurney Terminal Velocity

As explained in chapter 3, the Gurney terminal velocity for a Mylar flyer accelerated by an electric gun depends essentially on the burst energy density, the exploding foil thickness and the flyer thickness. Equation (6-7) may be used to predict the terminal flyer velocity if the mass density of the exploding foil ρ_f and the flyer ρ_{flyer} are known, while the free parameters are the flyer thickness δ_{flyer} and the characteristic Gurney energy density ε_G . The velocity is recorded in Fig 6-2 and Table 6-1 for flyer thicknesses between $75 \mu m$ and $300 \mu m$ and for Gurney energy densities between $1 MJ/kg$ and $20 MJ/kg$. $25 \mu m$ thick aluminium foil has been chosen as the exploding metallic foil for calculation.

The variation of flyer trajectory with time obtained by solving equations (6-31) and (6-32), for different combination of energy density and flyer thickness differ only very slightly from those for the planar configuration.

Table 6-1 Gurney terminal velocity for Mylar flyer

Energy density (MJ/kg)	Gurney velocity (<i>km/s</i>)	
	250 μm Mylar flyer	75 μm Mylar flyer
1	0.70	1.09
5	1.56	2.43
10	2.21	3.44
15	2.71	4.21
20	3.13	4.87

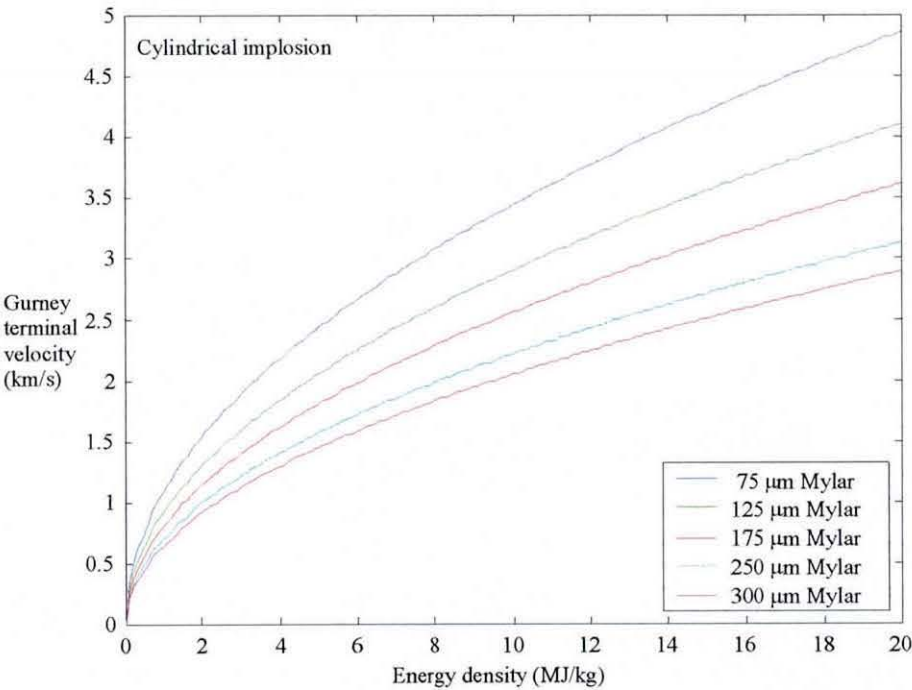


Figure 6-2 Gurney terminal velocity for different flyer thicknesses and energy densities.

6.1.4 Explosive Pressure at Foil Burst

Figs 6-3 shows the explosion pressure calculated using equation (6-33) for 250 μm thick Mylar flyers. Again, the shape and the duration of the pressure pulses shown in Fig 6-3 do not differ greatly from those for a planar configuration.

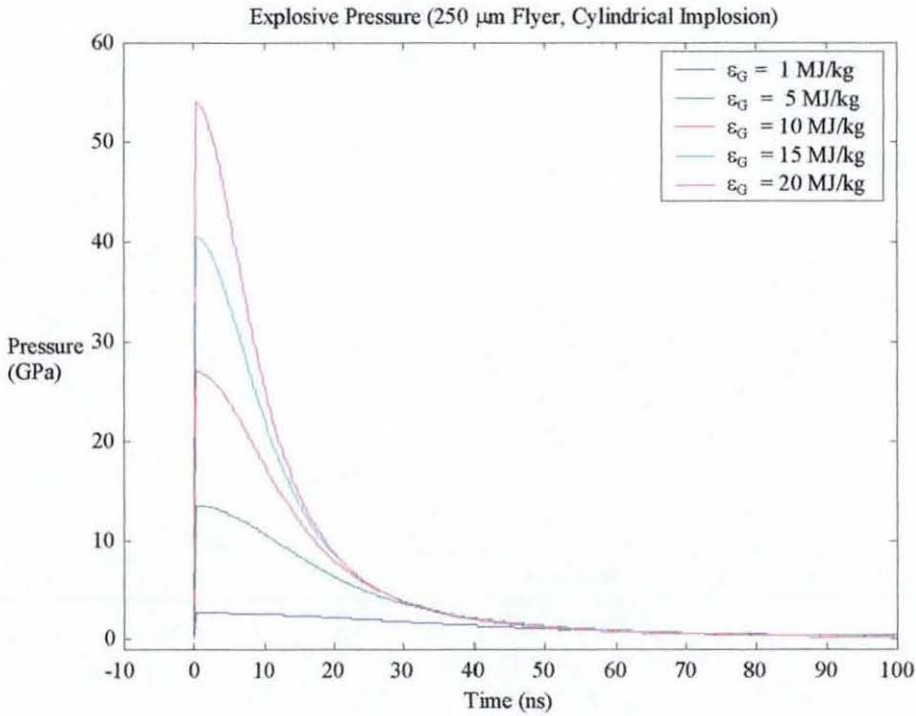


Figure 6-3 Foil explosion pressure for a 250 μm Mylar flyer.

6.1.5 Integrated Model for the Cylindrical Electric Gun

In this section, the Gurney acceleration solution is combined with the equations for the electrical circuit to form an integrated model for the cylindrical electric gun (shown in Fig 6-4a) to obtain a complete and detailed description of the gun performance. For purpose of clarity, the system of equations is listed in an order consistent with that of chapter 3

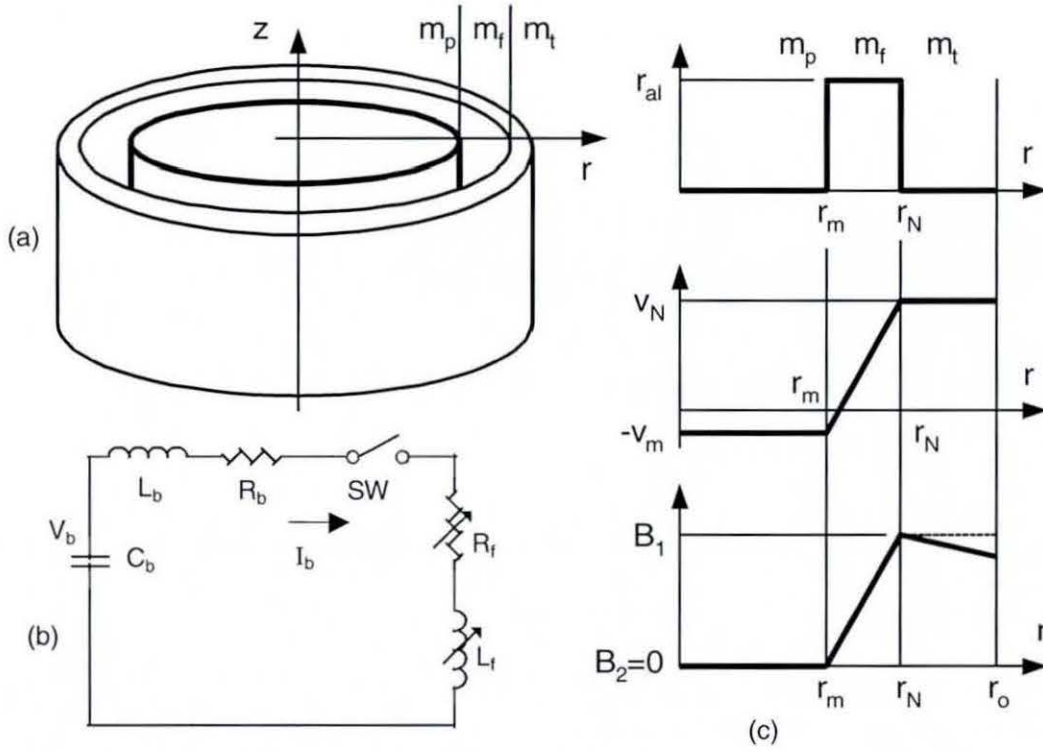


Figure 6-4 Electric gun (a) cylindrical geometry, (b) equivalent electrical circuit and (c) approximation for mass density, velocity distribution and magnetic flux density.

a) Mass of flyer, exploding foil and tamper

The foil mass m_f is related to the explosive mass C per unit length by the expression

$$C = \frac{m_f}{l_f} \quad (6-34)$$

and similar expressions apply for the tamper and flyer mass per unit length

$$M = \frac{m_p}{l_f}, \quad N = \frac{m_t}{l_f} \quad (6-35)$$

b) Gurney assumptions

The two fundamental assumptions of chapter 3 will be used again. Following the explosion, the mass density of the foil plasma is assumed to be uniform, so that

$$\rho(r) = \frac{C}{\pi(r_N^2 - r_m^2)} \quad (6-36)$$

The velocity profile for the explosion product is assumed to be linear, so that

$$v(r) = -v_m + \frac{v_N + v_m}{r_N - r_m}(r - r_m) \quad (6-37)$$

c) Magnetic field equation

The thickness of the foil plasma is assumed to be much less than the magnetic diffusion skin-depth, so that the magnetic flux density varies linearly across the foil as shown in Fig 6-4c.

$$B(r) = \frac{B_1}{r_N - r_m}(r - r_m) \quad (6-38)$$

d) Initial conditions

Initially, at $t = 0$, the metallic foil occupies the space between r_{mo} and r_{No} and the return conductor is located at $r = r_o$. The thickness of the metallic foil δ_f is given by

$$\delta_f = r_{No} - r_{mo} \quad (6-39)$$

e) Resistance and inductance of foil

For the cylindrical geometry of Fig 6-4a, the initial foil resistance is given by

$$R_{fo} = \eta \frac{l_f}{2\pi r_{avg} \delta_f} \quad (6-40)$$

where $r_{avg} = 0.5(r_m + r_N)$ is the mean radius of the foil (or foil plasma).

If the foil inductance is separated into two parts $L_f = L_1 + L_i$, where L_1 is associated with the tamper and L_i with the foil plasma, the component inductances are

$$L_1 = \frac{\mu_o I_f}{2\pi} \ln \left(\frac{r_o}{r_N} \right) \quad (6-41)$$

$$\text{and } L_i = \frac{\mu_o I_f}{2\pi} \ln \left(\frac{r_N}{r_{avg}} \right) = \frac{\mu_o I_f}{2\pi} \ln \left(\frac{2r_N}{r_m + r_N} \right) \quad (6-42)$$

f) Electrical circuit

The equations for the equivalent electrical circuit of Fig 6-4b are

$$C_b \frac{dV_b}{dt} = I_b \quad (6-43)$$

$$R_b I_b + L_b \frac{dI_b}{dt} + \frac{d}{dt} [(L_1 + L_i) I_b] + R_f I_b = V_b \quad (6-44)$$

$$\text{and } R_f(\varepsilon) = R_{fo} f(\varepsilon) \quad (6-45)$$

where ε is the specific energy density deposited in the metallic foil and $f(\varepsilon)$ is the fractional resistance increase as a function of specific energy deposited in the foil as defined in the LU model of chapter 3.

g) Foil burst criterion and burst energy density

The time of foil burst t_{burst} is determined by the burst criterion $\frac{dI_b}{dt} = 0$, when the corresponding energy density deposited in the foil is

$$\varepsilon_{burst} = \varepsilon(t_{burst}) \quad (6-46)$$

The burst energy density used in the Gurney acceleration solution is

$$\varepsilon_G = \varepsilon_{burst} k_{corr} \quad (6-47)$$

where $k_{corr} \leq 1.0$ is the explosive quality factor.

h) Motion of flyer

The equations of motion for the flyer are

$$\frac{dr_m}{dt} = v_m \quad (6-48)$$

$$\text{and} \quad \frac{dv_m}{dt} = \begin{cases} -\frac{2\pi r_m}{M} P_B & \text{if } t < t_{burst} \\ -\frac{2\pi r_m}{M} (P_{ex} + P_B) & \text{if } t \geq t_{burst} \end{cases} \quad (6-49)$$

where P_B is the magnetic pressure, given by

$$P_B = \frac{B_1^2}{2\mu_o} = \frac{1}{2\mu_o} \left(\frac{\mu_o I_b}{2\pi r_N} \right)^2 = \frac{\mu_o}{2} \left(\frac{I_b}{2\pi r_N} \right)^2 \quad (6-50)$$

and P_{ex} is the foil explosion pressure given by equation (6-33).

i) Motion of tamper

The equations of motion for the tamper are

$$\frac{dr_N}{dt} = v_N \quad (6-51)$$

$$\text{and} \quad \frac{dv_N}{dt} = -A \frac{dv_m}{dt} \quad (6-52)$$

j) Kinetic energy

By integrating the velocity profile in equation (6-37), the combined kinetic energy of the foil plasma, tamper and flyer is

$$W_k = \frac{m_f}{12} \left\{ (v_m + v_N)^2 + \frac{2(r_N v_N^2 + r_m v_m^2)}{(r_N + r_m)} \right\} + \frac{1}{2} m_t v_N^2 + \frac{1}{2} m_p v_m^2 \quad (6-53)$$

k) Magnetic energy

Integration of the magnetic field profile in equation (6-38) gives the magnetic energy within the foil as

$$W_B = \left(\frac{\mu_0 I_f}{2\pi} \right) \frac{(r_N - r_m)(3r_N + r_m)}{24r_N^2} I_b^2 \quad (6-54)$$

l) Conservation of energy

The conservation of energy [65] is expressed by

$$\frac{d}{dt} \left[m_f \varepsilon + W_B + W_K - \frac{1}{2} (L_i I_b^2) \right] = R_f I_b^2 + \frac{1}{2} I_b^2 \left(\frac{dL_l}{dt} + \frac{dL_i}{dt} \right) \quad (6-55)$$

while if $W_t = m_f \varepsilon + W_B + W_K$, equation (6-55) becomes

$$\frac{dW_t}{dt} = R_f I_b^2 + \frac{1}{2} I_b^2 \left(\frac{dL_l}{dt} + \frac{dL_i}{dt} \right) + \frac{1}{2} \frac{d}{dt} (L_i I_b^2) \quad (6-56)$$

6.1.6 Numerical Solution

Equations (6-43), (6-44), (6-48), (6-49), (6-51), (6-52) and (6-56) form a set of seven independent ordinary differential equations, with the principal dependent variables being V_b , I_b , r_m , v_m , r_N , v_N and W_t . The solution for the set of non-linear coupled ordinary differential equations describes the behaviour of the electrical circuit as well as the temporal evolution of the exploding foil plasma, the flyer and the tamper. When the solution is combined with the ideal gas law EOS, important foil plasma properties (e.g. mass density, and temperature) and the explosion pressure can be obtained. In the present research, a computer program is implemented in *Matlab*© to provide all the information needed for comparison with experimental data.

6.2 Magnetohydrodynamic Model

The development of the present MHD model, which is an extension of the one-dimensional hydrodynamic code and is used to describe the flow of a conducting fluid or plasma in a magnetic field, involves two main efforts (1) a conversion to curvilinear cylindrical co-ordinate system and (2) the inclusion of Maxwell's equation for the electric and magnetic field.

The conversion to a curvilinear cylindrical co-ordinate system did not pose any major difficulties, with the most difficult task being the inclusion of Maxwell's equation in an appropriate form suitable for computer iterations.

Although numerous MHD models have been reported [114] – [117] for different areas of applications, only a small number are concerned specifically with magnetic flux compression by cylindrical implosion. Kidder [116] and Almström [100] have carried out numerical calculation in one dimension while Tipton [117] has developed a 2-D MHD model for cylindrical implosion. The work of both Kidder and Almström contains detailed descriptions of the scalar one-dimensional MHD equations using the Lagrangian form, with the system of equation described by Almström being simpler than that by Kidder through neglect of the heat conduction term. However, insufficient information on the numerical scheme was given to facilitate computer programming. Recently, Humphries Jr [61] reported a one-dimensional MHD code termed CRUNCH, with a description of the finite difference equations used in the numerical scheme. While the CRUNCH code was designed for a Z-pinch driven imploding metal liner used for generating high-pressure impact on a centrally located target, and not for magnetic flux compression, it nevertheless provided useful insight for solving the difficult problem of combining the hydrodynamic solution with Maxwell's equations. To some extent, the present MHD model contains different ideas and techniques that result from a detailed study of the published works of previous researchers.

6.2.1 MHD Equations

The equations for the conservation of mass, momentum and energy are [118]

$$\frac{\partial \rho}{\partial t} + \nabla \cdot (\rho \vec{v}) = 0 \quad (6-57)$$

$$\rho \left(\frac{\partial \vec{v}}{\partial t} + (\vec{v} \cdot \nabla) \vec{v} \right) = -\nabla P + (\vec{J} \times \vec{B}) \quad (6-58)$$

$$\text{and} \quad \rho \frac{\partial}{\partial t} \left(\varepsilon + \frac{v^2}{2} \right) + \rho (\vec{v} \cdot \nabla) \left(\varepsilon + \frac{v^2}{2} \right) = -\nabla \cdot (\vec{v} P) + \vec{J} \cdot \vec{E} \quad (6-59)$$

which describe the continuum-mechanical model for a material subjected to shockwave.

Maxwell's equations for the simplified single-fluid form of Ohm's law are [116]

$$\nabla \cdot \vec{B} = 0 \quad (6-60)$$

$$\nabla \cdot \vec{D} = \rho_{el} \quad (6-61)$$

$$\nabla \times \vec{E} = -\frac{\partial \vec{B}}{\partial t} \quad (6-62)$$

$$\nabla \times \vec{H} = \vec{J} + \frac{\partial \vec{D}}{\partial t} \approx \vec{J}, \quad \frac{\partial \vec{D}}{\partial t} = 0 \quad (6-63)$$

$$\text{and} \quad \vec{J} = \sigma (\vec{E} + \vec{v} \times \vec{B}) \quad (6-64)$$

For shockwave calculation, viscous and body forces (such as gravitation) are neglected in comparison to the pressure gradient and the magnetic pressure term in the momentum equation. Furthermore, the thermal conductivity term in the energy equation is ignored, because the magnetic flux compression process is sufficiently rapid for there to be time for significant heat conduction to take place, and the displacement current term because the shockwave velocity is many orders of magnitude smaller than the speed of light. The model is considered quasi-static from the electrodynamic point of view and effects of electromagnetic radiation are not considered.

Introducing the total time derivative $\frac{d}{dt} = \frac{\partial}{\partial t} + \vec{v} \cdot \nabla$ and the electric field $\vec{E}^* = \vec{E} + \vec{v} \times \vec{B}$ in the frame of reference moving with the shockwave, the system of equations takes the form

$$\frac{d\rho}{dt} + \rho \nabla \cdot \vec{v} = 0 \quad (6-65)$$

$$\rho \frac{d\vec{v}}{dt} = -\nabla P + (\vec{J} \times \vec{B}) \quad (6-66)$$

$$\rho \frac{d}{dt} \left(\varepsilon + \frac{v^2}{2} \right) = -\nabla \cdot (\vec{v} P) + \vec{J} \cdot \vec{E}^* \quad (6-67)$$

$$\frac{d\vec{B}}{dt} = -\nabla \times \vec{E}^* + \nabla \times (\vec{v} \times \vec{B}) + (\vec{v} \cdot \nabla) \vec{B} \quad (6-68)$$

$$\vec{J} = \frac{1}{\mu_0} \nabla \times \vec{B} \quad (6-69)$$

$$\text{and} \quad \vec{E}^* = \frac{\vec{J}}{\sigma} \quad (6-70)$$

which provides one of many possibilities of combining the hydrodynamic and Maxwell equations. The model is simplified by assuming cylindrical symmetry, with all variables depending only on the radial co-ordinate and time. The magnetic field is assumed to be directed along the cylindrical axis, with the electric field and current density having only azimuthal component. The particle velocity is in the radial direction.

For one-dimensional cylindrical symmetry

$$\begin{aligned} \vec{B} &= B_z(r) \vec{z}, & \rho &= \rho(r) \\ \vec{E}^* &= E_\theta(r) \vec{\theta}, & P &= P(r) \\ \vec{J} &= J_\theta(r) \vec{\theta}, & \varepsilon &= \varepsilon(r) \\ \vec{v} &= v(r) \vec{r} \quad \text{and} \quad \sigma &= \sigma(r) \end{aligned} \quad (6-71)$$

which gives the scalar system of equations

$$\frac{d\rho}{dt} = -\frac{\rho}{r} \frac{\partial}{\partial r}(rv) \quad (6-72)$$

$$\rho \frac{dv}{dt} = -\frac{\partial P}{\partial r} + J_\theta B_z \quad (6-73)$$

$$\rho \frac{d}{dt} \left(\varepsilon + \frac{v^2}{2} \right) = -\frac{1}{r} \frac{\partial}{\partial r}(rvP) + J_\theta E_\theta^* + J_\theta v B_z \quad (6-74)$$

$$\frac{dB_z}{dt} = -\frac{1}{r} \frac{\partial}{\partial r}(rE_\theta^*) - \frac{B_z}{r} \frac{\partial}{\partial r}(rv) \quad (6-75)$$

$$J_\theta = \sigma E_\theta^* = -\frac{1}{\mu} \frac{\partial B_z}{\partial r} \quad (6-76)$$

and $E_\theta^* = E_\theta - B_z v \quad (6-77)$

In equation (6-70), E_θ^* is the electric field measured in the moving frame of reference and E_θ is the electric field in Eulerian form. Further simplification is possible by eliminating E_θ^* from the magnetic field equation and using the Lagrangian mass co-ordinates

$$s = \int_0^r \rho(r') r' dr' \quad \text{i.e.} \quad \frac{\partial s}{\partial r} = \rho r \quad (6-78)$$

$$V = \frac{1}{\rho} = r \frac{\partial r}{\partial s} = \frac{\partial}{\partial s} \left(\frac{r^2}{2} \right) \quad (6-79)$$

The final simplified system of scalar differential equations becomes

$$\frac{dr}{dt} = v \quad (6-80)$$

$$\frac{d}{dt} \left(\frac{1}{\rho} \right) = \frac{\partial}{\partial s}(rv) \quad (6-81)$$

$$\frac{dv}{dt} = -r \frac{\partial}{\partial s} \left(P + \frac{B_z^2}{2\mu_0} \right) \quad (6-82)$$

$$\frac{d\varepsilon}{dt} = -P \frac{\partial}{\partial s}(rv) + \frac{J_\theta E_\theta^*}{\rho} \quad (6-83)$$

$$\frac{dB_z}{dt} = \frac{1}{\mu_o} \frac{1}{r} \frac{\partial}{\partial r} \left(r \frac{\partial B_z}{\partial r} \right) - \frac{B_z}{r} \frac{\partial}{\partial r}(rv) \quad (6-84)$$

$$J_\theta = \sigma E_\theta^* = -\frac{1}{\mu} \frac{\partial B_z}{\partial r} \quad (6-85)$$

$$\text{and } E_\theta^* = E_\theta - B_z v \quad (6-86)$$

Equation (6-84) is the generalized diffusion equation for magnetic fields, in which the first term is the diffusion term and the second represent the field increase due to magnetic flux compression (i.e. it is a generation term). The equation can alternatively be written as [100]

$$\frac{d}{dt} \left(\frac{B_z}{\rho} \right) = -\frac{\partial}{\partial s} (r E_\theta^*) \quad (6-87)$$

6.2.2 Computational Domain

In Fig 6-5, the mesh points r_j^{n+1} are the boundaries between elements and the particle velocities v_j^{n+1} are defined at the cell-boundaries. The index j denotes the spatial position of the elements. Integer superscripts n and $n+1$ mean element properties at integer multiples of the time step, e.g. $v_j^n \equiv v_j(n\Delta t)$, $v_j^{n+1} \equiv v_j((n+1)\Delta t)$. For time-centering, the average values (over time) of the cell boundaries and particle velocities are denoted by superscript $n+0.5$, e.g. $r_j^{n+0.5} = 0.5(r_j^n + r_j^{n+1})$ and $v_j^{n+0.5} = 0.5(v_j^n + v_j^{n+1})$

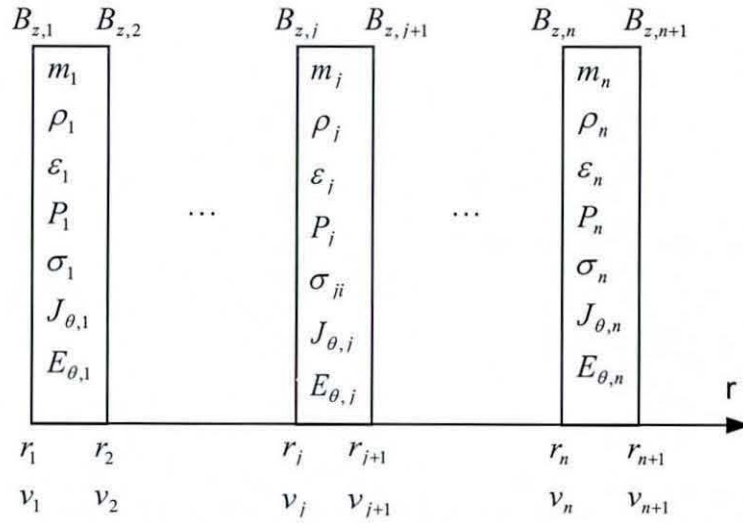


Figure 6-5 Computational Domain.

The cell boundaries divide the material into elements of equal mass. Using the definition of the Lagrangian co-ordinate for one-dimensional symmetry, the total mass per unit length is

$$S_o = \rho_o \int_{R_i}^{R_o} r dr = \rho_o \frac{R_o^2}{2} \quad (6-88)$$

where R_i and R_o are the inner and outer radii (i.e. the limits) of the computational region. The computational grid is divided into n elements of $ds = \frac{S_o}{n} = \rho_o \frac{R_o^2}{2n}$ mass per unit length. From the definition of the Lagrangian mass co-ordinate, we have

$$m_j \equiv \partial s = \rho_o \frac{(r_{j+1}^0 - r_j^0)}{2} \quad (6-89)$$

enabling the initial cell boundaries to be computed using a recursive algorithm starting at the inner radius

$$r_1 = R_i \quad (6-90)$$

$$ds = \rho_o \frac{r_2^2 - r_1^2}{2} = \rho_o \frac{R_o^2}{2n} \quad r_2 = \sqrt{\frac{R_o^2}{n} + R_1^2} \quad (6-91)$$

$$r_{j+1} = \sqrt{\frac{R_o^2}{n} + r_j^2}, \quad j = 3 \cdots (n+1) \quad (6-92)$$

6.2.3 Finite Difference Scheme

The finite difference scheme for solving the set of scalar MHD equations is similar to that described in chapter 4 for the hydrodynamic model. The location and the velocity of the conducting shock front provide essential links that couple the hydrodynamic calculation with the Maxwell's equations.

The hydrodynamic and the magnetic solutions are advanced in synchronism. The magnetic solution couples to the hydrodynamic solution, partly through the contribution of resistive heating to changes in the internal energy. In addition, magnetic forces contribute to velocity changes at the element boundaries. In turn, the hydrodynamic solution influences the magnetic diffusion through changes in the element sizes and variations in electrical conductivity with mass density.

6.2.4 Finite Difference Equations

The finite difference equations are listed below in the order of their computation.

a) Momentum equation

Firstly, the velocity is updated by determining the acceleration at each mesh point from the sum of the average pressure forces at the weighted average positions of the surrounding elements and the total enclosed mass. Δs is replaced by the average value of the two adjacent mass elements $0.5(m_j + m_{j-1})$

$$\frac{v_j^{n+1} - v_j^n}{\Delta t} = -r_j^{n+0.5} \frac{1}{\Delta s} \left[\left(P_j^{n+0.5} + \frac{(B_{z,j}^{n+0.5})^2}{2\mu_o} \right) - \left(P_{j-1}^{n+0.5} + \frac{(B_{z,j-1}^{n+0.5})^2}{2\mu_o} \right) \right]$$

$$v_j^{n+1} = v_j^n - r_j^{n+0.5} \frac{\Delta t}{0.5(m_j + m_{j-1})} \left[(P_j^{n+0.5} - P_{j-1}^{n+0.5}) + \left(\frac{B_{z,j}^n B_{z,j}^{n+1}}{2\mu_o} - \frac{B_{z,j-1}^n B_{z,j-1}^{n+1}}{2\mu_o} \right) \right] \quad (6-93)$$

$$v_j^{n+0.5} = 0.5(v_j^n + v_j^{n+1}) \quad (6-94)$$

Boundary conditions v_1^{n+1} and v_{N+1}^{n+1} are considered in the solution of the equation of motion. The new velocity values are used for a time-centred update of the element boundaries

$$\frac{r_j^{n+1} - r_j^n}{\Delta t} = v_j^{n+0.5}$$

$$\text{or} \quad r_j^{n+1} = r_j^n + v_j^{n+0.5} \Delta t \quad (6-95)$$

$$r_j^{n+0.5} = 0.5(r_j^n + r_j^{n+1}) \quad (6-96)$$

b) Continuity (or conservation of mass) equation

The mass within a cell is invariant, but its volume may change with time due to expansion or compression of the material

$$V_j^{n+1} = \frac{(r_{j+1}^{n+1})^2 - (r_j^{n+1})^2}{2m_j} \quad (6-97)$$

$$\rho_j^{n+1} = \frac{1}{V_j^{n+1}} \quad (6-98)$$

c) Electrical conductivity

The density-dependent electrical conductivity model that describes the insulator-to-conductor transition of shock-loaded metallic powder is used to provide new values of electrical conductivity for each element. Thus

$$\sigma_j^{n+1} = \sigma(\rho_j^{n+1}) \quad (6-99)$$

d) Conducting shock front

The location and velocity of the conducting shock front is updated using new values of electrical conductivity.

e) Magnetic field equation

The magnetic field equation (6-84) is decomposed into (1) a generation equation and (2) a diffusion equation. The location of the conducting shock front in the shock-compressed powder separates the computational domain into two regions of calculation. Ahead of the shock front, and in the unshocked, insulating aluminium powder, the generation equation is solved to obtain the new, compressed value of magnetic flux density. Behind the conducting shock front, the magnetic diffusion equation is solved by the Crank Nicholson method [67] with the resulting tri-diagonal matrix system solved by an efficient iterative algorithm known as the Thomas method [67].

f) Azimuthal electric field and current density

The azimuthal electric field and current density are calculated from the derivative of the axial magnetic field. Thus

$$j_{\theta,j}^{n+1} = -\frac{1}{\mu} \frac{r_j^{n+1}}{V_j^{n+1}} \frac{(B_{z,j}^{n+1} - B_{z,j-1}^{n+1})}{0.5(m_j + m_{j-1})} \quad (6-100)$$

$$E_{\theta,j}^{*,n+1} = \frac{j_{\theta,j}^{n+1}}{\sigma_j^{n+1}} \quad (6-101)$$

g) Energy equation

The change in internal energy is determined from the work performed by the pressure and the resistive heating due to the current density, or

$$\varepsilon_j^{n+1} = \varepsilon_j^n + \Delta t \left(W_j - P_j^{n+0.5} \frac{r_{j+1}^{n+0.5} v_{j+1}^{n+0.5} - r_j^{n+0.5} v_j^{n+0.5}}{m_j} \right) \quad (6-102)$$

where $W_j = V_j^{n+1} \frac{(J_{\theta,j}^{n+1} + J_{\theta,j}^n)}{2} \frac{(E_{\theta,j}^{*,n+1} + E_{\theta,j}^{*,n})}{2}$ is an intermediate quantity representing Joule heating.

h) Equation of state

The internal energy and mass density give new values for the pressure through the EOS

$$P_j^{n+1} = P(\rho_j^{n+1}, \varepsilon_j^{n+1}) \quad (6-103)$$

i) Artificial viscosity

The new velocity flow field is inspected for calculation of the artificial viscosity

$$\text{if } v_j^{n+1} \leq v_{j+1}^{n+1}, \quad Q_j^{n+1} = 0 \quad (6-104)$$

$$\text{if } v_j^{n+1} > v_{j+1}^{n+1}$$

then in quadratic form

$$Q_j^{n+1} = \frac{c_1^2}{V_j^{n+1}} |v_{j+1}^{n+1} + v_j^{n+1}| (v_{j+1}^{n+1} - v_j^{n+1}) \quad (6-105)$$

or in linear form

$$Q_j^{n+1} = \frac{c_2}{V_j^{n+1}} c_s (v_{j+1}^{n+1} - v_j^{n+1}) \quad (6-106)$$

where c_1 and c_2 are constants and c_s is the local speed of sound.

j) Hydrodynamic pressure

A modified two-step method is used to update the pressure field, which will be used in the solution of the equation of motion in the next iteration

$$P_j^{n+0.5} = 0.5(P_j^n + Q_j^n + P_j^{n+1} + Q_j^{n+1}) \quad (6-107)$$

6.2.5 Alfven Velocity and Stability Criteria

At the end of each computing loop, the time step dt to be used in the next iteration is obtained by considering the stability criteria for both the flow calculation and the algorithm used in calculating the diffusion of magnetic flux through the conducting shock front. Choosing a time step that is the smaller of the two values so obtained ensures numerical stability.

$$dt = \min(\tau_{diff}, \tau_{hd}) \quad (6-108)$$

where

$$\tau_{diff} \leq \frac{1}{2} \mu \sigma [\min(\Delta r_j^{n+1})]^2 \quad (6-109)$$

$$\text{and } \Delta r_j^{n+1} = r_{j+1}^{n+1} - r_j^{n+1} \quad (6-110)$$

is the stability criterion for the Crank-Nicholson algorithm used in calculating the diffusion of magnetic flux through the conducting shock front and τ_{hd} is the stability criterion for the flow calculation.

The presence of a magnetic field in the flow calculation introduces an intrinsic velocity termed the Alfven velocity [75], which is the velocity at which the kinetic energy density of the fluid is equal to the magnetic energy density

$$\frac{1}{2} \rho v_A^2 = \frac{B_z^2}{2\mu_o} \quad \text{or} \quad v_A = \frac{B_z}{\sqrt{\mu_o \rho}} \quad (6-111)$$

The speed of sound c_s in the Courant-Friedrichs-Levy (CFL) stability condition [72] is replaced by an effective speed c_A , defined as the geometric mean of the Alfven velocity v_A and the speed of sound c_s or

$$c_A = \sqrt{c_s^2 + v_A^2} = \sqrt{c_s^2 + \frac{B_z^2}{\mu_0 \rho}} \quad (6-112)$$

to give the stability criterion for the flow calculation as

$$\tau_{hd} \leq \frac{\min(\Delta r_j^{n+1})}{\max(|c_{Aj}|)} \quad (6-113)$$

6.3 Numerical Analysis of Nagayama Experiment

In this section, the MHD model is applied to the analysis of the explosive driven flux compression experiment using porous metal powder [29]. It is used (1) to verify the computer code that has been implemented using *Matlab*© and (2) to obtain a better understanding of the physical processes in shockwave magnetic flux compression using metal powder.

6.3.1 Experimental Conditions

In the experimental arrangement used by Nagayama (see Fig 6-6), a solenoid at the outer-most part of the assembly is used to produce the initial magnetic field. Ring-shaped layers of plastic explosive are placed inside a 3.0 mm thick PMMA (Polymethylmethacrylate) pipe, with a magnetic probe located at the centre of the assembly holding the metal powder. The outer diameter of the powder is 46 mm (radius = 23 mm), but that of the magnetic probe was not reported. However, for numerical purposes, it will be assumed as 2.3 mm, giving a convenient theoretical compression ratio of 100.

To verify the previous analysis, modelling was performed for experiment number 1 reported in [29], where aluminum powder with an initial density of 0.41 g/cm^3 and a maximum particle diameter of $46 \mu\text{m}$ was used to compress an initial magnetic field

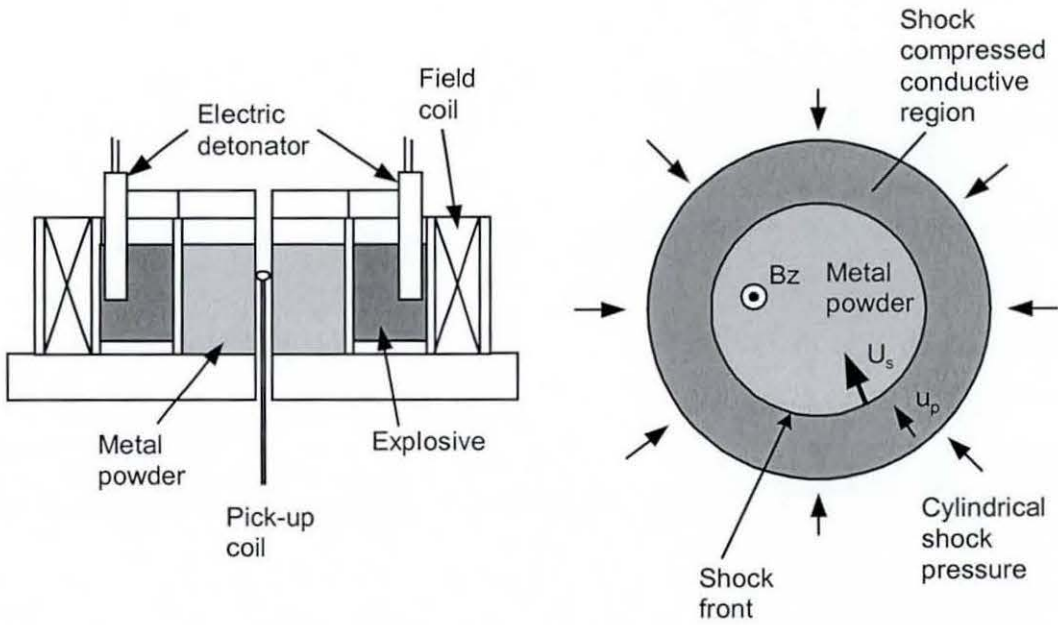


Figure 6-6 Explosively driven shockwave magnetic flux compression [29].

6.3.2 Considerations for Numerical Simulations

The plastic explosive SEP used by Nagayama is not well known outside Japan. However, based on the mean shock speed of 2.62 km/s inside the loose aluminium powder, it appears to be less energetic than TNT or composition B, which have detonation speeds of between 6 km/s to 8 km/s . From Fig 1 in [29] it can be observed that the thickness of the explosive is comparable to the outer radius of the powder container. It is therefore reasonable to assume that the pressure exerted by the 20 mm thick explosive would have a duration considerably larger than the implosion time of about $7.9 \mu\text{s}$. For numerical simulation, the explosive is represented as a constant pressure applied to the external boundary of the aluminium powder (Fig 6-7). The magnitude of this explosive pressure becomes a free parameter in the calculation and it is chosen heuristically to reproduce the implosion time of $7.9 \mu\text{s}$.

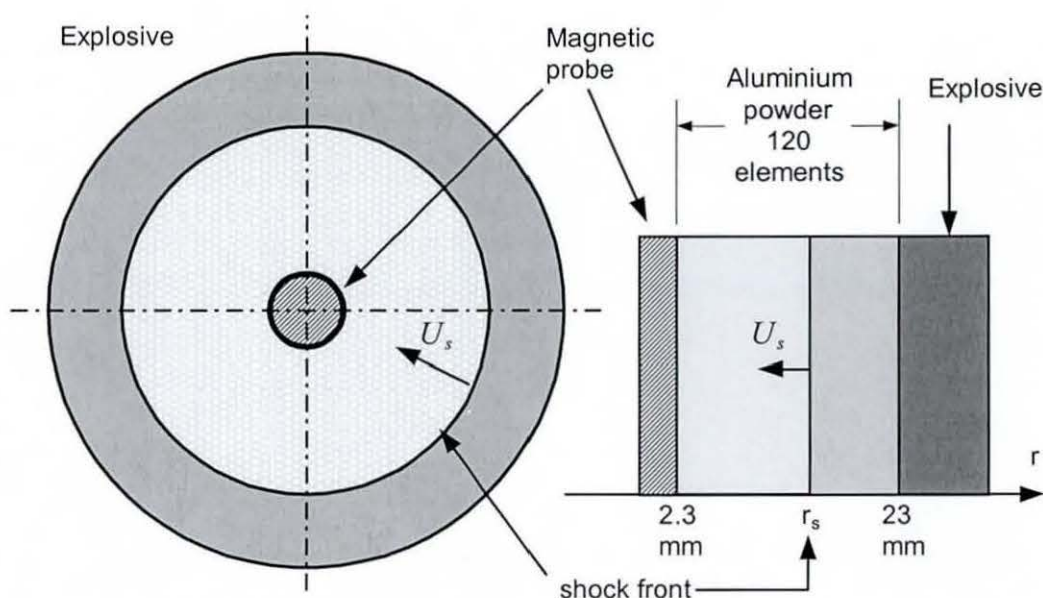


Figure 6-7 Computational grid for Nagayama's experiment.

The powder material was represented by 120 computing elements, with an initial grid spacing ranging from $100\ \mu\text{m}$ at the outer boundary (near the explosive) to $800\ \mu\text{m}$ at the inner boundary (near the magnetic probe). On a PC computer the computation time required for each iteration is about 0.1 s, which is estimated from the total computing time of about 30 minutes to complete a calculation with 30,000 time steps. The time step between iteration is usually less than 0.1 ns.

6.3.3 Numerical Results

The results of a calculation for a constant explosive pressure of 3.4 GPa are shown in Fig 6-8 to 6-13. The value of 3.4 GPa used for representing the explosive pressure is consistent with the low average shock speed of 2.62 km/s, because high explosives such as TNT or composition B are known [55] to generate pressures in the range of 15 GPa to 25 GPa.

Fig 6-8 shows the distortion of the Lagrangian computational grid for the aluminium powder, with the compression of the aluminium powder by the constant shock pressure of the explosive being clearly visible. The shock front arrives at the magnetic probe at a time of $8.2\ \mu\text{s}$, followed by the compressed and conducting region that moves with a

lower particle velocity. In Fig 6-9, the trajectory of the conducting shock front is shown in relation to the experimental configuration. The shock velocity in Fig 6-10 has an initial delay of $0.3 \mu s$, corresponding to the time needed to compress the powder to near-solid density, to give the flux compression time of $7.9 \mu s$ reported by Nagayama. Initially the imploding shock velocity is almost constant, but as it moves nearer to the axis, the shock velocity begins to increase at a growing rate because of (1) the focussing effect of a converging cylindrical shockwave and (2) the snow-plow effect caused by an elastic precursor (see section 5.3.5.3). At the origin (or axis), the shock pressure will theoretically increase to infinity. In the calculation, the shockwave collides with the magnetic probe at a radius of 2.3 mm , so that the shock speed reaches a finite maximum at about 4 km/s .

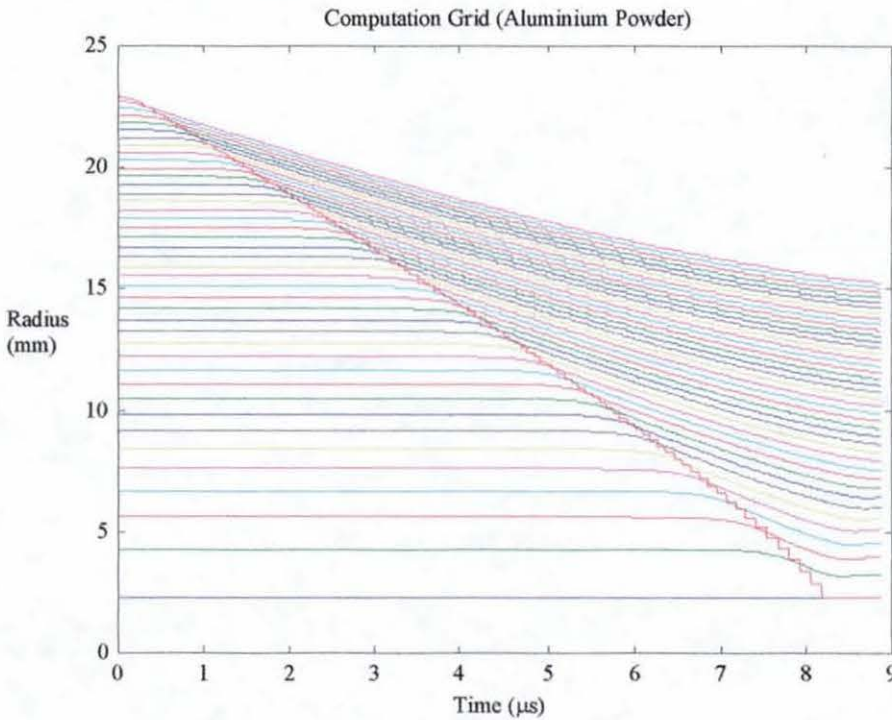


Figure 6-8 Computation grid for the aluminium powder.
The conducting shock is shown in red.

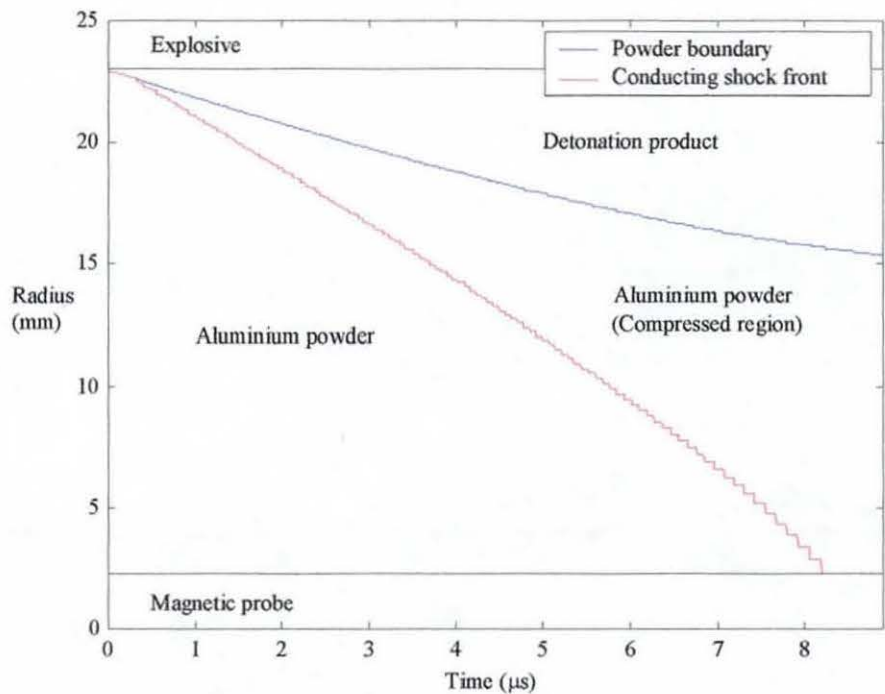


Figure 6-9 Conducting shock front from computer model.

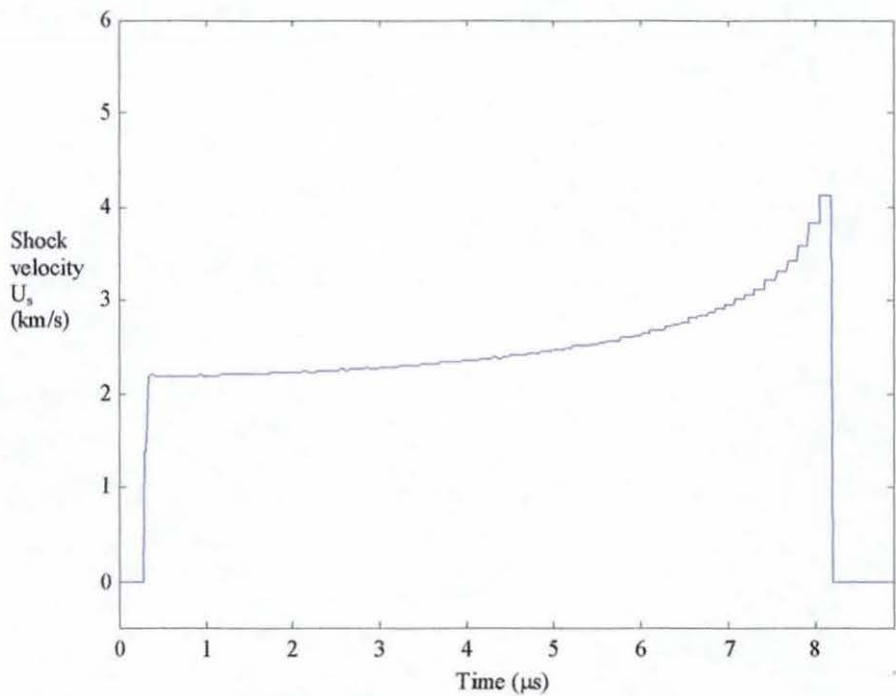


Figure 6-10 Variation of shock velocity with time.

Fig 6-11 shows the solutions for the electric and magnetic fields, with the simple switch model for the electrical conductivity of the shock-compressed aluminium powder being used in the calculation. It is assumed that the shock-compressed powder will attain a fraction k of the electrical conductivity of aluminium at solid density and STP. The factor k is a free parameter that was chosen as 140 (Fig 6-13a) to reproduce the compressed magnetic flux density of 1 MG (100 T) obtained by Nagayama. It is probably over simplistic to assume that the electrical conductivity remains constant over the duration of the flux compression process, but this analysis nevertheless improves the understanding of the powder compaction and flux compression processes. It is interesting to note that the electrical conductivity of the converging liner (in this case shock-compressed powder) remains the dominant flux loss mechanism.

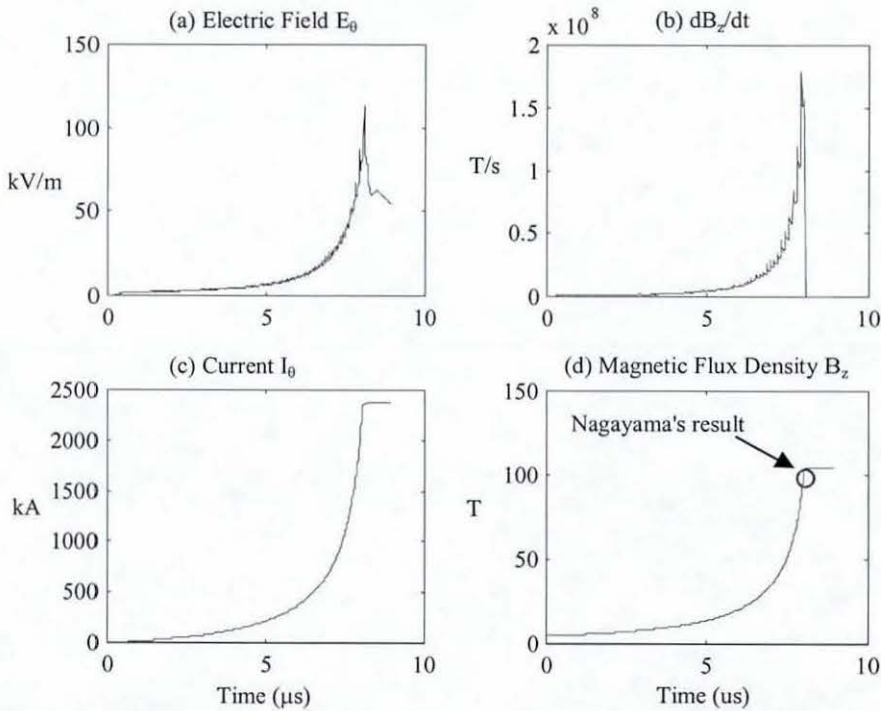


Figure 6-11 Computer results (a) azimuthal electric field E_θ , (b) dB_z/dt , (c) azimuthal current I_θ and (d) compressed magnetic flux density B_z .

The compression of the magnetic flux density with time is shown in Fig 6-12, with $0.5 \mu s$ as the interval between plots. The magnetic flux density of $4.9 T$ is initially constant throughout the powder and it is compressed by the shockwave to $100 T$, with a significant diffusion loss being shown by the presence of magnetic flux behind the shock front.

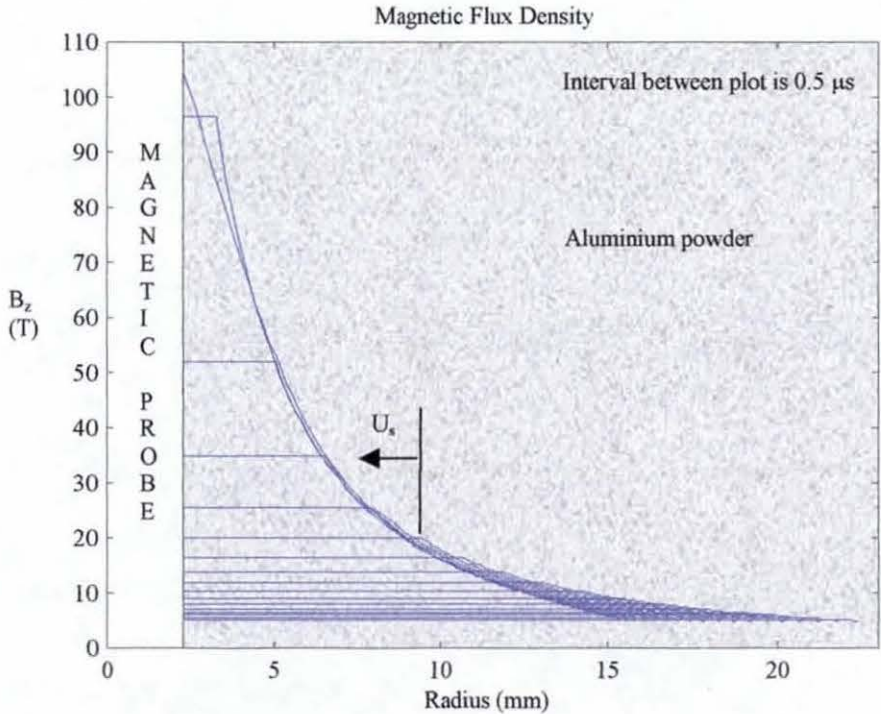


Figure 6-12 Magnetic flux density B_z .

The time variation of the magnetic Reynolds number shown in Fig 6-13 reveals an important characteristic of flux compression using metallic powder. If the electrical conductivity of the compressed powder remains constant, the increase in the powder thickness and the increase in the shock velocity (due to the focussing effect of converging cylindrical shockwave) both imply that the flux compression process should improve rather than deteriorate with time. This is distinctly different from many physical processes that tend to deteriorate with time due to various instabilities.

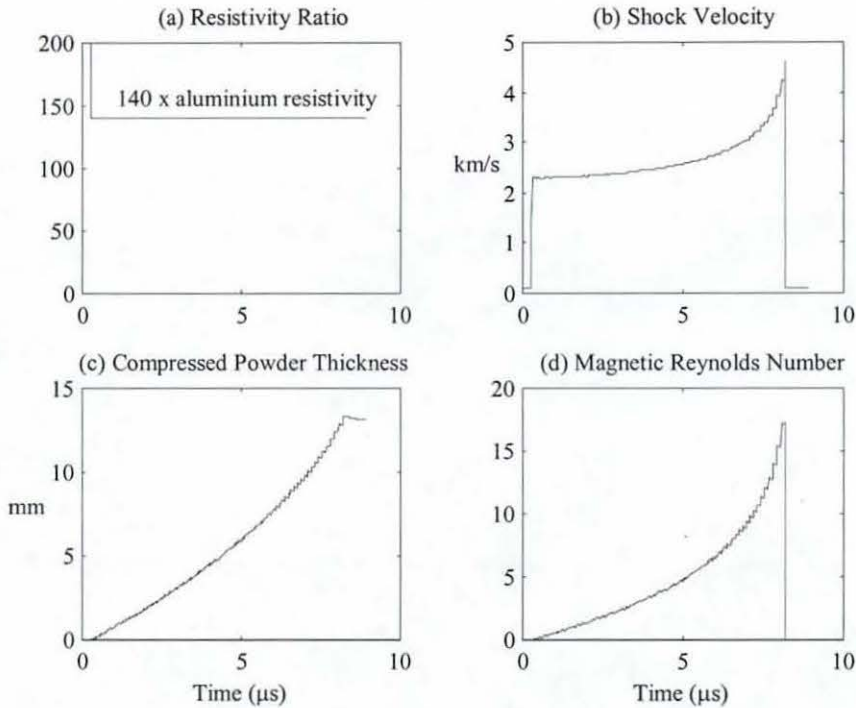


Figure 6-13 Computer results (a) resistivity profile, (b) shock velocity, (c) powder thickness and (d) magnetic Reynolds number.

It is clear from the present analysis that the explosive driven shockwave generation method is much simpler than that of the exploding foil driven technique described in chapter 5. Detailed hydrodynamic calculation is only required for the powder material, while the explosion product is represented fairly accurately by a constant or quasi-static shock pressure at the powder boundary. The simplicity in the physical processes usually leads to a more reliable technique, which could be another advantage of the explosive driven shockwave generation method, to add to the longer pressure pulse duration.

6.3.4 Initial Powder Density and Magnetic Flux Compression

It was reported by Nagayama et al [29] that (1) the resulting magnetic flux compression was highly sensitive to the initial powder density and (2) a lower initial powder density gave better results.

The relationship between initial powder density and flux compression efficiency can be understood by combining equation (2-30) for shockwave flux compression with equation (4-78) for the EOS of powder material to give

$$\frac{dB}{dt} = \frac{2}{r_s} (1 - TD) U_s B \quad (6-114)$$

which implies that, the lower the TD (i.e. the higher the porosity) the better the flux compression efficiency. This equation is of course not valid at the extremes of 0% TD and 100% TD, since it is known [9], [10], [22], [23], [119] that a solid metal liner has been successfully used in magnetic flux compression by cylindrical implosion. At the limit of 0% TD, which implies the absence of any conducting liner, it is clear that flux compression cannot take place with perfect conductivity in air (or vacuum) without any losses. The lowest practical powder density appears to be 15% TD, as reported by Nagayama [29].

Since equations (4-78) and (4-79) for the EOS of powder material are valid only for high-porosity material with $\alpha \geq 2$ (or $TD \leq 50\%$), it is reasonable to assume that equation (6-114) is valid for initial powder density in the range of 15% TD to 50% TD.

6.4 Conclusion

In this chapter, the mathematical model for the planar electric gun has been extended to the cylindrical implosion configuration. The $P - \alpha$ model (for the EOS of aluminium powder) and the simple switch model (for the electrical conductivity of shock-compressed powder) have been shown to be suitable for use in a MHD model to analyse Nagayama's explosive driven flux compression experiment. The results obtained from the computer model have helped to identify the key characteristics of the explosive pressure necessary for successful powder compaction and flux compression to megagauss level, with the dominant flux loss mechanism being undoubtedly the electrical conductivity of the shock-compressed powder.

MAGNETIC FLUX COMPRESSION BY A CONVERGING SHOCKWAVE

This chapter describes the detailed design of the major components of the cylindrical imploder and the experimental programme for shockwave flux compression using aluminium powder. The TOA data thereby obtained is analysed, using the new electric gun model of chapter 3 to provide useful insight into the implosion process. To understand this process, the rate-of-change of magnetic flux density ($B\text{-dot}$) is analysed using (1) a simple model for flux compression and (2) the MHD model of chapter 6. Although the quality of the foil explosion was not ideal, the large stand-off between the exploding foil and the powder assembly nevertheless allowed the flyer to be accelerated to an impact velocity of between 1.1 km/s and 1.5 km/s , thus enabling magnetic flux densities of about $40T$ to be obtained from an initial flux density of $6T$.

7.1 Cylindrical Imploder

The cylindrical imploder used here has the cylindrical electric gun configuration of Fig 7-1, consisting of (1) a parallel-plate transmission line (2) a cylindrical current conductor (3) a high-voltage insulator and (4) an exploding foil/flyer package. Two end-plugs are used (1) to secure the magnetic field probe and the powder assembly (2) to form the barrel for guiding the Mylar flyer on its flight towards the powder assembly and (3) to provide the necessary stand-off between the powder assembly and the exploding foil/flyer package. For the present experimental programme, the main capacitor bank powers the gun to explode and accelerate the Mylar flyer, while the auxiliary capacitor bank powers the field coil, to establish an initial magnetic field which is compressed by the shockwave in the powder and measured by a centrally located magnetic field probe.

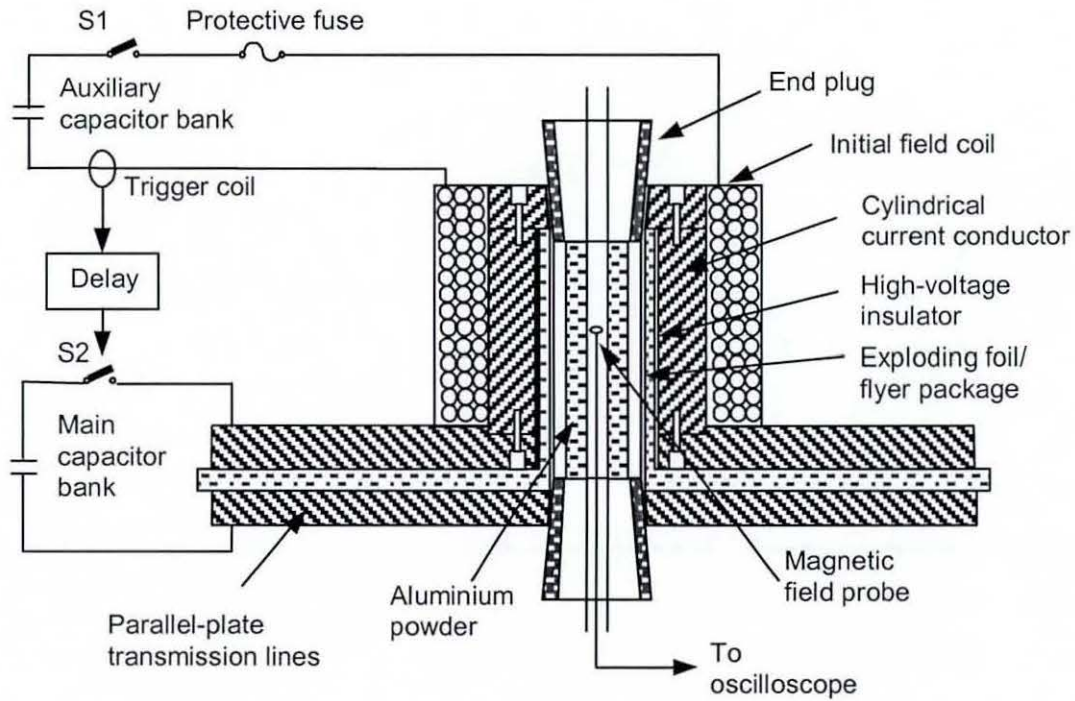


Figure 7-1 Schematic of the cylindrical imploder (electric gun).

7.1.1 Design Considerations

The design of the cylindrical imploder for magnetic flux compression is guided by three main considerations (1) a high initial magnetic field, determined by the stored energy of the auxiliary capacitor bank (2) a high flux compression ratio, determined by the ratio of the initial to the final radius of the imploding liner and (3) a high flux conservation coefficient, determined primarily by magnetic flux diffusion through the liner during implosion. The stability of the implosion process is also important for achieving repeatable performance.

In the case of a metallic liner, the initial radius is usually chosen to be ten times the final compressed radius [29], which depends on the overall radius of the magnetic field probe. If the smallest epoxy-cast probe has an overall diameter of about 4 mm (2 mm radius), the initial liner radius would have to be at least 20 mm to achieve a flux compression ratio of 100.

In the case of shockwave flux compression in aluminium powder, the flux compression ratio is determined by the ratio of the outer to the inner radii of the powder assembly. In turn, the outer diameter of the assembly depends on the radius of the cylindrical exploding foil and the stand-off distance needed for the Mylar flyer to reach terminal velocity. The inner diameter of the powder assembly (or indirectly the thickness of the powder sample) depends however on the attenuation of the shock pressure (and with it the shock velocity) in the powder. Although detailed information on the shock propagation in powder was not available at the beginning of the experimental programme, it was assumed, based on a TOA measurement with a coaxial contact probe situated 10 mm into the powder (see chapter 5), that the conducting shock front is able to penetrate at least 5 mm into the powder. Thus for the experimental programme, the thickness of the powder sample was between 2 mm and 6 mm.

7.1.2 Main Capacitor Bank

The main capacitor bank used for powering the cylindrical imploder (or electric gun) is an existing pulsed current source that comprises nine low-inductance high-voltage capacitors that can be charged to a maximum of 30 kV. The capacitor bank is usually charged to 25 kV (with a stored energy of about 80 kJ) and operated by a solid dielectric switch with a 60 kV trigger pulse supplied by a Blumlein system. An inductive (I-dot) probe is used to measure the rate-of-change of current in the electric gun.

The bank has a total capacitance C_b of 248 μF , and the inductance L_b and resistance R_b of the parallel-plate transmission line were determined by a short-circuit test as 40 nH and 3.5 m Ω respectively.

7.1.3 Aluminium Exploding Foil

A parametric study using the system of equations for the cylindrical electric gun (chapter 6) was carried out to determine the dimension of the exploding foil. An insulator thickness of 3 mm was assumed, and the foil diameter was varied between 22 mm and 80 mm . The height (or length) of the exploding aluminium foil was varied between 60 mm and 80 mm . Figs 7-2 and 7-3 show the predicted discharge current and foil voltage for a calculation using a 60 mm foil height. The time of foil burst obtained by the model ranges from $1.27\text{ }\mu\text{s}$ for a 22 mm diameter foil to $3.08\text{ }\mu\text{s}$ for one of 80 mm diameter (Fig 7-2). The final foil diameter selected for the cylindrical electric gun was 22 mm diameter, giving a foil burst time of as close to $1.0\text{ }\mu\text{s}$ as could be achieved. The current at burst is close to 600 kA (Fig 7-2) and the foil voltage is theoretically close to 100 kV peak (Fig 7-3).

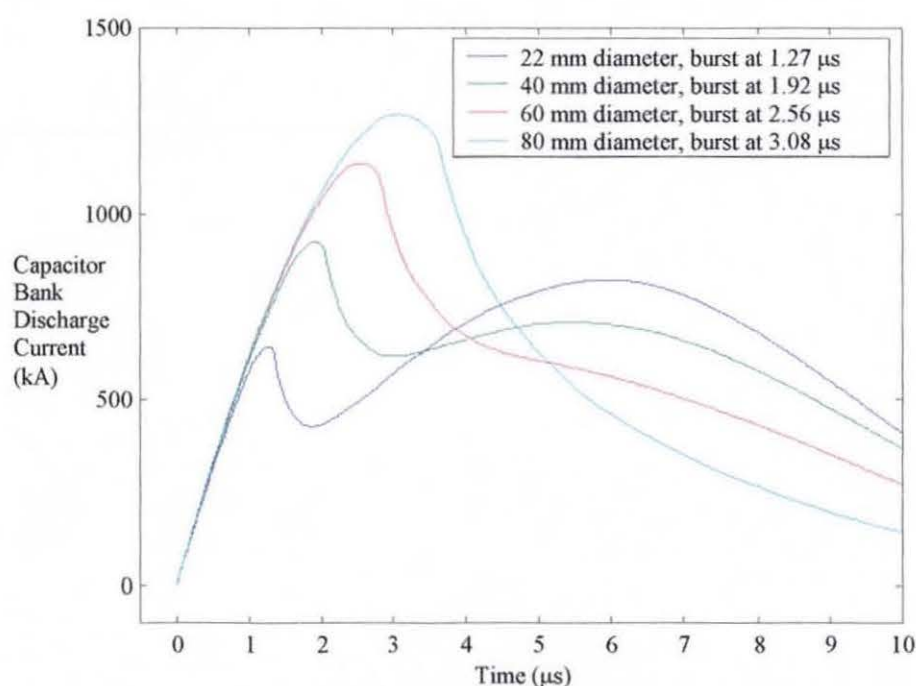


Figure 7-2 Foil burst time for 60 mm (height) \times $25.4\text{ }\mu\text{m}$ aluminium foil.

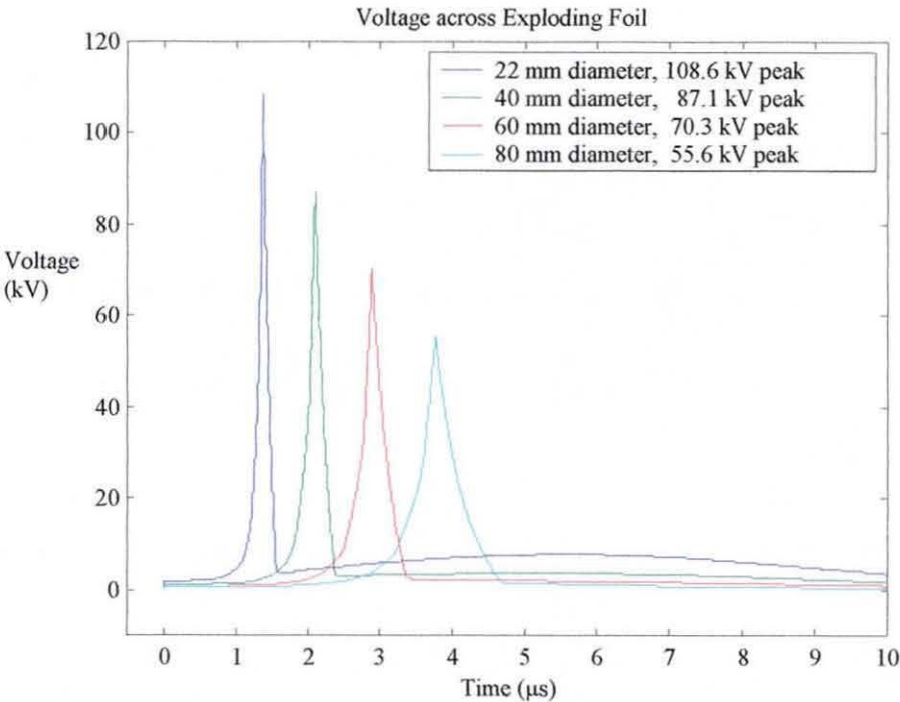


Figure 7-3 Peak fuse voltage for 60 mm (height) x 25.4 μm aluminium foil.

7.1.4 High-Voltage Insulator

The high-voltage insulator adjacent to the cylindrical exploding foil provides the necessary insulation to guide the current flow through the cylindrical imploder. The main design considerations were (1) the dielectric breakdown strength and (2) the foil inductance. Two types of insulator material were considered in the design of the cylindrical imploder and their material properties are given in Table 7-1.

Table 7-1 Characteristics of plastic insulators

	Polyvinylchloride (PVC)	Polyethylene (PE)
Specific gravity	1.46	0.93
Dielectric Strength (<i>kV/mm</i>)	20 to 50	20
Thermal Conductivity (<i>W / K · m</i>)	0.14	0.42
Melt Point (<i>°C</i>)	-	130

Initially, the insulator was made from two pieces of PVC material, with a hollow cylindrical PVC piece glued to a flat PVC plate using a PVC adhesive. This design was however soon rejected because (1) the PVC was found to be brittle, and easily broken into numerous pieces by the shockwave from the exploding foil and (2) the joint at the base of the cylindrical piece and the PVC adhesive was susceptible to high-voltage breakdown. The PVC material was replaced by polyethylene (PE) and the joint at the base avoided by machining the insulator from a single polyethylene block. Additional Mylar sheets (10 of $700 \times 700 \text{ mm} \times 100 \mu\text{m}$ thickness) were used to supplement the polyethylene insulator to prevent breakdown between the two brass transmission plates.

The inductance of the exploding foil is given by the formula for a co-axial conductor

$$L_f = \frac{\mu_o l_f}{2\pi} \ln \left(\frac{r_o}{r_i} \right) \quad (7-1)$$

where r_o is the inner radius of the cylindrical current conductor and r_f is the outer radius of the exploding foil. For an insulator with 22 mm inner diameter and 3 mm thickness, the cylindrical exploding foil contributes an inductance of about 3 nH to the overall circuit.

7.1.5 Cylindrical Current Conductor

The cylindrical current conductor on the outside of the imploder device must meet several requirements. It must be sufficiently strong structurally to withstand the intense pressure from a foil explosion and it must be low in resistance to carry the pulsed current ($> 500 \text{ kA}$) discharged by the main capacitor bank. However, its resistance must not be too low, in order to allow the initial magnetic field to penetrate quickly into the imploding device. Stainless steel with a thickness of about 10 mm was selected because of its high mechanical strength and moderate electrical conductivity.

7.2 Initial Field Coil

The design goal was to achieve an initial magnetic flux density of 6 T , using a simple and robust configuration that will allow the field coil to be constructed in a short time and possibly to be re-used in a number of experiments. Among the solutions considered for the initial field coils were (1) a Helmholtz coil pair [119] and (2) a multi-layer helical coil (sometimes referred to as a thick solenoid). Due mainly to the relatively simple construction of helical coils, the latter design was selected for implementation.

7.2.1 Auxiliary Circuit

The main components in the auxiliary circuit of Fig 7-1 are (1) the auxiliary capacitor bank (2) the start switch $S1$ (3) the protective fuse (4) the initial field coil and (5) the trigger coil.

The auxiliary capacitor bank consisted of eight capacitors (Fig 7-4), each rated at $300\mu\text{F} / 4\text{kV}$ but usually operated at a 3.5 kV to give a stored energy of 14.7 kJ .

The start switch $S1$ (Fig 7-4) was modified from a simple nail-switch, and is operated by an electromagnetically-controlled striker to close a pair of scissor-shape electrodes. Despite a high-current pulse of about 15 kA in the auxiliary circuit, this simple construction was possible because of the relatively low-speed of the capacitor discharge. After each experiment, the electrodes have to be repaired, using a metal file to provide the clean and smooth surfaces essential for reliable operation.

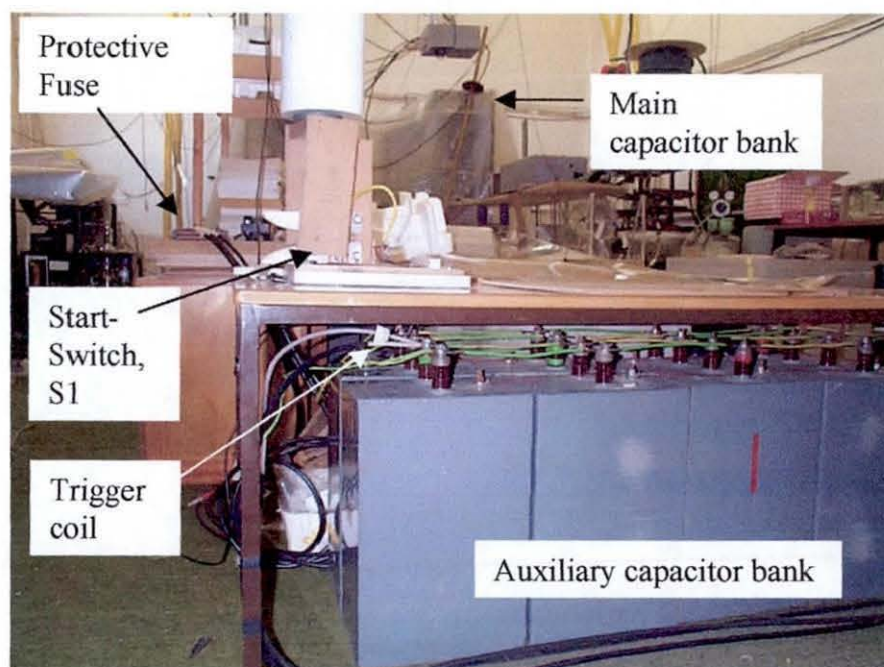


Figure 7-4 Auxiliary capacitor bank.

The trigger coil of Fig 7-4 is simply an epoxy-cast multi-turn solenoid. It is used to detect the start of current flow in the auxiliary circuit by producing a voltage that is proportional to the rate-of-change of current, as with an inductive probe.

The protective fuse, which is used to prevent reverse voltage damage to the auxiliary capacitor bank, was made from a copper exploding foil ($55 \times 55 \text{ mm} \times 17 \mu\text{m}$) and embedded in fine silicon sand.

7.2.2 Circuit Analysis

Since the field coil has to produce a uniform magnetic field inside the cylindrical imploder, its design is tightly coupled to that of the cylindrical electric gun and the starting point is the outer diameter of the cylindrical current conductor. After allowing a small gap of 1.5 mm to accommodate a thin PVC mandrel, the inner radius (r_a in Fig 7-5) of the coil can be defined. The height of the coil ($h = 55 \text{ mm}$) is determined by the height of the implosion region. The dimensions and current-carrying capacity of the wire used for the coil was another consideration for the coil design. For the present experiment, insulated wire of 4.0 mm^2 conductor cross sectional area and overall diameter 4.0 mm suitable for up to a 20 kA current pulse [24] was chosen.

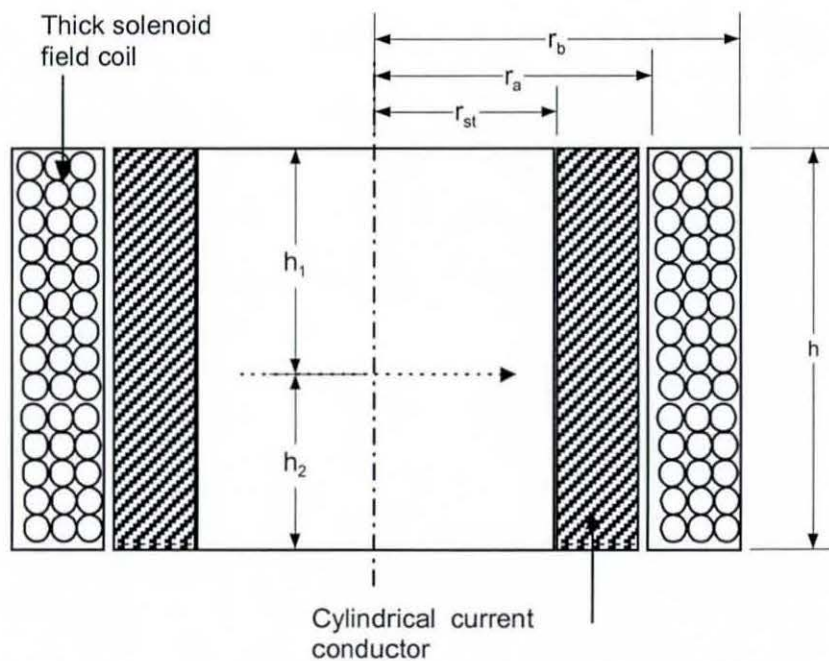


Figure 7-5 Multi-layer initial field coil and cylindrical current conductor.

The equations for the auxiliary circuit of Fig 7-6 are

$$C_{aux} \frac{dV_{aux}}{dt} = I_{aux} \quad (7-2)$$

$$(R_{aux} + R_{fuse} + R_{coil})I_{aux} + (L_{aux} + L_{fuse} + L_{coil})\frac{dI_{aux}}{dt} = V_{aux} \quad (7-3)$$

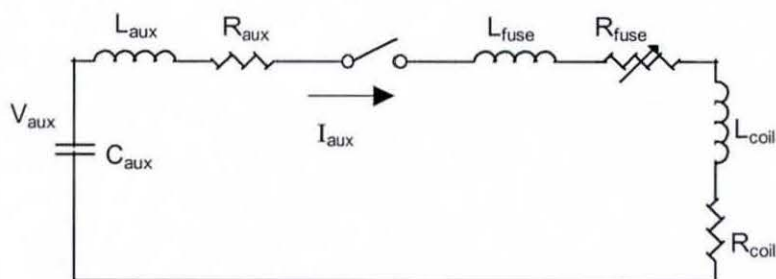


Figure 7-6 Auxiliary circuit, subscript 'aux' is for the auxiliary capacitor bank, 'fuse' for the protective fuse and 'coil' for the field coil.

The inductance of a multi-layer solenoid coil of Fig 7-5 is [120]

$$L_{coil} = \frac{\mu_o N^2 \pi r^2}{h} K_n \quad (7-4)$$

where $r = 0.5(r_b + r_a)$ and $t = r_b - r_a$ and K_n is the coil correction factor

$$K_n = \frac{1}{1 + 0.9\left(\frac{r}{h}\right) + 0.32\left(\frac{t}{r}\right) + 0.84\left(\frac{t}{h}\right)} \quad (7-5)$$

The correction factor K_n for the thick cylindrical coil varies between 0 and 1.0, depending on the geometric factors $\frac{h}{2r}$ and $\frac{t}{2r}$ (see Fig 7-7)

$$K_n\left(\frac{h}{2r}, \frac{t}{2r}\right) = \frac{\frac{h}{2r}}{0.45 + \frac{h}{2r} + 0.64\left(\frac{h}{2r}\right)\left(\frac{t}{2r}\right) + 0.84\left(\frac{t}{2r}\right)} \quad (7-6)$$

The magnetic flux density at any point along the axis of the coil is [121]

$$B_z = \mu_o \frac{1}{2} \frac{NI_{aux}}{h} \left[\frac{h_1}{r_b - r_a} \ln \left(\frac{r_b + \sqrt{r_b^2 + h_1^2}}{r_a + \sqrt{r_a^2 + h_1^2}} \right) + \frac{h_2}{r_b - r_a} \ln \left(\frac{r_b + \sqrt{r_b^2 + h_2^2}}{r_a + \sqrt{r_a^2 + h_2^2}} \right) \right] \quad (7-7)$$

At the centre of the coil where $h_1 = h_2 = \frac{h}{2}$

$$B_z = \mu_o \frac{NI_{aux}}{2(r_b - r_a)} \ln \left(\frac{2r_b + \sqrt{(2r_b)^2 + h^2}}{2r_a + \sqrt{(2r_a)^2 + h^2}} \right) \quad (7-8)$$

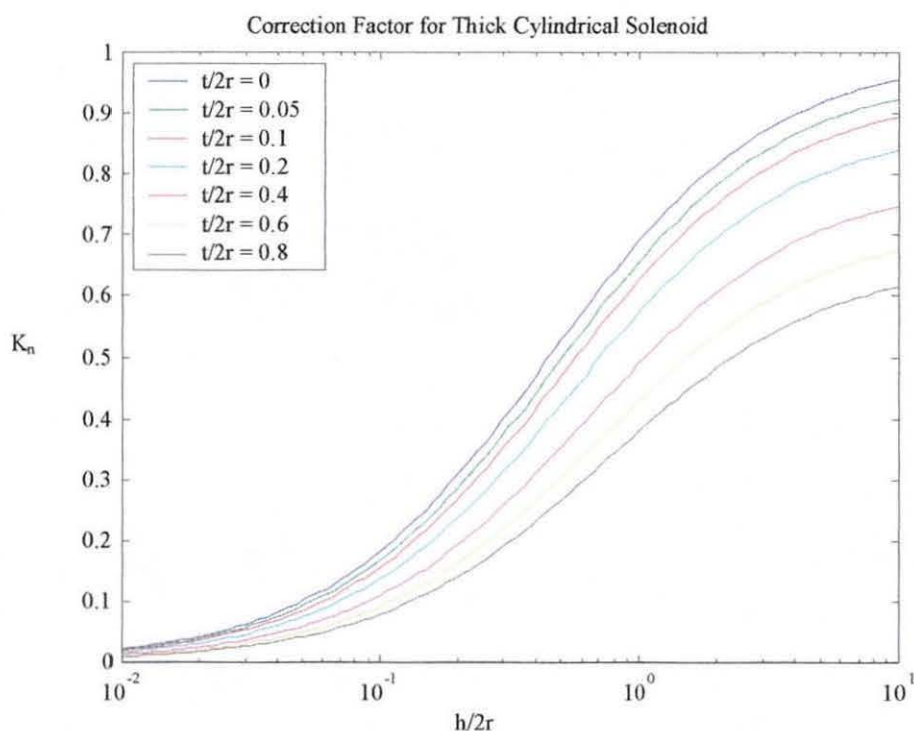


Figure 7-7 Correction factor for thick cylindrical solenoid.

7.2.3 Design Calculation

Equations (7-2) and (7-3) were solved numerically for different field coil configurations (from 1 to 6 layers) with the circuit inductance L_{aux} and resistance R_{aux} estimated respectively as $6 \mu H$ and $35 m\Omega$, and R_{coil} determined from the total length of the coil wire. In the initial design calculation, the protective fuse was not included because its dimensions were still unknown.

It is clear from Fig 7-8 that the peak discharge current is inversely proportional to the number of coil layers, while the discharge period is directly proportional to this number. Although the magnetic flux density for different solenoid coils has the same oscillating period as the current (Fig 7-9), the peak values of between 8 to 10 T are fairly independent (see also Fig 7-10) of the number of coil layers.

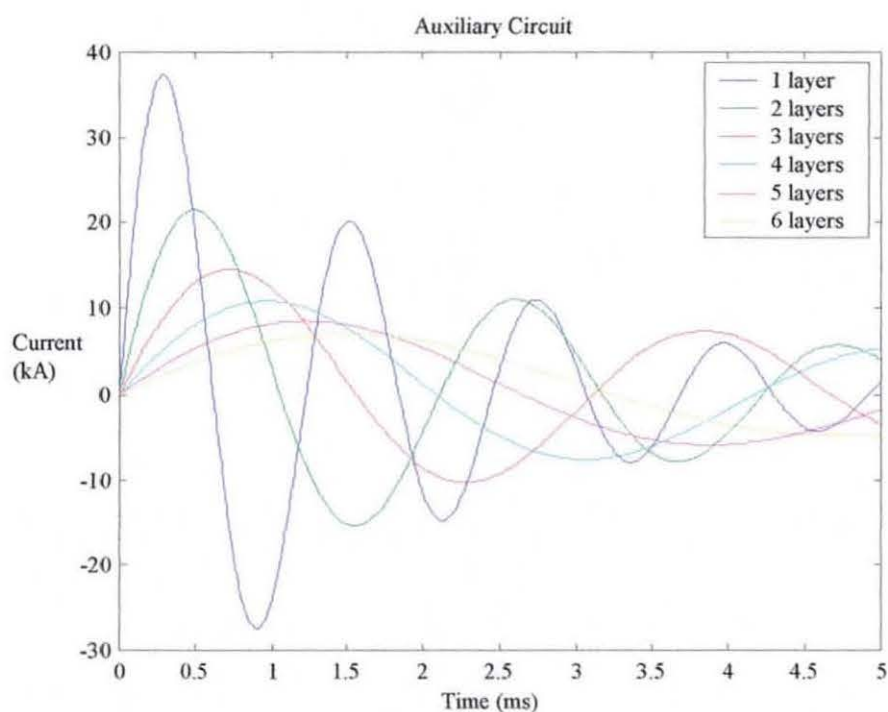


Figure 7-8 Auxiliary current for 1 to 6 layer field coil.

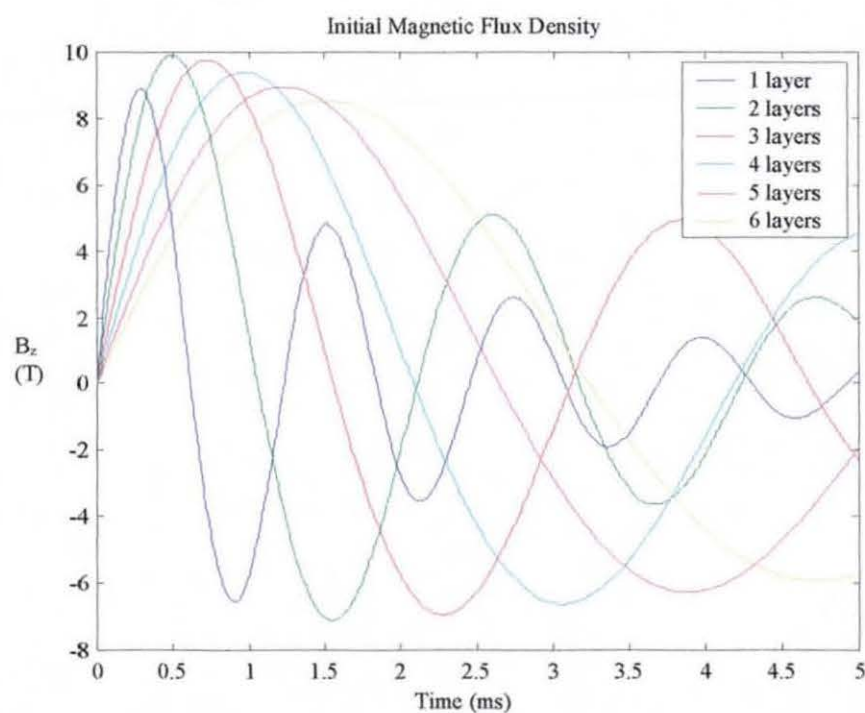


Figure 7-9 Initial magnetic field for 1 to 6 layer field coil.

The peak auxiliary currents and maximum flux densities of Figs 7-8 and 7-9 are summarised in Fig 7-10. The times for the magnetic flux densities to reach their peak values (sometimes referred to as the rise-time) are listed in Table 7-2, with the shortest value being $275 \mu s$ for the single-layer coil and the longest $1.42 ms$ for the 6-layer coil.

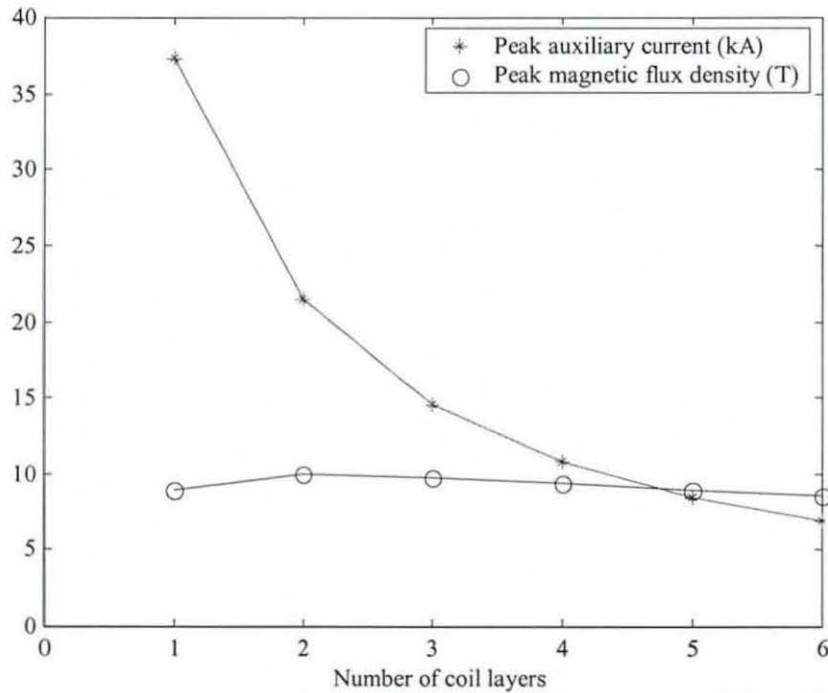


Figure 7-10 Peak auxiliary current and peak magnetic flux density.

Table 7-2 Multilayer solenoid coil

Number of layer	Time at peak flux density, (μs)	Peak magnetic flux density, (T)	Peak auxiliary current, (kA)
1	275	8.9	37.4
2	470	9.1	21.5
3	690	9.8	14.5
4	925	9.4	10.8
5	1165	9.0	8.5
6	1420	8.5	6.9

7.2.4 Construction of Field Coil

For the present experimental programme, a 4-layer field coil was chosen to produce a peak magnetic field of at least $6.0 T$ with a rise-time of about $800 \mu s$. This would give a small auxiliary current (and thereby lower mechanical stresses within the coil) and sufficient time for the magnetic field to diffuse into the imploder device.

A total of 12 field coils was built for the entire experimental programme. Each of these was wound on a PVC mandrel with epoxy applied to every layer. A thin Mylar sheet between the layers improved the electrical insulation strength. The whole field coil is cast in epoxy resin and potted in concrete for mechanical strength. Photographs taken at various stages of the construction are given in Appendix B.

The inductance of the field coil was nominally $128 \mu H$ and the measured resistance varied between $58 m\Omega$ and $60 m\Omega$. Each coil was checked for electrical integrity by subjecting it to a full charge voltage of $3.5 kV$ before an implosion experiment. The magnetic flux density at the centre of the field coil was measured with and without the imploder, to verify the time needed for magnetic diffusion through the current conductor.

7.2.5 Magnetic Diffusion through Cylindrical Current Conductor

Diffusion of the magnetic field through the cylindrical current conductor was analyzed by the method of Weinstein [122], who treated the inward diffusion as complementary to the decay of an axial magnetic field contained within a hollow circular cylinder. The decay time was expressed in terms of a geometrical form factor $g(r_b/r_a)$ as

$$\tau = \mu_o \sigma_{st} r_b^2 g\left(\frac{r_b}{r_a}\right) \quad (7-9)$$

where σ_{st} is the electrical conductivity of the conductor (steel in this case) and values for $g(r_b/r_a)$ are given in Table 7-3. For the cylindrical current conductor of the electric

gun with 28.5 mm inner diameter and 50 mm outer diameter, the diffusion time is about 160 μ s.

Table 7-3 Values of $g(r_b/r_a)$ for hollow circular cylinder

r_b/r_a	$g(r_b/r_a)$	r_b/r_a	$g(r_b/r_a)$
0.00	2.173	0.60	1.720
0.05	2.173	0.65	1.587
0.10	2.172	0.70	1.431
0.15	2.170	0.75	1.253
0.20	2.164	0.80	1.052
0.25	2.153	0.85	0.8267
0.30	2.133	0.90	0.5766
0.35	2.102	0.95	0.3011
0.40	2.059	0.96	0.2430
0.45	2.001	0.97	0.1838
0.50	1.926	0.98	0.1236
0.55	1.844	0.99	0.0623
		1.00	0

The measured $\frac{dB_z}{dt}$ signals at the centre of the field coil with and without the cylindrical current conductor are shown in Fig 7-11. The initial flux densities B_z of Fig 7-12, obtained by numerical integration of the measured $\frac{dB_z}{dt}$ signals, show a small delay of about 160 μ s, consistent with predictions using the method of Weinstein.

The diffusion of the magnetic field through the current conductor has also been verified by numerical integration of the magnetic diffusion equation, obtained by setting $v = 0$ in equation (6-84) to give

$$\frac{dB_z}{dt} = \frac{1}{\mu_o} \frac{1}{r} \frac{\partial}{\partial r} \left(\frac{r}{\sigma} \frac{\partial B_z}{\partial r} \right) \quad (7-10)$$

or

$$\frac{dB_z}{dt} = \frac{1}{\mu_o \sigma} \left(\frac{\partial^2 B_z}{\partial r^2} + \frac{1}{r} \frac{\partial B_z}{\partial r} \right) \quad (7-11)$$

Equation (7-11) has been solved by the Crank-Nicholson method [67] and the resulting tri-diagonal matrix system by an iterative algorithm known as the Thomas method [67]. The time-varying magnetic flux density measured without the imploder was used as the initial and boundary conditions at the outer surface of the conductor, and Fig 7-12 demonstrates that reasonable agreement was obtained between the computed and measured flux densities.

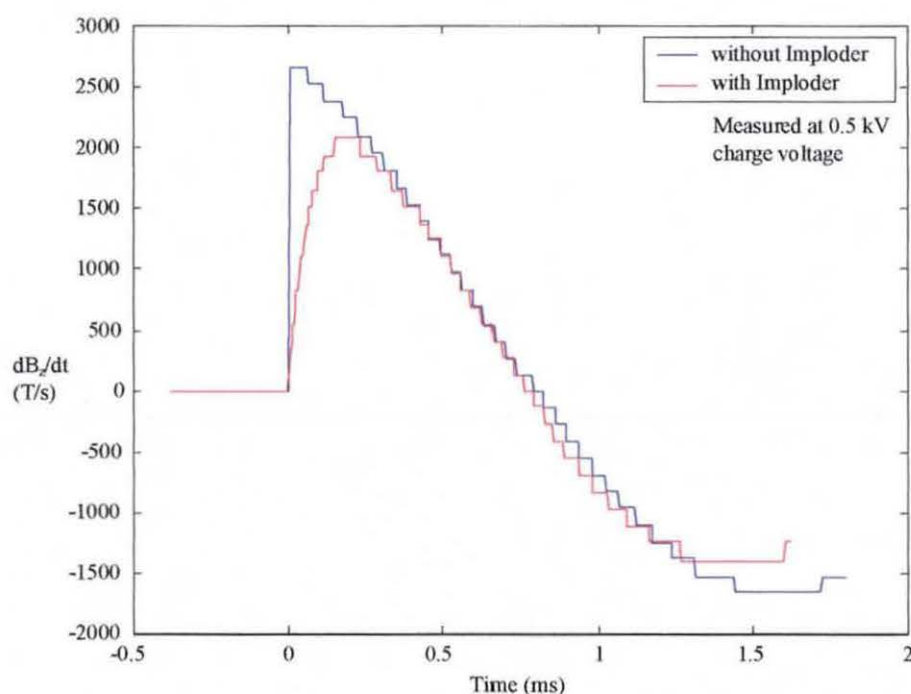


Figure 7-11 $\frac{dB_z}{dt}$ measured in the centre of field coil.

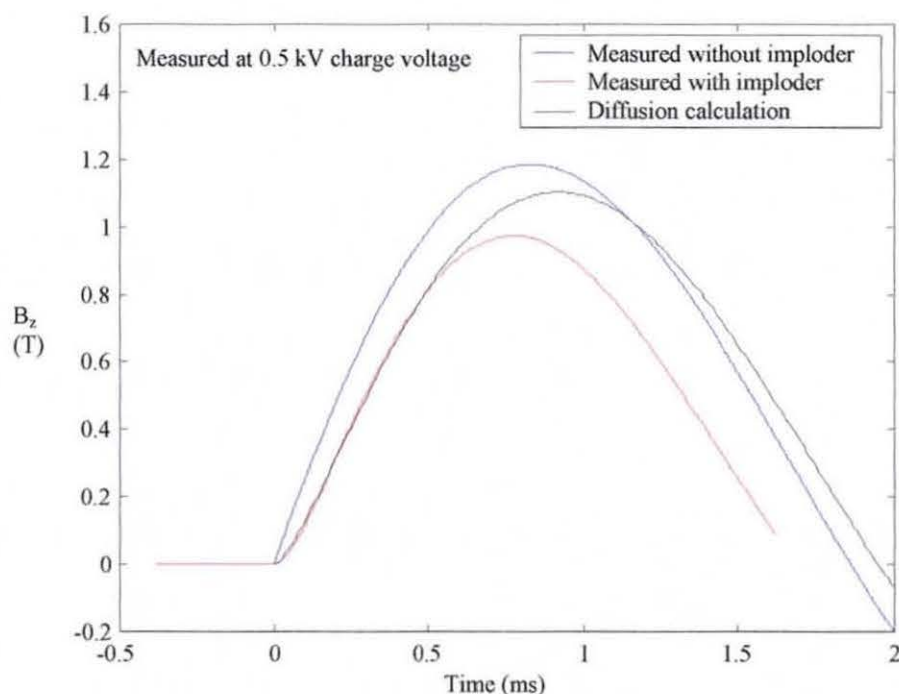


Figure 7-12 Initial magnetic flux density.

7.2.6 Measured Performance

The performance of the auxiliary circuit and the initial field coil was measured at the full charge voltage of 3.5 kV (independently of the electric gun circuit) and the results are shown in Figs 7-13 and 7-14. The auxiliary current of Fig 7-13 measured using a calibrated shunt agrees reasonably well with that predicted by the circuit model. There is also reasonable agreement between the measured $\frac{dB_z}{dt}$ signal and the computed results in Fig 7-14. In Fig 7-15, the initial flux density obtained by numerical integration of the measured $\frac{dB_z}{dt}$ signal shows a peak value very close to the design value of 6.0 T. The magnetic field probe used to measure the flux density is discussed in the next section.

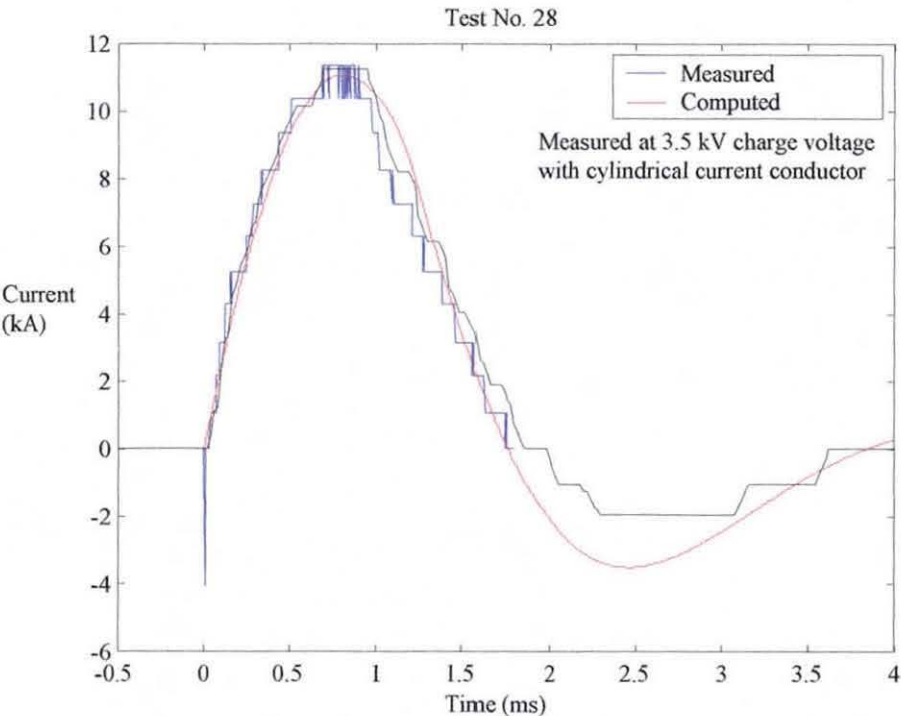


Figure 7-13 Current in auxiliary capacitor bank circuit.

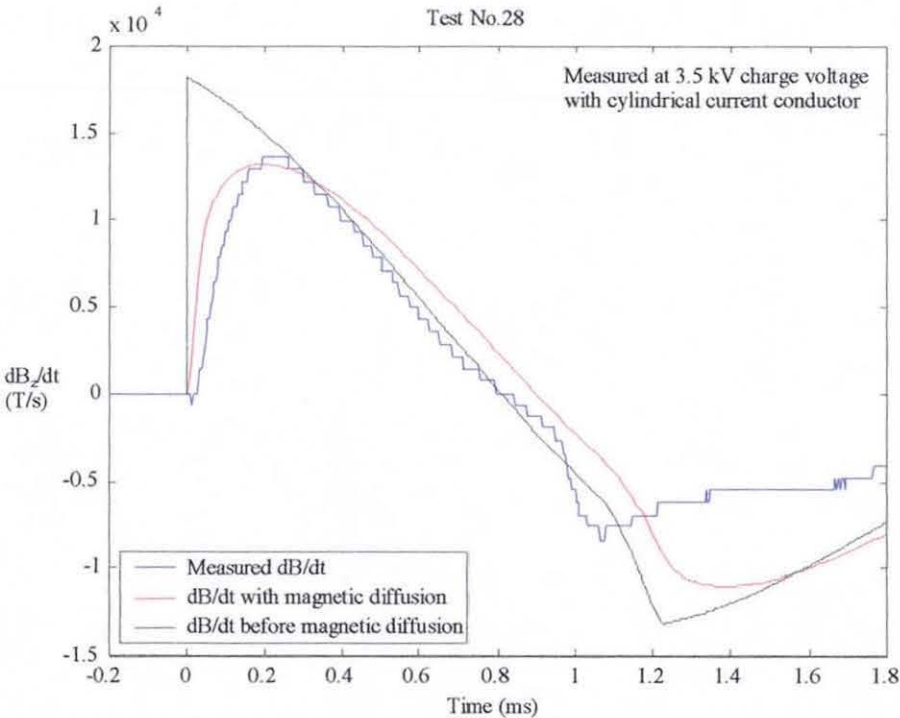


Figure 7-14 $\frac{dB_z}{dt}$ in initial field coil.

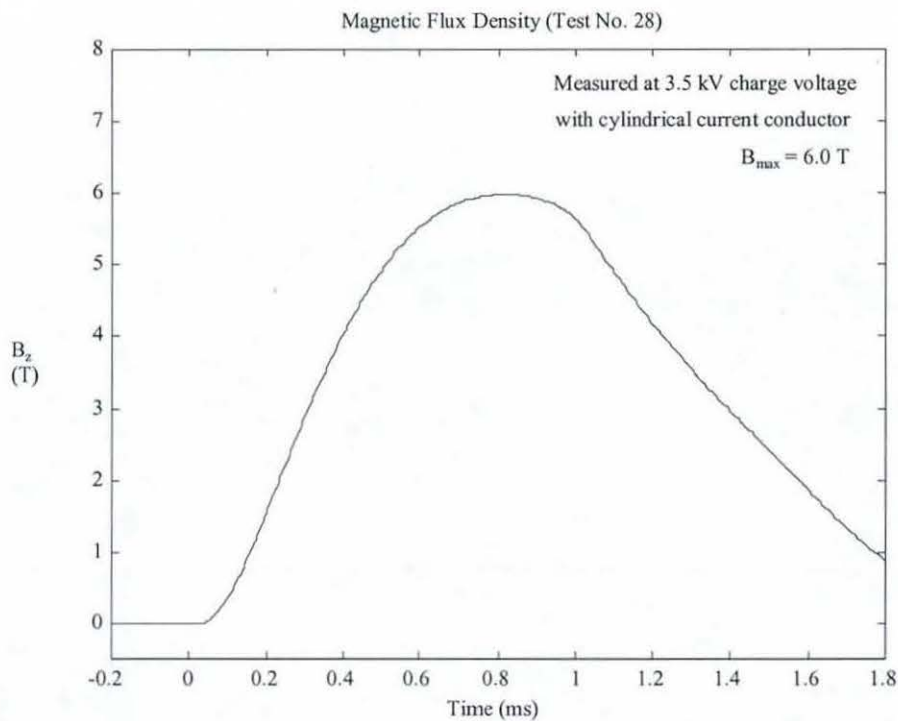


Figure 7-15 Initial magnetic flux density.

7.3 Magnetic Field Probes

Magnetic field probes, commonly known as B-dot probes, are based on the simple single-turn pick-up coil or multi-turn solenoid. When a solenoid coil with N turns, each of cross sectional area A , is placed inside a time-varying magnetic field, the induced voltage $V(t)$ appearing at the terminal is

$$V(t) = (NA + S_a) \frac{dB}{dt} = A_{\text{eff}} \frac{dB}{dt} \quad (7-12)$$

where S_a is an additional stray pick-up area formed by the leads and connections, and A_{eff} is the effective pick-up area, which includes the stray pick-up area of the probe. In carefully prepared probes, the undesired S_a term can be limited to less than 1 mm^2 .

It follows from equation (7-12) that the magnetic flux density is

$$B(t) = \frac{1}{A_{eff}} \int_0^t V(\tau) d\tau \quad (7-13)$$

enabling the flux density to be obtained by numerical integration of the measured voltage. Alternatively, the voltage produced by the probe can be integrated using an electronic integrator circuit or a simple RC circuit (with an integration time constant $\tau = RC$ much longer than the pulse duration) to give a voltage that is directly proportional to the flux density.

7.3.1 Initial Field Probe

The initial field probe of Fig 7-16 was made from 6 turns of $125 \mu m$ enamel wire wound on a $14.1 mm$ mandrel, with the ends of the wire twisted into a braid to minimise the stray pick-up area S_a . It has an effective pick-up area of $NA = 935.8 mm^2$, enabling the stray pick-up area S_a to be assumed to be negligible. This initial field probe was used only for measuring the initial flux density of all the field coils, and was never used during any implosion experiments.

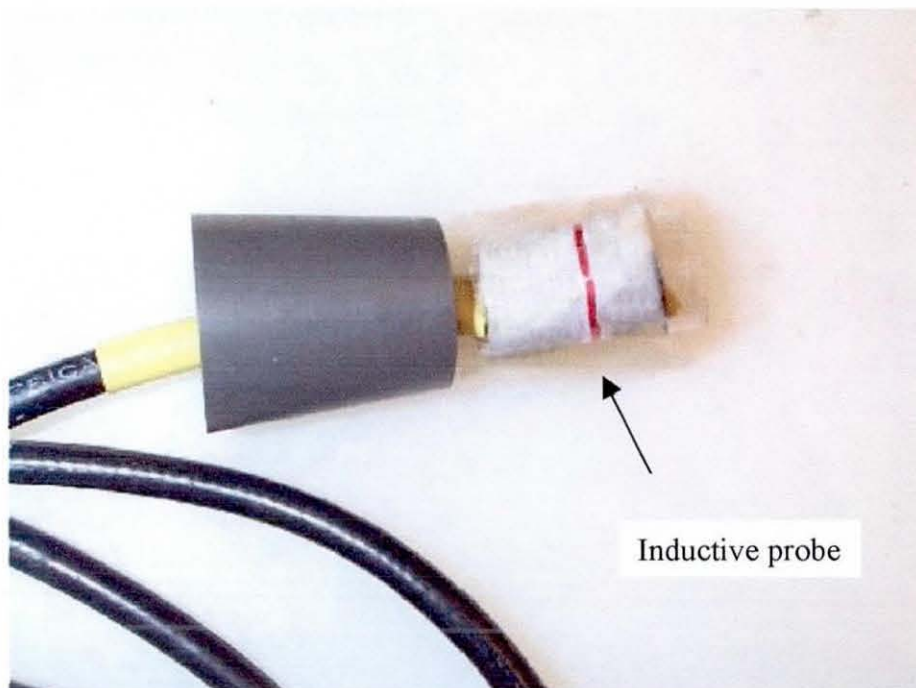


Figure 7-16 Inductive Probe for measuring initial magnetic field.

7.3.2 Final Field Probe

The probe used for measuring the final compressed magnetic flux density is shown schematically in Fig 7-17. It was made from a single turn of $125\text{ }\mu\text{m}$ enamel wire wound on a 0.8 mm diameter glass bead and cast in epoxy resin inside a thin glass tube of about 2.0 mm diameter. An epoxy casting technique [123] was used to solve the difficult problem of providing adequate mechanical and electrical insulation strength in a confined space.

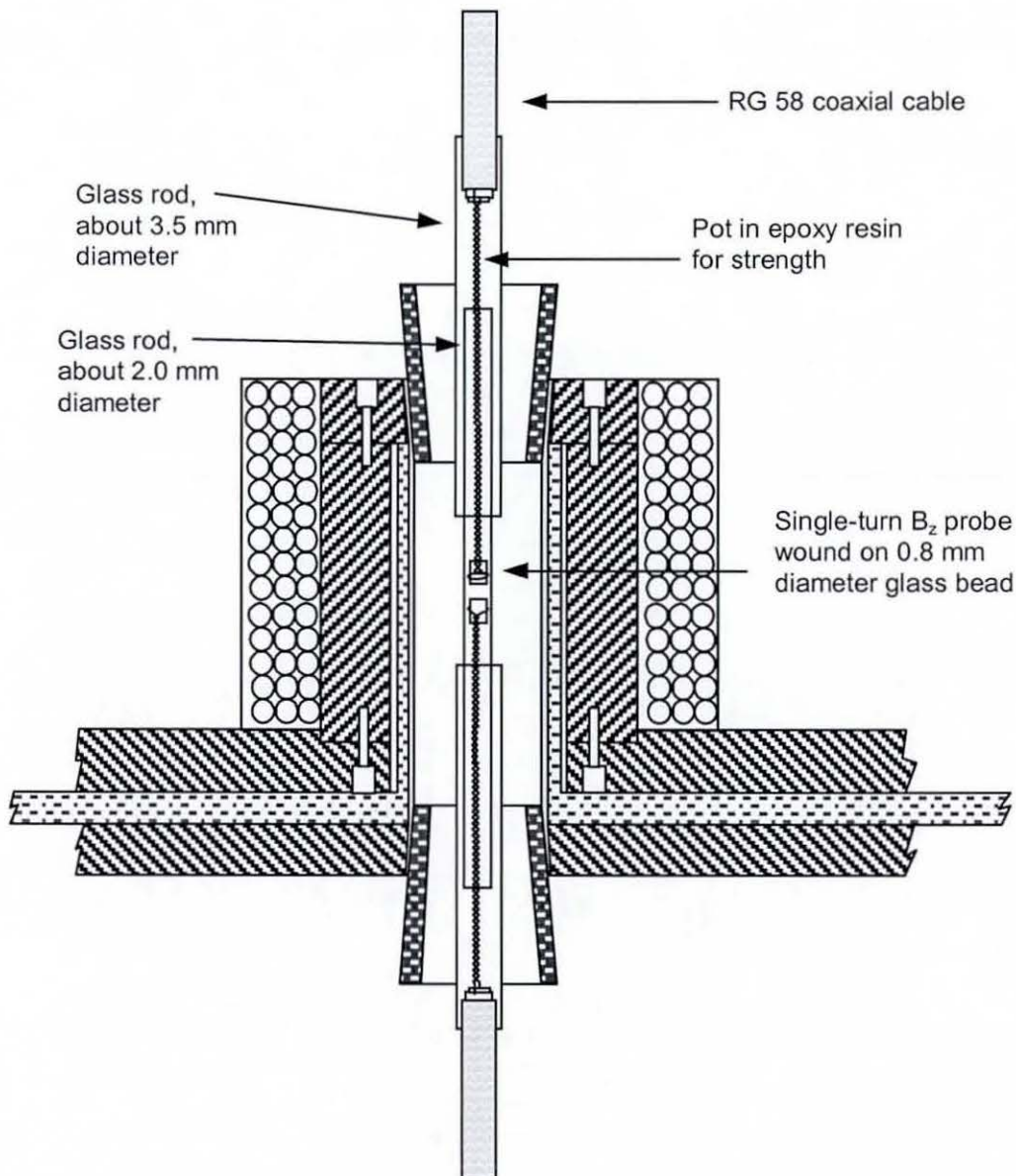


Figure 7-17 Constructional details of final magnetic field probe.

7.3.3 Aluminium Powder Assembly

For shockwave flux compression in aluminium powder, a thin layer (up to 5.0 mm thick) of powder surrounded the magnetic probe and was held in place by the cylindrical Mylar container and two PVC holders shown in Fig 7-18. The holders form the barrel and guide the Mylar flyer during its flight towards the powder. The powder is normally kept in a sealed container and is placed in the Mylar container very shortly before experimentation, to ensure that its properties (especially the thickness of the insulating layer around individual powder particles) are not significantly altered by exposure to air.

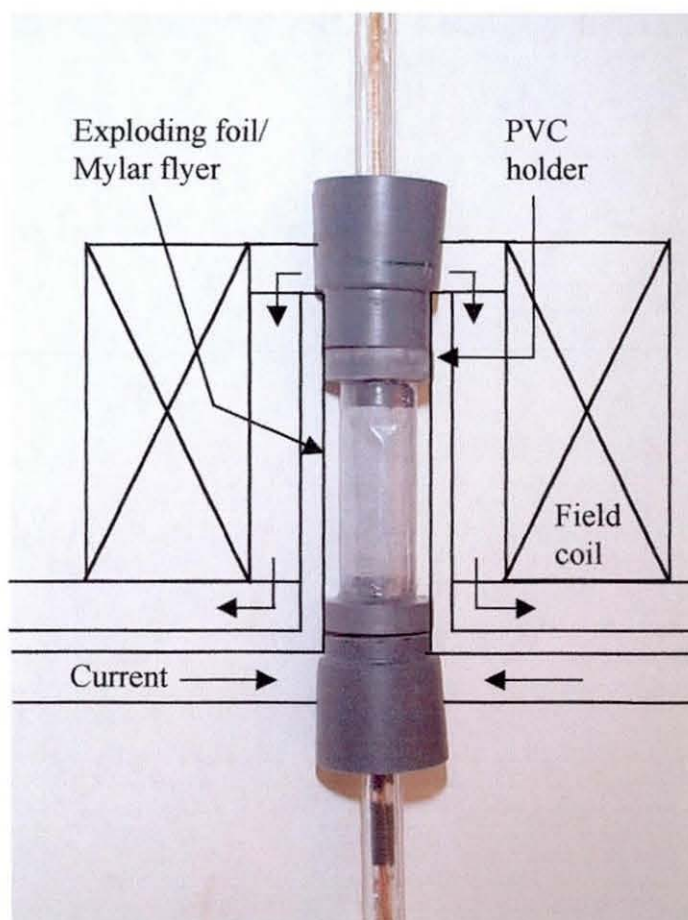


Figure 7-18 Aluminium powder assembly.

The magnetic probe with the powder assembly was tested in a B_x calibration fixture (see following section), which confirmed that the presence of the aluminium powder did not alter the magnetic field measured by the pick-up coil. In other words, the thin layer of aluminium powder at ambient, uncompressed conditions did not behave like an electrical conductor providing a shield against the penetration of magnetic field.

7.3.4 Calibration of Magnetic Field Probe

The *reference probe* method [124] was used for calibration of the magnetic probes. It consists of a carefully wound inductive probe with a relative large pick-up area ($NA > 100 \text{ mm}^2$) and a negligibly small stray pick-up area, so that its sensitivity (or conversion factor) is determined solely by equation (7-12). The probe used in the calibration of the final field probe was made of 10 turns of $125 \mu\text{m}$ enamel wire wound on the outer surface of the epoxy-cast probe and temporarily held in position by epoxy glue. After calibration, the windings for the reference probe were removed from the epoxy-cast probe using a sharp knife.

Fig 7-19 shows a schematic of the simple but accurate fixture used when calibrating B_z probes, using a high-voltage capacitor of $26.9 \mu\text{F}$ as a pulse current source. Discharge of the capacitor into a short parallel-plate transmission line provided a 250 kA current pulse with a oscillation frequency of about 10 kHz . A single-turn coil (see Fig 7-19) is formed in the transmission line to give a uniform axial (or B_z) magnetic flux density at its centre of

$$B_z(r, z) = B_z(0, 0) = \frac{\mu_o I_\theta}{\sqrt{(2a)^2 + l^2}} \quad (7-14)$$

where a and l are the radius and axial length of the single-turn coil respectively.

The rate-of-change of current $\frac{dI_\theta}{dt}$ is monitored by an inductive (I-dot) probe and is used together with the voltage measured by the magnetic probe to calibrate the pick-up coil.

$$A_{eff} = \frac{V(t)}{\frac{dB_z}{dt}} \quad (7-15)$$

$$\text{where } \frac{dB_z}{dt} = \frac{\mu_0}{\sqrt{(2a)^2 + l^2}} \frac{dI_\theta}{dt} \quad (7-16)$$

A more exact formula for the magnetic flux density inside the single-turn coil has been obtained by Miura [21] and has been used in place of equation (7-14) for calibrations involving the magnetic field probe.

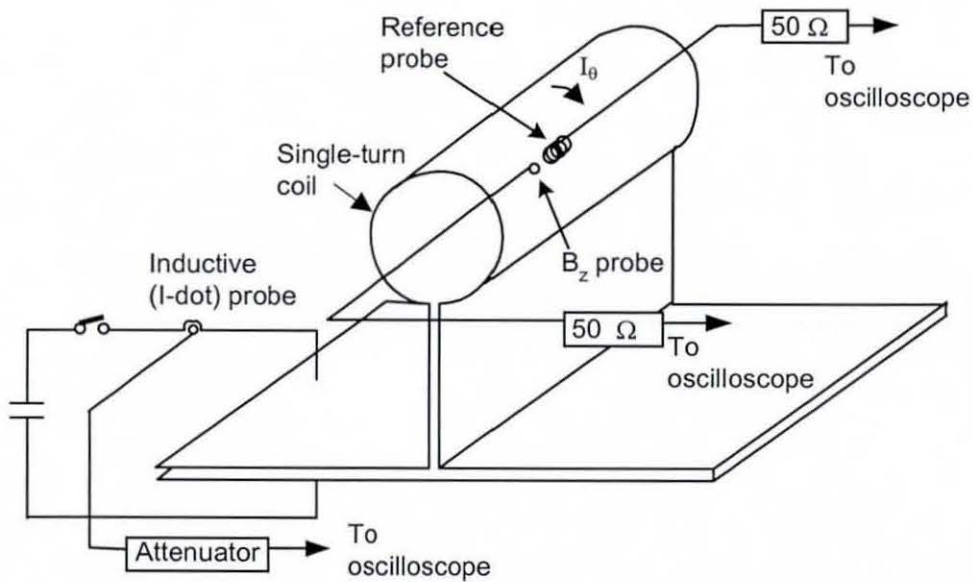


Figure 7-19 Schematic of calibration fixture for B_z probes.

7.4 Magnetic Flux Compression Experiments

7.4.1 Experimental Programme

A total of three implosion experiments was conducted to investigate shockwave flux compression in aluminium powder. In all these, the dimension for the cylindrical exploding foil was nominally 22 mm (diameter) x 60 mm (height) x 25.4 μm and the Mylar flyer was 250 μm thick. Due to a lack of information on the flyer acceleration process at the start of the experimental programme, the stand-off distance between the exploding foil and the powder assembly (shown in Table 7-4), was chosen as 3.0 mm or more, to accommodate powder samples of different thicknesses. It will be shown in the next section that the large stand-off distance was useful for flyer acceleration by magnetic pressure, which is an important supplement to the foil explosion pressure.

Table 7-4 Flux compression experiments with aluminium powder

Test No.	Initial B_{zo} (T)	Stand-off distance (mm)	Aluminium Powder	
			Outer radius (mm)	Inner radius (mm)
137	6.0	4.0	7.0	2.0
149	6.0 ¹	7.0	4.0	2.0
172	1.0	3.0	8.0	2.0

¹No initial magnetic field, due to premature discharge of main capacitor bank

7.4.2 Experimental Arrangements

Fig 7-20 shows the typical arrangement of a magnetic flux compression experiment. After both the main and auxiliary capacitor have been charged to the required voltage, switch *S1* in the auxiliary circuit is closed to discharge the auxiliary capacitor bank and so establish the initial magnetic field. A pulse generator (with a programmable delay setting) and a trigger coil, detect the initiation of current flow in the auxiliary circuit and ensure synchronisation with the main capacitor bank. After a preset delay, corresponding to the time needed for the initial magnetic field to reach its peak value

and to enter the implosion region (and also the powder assembly), the pulse generator sends a voltage pulse to the Blumlein system to close the main dielectric switch $S2$ and start the implosion process.

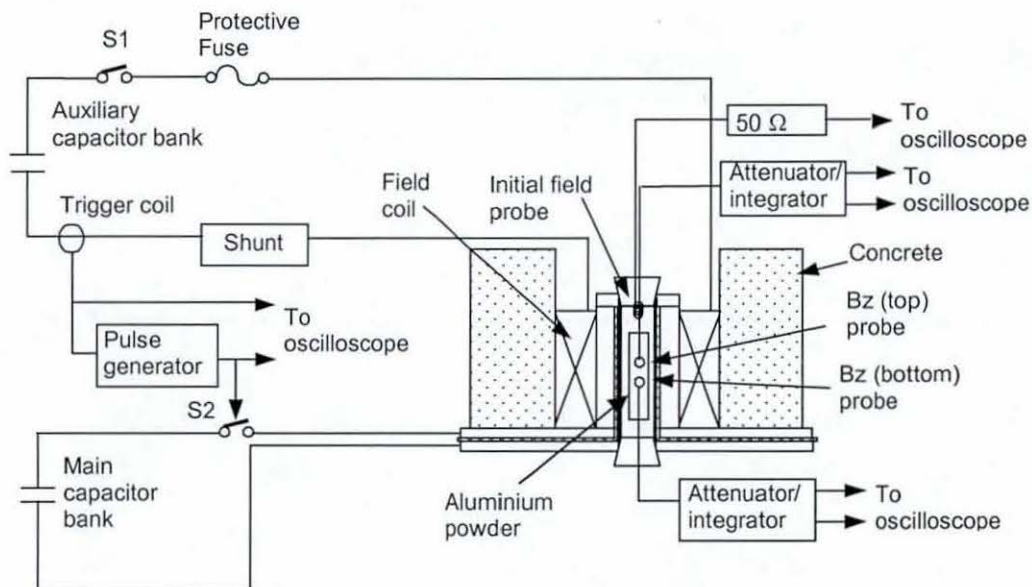


Figure 7-20 Typical arrangement for cylindrical implosion experiment.

a) Test Preparation

The single-shot nature of the experiments demanded meticulous preparation before each implosion experiment. Test preparation included

- 1) fabrication of the aluminium foil/Mylar flyer package and assembly of the cylindrical imploder, including the brass base plates, polyethylene high-voltage insulator etc.,
- 2) fabrication of switch packages for the solid dielectric closing-switch in the main capacitor bank and the Blumlein trigger system,
- 3) fabrication of magnetic field probes and aluminium powder assembly,
- 4) calibration of the magnetic field probe, using the B_z calibration fixture and determination of the direction of the initial magnetic field produced by the external field coil,

- 5) measurement of the performance of the initial field coil.
- 6) confirmation of the synchronisation delay between main and auxiliary capacitor bank,
- 7) ensuring that all oscilloscopes are properly connected to the correct sensors, armed and waiting for the trigger signal and
- 8) checking the voltage hold-off capacity of the solid dielectric switch by charging to 28 kV , immediately before the actual test

The step-by-step construction of the imploder is shown in a series of photographs in Appendix C.

On average, before an implosion experiment a total of 15 to 20 pre-tests need to be carried out, to verify the performance of the individual parts of the complex system and minimise any possibilities of failure in the full experiment. The data for all experiments are recorded on computer, which allows simple and continuous monitoring of trends in the measured data. Minor faults in the system have in fact been detected before an implosion test (and disaster prevented), simply by comparing the data with those previously obtained. In one case, the onset of an insulation failure in the trigger coil was discovered (and repaired) as part of the test preparation.

b) Instrumentation

For an implosion test, a low-bandwidth digital oscilloscope was used to record slower processes (on a ms time scale) associated with the auxiliary capacitor bank, while a high-bandwidth oscilloscope records faster processes (at or below μs time scale) associated with the electric gun. The signals recorded by the low-bandwidth oscilloscope included (1) the initial magnetic flux density B_{z0} (2) the trigger coil output voltage and (3) the pulse generator output voltage. Those recorded by the high-bandwidth oscilloscope are (1) the rate of change of current $\frac{dI_b}{dt}$ (or $I\text{-dot}$) in the main capacitor bank circuit (2) the rate of change of flux density, $\frac{dB_z}{dt}$ (or $B\text{-dot}$) and (3) the compressed flux density B_z measured by RC integrators. In situations where multiple

B_z probes were used, up to two high-speed oscilloscopes (with 4 channels) and three low-speed oscilloscopes (with 2 or 4 channels) were used.

7.4.3 Electric Gun Performances

With the development of the new electric gun model (described in chapter 6 for the case of cylindrical implosions), it becomes possible to analyse the foil explosion and flyer acceleration process using TOA data obtained from the measured $\frac{dB_z}{dt}$ signals. Figs 7-21 to 7-26 compare measured results from three experiments (with aluminium powder) with those predicted by the computer model. As shown previously in chapter 5, the performance of the gun is summarised by two sets of four graphs for each experiment. Seven of the eight graphs are associated with the main performance parameters of the electric gun, with the eighth being reserved for the measured $\frac{dB_z}{dt}$ signal, from which TOA data for the flyer impact with the powder can be obtained.

Figs 7-22 and 7-26 show that the explosion pressure in both tests no. 137 and 172 was estimated at about 1 *GPa*, which is a good indication of a less than ideal explosion process. The magnetic pressure accelerated the Mylar flyer to a velocity of about 1.1 *km/s*. In Fig 7-24 for test no. 149, the TOA data indicated a better foil explosion and the explosion pressure is estimated at about 10 *GPa*, giving a velocity of about 1.7 *km/s* on impact with the probe. Unfortunately the better foil explosion was obtained in an experiment that suffered from a possible breakdown of the Blumlein system, causing a premature discharge of the main capacitor bank before the initial magnetic field was established. As a result there was no initial magnetic field to be compressed by the imploding flyer.

In all the three sets of results, the energy density at burst was calculated at about 15 *MJ/kg* and there is reasonably good agreement between the computed and measured $\frac{dI_b}{dt}$ and current. The modelling of the Blumlein failure is described in a later section.

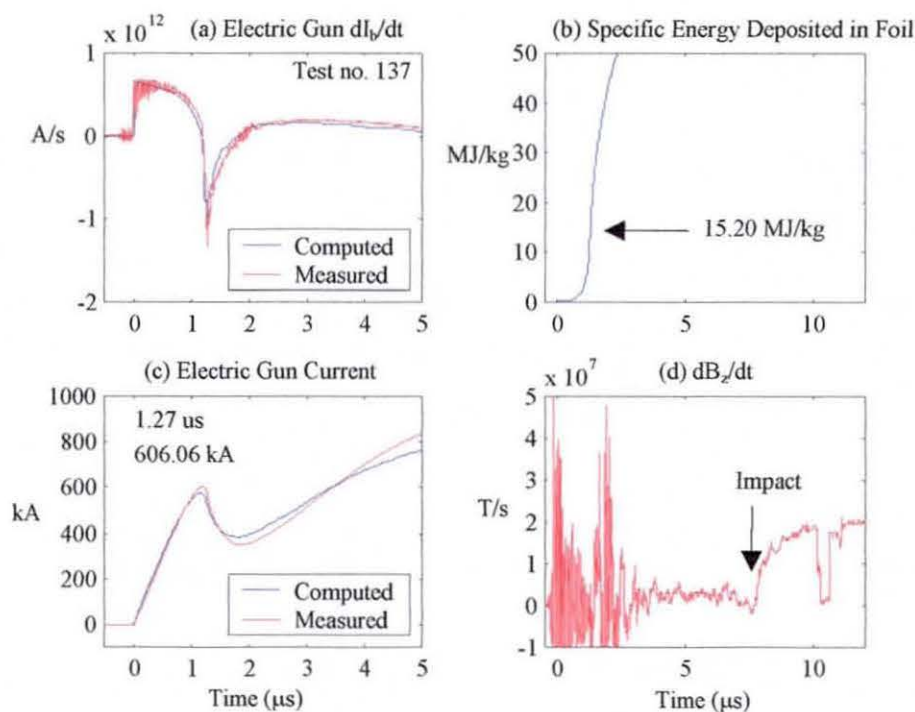


Figure 7-21 Computed and experimental results (test no. 137).

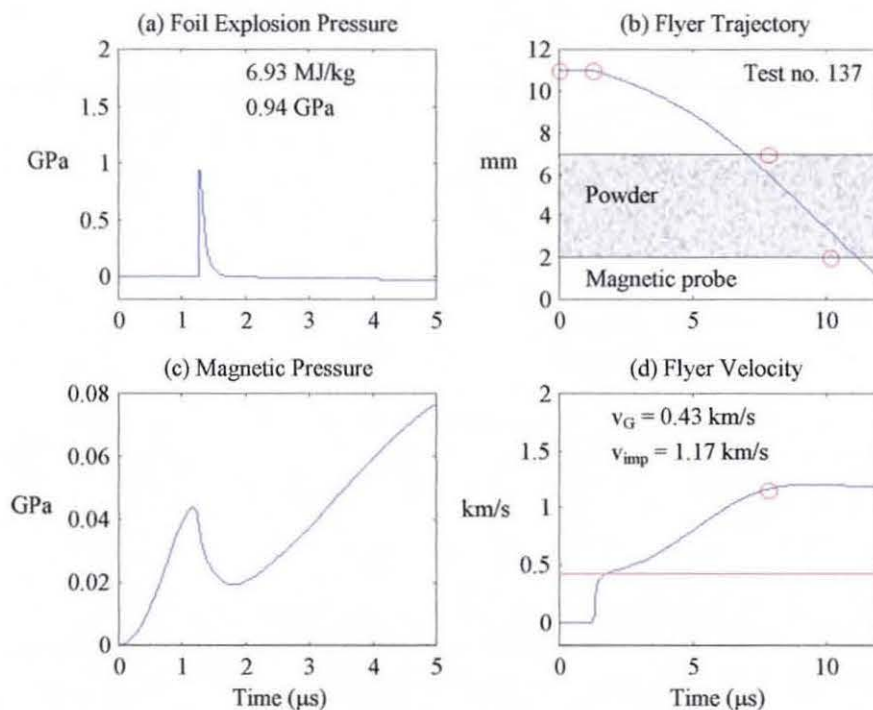


Figure 7-22 Computed and experimental results (test no. 137).

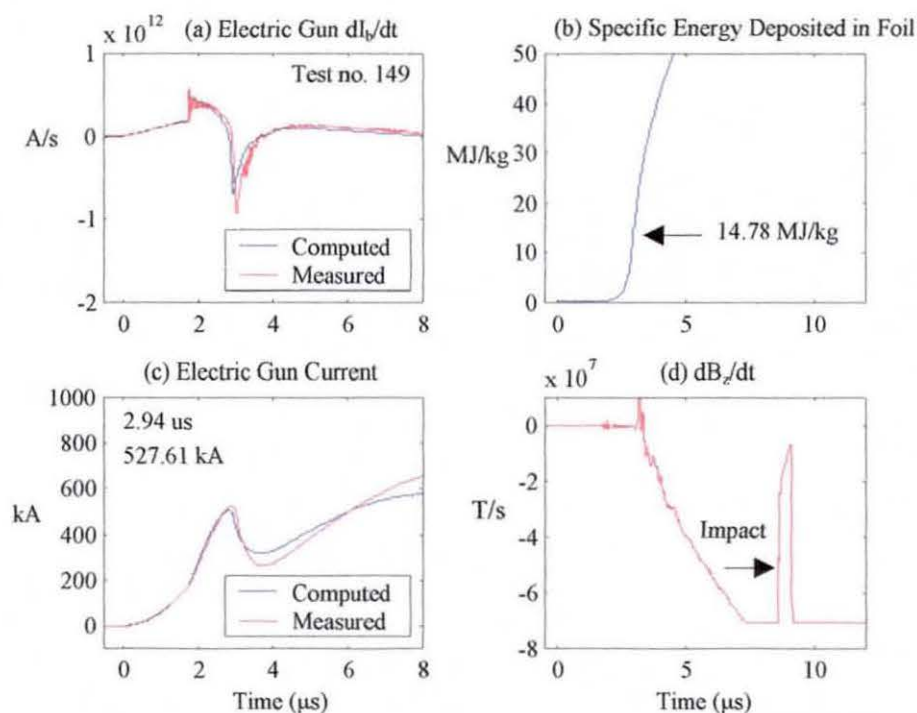


Figure 7-23 Computed and experimental results (test no. 149).

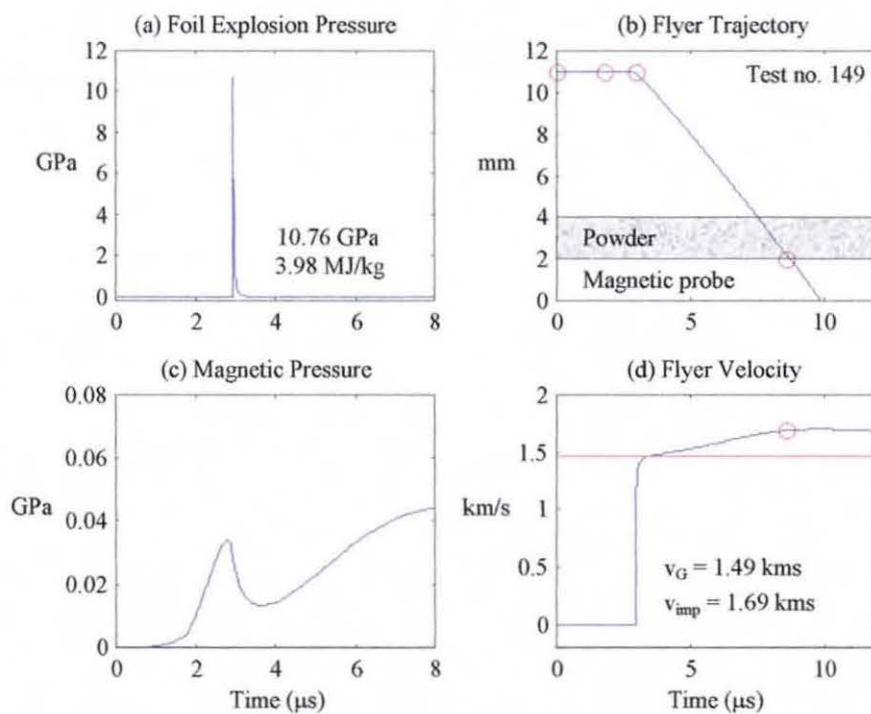


Figure 7-24 Computed and experimental results (test no. 149).

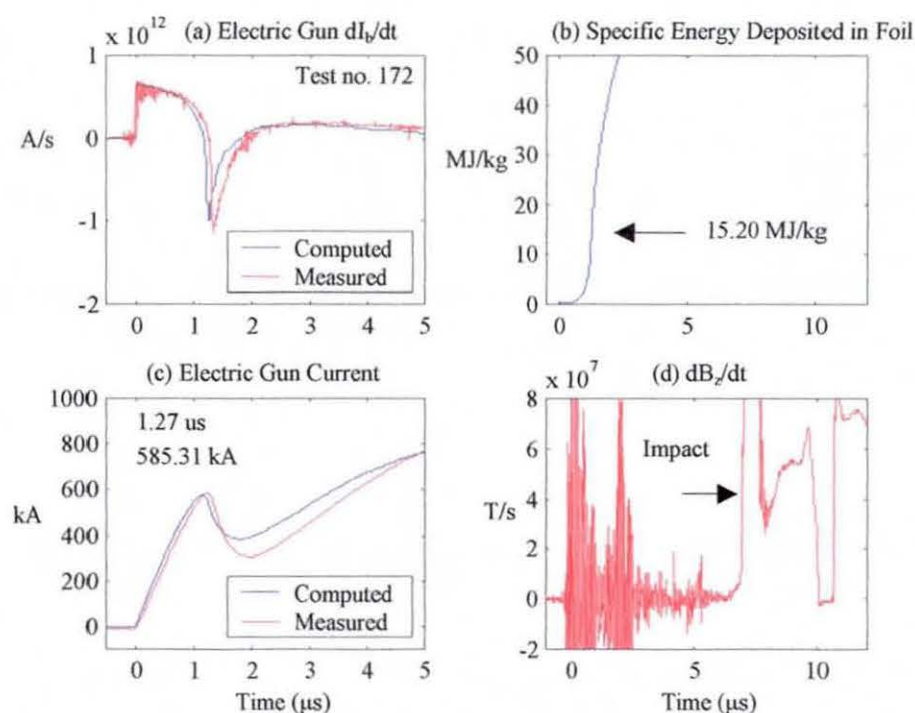


Figure 7-25 Computed and experimental results (test no. 172).

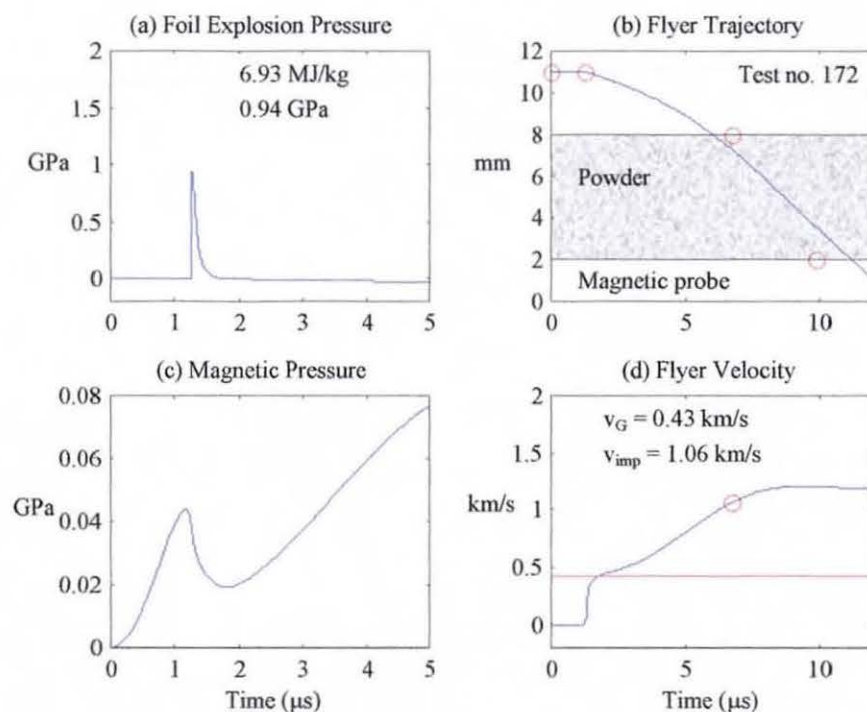


Figure 7-26 Computed and experimental results (test no. 172).

a) Modelling of breakdown phenomenon

Modelling of the breakdown phenomenon in test no. 149 is necessary if the computer model is to take into account the electrical energy deposited in the foil before discharge of the main capacitor bank. Since the breakdown in the Blumlein trigger system is manifested in Fig 7-27 by a linearly increasing $\frac{dI_b}{dt}$ between the onset of failure and discharge of the capacitor bank, it can be included in the computer model by the additional equation

$$\frac{dI_b}{dt} = St \quad \text{for } 0 < t \leq t_{start} \quad (7-17)$$

where the gradient $S = \frac{a}{t_{start}}$ is shown in Fig 7-27.

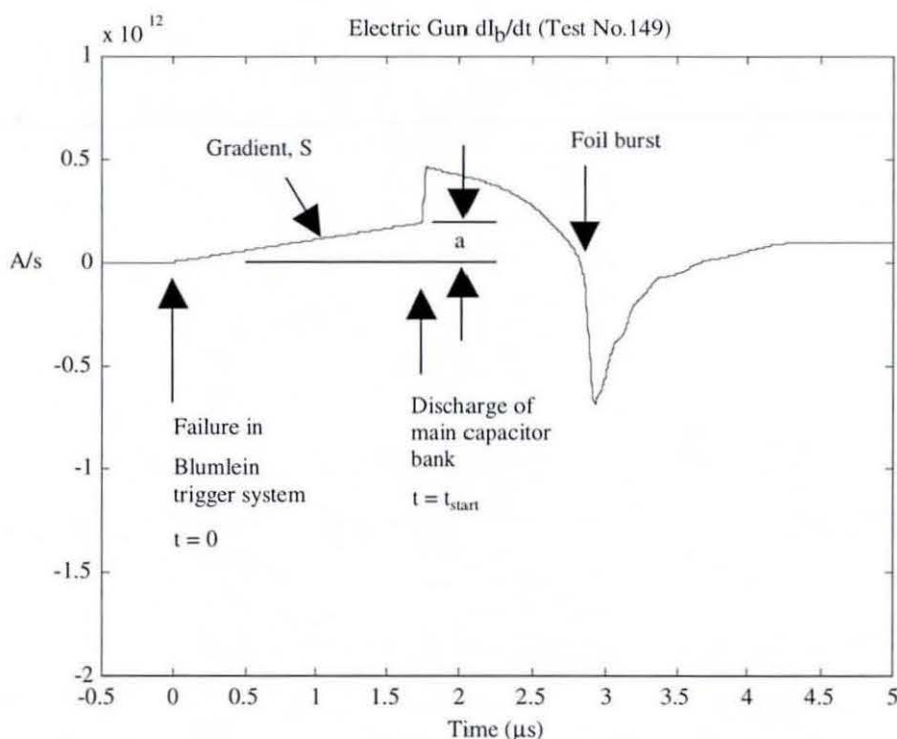


Figure 7-27 Modelling the initial breakdown in the Blumlein trigger system.

7.4.4 Initial Magnetic Flux Density

The start of the implosion process at near maximum initial magnetic flux density is shown in Fig 7-28. Synchronisation is achieved by means of the trigger coil in the auxiliary circuit and a preset delay programmed into the pulse generator. The trigger coil produces a voltage pulse (Fig 7-28a) that is proportional to the rate-of-change of flux density in Fig 7-28b and forwards it to the pulse generator, which detects the initial crossing of a threshold level (at about 5 V). After a preset delay, a voltage pulse (of Fig 7-28c) is sent to the Blumlein system to trigger the closing of the dielectric switch (S_2 in Fig 7-20) and initiate the implosion process.

Implosion starts when the initial magnetic flux density is near its maximum value, indicated by a near zero $\frac{dB_z}{dt}$ signal. The initial magnetic flux density B_{z0} of Fig 7-28d is obtained by numerical integration of Fig 7-28b, using the trapezoidal method to give an initial magnetic flux density of about 6.0 T.

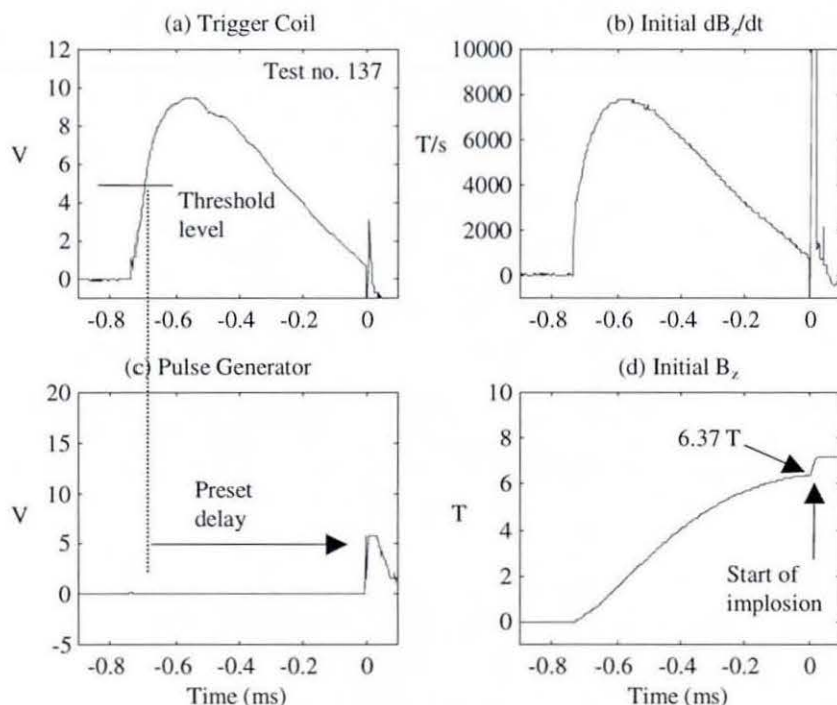


Figure 7-28 Experimental results

7.4.5 Final Compressed Flux Density – with Aluminium Powder

Fig 7-29 shows the $\frac{dB_z}{dt}$ signal obtained in test no. 137, where a layer of aluminium powder surrounded the epoxy-cast magnetic field probe. The stand-off distance between the exploding foil and the powder assembly was 4 mm (see Fig 7-22b) and the thickness of the powder layer was 5 mm. The distinctive notch in the $\frac{dB_z}{dt}$ signal indicates the arrival of the conducting shock front (in the powder) at the outer surface of the epoxy-cast magnetic probe, where the conducting front remained quasi-stationary for the time needed by the shock to compress (and possibly break) the glass wall and enter the epoxy-resin at a higher-speed. The increase in shock speed on entering the epoxy-resin, which has a lower shock impedance, is similar to the phenomenon at a free-surface. The behaviour of the conducting shock front in the powder is discussed in greater detail in section 7.5.1

The variation of magnetic flux density B_z obtained by numerical integration of the $\frac{dB_z}{dt}$ signal of Fig 7-29 is shown in Fig 7-30, and the value at the points of flyer impact with the powder and shock collision with the magnetic probe are highlighted. A multi-stage process is evident in Fig 7-30, with the first stage being the flux compression by the exploding foil plasma. This is followed by the shockwave flux compression in aluminium powder and a final stage due to shock compression of the epoxy-cast probe (described in section 7.5.1). The flux conservation coefficient calculated using the basic flux compression equation (2-17) and the dimensions of the initial foil radius (11 mm), the powder assembly (7 mm) and the magnetic probe (2 mm), gives a figure of 9.8% for the foil plasma flux compression stage and 24% for the shockwave in powder stage.

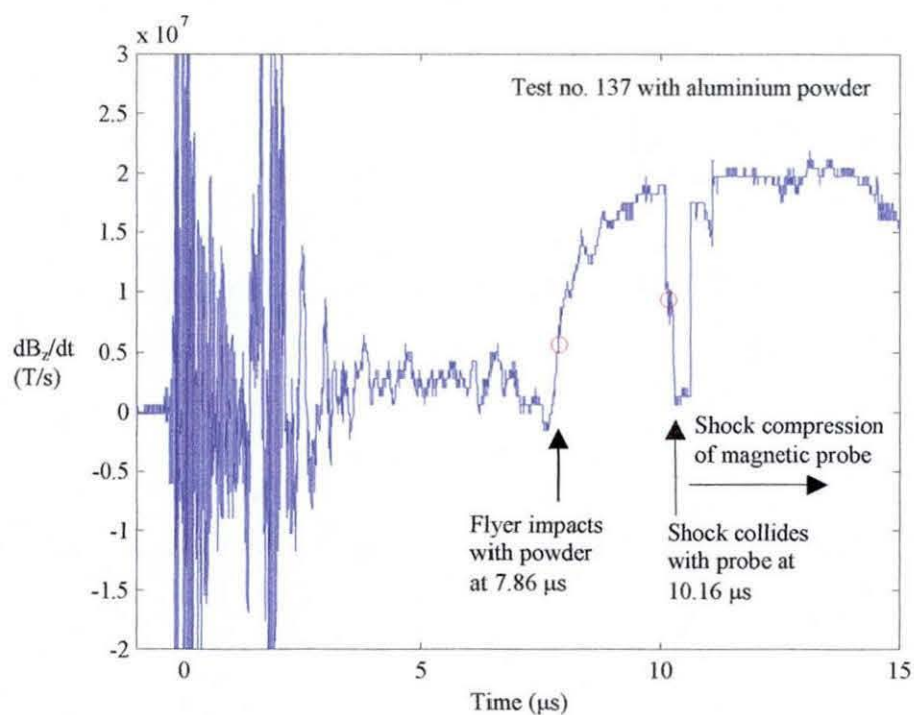


Figure 7-29 Measured $\frac{dB_z}{dt}$ for experiment with aluminium powder.

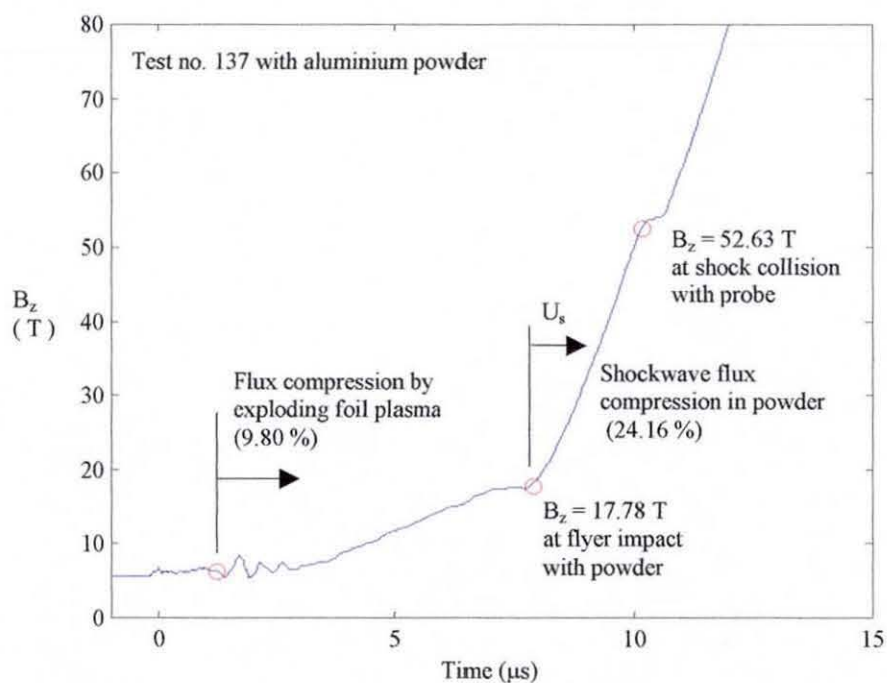


Figure 7-30 Flux density obtained by integration of Fig 7-29.

7.4.6 Final Compressed Flux Density – without Aluminium Powder

One of the best results for a flux compression experiment without aluminium powder is described below, to highlight the difference between flux compression by the foil plasma and that by a shockwave in powder.

From Fig 7-32a, it can be seen that the quality of the foil explosion in test no. 181 was better than that in test no. 137, with the flyer velocity estimated at 1.5 km/s on impact with the magnetic probe (Fig 7-32d). The other parameters of the electric gun of Figs 7-31 and 7-32 are similar to those for test no. 137. The high-frequency noise in the $\frac{dI_b}{dt}$ signal of 7-32a was caused by the poorer signal conditioning circuit in the Hewlett-Packard digital oscilloscope used for this experiment.

Fig 7-33 shows the $\frac{dB_z}{dt}$ signal obtained in test no. 181, when no aluminium powder was used. The distinctive pulse in the signal indicates the initial flyer impact with the epoxy-cast magnetic probe, which is followed by shock compression of the probe and possibly by its eventual destruction. Although the magnetic flux density of Fig 7-34, obtained by numerical integration of the $\frac{dB_z}{dt}$ signal of 7-34, shows a peak value of about 37 T , this includes the increase in the flux density resulting from shock compression of the magnetic probe. Thus when calculating the flux conservation coefficient, the B_z value (19.35 T) at the point of flyer impact with the probe should be used, giving a flux conservation coefficient of 10.67%, which is consistent with the 9.8% obtained for the foil plasma compression stage in test no. 137.

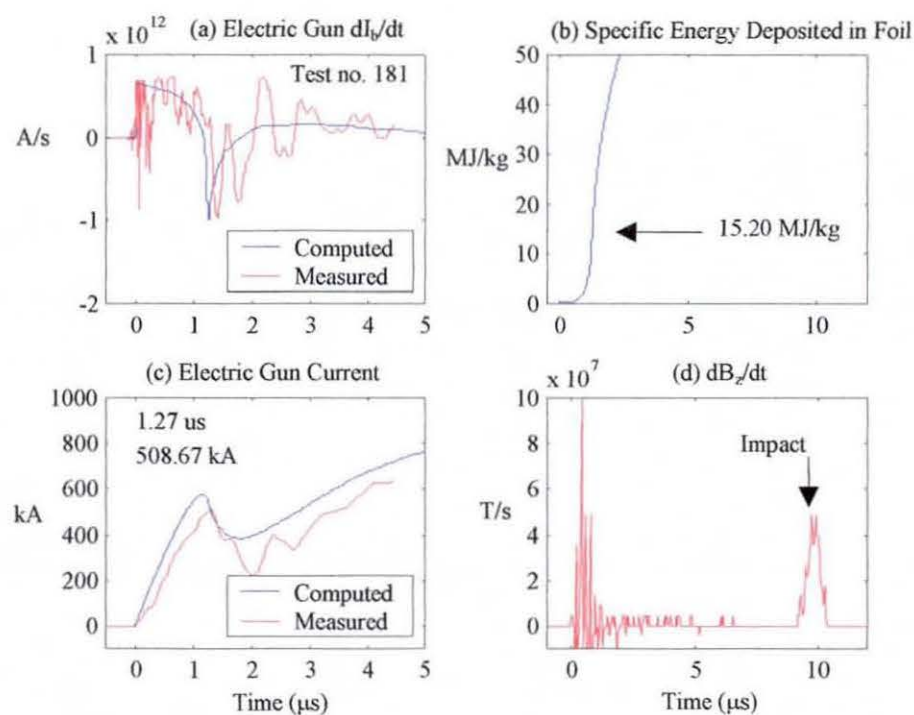


Figure 7-31 Computed and experimental results (test no. 181).

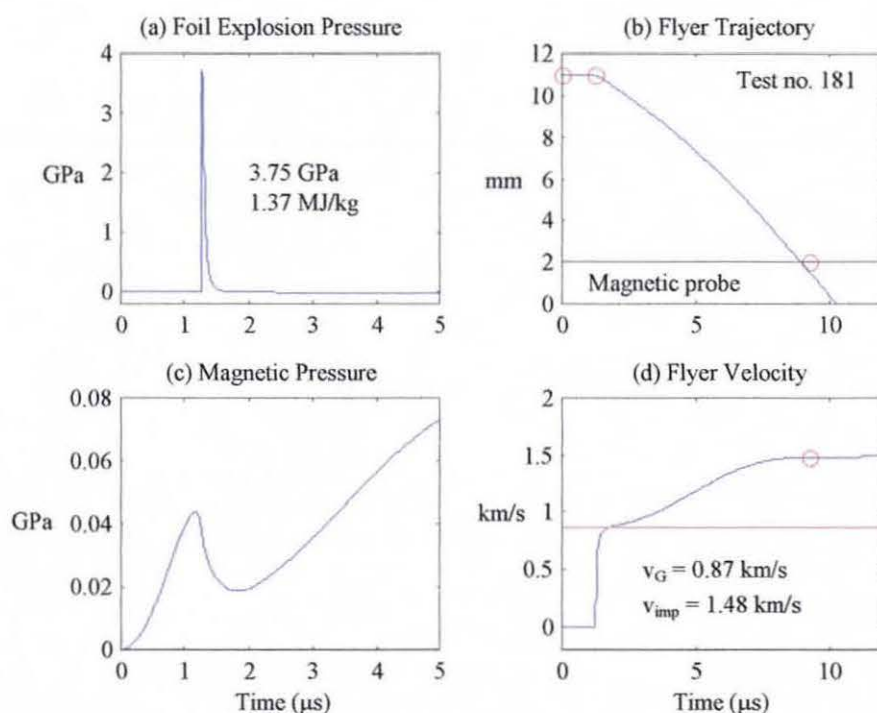


Figure 7-32 Computed and experimental results (test no. 181).

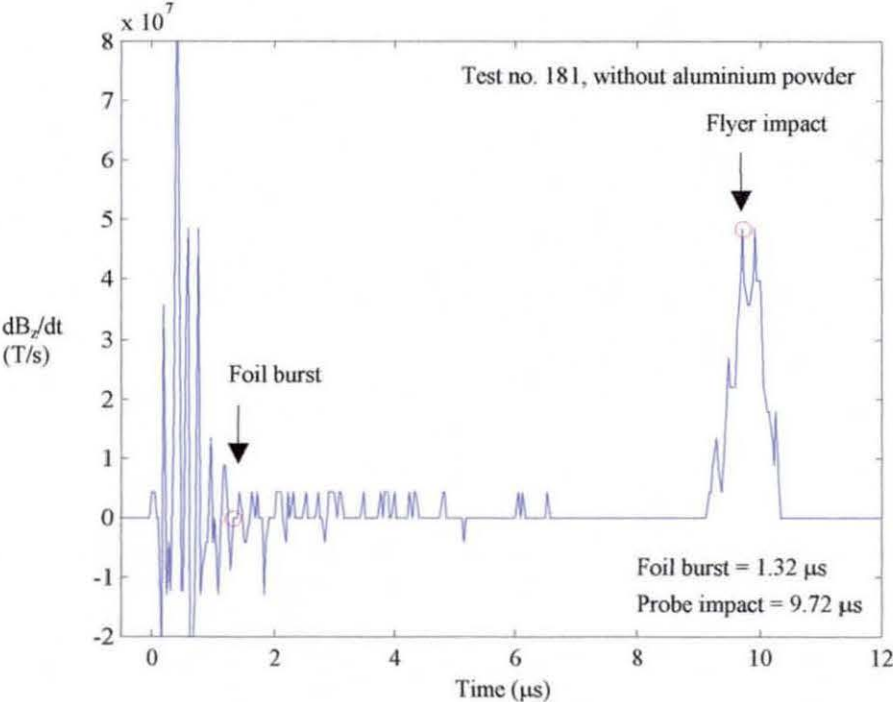


Figure 7-33 Measured $\frac{dB_z}{dt}$ for experiment without aluminium powder.

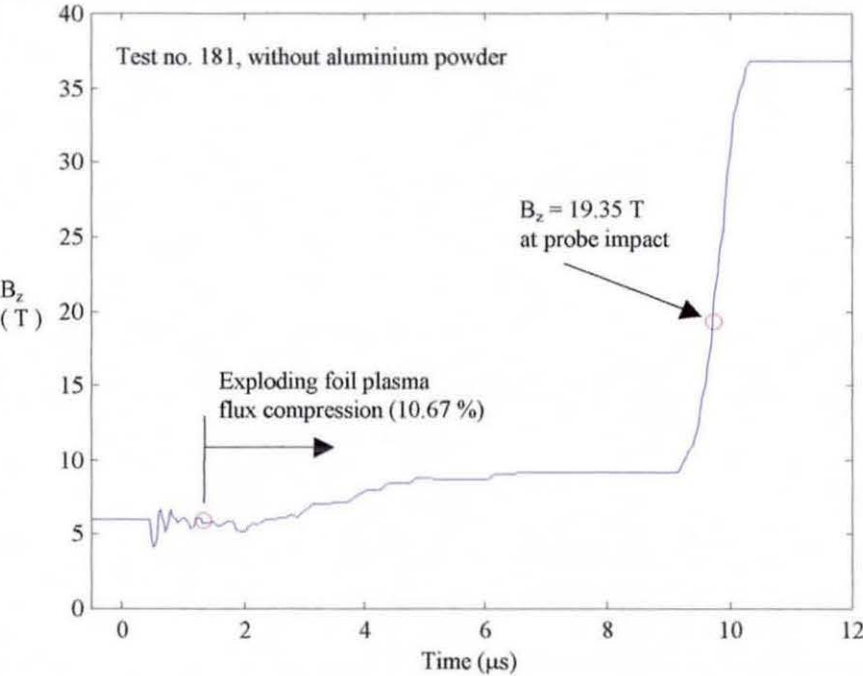


Figure 7-34 Flux density obtained by integration of Fig 7-33.

7.5 Numerical Analysis

7.5.1 Flux Compression Model

Although the MHD model of chapter 6 could be used to analyse the experimental results, the close coupling of the hydrodynamic flow calculation with Maxwell's equations makes it unwieldy, because partitioning of the MHD model in the way described in chapter 5 is not possible.

In this section a flux compression model is described, based on a system of coupled, first-order ordinary differential equations, that can be used to reveal the important controlling parameter for the flux compression process. This resulting information can be used to guide the analysis by the MHD model.

If the effect of the magnetic pressure on the flow calculation can be neglected, the flux compression process is effectively described by the equation of motion for the shockwave

$$\frac{dr_s}{dt} = U_s \quad (7-18)$$

$$\frac{dU_s}{dt} = g(t) \quad (7-19)$$

and the equation for magnetic flux compression (see section 6.3.4)

$$\frac{dB_z}{dt} = -\frac{2}{r_s}(1-TD)B_zU_s \quad (7-20)$$

In equation (7-19), $g(t)$ is the derivative of the shock velocity function U_s , and is readily obtainable if the shock velocity U_s may be expressed in an analytical form. If however U_s is available in a functional form, equations (7-18) to (7-20) can be solved for a given set of initial conditions as in any initial value problem.

For the present analysis however, the primary aim (illustrated by Fig 7-35) is to make use of the available boundary conditions (in the form of measured TOA data and the dimensions of the powder sample) and the measured $\frac{dB_z}{dt}$ signal, to determine the characteristics of the shock velocity in the powder. Thus the problem becomes one of determining the unknown shock velocity function U_s that was responsible for producing the measured $\frac{dB_z}{dt}$ signal.

SIMPLIFIED ANALYSIS PROCESS

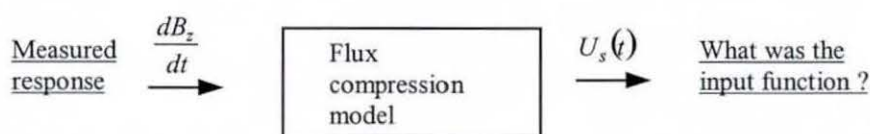


Figure 7-35 Simplified analysis method.

If the conducting shock front in the powder is assumed to travel at a constant speed, its trajectory can conveniently be described by a straight line connecting the TOA data ($t = 0$) at initial flyer impact with the TOA data ($t = t_{dur}$) for shock collision with the epoxy-cast probe, as shown in Fig 7-36. If a rigid wall boundary is further assumed for the outer surface of the probe, the shock front will remain at this position for all time after $t > t_{dur}$ (see Fig 7-36).

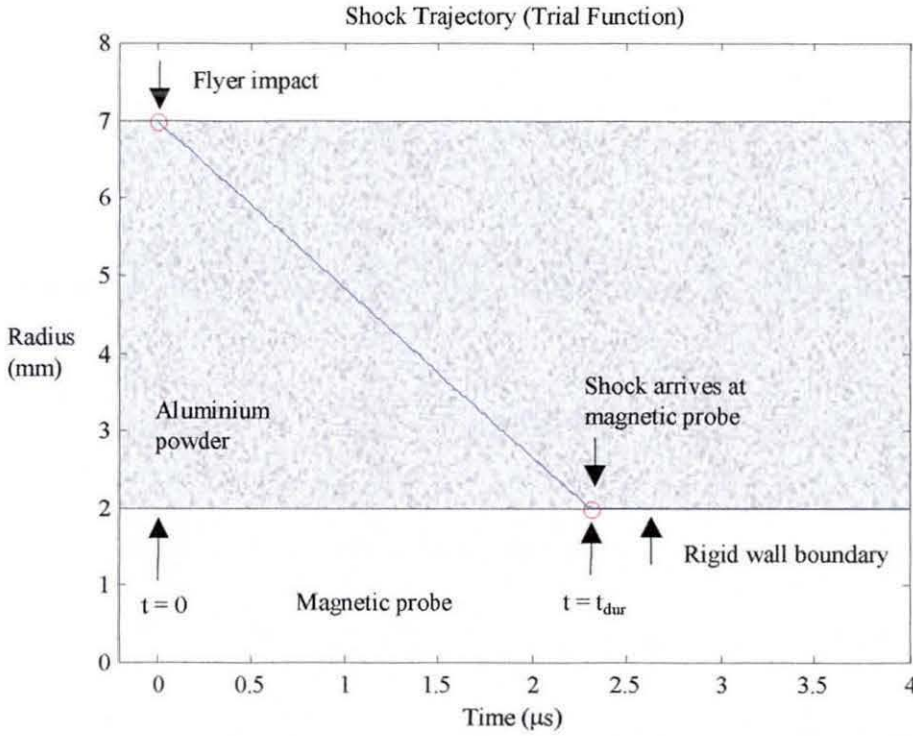


Figure 7-36 Shock trajectory (first estimate) in the simplified analysis method.

Once a trial function for the shock trajectory $r_s(t)$ is defined, the shock velocity $U_s(t)$ becomes the only unknown in equation (7-20), where $TD = 33\%$ is the theoretical density of the powder material, $\frac{dB_z}{dt}$ is the measured signal and B_z can be obtained by numerical integration (e.g. using a trapezoidal algorithm).

Re-writing equation (7-20) yields the shock velocity as

$$U_s = -\frac{r_s(t)}{2(1-TD)B_z} \frac{dB_z}{dt} \quad (7-21)$$

which can be solved readily to obtain a trial solution for the shock velocity function.

The trial solution for equation (7-21) shown in Fig 7-37 suggests that the shock velocity may be described by a constant 'flat top' velocity, followed by a linearly decreasing function. There is a short dwell-time of about $0.3 \mu s$ when the shock remained quasi-stationary at the outer surface of the magnetic probe, before continuing its inward

motion. This suggests that the epoxy-cast probe did not act as a rigid-wall boundary (to reflect the shock) but was actually compressed by the shockwave. The thin outer glass tube (of about 1 mm thickness) for the epoxy-cast probe may account for the $0.3 \mu\text{s}$ dwell-time, which could be the time needed by the shock to traverse the glass layer and enter the epoxy resin. It is believed that the epoxy resin may possibly not have been fully cured or hardened, making it susceptible to compression by the shockwave and giving a small abrupt jump in velocity at the glass-epoxy interface. This is similar to the situation at a free-surface, when a shock emerges from a material of a higher density.

Based on this possible explanation, only the $\frac{dB_z}{dt}$ signal before shock collision with the epoxy-cast probe should count towards the actual shockwave flux compression in powder, and any signal picked up by the magnetic probe thereafter should be considered as spuriously contributed by the shock compression of the epoxy-cast probe.

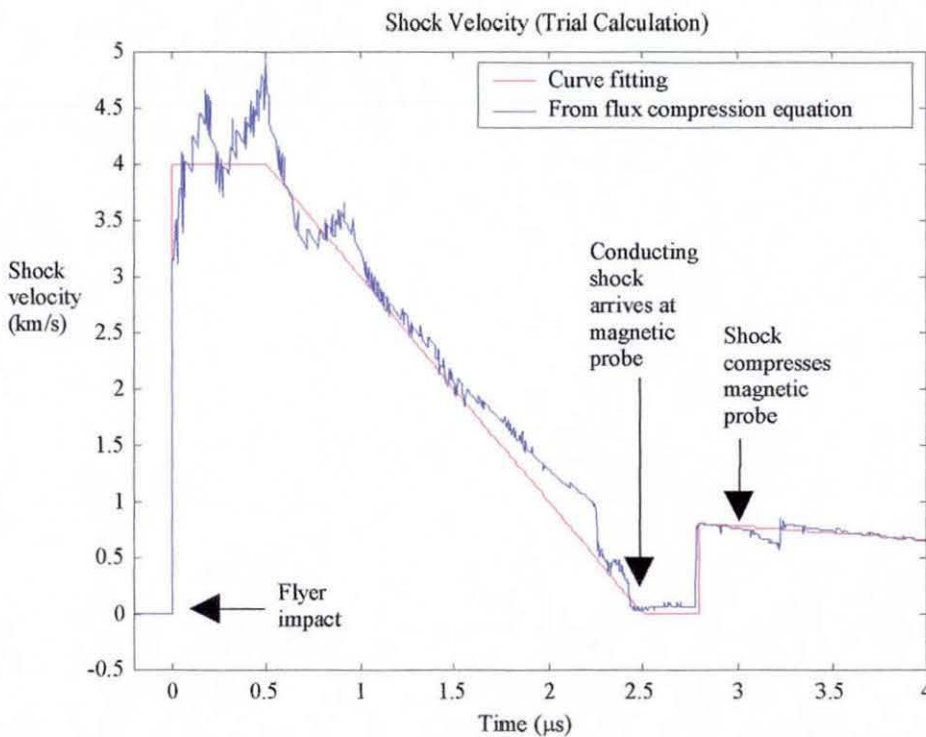


Figure 7-37 Shock velocity obtained by solving equation (7-21).

Although the trial solution of Fig 7-37 is only a first estimate based on the (inexact) linear shock trajectory of Fig 7-36, it nevertheless demonstrates the main characteristics of the shock velocity function. To facilitate the search for the function that has produced the measured $\frac{dB_z}{dt}$ signal, the trial solution of Fig 7-37 is approximated by an analytical trial function, so that $g(t)$ of equation (7-19) can be replaced by the derivative of the analytical trial function. The resulting system of ordinary differential equations (7-18) to (7-20) can be solved numerically, with the free parameters being those needed to define the analytical trial functions. These are adjusted until good agreement is obtained between computed and measured $\frac{dB_z}{dt}$ signals.

Initially, the analytical trial function consisted of (1) a constant (flat-top) velocity followed by (2) a linearly decreasing term. However, after several iterations, it was found that an exponentially decreasing term produced results that agreed better with the measured $\frac{dB_z}{dt}$ signal. The shock velocity function, which takes into account the shock compression of the magnetic field probe, is defined by

$$U_s(t) = \begin{cases} U_{s1} & \text{if } t_{imp} < t \leq (t_{imp} + t_1) \\ U_{s1} \exp\left(-\frac{t - t_{imp} - t_1}{\tau_1}\right) & \text{if } (t_{imp} + t_1) < t \leq (t_{imp} + t_2) \\ 0 & \text{if } (t_{imp} + t_2) < t \leq (t_{imp} + t_3) \\ U_{s2} \exp\left(-\frac{t - t_{imp} - t_3}{\tau_2}\right) & \text{if } t > (t_{imp} + t_3) \end{cases} \quad (7-22)$$

with the definition for the free-parameters shown in Fig 7-38.

The results of Figs 7-39 and 7-40 were obtained by solving the system of ordinary differential equations (7-18) to (7-20), with the free-parameters $U_{s1} = 4.0 \text{ km/s}$, $t_1 = 0.5 \mu\text{s}$, $\tau_1 = 0.96 \mu\text{s}$, $t_2 = 2.5 \mu\text{s}$, $t_3 = 2.8 \mu\text{s}$, $U_{s2} = 0.5 \text{ km/s}$ and $\tau_2 = 1.5 \mu\text{s}$.

It is clear from Fig 7-40 that reasonable agreement exists between the measured and the computed results.

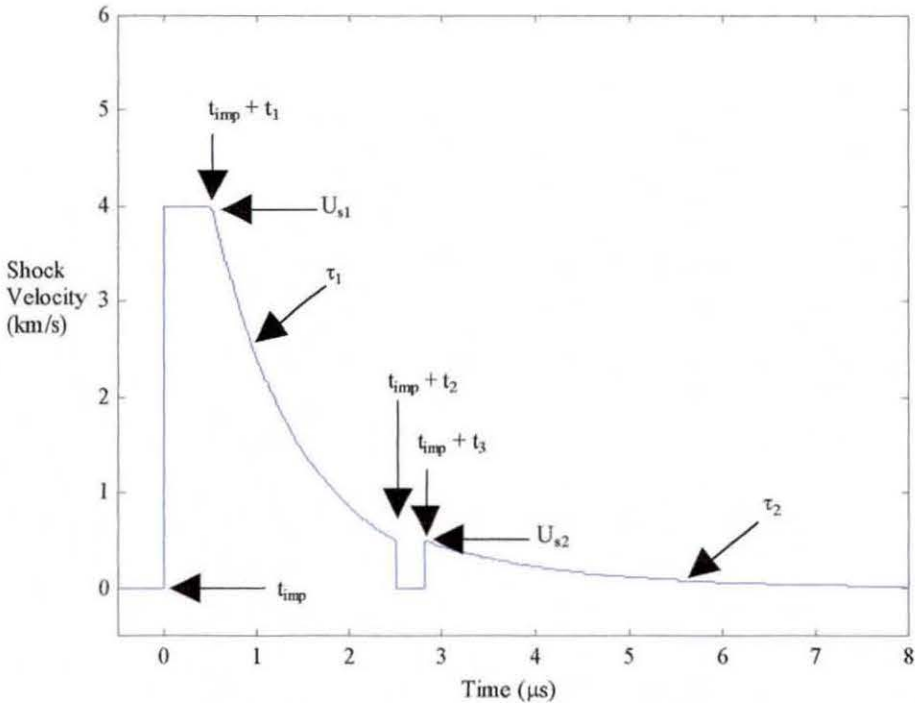


Figure 7-38 Definition of shock velocity function.

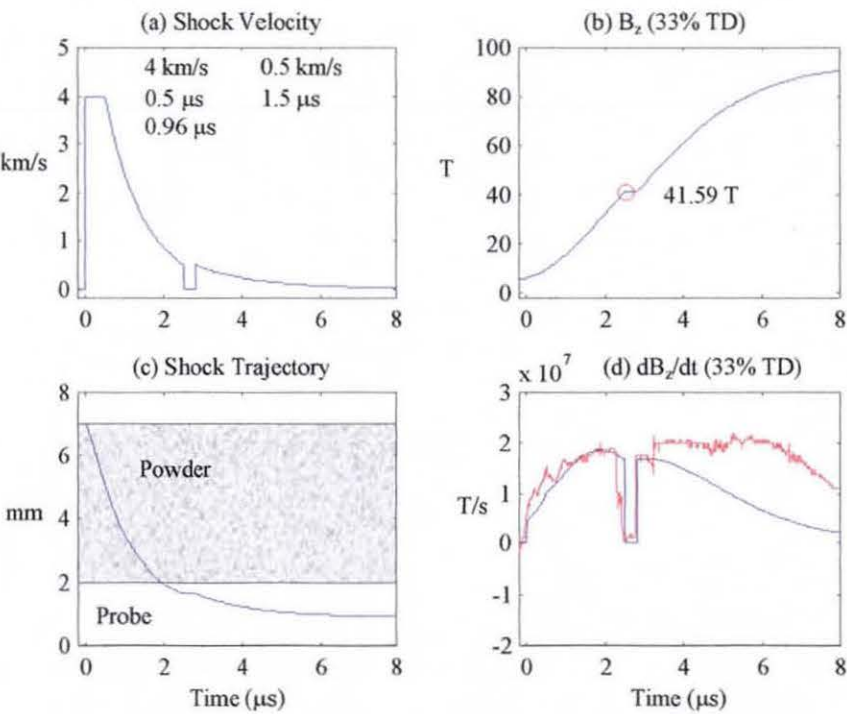


Figure 7-39 Results from the flux compression model.

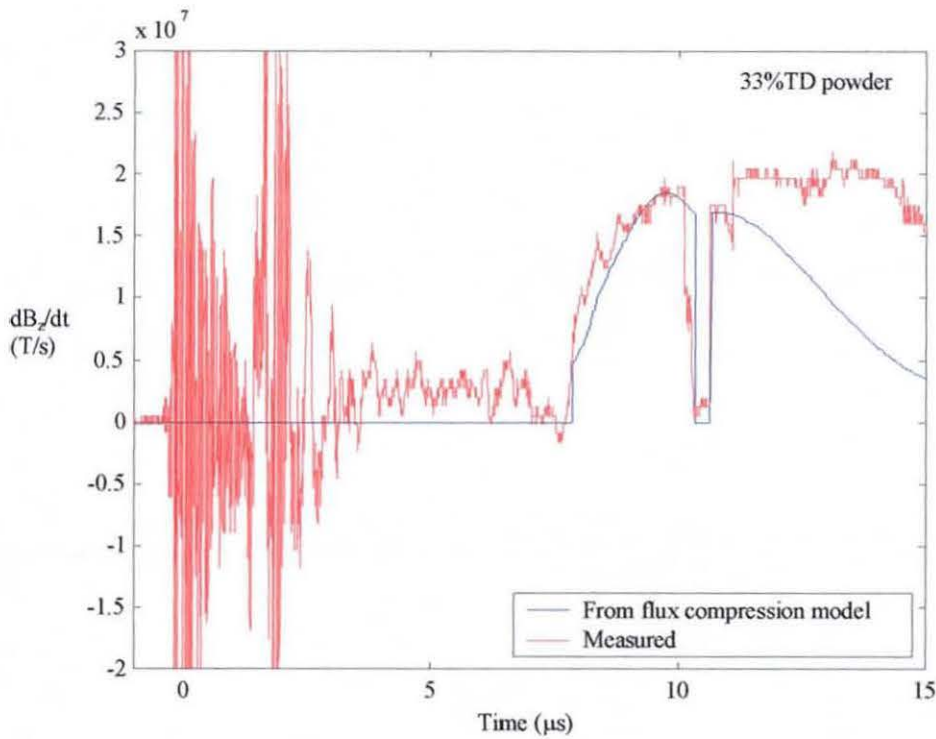


Figure 7-40 Comparison of measured and computed $\frac{dB_z}{dt}$ signals.

7.5.2 MHD Model

The results from the flux compression model of the previous section indicate that the shock velocity (and with it the shock pressure) on impact has the shape of an initial 'flat-top' period, followed by an exponential decay. This information was used as a guide to define the impact pressure required by the MHD model.

a) Considerations for numerical simulation

Since the compression of magnetic flux by the exploding foil plasma has been found (see section 7.4.6) to be somewhat low (about 10%), it is not included in the MHD model. A single-material MHD code was therefore used to describe the shockwave flux compression process in powder, starting from the point of flyer impact. The powder material was represented by 60 computing elements (Fig 7-41) and the flyer impact was simulated by applying an impact pressure (Fig 7-42a) to the external boundary of the powder material.

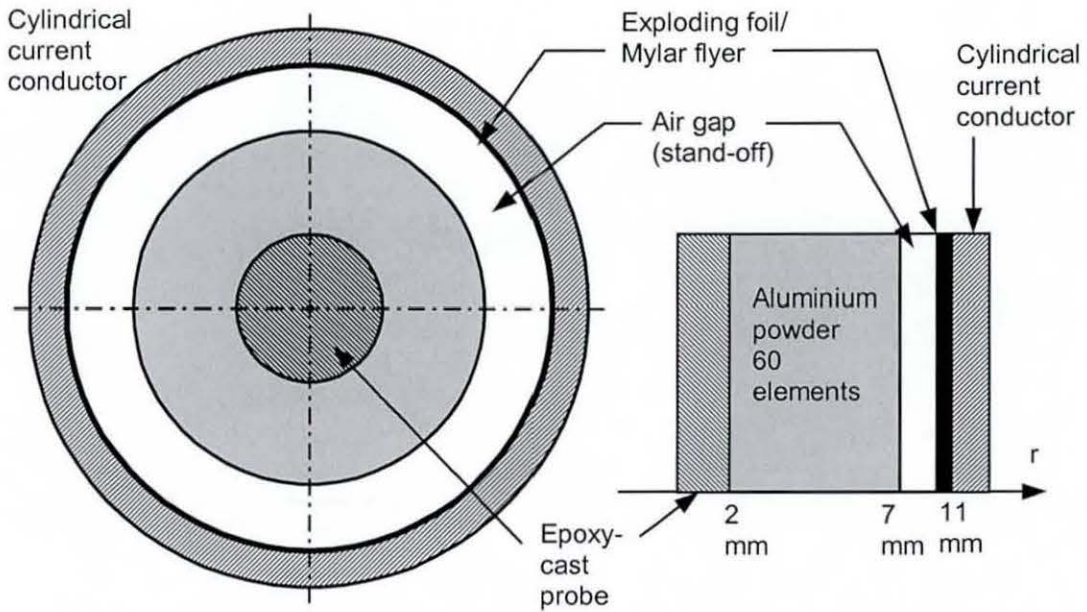


Figure 7-41 Computational grid for magnetic flux compression by cylindrical implosion.

The outer surface of the epoxy-cast probe is modelled as a rigid-wall boundary to limit the scope of the computation, and calculation ceases when the conducting shock front collides with the magnetic probe. At this time all the powder elements are behind the shock front and are in a highly compressed and conducting state. Despite the continued movement of the powder elements at their particle velocities, the conducting shock front remains quasi-stationary at the powder-probe interface, resulting in an abrupt drop in the shock velocity to zero ($U_s = 0$) and the distinctive notch in the $\frac{dB_z}{dt}$ signal.

b) Numerical results

Figs 7-42 and 7-43 show the results obtained by the MHD model for an impact pressure with a peak value of 12 GPa and a flat-top duration of 190 ns, followed by an exponential decay at a time constant of 20 ns (Fig 7-42a). A small quasi-constant pressure term of 0.1 GPa, consistent with results from the electric gun model (Fig 7-22c), was used for simulation of the magnetic pressure.

The shape of the pressure pulse (flat-top with exponential decay) used for simulating the impact pressure appears to be consistent with predictions using shockwave theory (see section 5.3.6). The flat-top duration has previously been calculated (section 5.3.6.4) as between 166.7 ns and 224.8 ns for a $250\text{ }\mu\text{m}$ Mylar flyer impacting 33% TD aluminium powder at an impact velocity of 3.0 km/s .

Compression of the aluminium powder is shown in the distortion of the Lagrangian computational grid of Fig 7-42c, with the conducting shock front (Fig 7-42b) arriving at the magnetic probe after a time of about $2.5\text{ }\mu\text{s}$, consistent with TOA data from the measured $\frac{dB_z}{dt}$ signal. The shock velocity of Fig 7-42d has a shape very similar to that obtained previously using the flux compression model.

Following the same procedure as in chapter 6, the electrical conductivity of the aluminium powder is modelled by the simple switch model of chapter 4, and the shock-compressed region is assumed to have a conductivity that is a fraction k of the electrical conductivity of aluminium at solid density and stp. The free parameter k has been chosen as 30 (Fig 7-43a) to match the compressed magnetic flux density B_z of about 40 T (Fig 7-43d).

The somewhat significant difference in the shape of the computed and measured $\frac{dB_z}{dt}$ signals of Fig 7-43b is traceable to the constant value of k (30) used in modelling the shock-compressed aluminium powder. A time-varying function for the free-parameter k to take into account the effect of Joule-heating etc., is likely to produce results that agree better with the measured $\frac{dB_z}{dt}$ signal.

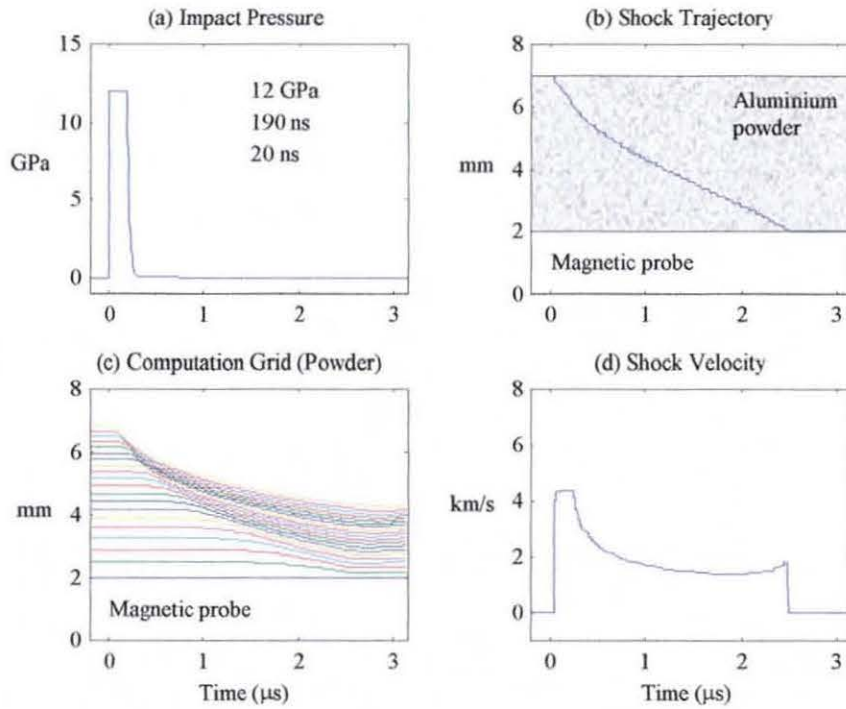


Figure 7-42 Results from MHD model, (a) impact pressure, (b) shock trajectory, (c) computational grid for powder, and (d) shock velocity.

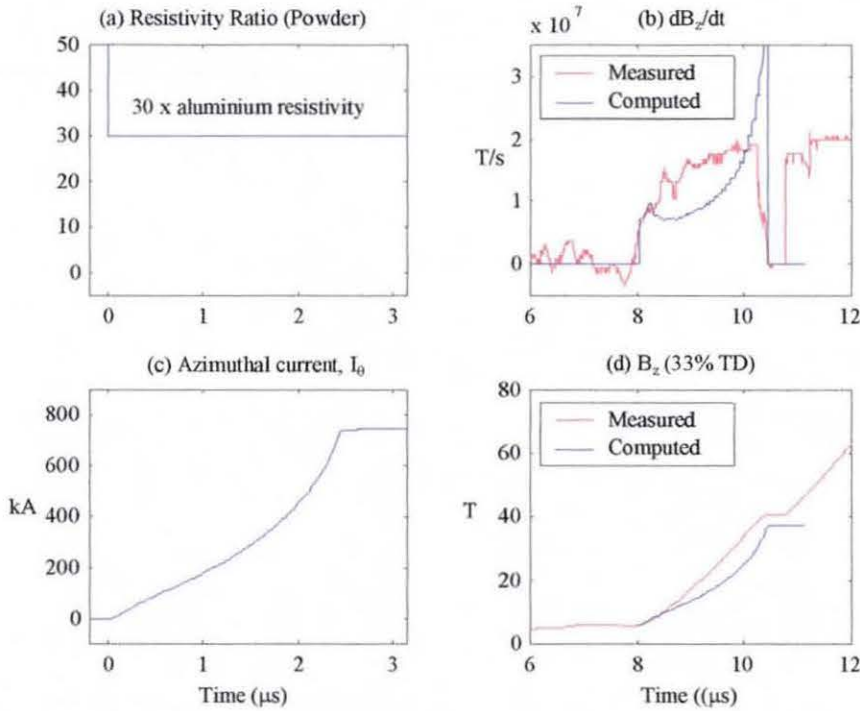


Figure 7-43 Results from MHD model, (a) resistivity ratio for shock compressed powder, (b) $\frac{dB_z}{dt}$, (c) azimuthal current I_θ and (d) B_z .

Fig 7-44 shows the compression of the magnetic flux density with time, with $0.1 \mu s$ as the interval between plots. Initially, the magnetic flux density of $6 T$ is uniformly distributed throughout the powder. It is compressed by the shockwave to a final value of $37 T$, with significant flux loss being indicated by the presence of magnetic flux behind the shock front.

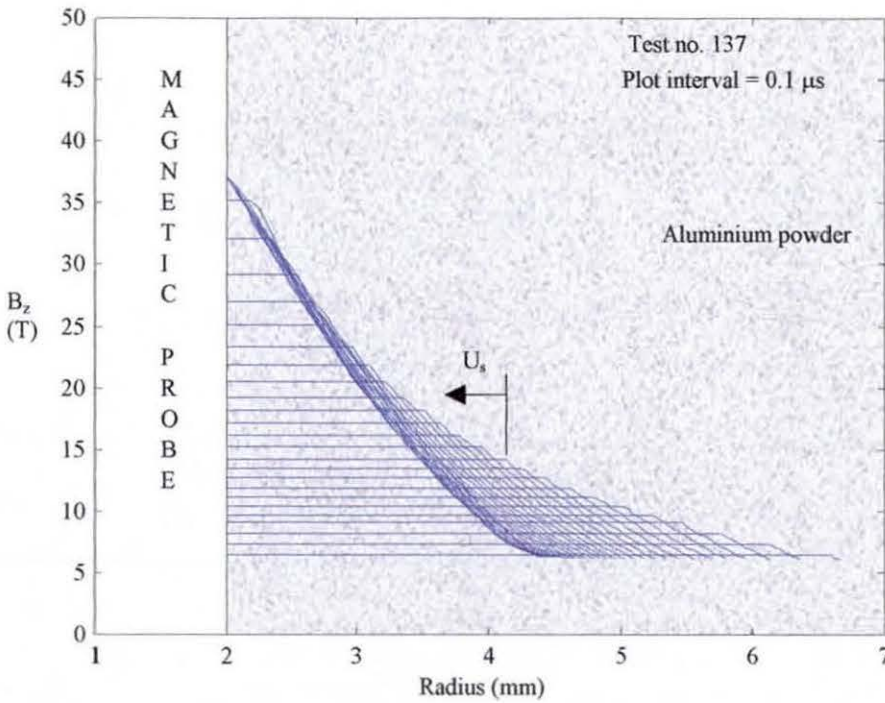


Figure 7-44 Magnetic flux density B_z .

7.6 Conclusions

Compression of magnetic flux by a shockwave in aluminium powder has been demonstrated in proof-of-principle experiments, where magnetic flux densities of about $40 T$ were obtained from an initial flux density of $6 T$. Although the quality of the foil explosion was not ideal, the large stand-off between the exploding foil and the powder assembly nevertheless allowed the flyer to be accelerated to impact velocity of between $1.1 km/s$ and $1.5 km/s$. Experimental data also provided additional proof of the rapidly decaying shock velocity resulting from Mylar flyer impact with aluminium

powder, in direct contrast with the steady shock velocity (due to quasi-static explosion pressure) in explosive driven experiments [29] previously analysed in chapter 6.

A simplified analysis using the flux compression model has enabled the main characteristics of the shock velocity in powder to be determined with reasonable accuracy. The simplified method is used again in chapter 8 for the analysis of experimental results from the dynamic powder transformer.

SHOCKWAVE GENERATION OF HIGH-VOLTAGE PULSES

This chapter details experiments aimed at producing high-voltage pulses by installing a helical coil (surrounded by a thin layer of aluminium powder) inside the cylindrical imploder of a dynamic transformer configuration. Although experiment results were obtained for a pulse with only about 10 kV peak voltage and 3 μ s duration, the data nevertheless provided a unique insight into the mechanism of high-voltage generation by exploding-foil flyer impact. A simplified analysis and design method that combines the shock propagation model with the dynamic transformer model is described, to allow the systematic design and performance prediction of such transformer. Performance limits are indicated for the present cylindrical imploder configuration.

8.1 Dynamic Powder Transformer

The term dynamic powder transformer is used here to describe a configuration in which an electrically conducting converging shockwave in aluminium powder acts as the dynamic primary coil and a centrally-located helical coil as the secondary coil. In the configuration shown in Fig 8-1, a converging shockwave generated by flyer impact with aluminium powder compresses an initially established magnetic field to provide a time-varying magnetic flux density, which is coupled by the helical coil to produce a high-voltage pulse in the load.

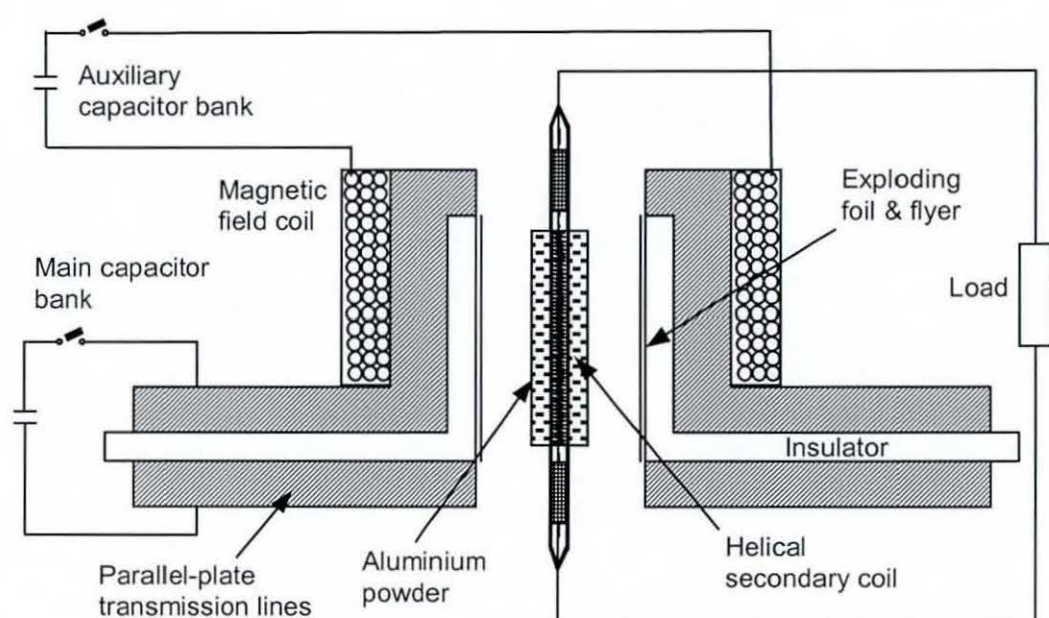


Figure 8-1 Generation of high-voltage pulses using dynamic powder transformer.

8.1.1 Helical Coil with Epoxy Insulation

Following the method of inductive probe construction described in chapter 7, epoxy resin was used to insulate the helical secondary coil. Epoxy resin is known to have excellent properties for use as high-voltage insulation, see Table 8-1, and it has been used as an encapsulating medium for high-power transformers [125].

Table 8-1 Properties of epoxy-cast mouldings [126]

Breakdown field strength	15 kV / mm
Resistivity	$10^{12} \Omega m$
Dielectric constant	3 to 4
Mass density	1.2 to 1.8 g / cc
Tensile strength	80 to 90 MPa
Young's E-modulus	4 to 12 GPa

Fig 8-2 shows the epoxy-cast helical coil that was used with a single-turn primary coil in a static transformer configuration to obtain an estimate of the electrical breakdown strength of epoxy resin. The helical coil was wound using 0.3 mm diameter wire with a 1.0 mm pitch on a 17 mm PVC mandrel, giving 79 turns over a length of 80 mm . An exploding copper foil in the primary circuit produced a current pulse with a $\frac{dI}{dt}$ exceeding 1 TA/s , which is coupled to the helical secondary coil to produce a high-voltage pulse of several hundred kilovolts on a non-inductive load. The measured peak voltage of up to 200 kV (Fig 8-3) indicates that the epoxy-cast helical coil is capable of withstanding a peak electric field of about 2.5 kV/mm (equivalent to 2.5 kV between turns).



Figure 8-2 Epoxy-cast helical coil used for static transformer testing.

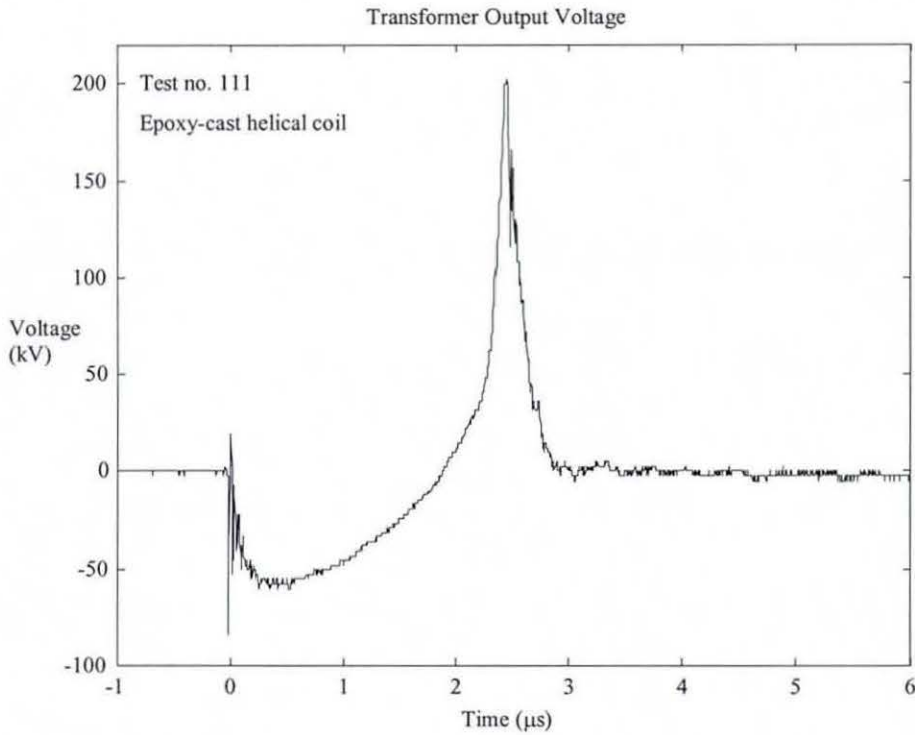


Figure 8-3 Result from static transformer testing.

8.1.2 Helical Coil with Powder Assembly

Fig 8-4 shows a 600-turn helical secondary coil wound on a 3.3 mm diameter glass mandrel using 62.5 μm diameter enamel wire and cast in epoxy resin in a glass tube with an outer diameter of 5.9 mm. The length of the helical coil was 50 mm, corresponding to the width of a barrel formed by the set of PVC holders that are used to guide the Mylar flyer on its flight towards the powder assembly. After the epoxy resin has set, a layer of aluminium powder is placed around the coil assembly and held in place by a cylindrical container made from 7 μm Mylar sheet. The ends of the PVC barrel were machined to give a sharp edge, termed the clipper, [40] to give a clean shearing of the Mylar flyer during the initial foil explosion and acceleration stage.

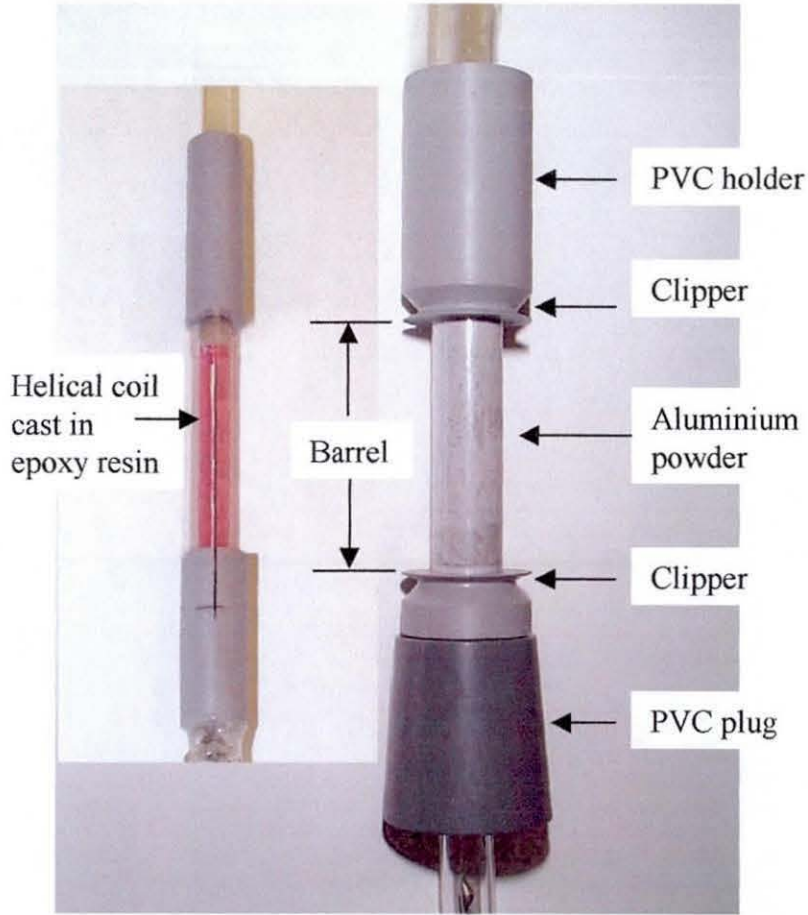


Figure 8-4 Epoxy-filled multi-turn helical coil with powder assembly.

8.2 Experiments with Dynamic Powder Transformer

8.2.1 Experimental Arrangements

The experimental arrangement of Fig 8-5 is in many ways similar to that used for the flux compression experiments of chapter 7, but with the inductive pick-up probe replaced by the multi-turn helical secondary coil with a thin layer of aluminium powder surrounding it. A voltage divider formed by a pair of copper-sulphate resistors is used to attenuate the output voltage to a level suitable for measurement by a Tektronix high-voltage probe. In addition, a Rogowski coil measures the current in the output circuit. A trigger coil in the auxiliary capacitor bank circuit provides the means to trigger the discharge of the main capacitor bank at a time when the magnetic flux density in the imploder has reached a maximum.

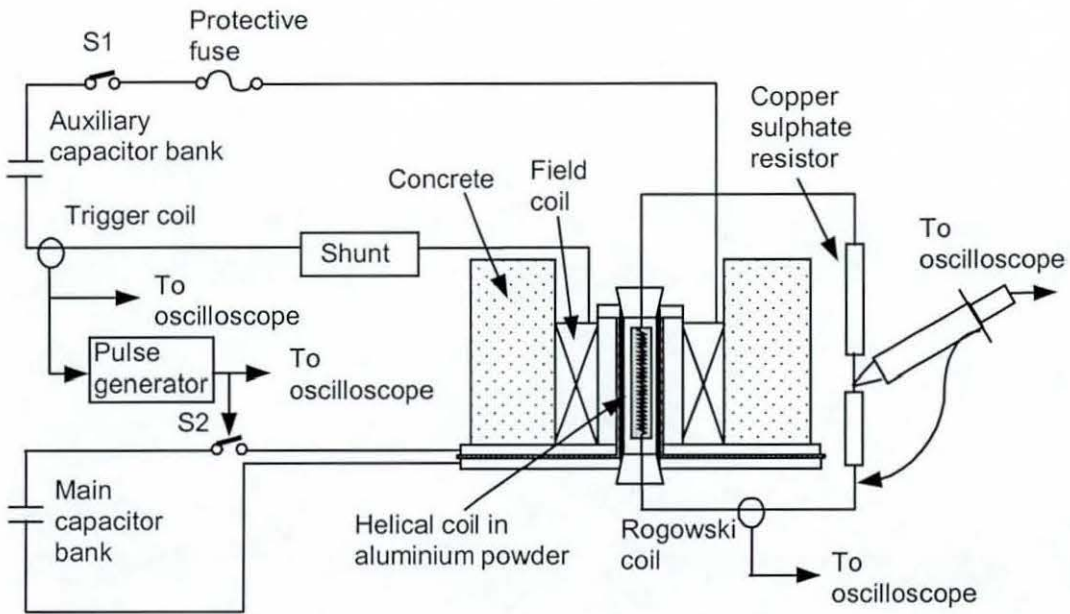


Figure 8-5 Experimental arrangements for dynamic powder transformer experiments.

8.2.2 Electric Gun Performance

Figs 8-6 and 8-7 compare experimental results with corresponding results from the new electric gun model described in chapter 3. Figs 8-6a and 8-6b show good agreement between computed and measured results for current and $\frac{dI_b}{dt}$ in the gun circuit following closure of the main switch $S2$, which is an indication of the accuracy of the exploding foil model used in the calculation. The energy density at burst is calculated at 15.13 MJ/kg (Fig 8-6c), giving an explosion pressure of 18 GPa (Fig 8-7a), while from Fig 8-7c the magnetic pressure exerted by the current in the gun circuit on the Mylar flyer can be seen to have a maximum of 0.06 GPa .

In Fig 8-6d, the current in the load circuit measured by the Rogowski coil shows an abrupt jump at $2.80 \mu\text{s}$, which is indicative of the flyer impact and the impulsive start of the conducting shock front in the powder. The energy density at burst (15.13 MJ/kg) gives a Gurney terminal velocity of 3.23 km/s (fig 8-7d) and the flyer trajectory of Fig 8-7b, both of which confirm the interpretation of the TOA data of Fig 8-6d.

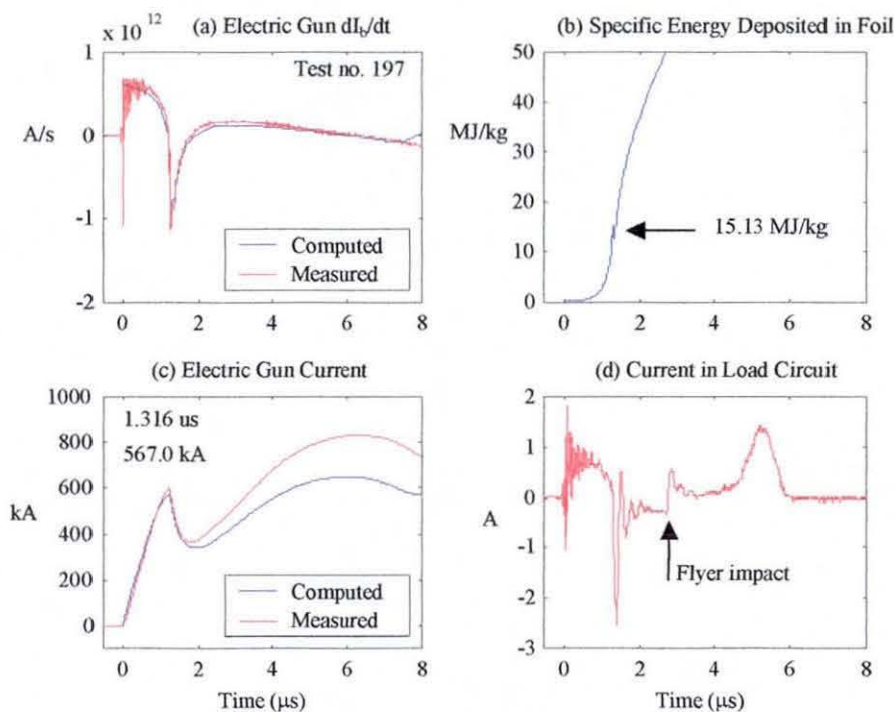


Figure 8-6 Comparison of measured and computed results.

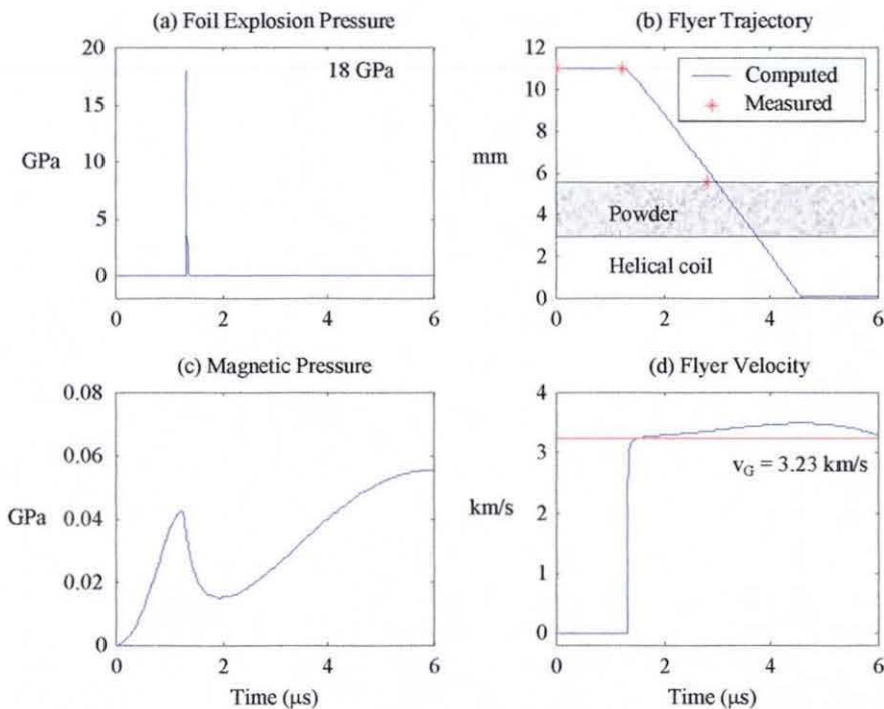


Figure 8-7 Computed results for flyer acceleration process (75 μm Mylar).

8.2.3 Initial Magnetic Flux Density

The shape of the voltage pulse of Fig 8-8a shows that the trigger-coil (see Fig 8-5) produces an output pulse that is proportional to the time-rate-of-change of current in the auxiliary circuit. This pulse is sent to the pulse generator, which detects the initial crossing of a threshold level (at about 5 V) and, after a preset delay, sends a 18 V pulse (of Fig 8-8b) to the Blumlein system to trigger closure of the dielectric switch (*S2* in Fig 8-5) in the main capacitor bank circuit and start the implosion process. At time $t = 0$ in Fig 8-8, the trigger coil has a near-zero voltage, indicating that the current in the auxiliary circuit (and with it the external magnetic field) is near its maximum value. Although the initial magnetic flux density was not measured during the experiment, comparison of Fig 8-8 with previously measured trigger-coil data nevertheless confirms that the experiment proceeded as planned with an initial flux density of 6 T.

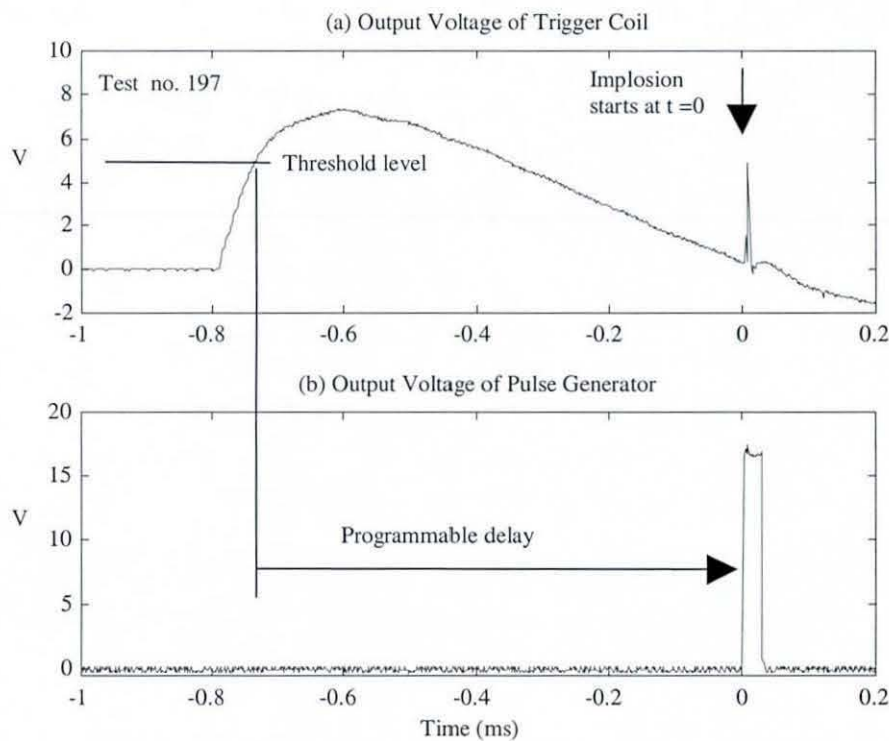


Figure 8-8 Experimental results.

8.2.4 Transformer Output Voltage

Fig 8-9 shows that good agreement exists between the voltage measured by a Tektronix probe and that calculated by multiplying the current measured by the Rogowski coil by the total resistance of the copper-sulphate voltage divider

$$V_{out} = I_{out} R_{load} \quad (8-1)$$

In this experiment, the outer diameter of the powder layer was 5.5 mm (Fig 5-5b) from the exploding foil and the time to flyer impact was 1.58 μs (2.80 μs - 1.22 μs). This gives an average flyer velocity of 3.49 km/s, which is in good agreement with the Gurney terminal velocity of 3.23 km/s calculated by the electric gun model.

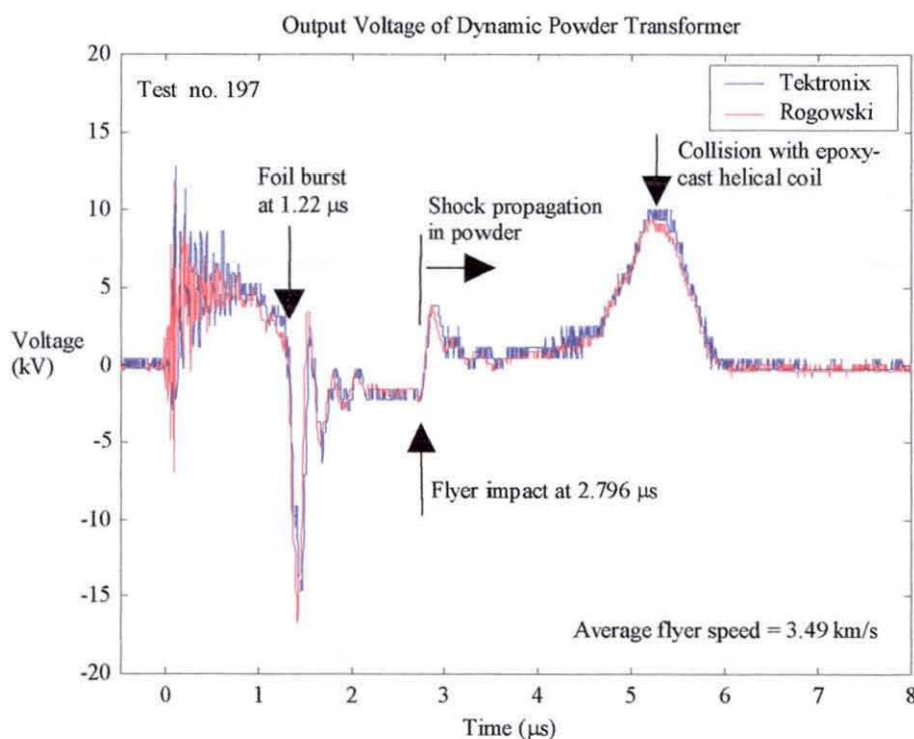


Figure 8-9 Average flyer speed determined from TOA data.

8.2.5 Circuit Analysis

8.2.5.1 Circuit Model for Dynamic Powder Transformer

The shape of the output voltage in Fig 8-9 suggests that two mechanisms are involved in its production (1) mutual coupling with the current in the electric gun circuit and (2) propagation of a conducting front in the shock-compressed powder. Operation of the dynamic powder transformer in this particular configuration can thus be described in two phases using the equivalent circuit of Figs 8-10a and 8-10b, where L_s and R_s are the inductance and resistance of the helical secondary coil and R_{load} is the total resistance of the copper-sulphate voltage divider. L_{load} is the self-inductance of the output circuit and I_{out} is the current measured by the Rogowski coil.

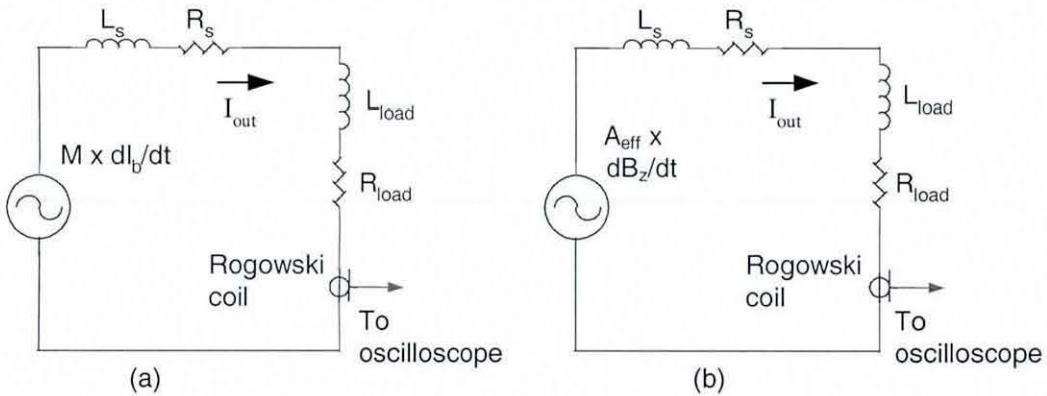


Figure 8-10 Equivalent circuit (a) before flyer impact and (b) after flyer impact.

Before flyer impact ($t < t_{imp}$), the current in the secondary (or output) circuit is governed by

$$M \frac{dI_b}{dt} = (R_s + R_{load}) I_{out} + (L_s + L_{load}) \frac{dI_{out}}{dt} \quad (8-2)$$

where M is the mutual inductance and $\frac{dI_b}{dt}$ is the rate of change of current in the electric gun circuit.

A simplified form

$$M \frac{dI_b}{dt} = R_{load} I_{out} = V_{out} \quad (8-3)$$

can be used when the inductive voltage component is much less than the resistive one, or

$$(R_s + R_{load}) I_{out} \gg (L_s + L_{load}) \frac{dI_{out}}{dt} \quad (8-4)$$

After flyer impact ($t \geq t_{imp}$), the output current measured by the Rogowski coil is governed by

$$A_{eff} \frac{dB_z}{dt} = (R_s + R_{load}) I_{out} + (L_s + L_{load}) \frac{dI_{out}}{dt} \quad (8-5)$$

where A_{eff} is the effective pick-up area of the helical secondary coil (with radius r_h), given by

$$A_{eff} = N\pi r_h^2 \quad (8-6)$$

and $\frac{dB_z}{dt}$ is the time rate of change of magnetic flux density resulting from the converging shock front in the aluminium powder. In the absence of a load, the open-circuit output voltage for the secondary coil is

$$V_{out} = A_{eff} \frac{dB_z}{dt} \quad (8-7)$$

Following the simplified analytical treatment of chapter 7, a set of coupled first-order differential equations may be used to described the dynamic powder transformer as

$$\frac{dr_s}{dt} = U_s \quad (8-8)$$

$$\frac{dU_s}{dt} = g(t) \quad (8-9)$$

$$\frac{dB_z}{dt} = -\frac{2}{r_s}(1-TD)B_z U_s \quad (8-10)$$

$$\frac{dI_{out}}{dt} = -\left(\frac{A_{eff}}{L_s + L_{load}}\right)\frac{dB_z}{dt} - \left(\frac{R_s + R_{load}}{L_s + L_{load}}\right)I_{out} \quad (8-11)$$

where $g(t)$ is the time-derivative of the shock velocity $U_s(t)$ and equation (8-11) is obtained by re-writing equation (8-5). Equation (8-10) is obtained by combining equation (2-30) for shockwave flux compression with equation (4-78) for the EOS of the powder material as previously shown in chapter 6.

Equations (8-8) to (8-11) form the basis of the dynamic powder transformer model, which describes completely the behaviour of the transformer if the shock velocity function $U_s(t)$ is available in a functional form that allows $g(t)$ to be obtained by differentiation.

8.2.5.2 Velocity of the Conducting Shock Front

It is clear from Fig 8-9 that the shock velocity in the powder has a characteristic 'U-shape', similar to that seen in chapter 5

$$U_s(t) = U_{s1} + U_{s2} \exp\left(-\frac{t-t_{imp}}{\tau_1}\right) + U_{s3} \exp\left(\frac{t-t_{imp}-t_{dur}}{\tau_2}\right) \quad (8-12)$$

where U_{s1} , U_{s2} , U_{s3} , τ_1 and τ_2 are constants previously defined in Fig 5-31 and t_{imp} and t_{dur} are TOA data obtainable from Fig 8-9.

By substituting the time-derivative of the shock velocity $\frac{dU_s}{dt}$ into equation (8-9), the system of equation becomes

$$\frac{dr_s}{dt} = U_s \quad (8-13)$$

$$\frac{dU_s}{dt} = -\frac{U_{s2}}{\tau_1} \exp\left(-\frac{t-t_{imp}}{\tau_1}\right) + \frac{U_{s3}}{\tau_2} \exp\left(\frac{t-t_{imp}-t_{dur}}{\tau_2}\right) \quad (8-14)$$

$$\frac{dB_z}{dt} = -\frac{2}{r_s}(1-TD)B_z U_s \quad (8-15)$$

$$\frac{dI_{out}}{dt} = \left(\frac{A_{eff}}{L_s + L_{load}}\right) \frac{dB_z}{dt} + \left(\frac{R_s + R_{load}}{L_s + L_{load}}\right) I_{out} \quad (8-16)$$

which can be solved to obtain the shock velocity function, using both the initial and boundary conditions corresponding to flyer impact and shock collision with the epoxy-cast helical coil.

The system of equations has been solved and the results obtained are compared with the output current measured by the Rogowski coil in Fig 8-11. For mathematical convenience, the calculation was carried out with the flyer impact time t_{imp} set to zero, and in Fig 8-11d the computed current is time-shifted to facilitate comparison with the measured current. It is clear from Fig 8-11d that the computer model is able to reproduce the measured current fairly accurately until the shock front collides with the helical coil, when the calculation is stopped.

The comparison of the computed results with the measured voltage in Fig 8-12 shows a DC offset error of about 2.5 kV , possibly because the helical secondary coil was not connected physically to the same ground (or 0 V) reference as the capacitor bank of the electric gun. However, the presence of a DC offset does not detract from the reasonably good agreement between computed and measured voltage shown in Fig 8-13, that is obtained following the introduction of a negative 2.5 kV offset to the computed results.

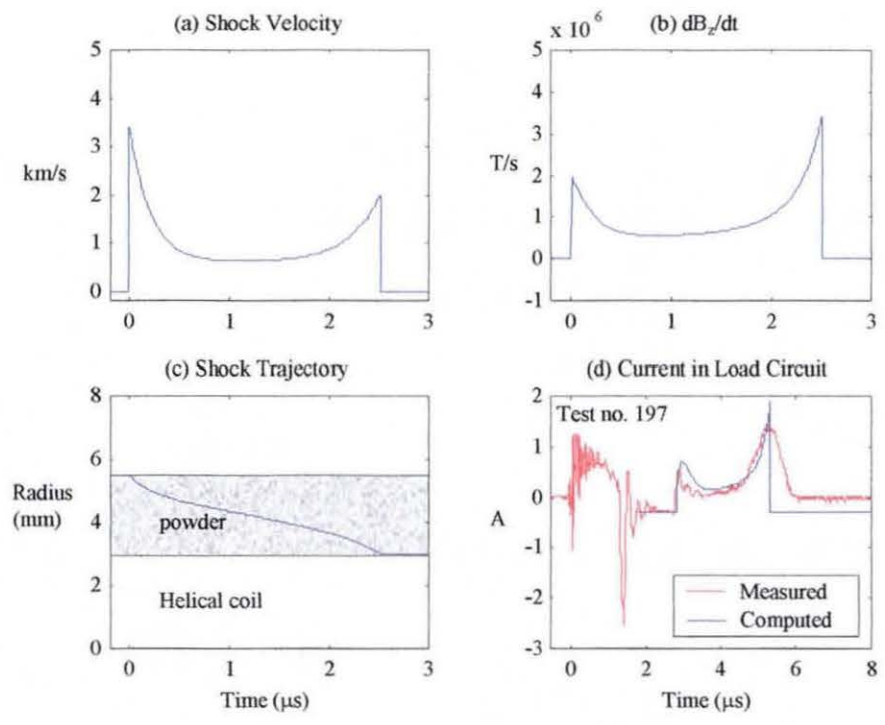


Figure 8-11 Computed results: (a) shock velocity U_s , (b) $\frac{dB_z}{dt}$ (c) shock trajectory and (d) current in the transformer secondary circuit.

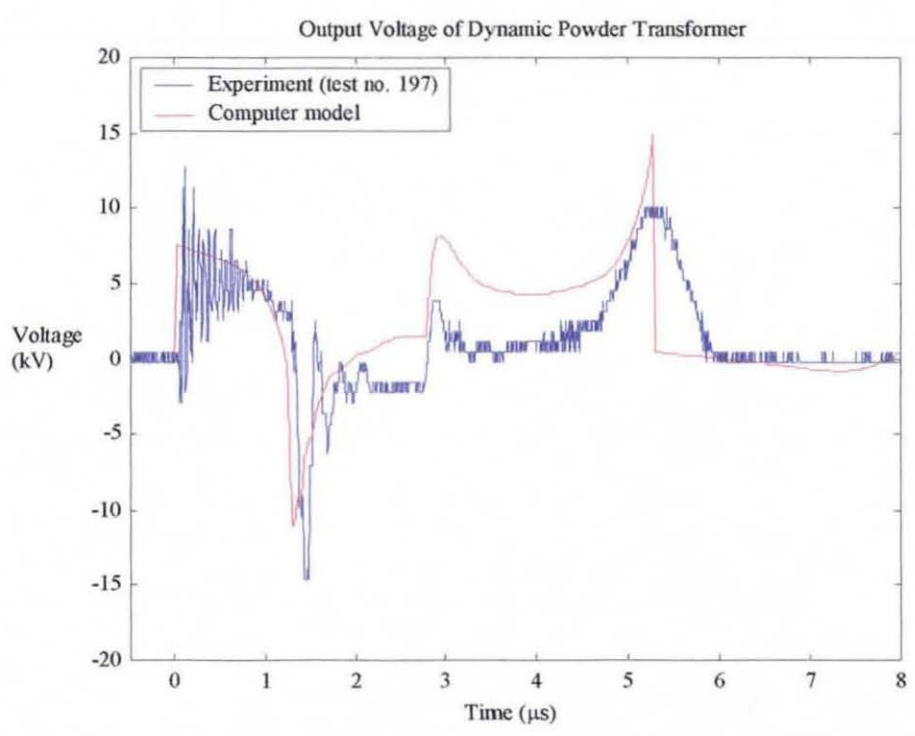


Figure 8-12 Comparison between measured transformer output voltage and computer model (before correction of offset error).

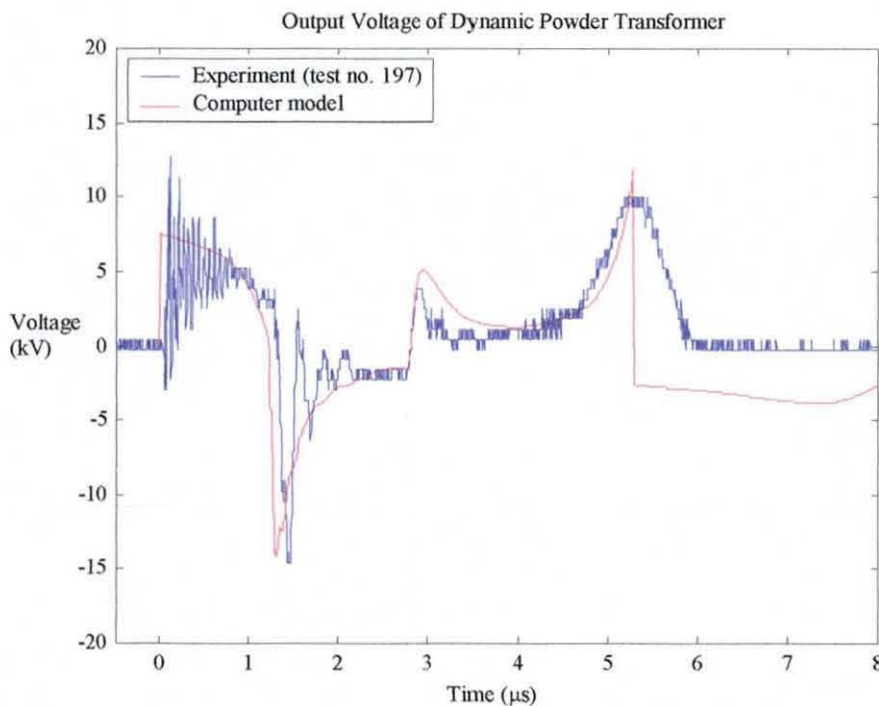


Figure 8-13 Comparison between measured transformer output voltage and computer model (after correction of offset error).

The five constants U_{s1} , U_{s2} , U_{s3} , τ_1 and τ_2 used to define the shock velocity function imply that a unique set of solution is not possible merely by fulfilling both initial and boundary conditions. An iterative approach similar to that described in chapter 5 is required to converge to a function (in Fig 8-11a) consistent with that produced by a calculation that begins at the electric gun model with the foil explosion and magnetic pressure.

8.2.5.3 Effect of Loading on Output Voltage

The inclusion of equation (8-16) in the dynamic powder transformer model allows the current in the load circuit to be calculated and the open-circuit voltage given by equation (8-7) to be compared with the individual voltage components in the load circuit. This is shown in Fig 8-14, where the inductance of the loop formed by the copper-sulphate resistors has been estimated at 0.5 mH while the other resistances and inductances were obtained from measurement or design calculation. In this particular case, the large inductance of the load (compared with that of the helical coil) is

responsible for rounding off the initial voltage spike to give the characteristic shape of Fig 8-13.

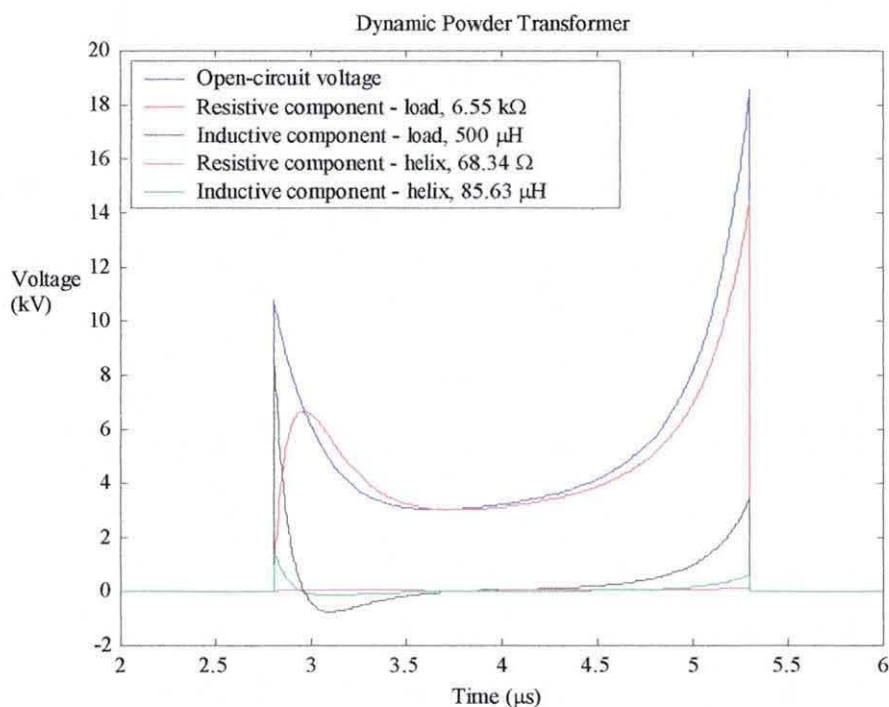


Figure 8-14 Open-circuit voltage and individual voltage components.

8.2.6 Elastic Precursor

Hydrodynamic calculations for the shock compression of aluminium powder in section 5.3.5.3 suggested that the phenomenon of the elastic precursor will be manifested by a sharp increase in shock velocity (and with it the pressure) at a rigid wall boundary. While the spiral probe data of chapter 5 could not confirm the presence of an elastic precursor, it is clear that the measured voltage of Fig 8-7 again has a characteristic U-shape, indicating a sharp increase in velocity as the shock front approaches the epoxy-cast helical coil. It was initially thought that the rising voltage near the end of the U-shape characteristics was due solely to the 'focussing' effect as the cylindrical shockwave [127] – [129] converges on the axis, to give a large increase in pressure and velocity before the shockwave is reflected. However, the material states of Figs 8-15 and 8-16 indicate that it is the elastic precursor ahead of the shock front that has been accentuated by the focussing effect, thus making it clearly visible in Fig 8-7. In Fig 8-17, further evidence of the precursor is provided by the pressure at the outer surface of the epoxy-cast helical coil.

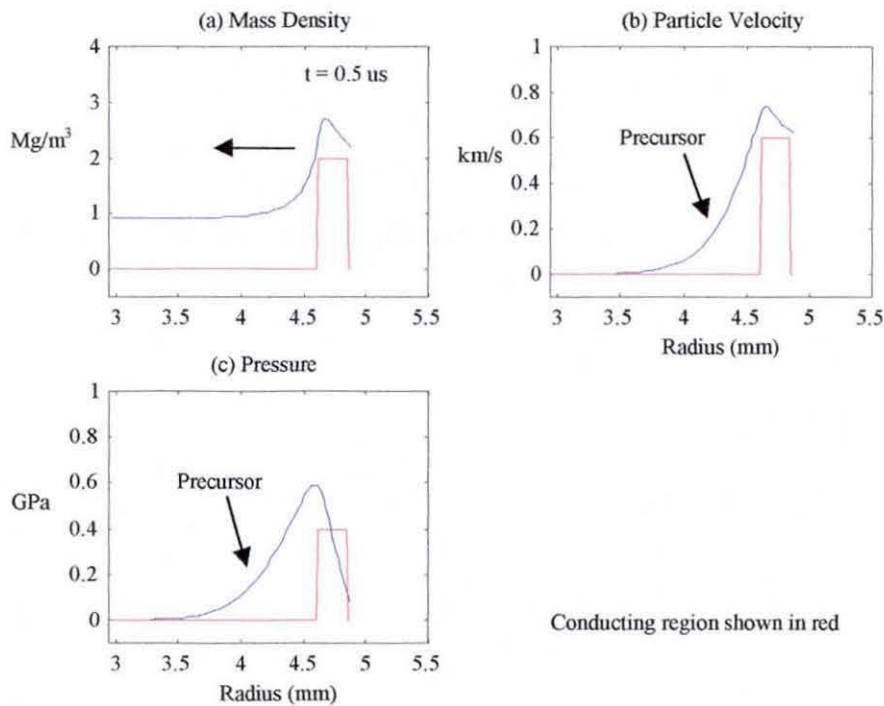


Figure 8-15 Material states at $t = 0.5 \mu s$.

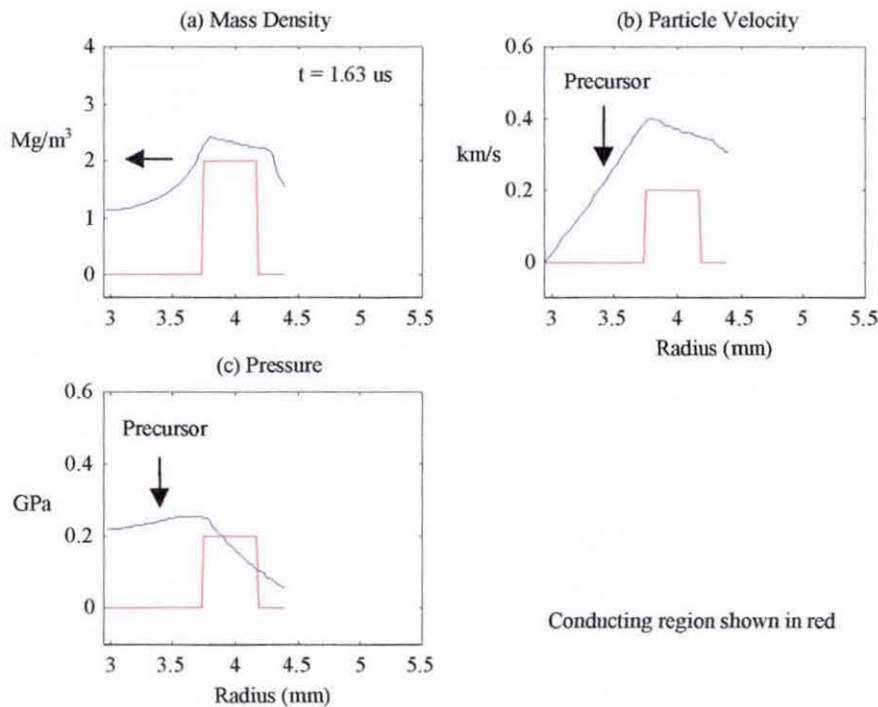


Figure 8-16 Material states at $t = 1.63 \mu s$, approaching the helical secondary coil modelled as a rigid wall boundary.

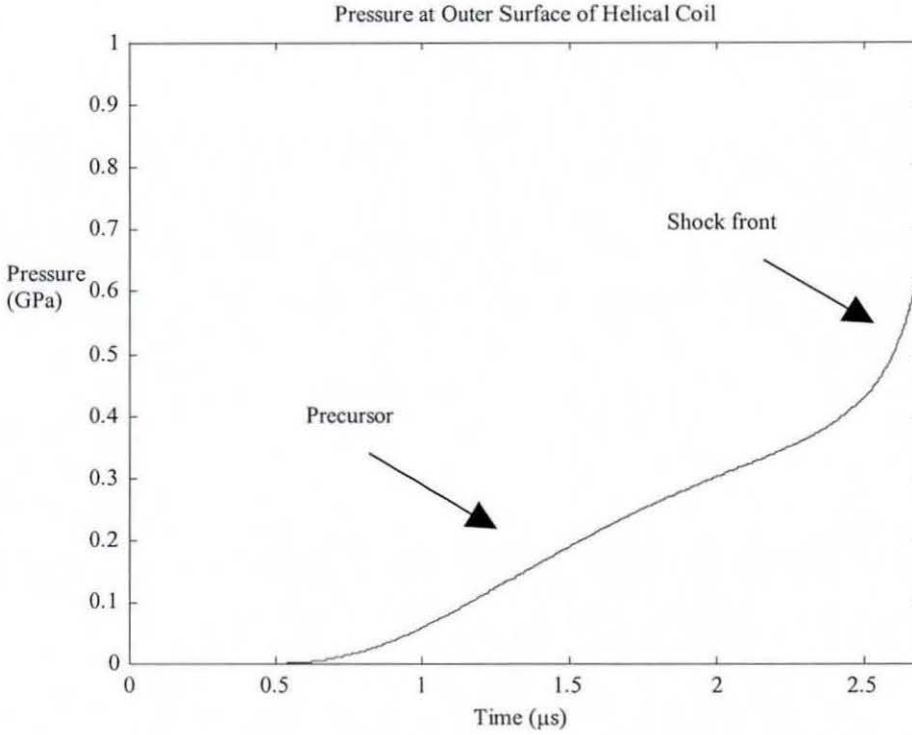


Figure 8-17 Pressure at outer surface of helical coil showing the effect of elastic precursor.

8.3 Design of Dynamic Powder Transformer

8.3.1 Simplified Analysis and Design Method

In the following sections, a method is described that extends the analysis process of the previous section to include the design and optimisation of the dynamic powder transformer. Essentially, the process illustrated in Fig 8-18 seeks to characterise the pressure generated by flyer impact during the experiment, by using the shock velocity function obtained from the dynamic powder transformer model. Once a reasonably accurate impact pressure is obtained, it can be used, together with the assumption that changes in the velocity of the flyer are small once it has reached Gurney terminal velocity, to calculate the shock velocity (and trajectory) in powder of a different thickness using the shock propagation model. The resulting shock velocity (and trajectory) is then used as an input to the dynamic powder transformer model to predict its output performance and to assess the effect of output loading.

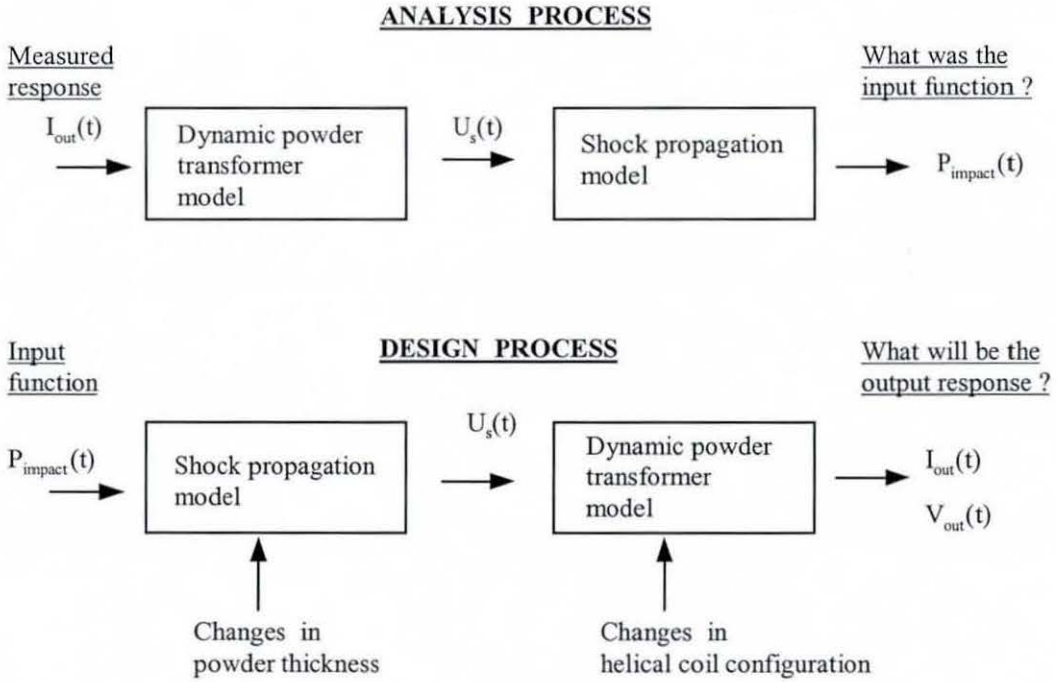


Figure 8-18 Simplified analysis and design method.

8.3.2 Estimated Pressure at Flyer Impact

Following the procedure described in chapter 5, the pressure on impact with the powder is approximated by a function with two components (1) a low-pressure, long-duration (or DC) component associated with the magnetic pressure and (2) an impulsive component associated with the actual flyer impact. Thus

$$P(t) = P_1 + P_2 \exp\left(-\frac{t}{\tau_p}\right) \quad (8-18)$$

where P_1 , P_2 and τ_p are constants defined in Fig 8-19.

Reasonably accurate estimates of the parameter P_1 can be obtained from the electric gun model (see Fig 8-7c), while the foil explosion pressure of Fig 8-7a provides a possible starting point in the search for P_2 . Figure 8-20 shows that an impact pressure with $P_1 = 0.05 \text{ GPa}$, $P_2 = 12.9 \text{ GPa}$ and $\tau_p = 50 \text{ ns}$ will produce a shock velocity function that is in reasonable agreement with that obtained from the dynamic powder transformer model.

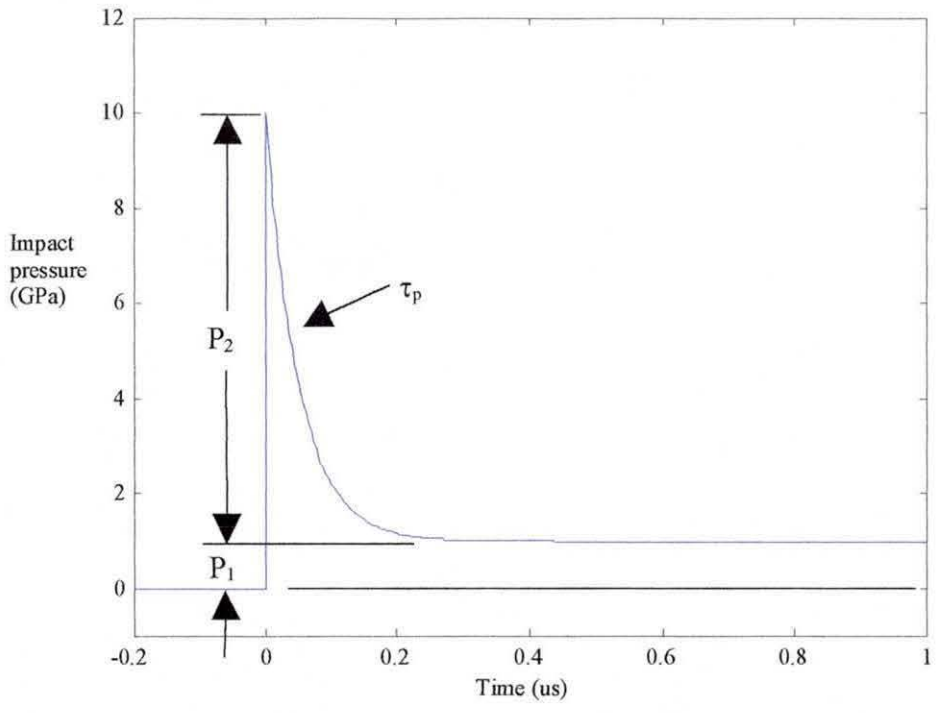


Figure 8-19 Functional approximation of impact pressure.

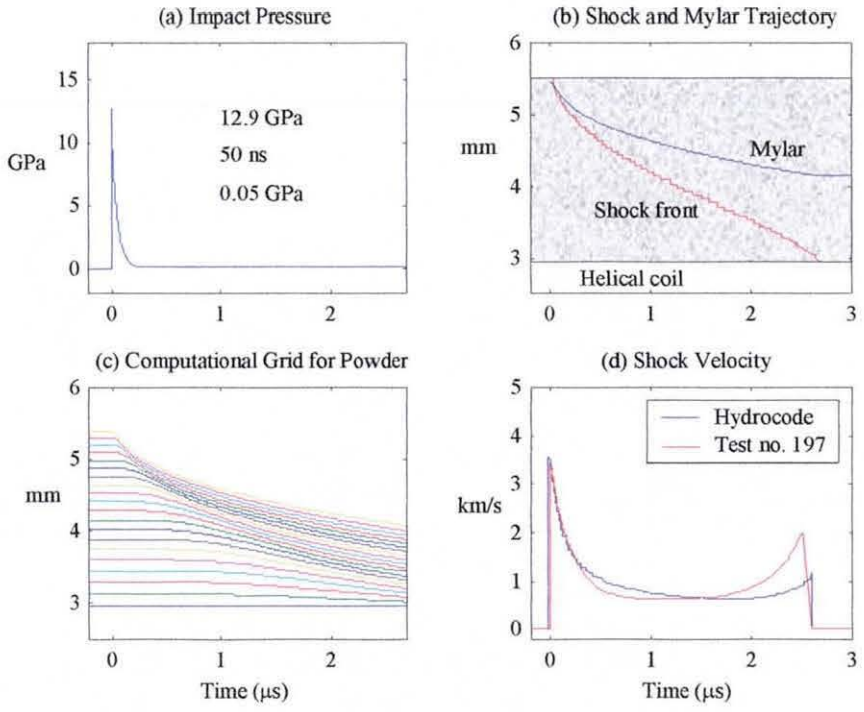


Figure 8-20 Results from shock propagation model.

8.3.3 Design Examples for High-Voltage Pulse Generation

It is clear from Fig 8-13 that the pulse duration is determined by the time taken for the shock front to travel from the point of impact to the boundary of the powder defined by the outer diameter of the helical coil. It is thus possible to control the pulse duration by choosing powder layers of different thicknesses.

It is also clear from equation (8-7) that the open-circuit output voltage is directly proportional to the effective coupling area A_{eff} , which may be increased by using a large-diameter mandrel and/or an increased number of turns. To achieve this, the stand-off distance between the exploding foil and the outer boundary of the powder has to be kept to a minimum, so that more space can be allocated to the epoxy-cast helical coil.

In the considerations that follow, a stand-off distance of 1.0 mm from the 22.0 mm diameter exploding foil is assumed, giving the outer boundary of the powder a diameter of 20.0 mm . Calculation is carried out for the three configurations labeled A, B and C in Table 8-2, using 33% *TD* powder with thicknesses of 2.0 mm , 1.0 mm and 0.5 mm . A thickness of 2.0 mm is assumed for the epoxy casting of the helical coil inside a thin-walled glass tube, so that the corresponding helix diameters are 12 mm , 14 mm and 15 mm . The initial magnetic field is assumed to be 6.0 T as provided by the field coil design of chapter 7. The three configurations are illustrated in Fig 8-21.

Table 8-2 Design examples for dynamic powder transformer

Design	Foil diameter (mm)	Powder boundary		Powder thickness (mm)	Helix diameter (mm)
		outer (mm)	inner (mm)		
A	22.0	20.0	16.0	2.0	12.0
B	22.0	20.0	18.0	1.0	14.0
C	22.0	20.0	19.0	0.5	15.0

$62.5\text{ }\mu\text{m}$ wire, 50 mm length, 600 turns, 6.0 T .

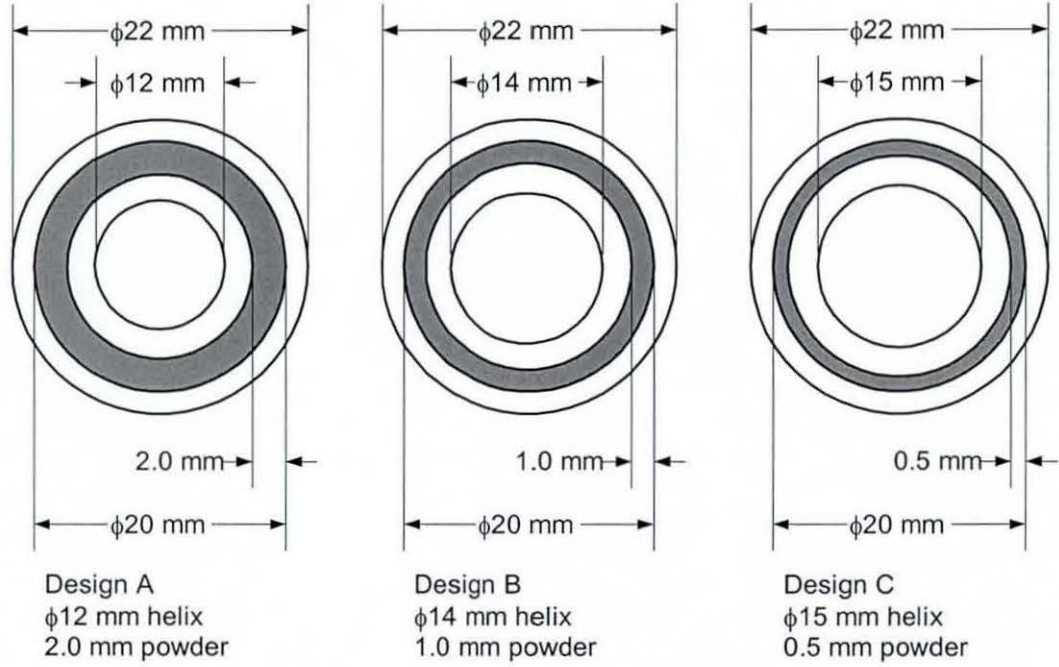


Figure 8-21 Three designs under consideration for dynamic powder transformer.

For the designs under consideration, the topology of the secondary circuit is modified as shown in Fig 8-22, to avoid encircling the current conductor for the electric gun and to eliminate mutual coupling with the electric gun current.

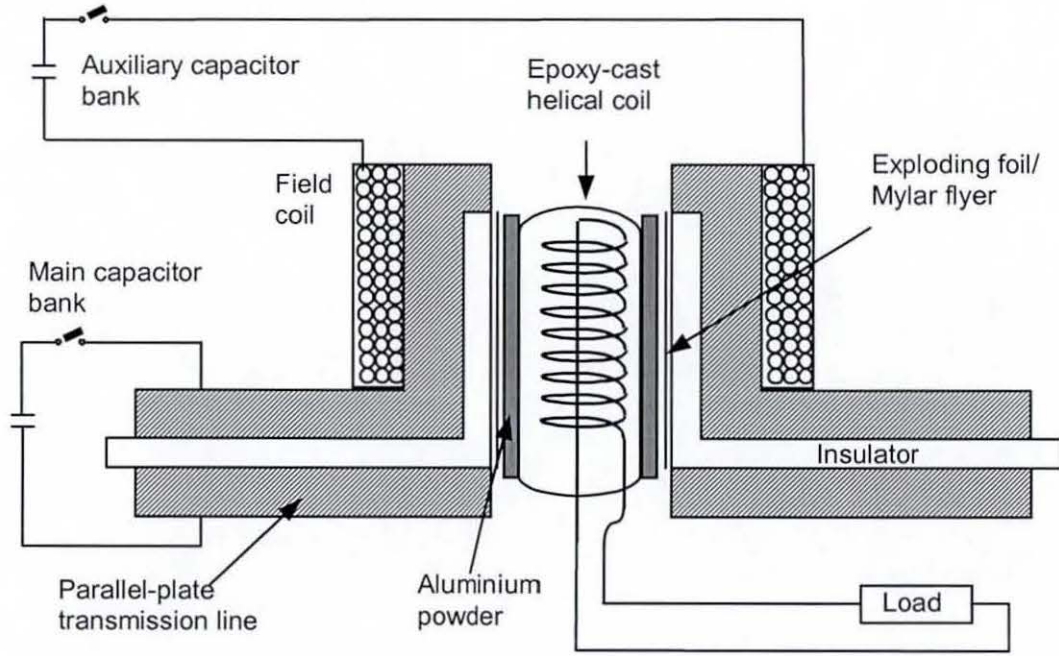


Figure 8-22 Design configuration for dynamic powder transformer.

Figs 8-23b and 8-23d show the shock trajectory and velocity calculated by the shock propagation model for a transformer of design A (2.0 mm powder thickness) using the impact pressure of Fig 8-23a.

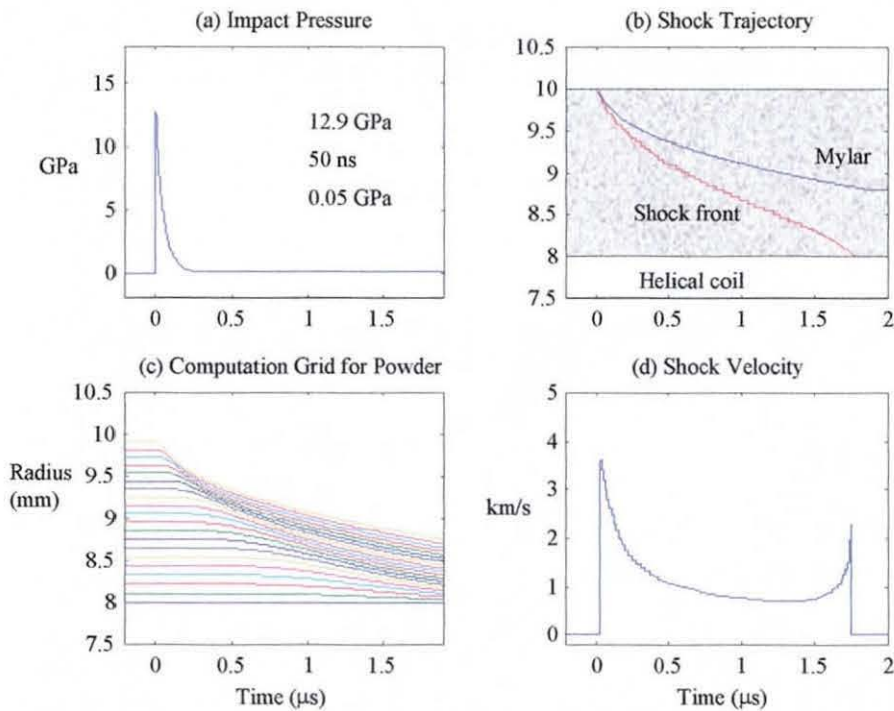


Figure 8-23 Results from shock propagation model – design A.

A functional description for the shock velocity of Fig 8-23d is obtained in Fig 8-24a, and is used to initiate calculation by the dynamic powder transformer model to give the current in the load circuit in Fig 8-24d. The load is assumed to be identical to that used in the experiment and the shape of the predicted current is thus identical with that of the experiment. However, with a large-diameter helical coil and more turns, the peak output voltage is expected to reach about 100 kV. The individual voltage components shown in Fig 8-25 indicate that a large inductive voltage is generated inside the helical coil. A better rise-time of the voltage on a non-inductive load can be achieved by minimising the self-inductance of the output circuit.

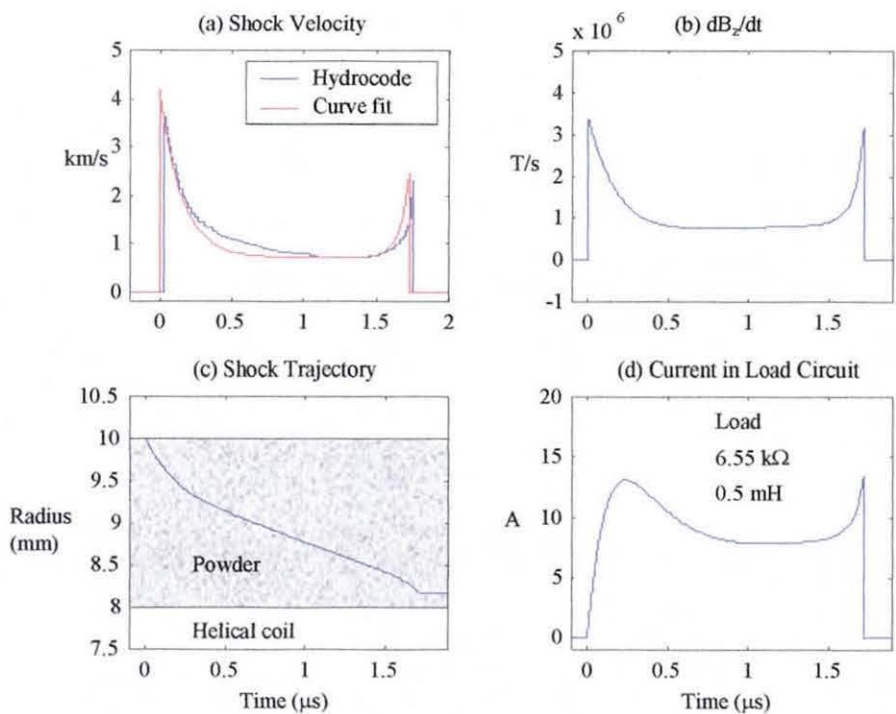


Figure 8-24 Results from dynamic transformer model – design A.

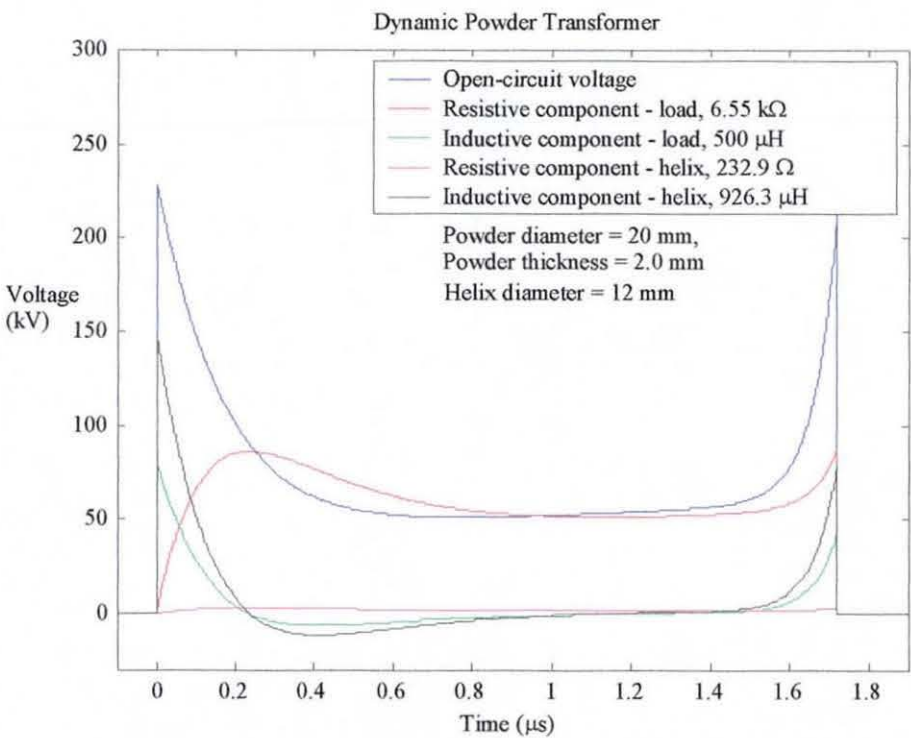


Figure 8-25 Results from dynamic transformer model – design A.

Results for transformer designs B and C, calculated by an identical procedure, are summarised in Table 8-3 for the shock velocity functions and in Fig 8-26 for the open circuit output voltages. Both designs are predicted to produce an open-circuit output voltage exceeding 300 kV, with design B having a longer pulse duration (500 ns) due to the greater thickness (1.0 mm) of the powder layer. The 0.5 mm powder layer of design C is predicted to give a short-duration pulse of 160 ns.

Table 8-3 Functional parameters for shock velocity equation (8-12)

Design	U_{s1} (km/s)	τ_1 (μs)	U_{s2} (km/s)	τ_2 (μs)	U_{s3} (km/s)	t_{dur} (μs)
A	0.7	0.15	3.5	0.06	1.75	1.72
B	1.0	0.15	3.3	0.006	1.65	0.49
C	0.6	0.15	3.9	0.006	1.95	0.16

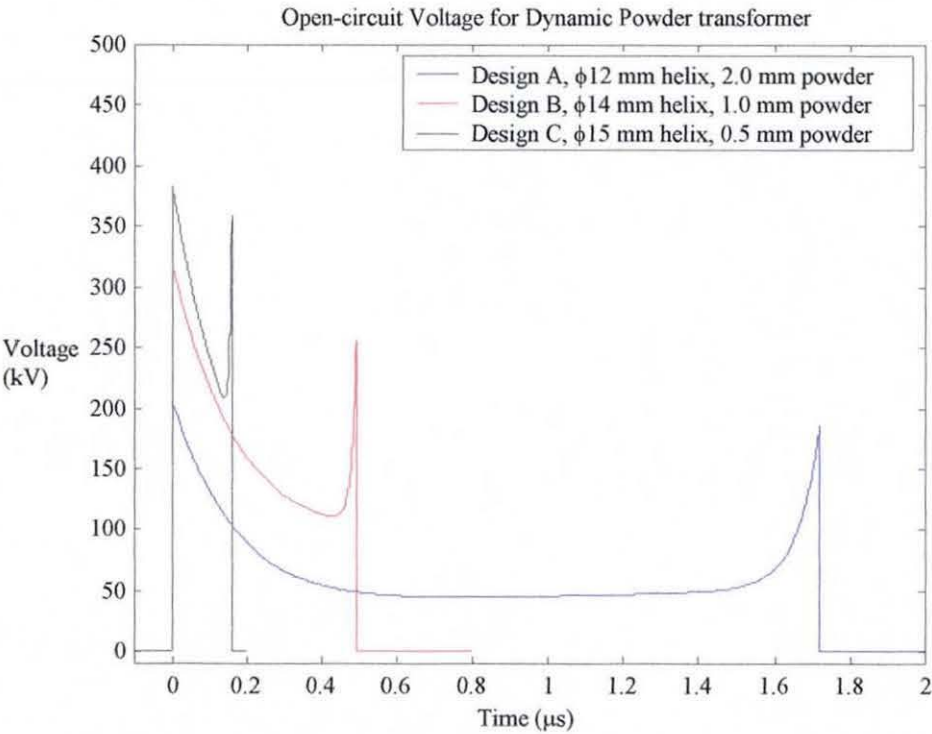


Figure 8-26 Open-circuit output voltage for the three designs under consideration.

In Fig 8-27, the shock trajectory obtained from design A (see Fig 8-23b) is re-arranged to emphasise the relationship between powder thickness and output pulse duration.

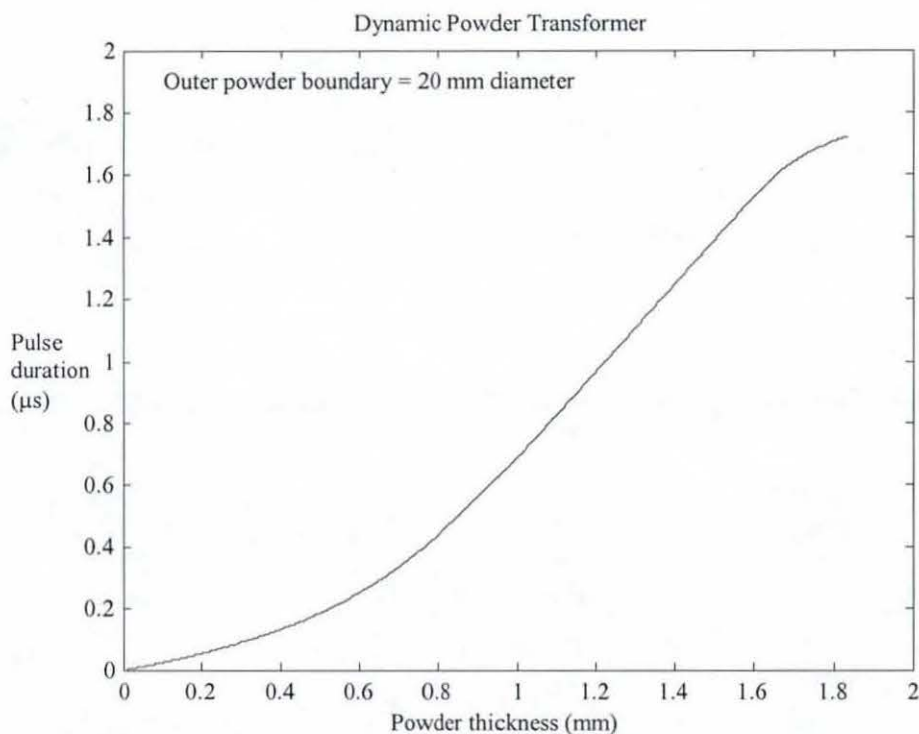


Figure 8-27 Relationship between pulse duration and powder thickness.

The resistive and inductive loading on the output pulse, which have been demonstrated in Figs 8-14 and 8-25, are especially severe in the case of designs B and C, due to the combined effects of (1) the large self-inductance associated with a large-diameter coil and (2) the short-duration pulse ($\leq 0.5 \mu s$). Despite the smaller load inductance ($0.5 \mu H$) assumed in the calculations for these designs, a significant portion of the open-circuit voltage appears as an inductive voltage within the coil (Figs 8-28 and 8-29). The characteristic pulse shape (with a sharp rising edge) is lost and the peak voltage is limited to about $120 kV$.

Due to the effect of loading, the copper-sulphate voltage divider used in the present experiment will not be suitable for measuring the open-circuit voltage of these transformers. Alternative techniques of measurement, such as a capacitive voltage divider (with $G\Omega$ impedance), will be required for future experimentation.

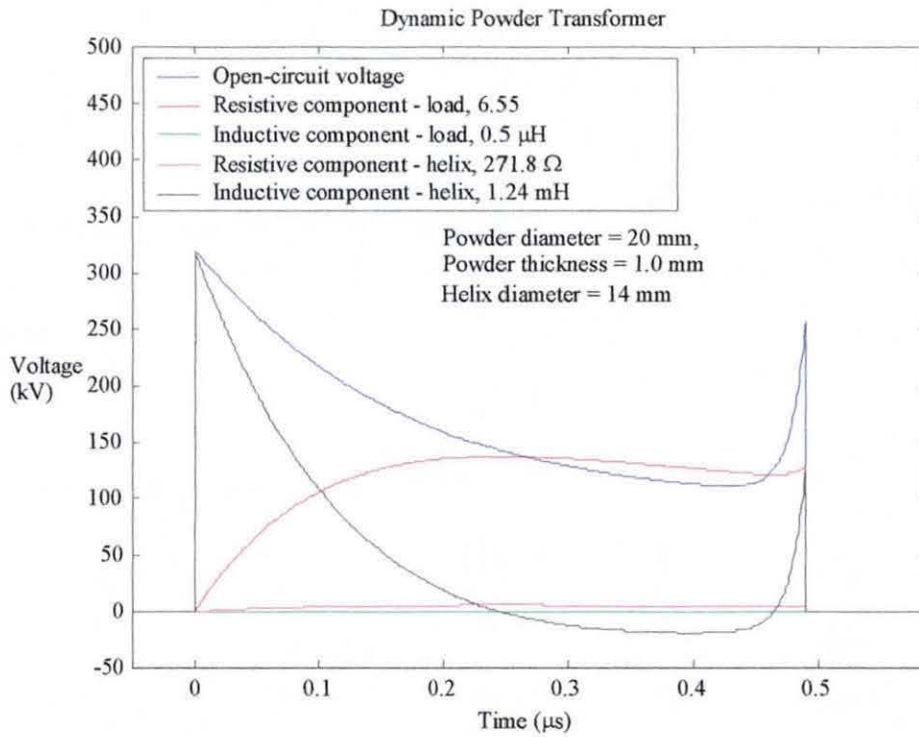


Figure 8-28 Open-circuit voltage and individual components (design B).

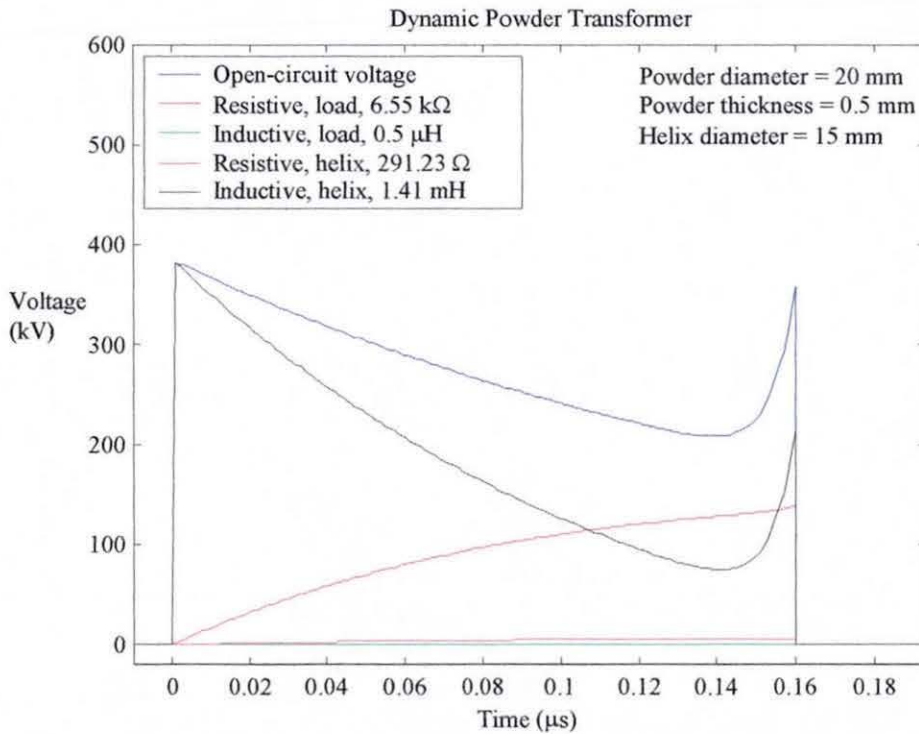


Figure 8-29 Open-circuit voltage and individual components (design C).

8.4 Efficiency of the Dynamic Powder Transformer

The efficiency of the dynamic powder transformer is primarily determined by the foil explosion and flyer acceleration processes, which convert electrostatic energy stored in the capacitor bank into kinetic energy in the Mylar flyer. For the experiment described in section 8.2, about 2.0 % of the electrostatic energy in the capacitor bank was converted into kinetic energy in the Mylar flyer (see Appendix E).

The rather poor efficiency is traceable to the requirement to explode the aluminium foil in a time of about $1.0 \mu\text{s}$ to ensure proper electric gun operation. On the other hand, the discharge current required a time of about $5.0 \mu\text{s}$ to reach its maximum. Consequently, a significant portion of the electrostatic energy remained on the capacitor bank and did not participate in the flyer acceleration process.

The efficiency can be further improved by better matching of the exploding foil, which represents a non-linear load, to the capacitor bank.

8.5 Conclusions

In this chapter, the concept of a dynamic powder transformer has been demonstrated by a single proof-of-principle experiment. Unfortunately, the significance of the experimental result was not initially recognised, because at the time the electric gun model (chapter 3), the hydrodynamic code (chapter 4) and the MHD code (chapter 6) had not been developed. Consequently, the idea was abandoned as unworkable. It was only after significant insight into the shock compression processes has been gained, following the development of these models, that a simplified analytical and design approach could be formulated for the prediction and optimisation of such transformer.

CONCLUSIONS AND FUTURE WORK

9.1 Conclusions

As an alternative to an explosive driver, exploding foil driven electric gun systems have been developed for generating shockwaves in aluminium powder under laboratory conditions. In the planar configuration, about 8 kJ of stored electromagnetic energy, corresponding to an equivalent chemical energy of about 2 g of TNT explosive, have been used in the shock compression study of aluminium powder (see chapter 5). In the cylindrical imploding configuration, about 80 kJ of stored energy, corresponding to some 20 g TNT explosive, have been used in the flux compression experiments (see chapter 7) and for high-voltage pulse generation (see chapter 8).

The conducting shock produced in aluminium powder by a $250\text{ }\mu\text{m}$ Mylar flyer at an impact velocity of 3 km/s has been characterised by both TOA measurement (using contact-pin probes) and continuous velocity monitoring (using spiral resistance probes). Experimental results from the shock compression of aluminium powder indicate a shock velocity of about 3 km/s that is rapidly attenuated. Numerical modelling of the shock compression process, using the $P - \alpha$ EOS for aluminium powder and a simple switch model for the electrical conductivity of the shock compressed powder, suggests that the insulator-to-conductor phase transition occurred at a threshold pressure of about 0.1 GPa (or 1 kbar), corresponding to the onset of plastic deformation. Both the pressure caused by flyer impact with powder and the magnetic pressure (exerted by the current in the electric gun circuit) have been found to contribute to the propagation of the conducting shock front in powder.

The shockwave compression of magnetic flux in aluminium powder has been demonstrated in proof-of-principle experiments (see chapter 7), where magnetic flux densities of about 40 T were obtained from an initial flux density of 6 T . Although the quality of the foil explosion was someway from being ideal, the large stand-off between the exploding foil and the powder assembly nevertheless allowed the flyer to be accelerated by magnetic pressure to an impact velocity of between 1.1 km/s and 1.5 km/s . Experimental data also provided further evidence of the rapidly decaying shock velocity resulting from Mylar flyer impact with aluminium powder, in direct contrast to the steady shock velocity (due to quasi-static explosion pressure) in explosive driven experiments.

The generation of a high-voltage pulse by the shockwave in aluminium powder has been demonstrated in dynamic powder transformer experiments (see chapter 8). Although experiment results were obtained for a pulse of only about 10 kV peak and $3\text{ }\mu\text{s}$ duration, the data nevertheless provided a unique insight into the mechanisms involved. By combining hydrodynamic calculation (e.g. the shock propagation model) with electrical circuit analysis (e.g. the dynamic transformer model), a simplified method was developed that leads to the systematic design and performance prediction of such transformers.

The elastic precursor phenomenon known to appear in shock compression experiments, and supported by the $P-\alpha$ EOS for aluminium powder in the present hydrodynamic code, has been observed in experiments using the dynamic powder transformer configuration (see chapter 8).

A new mathematical model for the electric gun has been developed, with the flyer acceleration process described by the Gurney model. In essence, the new model represents a simple extension of the empirical model for exploding foil opening switches already developed at Loughborough University [26], by monitoring the specific energy density and using the burst energy density to provide information on the flyer acceleration process. The validity of the new model has also been verified using

TOA data provided by different measurement techniques in a series of exploding foil driven experiments.

Powerful computational tools, in the form of one-dimensional hydrocodes and MHD codes, have been developed to help explain the complex phenomena observed experimentally, and to provide a critical insight into the fundamental shockwave processes. These codes are vital supplements to the actual experiments, where diagnostic means are sometimes inevitably scarce, in order not to influence or disturb the shockwave behaviour that is under investigation. By keeping track of all the key physical parameters, as functions of both time and space, hydrocodes and MHD codes enable the best-instrumented experiments to be performed. Reduction of the data collected during the experimental programme (for the shock compression of aluminium powder and magnetic flux density) to any meaningful conclusions was only possible with the aid of such computer codes. The hypothesis concerning the fundamental mechanism at work in the exploding foil shockwave generation of high-voltage pulses has been shown to be reproducible in code calculations. These codes have been used in a systematic study to determine the influence of important physical parameters. They can be further utilised to extend experimental data, by performing parametric studies of the variables.

The most significant difference between explosive and exploding foil shockwave generation techniques lies in the characteristics of the pressure pulse that are unique to each of these methods.

The technique used by Nagayama [29] for flux compression experiments belongs to one of two main classes. One of these is contact operation [130], where explosive is placed in direct contact with the work piece in the explosive working of metals. The other is stand-off operation, involving the use of a flyer, as is the case of the present research using exploding foil driven Mylar flyer. Apparently, a longer and quasi-static explosion pressure is associated with contact operations, whereas stand-off operations produce higher pressure at shorter duration.

Based on the results obtained by Nagayama, and confirmed by the MHD model, a long and quasi-static explosion pressure appears to be useful for shockwave flux

compression. But for short-duration high-voltage pulse generation, e.g. by exploiting the insulator-to-conductor phase change in the powder, stand-off operation (by flyer impact) may be advantageous.

Based on model calculations, the exploding foil has an energy density of about 15 MJ/kg at burst, which is more than three times higher than that of explosive (4.5 MJ/kg). However where system size, weight and volume are of concern, the exploding foil technique would suffer from the inherently lower energy density realisable using high-voltage capacitors (0.001 MJ/kg) as compared with explosive.

9.2 Future Work

Further experimental work should include

- i. better fabrication of the aluminium foil/dielectric flyer package to optimise the electrical explosion process and so achieve a strong and fast rising shock pressure. Vacuum deposition of aluminium [131] onto the Mylar polyester foil may significantly reduce any possibility of air bubbles being trapped in the foil/flyer interface. Complete removal of the bubbles and a seamless dielectric flyer package may significantly improve simultaneity of the foil explosion, and reduce or delay the onset of instability during the implosion process.
- ii. experiments with an exploding foil in direct contact with the aluminium powder (but protected by a thin Mylar film), to assess the performance of exploding foils in contact operations [130].
- iii. use of a second metallic foil (e.g. aluminium or copper) ahead of the Mylar flyer, which should not explode but rather play the role of a liner to compress the magnetic field. Schenk and Linhart [46] described experiments in which plasma generated by an electrically exploded cylindrical metallic foil reputedly compressed an axial magnetic field to a final magnetic flux density of

$6T$, with a compression ratio of about 10. They proposed an interesting concept in which a foil is used indirectly to propel a second foil, which does not explode but plays the role of a liner to compress the magnetic field

iv. use of a multiple-wire array to replace the exploding foil, as forms part of a new EPSRC Standard Research Grant (GR/R44645) at Loughborough. This technique has been successfully implemented in both magnetic flux compression experiments [132] and in plasma Z-pinch experiments that significantly improved the neutron yield and X-ray power [133]. It is believed that the initial spacing between the wires allows room for the plasma from individual wire explosion to expand freely, before coalescing into a uniform plasma shell that converges at high speed onto the axis under the $\vec{J} \times \vec{B}$ Lorentz force.

v. use of non-invasive, electro-optic diagnostic methods, such as laser interferometer, for shock velocity determination [134] and magneto-optic diagnostic methods, such as Faraday rotation probe for magnetic field measurement [135].

Further numerical modelling and computational work should include

- i. better simulation of the impact process of an air shockwave on low-density powder material. Either two-phase or multi-phase flow calculation may be required to handle mixing of the air and powder material in the computation mesh.
- ii. modelling of electrical conductivity for both ideal and non-ideal plasma production by exploding foils/wires.
- iii. detailed two- or three-dimensions calculations to allow a study of the physical effects that are overlooked by the assumption of one-dimensional symmetry.

REFERENCES

1. H. Knoepfel and F. Herlach (editors). *Megagauss magnetic field generation by explosives and related experiments*, EUR 2750c. Euratom, Brussels (1966).
2. P.J. Turchi (editor), *Megagauss physics and technology*, Proceedings of 2nd International Conference on Megagauss Magnetic Field and Related Topics, Plenum Press, New York (1980).
3. V.M. Titov and G.A. Shvetsov (editors), *Ultrahigh magnetic fields. Physics, techniques and applications*, Proceedings of the 3rd International Conference on Megagauss Magnetic Field and Related Topics, Moscow, Nauka (1984).
4. C.M. Fowler, R.S. Caird and D.J. Erickson (editors), *Megagauss technology and pulsed power applications*, Proceedings of 4th International Conference on Megagauss Magnetic Field and Related Topics, Plenum Press, New York (1987).
5. V.M. Titov and G.A. Shetsov (editors), *Megagauss fields and pulsed power systems*, Proceedings of 5th International Conference on Megagauss Magnetic Field and Related Topics, Nova Science, New York (1990).
6. M. Cowan and R.B. Spielaman (editors), *Megagauss magnetic field generation and pulsed power applications*, Proceedings of the 6th International Conference on Megagauss Magnetic Field and Related Topics, Nova Science (1994).
7. V.K. Chernyshev, V.D. Selemir and L.N. Plyashkevich (editors), *Megagauss and megaampere pulse technology and applications*, Proceedings of 7th International Conference on Megagauss Magnetic Field and Related Topics, Sarov, VNIEFF (1996).

8. C.M. Fowler, W.B. Garn and R.S. Caird. "Production of very high magnetic field by implosion". *Journal of Applied Physics*, vol.31, pp.588-594 (1960).
9. A.D. Sakharov. "Magnetoinplosive generators". *Soviet Physic Uspekhi* (English Translation), vol.9, pp.294-299 (1966).
10. F. Herlach and H. Knoepfel. "Megagauss fields generated through explosive-driven flux compression devices". *Review of Scientific Instruments*, vol.36, no.8, pp.1088-1095 (1966).
11. J.H. Degnan, M.L. Alme, W.L.Baker, J.S. Buff, C.B. Boyer, C.J. Clouse, S.K. Coffey, D.W. Conley, D.J. Hall, J.D. Graham, S.L.Gonzalez, K.E. Hackett, D.J. Hall, J.L. Holmes, E.A. Lopez, W.F. McCullough, D.W. Price, R.E. Reinovski, N.F. Roderick, P.J. Turchi and J.M. Welby. "Multi-megajoule solid liner implosions" in C.M. Fowler, R.S. Caird and D.J. Erickson (editors) *Megagauss technology and pulsed power applications*, pp.699-702 (1987).
12. J.H. Degnan, R.A. Nuttelman, G.F. Kiuttu, R.E. Reinovski and W.L. Baker. "Experimental and computational study of axial magnetic field compression by cylindrical plasma liners" in P.J. Turch (editor) *Megagauss physics and technology*, Plenum Press, NY and London, pp.511-517 (1980).
13. M.A. Liberman, A.L. Velikovich and F.S. Felber, "Magnetic flux compression in plasma: concept and theory" in C.M. Fowler, R.S. Caird and D.J. Erickson (editors) *Megagauss technology and pulsed power applications*, Plenum Press, pp.107-116 (1987).
14. F.S. Felber, F.J. Wessel, N.C. Wild, H.U. Rahman, A. Fisher, C.M. Fowler, M.A. Liberman and A.L. Velikovich, "Magnetic flux compression by plasma: experiments on a gas-puff z-pinch" in C.M. Fowler, R.S. Caird and D.J. Erickson (editors) *Megagauss technology and pulsed power applications*, Plenum Press, pp.117-124 (1987).

15. F.S. Felber, F.J. Wessel, N.C. Wild, H.U. Rahman, A. Fisher, C.M. Fowler, M.A. Liberman and A.L. Velikovich. "Gas-puff Z pinches with strong axial magnetic fields." *Laser and Particle Beams*, vol.5, no.4, pp.699-706 (1987).
16. R.K. Appartaim and A.E. Dangor. "Large magnetic fields generated by Z-pinch flux compression". *Journal of Applied Physics*, vol.84, no.8, pp.4170-4175 (1998).
17. F. Herlach and R. McBroom. "Megagauss fields in single-turn coils". *Journal of Scientific Instruments (Journal of Physics E)*, vol.6, pp.652-653 (1973).
18. E.C. Cnare. "Magnetic flux compression by magnetically imploded metallic foils". *Journal of Applied Physics*, vol.37, no.10, pp.3812-3816 (1966).
19. J.R. Freeman, E.C. Cnare and R.C. Wang. "Magnetically imploded metal foils" *Applied Physics Letters*, vol.10, no.4, pp.111-113 (1967).
20. S. Chikazumi, N. Miura, G. Kido and M. Akihiro. "Production of magnetic fields in megagauss range and related measuring techniques". *IEEE Transactions on Magnetics*, vol.14, no.5, pp.577-585 (1978).
21. N. Miura and S. Chikazumi. "Computer simulation of megagauss field generation by electromagnetic flux compression". *Japanese Journal of Applied Physics*, vol.18, pp.553-564 (1979).
22. S.G. Alikhanov, V.G. Belan, A.I. Ivanchenko, V.N. Karasjuk and G.N. Kichigin. "The production of pulsed megagauss fields by compression of the metallic cylinder in Z-Pinch configuration". *Journal of Scientific Instruments (Journal of Physics E)*, vol.1, pp.543-545 (1968).
23. R.E. Marrs and K. Wira. "Electromagnetic implosion of metal liners". *Journal of Applied Physics*, vol.53, no.1, pp.230-236 (1982).

24. B.M. Novac, I.R. Smith, H.R. Stewardson, P. Senior, V.V. Vadher and M.C. Enache. "Design, construction and testing of explosive-driven helical generators". *Journal of Physics D - Applied Physics*, vol.28, no.4, pp.807-823 (1995).
25. H.R. Stewardson, S.M. Miran, I.R. Smith, B.M. Novac and V.V. Vadher. "Fuse conditioning of the output of a capacitor bank to drive a PEOS". *Digest of Technical Papers. Tenth IEEE International Pulsed Power Conference* (Cat. No.95CH35833), vol.2, pp.1115-1120 (1995).
26. H.R. Stewardson, B.M. Novac and I.R. Smith. "Fast exploding-foil switch techniques for capacitor bank and flux compressor output conditioning". *Journal of Physics D - Applied Physics*, vol.28, pp.2619-2630 (1995).
27. K. Nagayama. "New method of magnetic flux compression by means of the propagation of shock-induced metallic transition in semiconductors". *Applied Physics Letter*, vol.38, no.2, pp.109-110 (1981).
28. K. Nagayama, T. Oka and T. Mashimo. "Experimental study of a new mechanism of magnetic flux cumulation by the propagation of shock-compressed conducting region in silicon". *Journal of Applied Physics*, vol.53, no.4, pp.3029-3033 (1982).
29. K. Nagayama, and T. Mashimo. "Explosive-driven magnetic flux cumulation by the propagation of shock-compressed conductive region in highly porous metal powders". *Journal of Applied Physics*, vol.61, no.10, pp.4730-4735 (1987).
30. M.H. Rice, R.G. McQueen and S.P. Marsh. "Compression of solids by strong shock waves" in F. Seitz and D. Turnbull (editors) *Solid state physics*, vol.6, pp.1-63, Academic Press (1958).

31. R.G. McQueen, S.P. Marsh, J.W. Taylor, J.N. Fritz. "The equation of state of solids from shock wave studies" in R. Kinslow (editor) *High-velocity impact phenomena*, pp.293-417, Academic Press, New York (1970).
32. H. Matsuo and Y. Nakamura. "Experiments on cylindrically converging blast waves in atmospheric air". *Journal of Applied Physics*, vol.51, no.6, pp.3126-3129 (1980).
33. H. Matsuo and Y. Nakamura. "Cylindrically converging blast waves in air". *Journal of Applied Physics*, vol.52, no.7, pp.4503-4507 (1981).
34. E.I. Bichenkov, S.D.Gilev, and A.M. Trubachev. "Shock wave method for generation of megagauss magnetic Fields" in C.M. Fowler, R.S. Caird and D.J. Erickson (editors) *Megagauss technology and pulsed power applications*, Plenum Press, pp.89-105 (1987).
35. M.A. Meyers and S.L. Wang. "An improved method for shock consolidation of powders". *Acta Metallurgica*, vol.36, no.4, pp.925-936 (1988).
36. E.A. Henry, D. Batani, A. Morelli, M. Bernasconi, M. Koenig, A. Benuzzi, I. Masclet, B. Marchet, M. Rebec, C. Reverdin, P.M. Celliers, L.B. Da Silva, R.C. Cauble, G. Collins G, T. Hall and C. Cavazzoni. "Preliminary results on the EOS of water in the Megabar range". *Proceedings of SPIE - the International Society for Optical Engineering*, vol.4424, pp.524-527 (2001).
37. R.S. Dennen and L.N. Wilson "Electrical generation of imploding shock waves" in W.G. Chace and H.K. Moore (editors) *Exploding wires*, vol.2, pp.145-158 (1964).
38. H.H. Chau, G. Dittbenner, W.W. Hofer, C.A. Honodel, D.J. Steinberg, J.R. Stroud and R.C. Weingart. "Electric gun: a versatile tool for high-pressure shock wave research". *Review of Scientific Instruments*, vol.51, pp.1676-1681 (1980).

39. H.H. Chau, G. Dittbenner, K. Mikkelsen, R.C. Weingart, K. Froeschner and R.S. Lee. "Performance of a 100 kV, 78 kJ electric gun system". *Shock Waves In Condensed Matter*, pp.691-695 (1981).
40. K.F. Froeschner, H.H. Chau, G. Dittbenner, R.S. Lee, K. Mikkelsen, D.J. Steinberg and R.C. Weingart. "Shock Hugoniot experiments using an electric gun". *Shock Waves in Condensed Matter*, pp.174-178 (1981).
41. J.E. Osher, H.H. Chau, R.S. Lee, R.E. Tipton and R.C. Weingart. "Electric-gun studies of conductors in high magnetic fields and experiments in dynamic flux compression" in V.M. Titov and G.A. Shvetsov (editors) *Megagauss fields and pulsed power systems*, Nova Science Publisher, pp.815-823 (1990).
42. F. Herlach and J.E. Kennedy. "The dynamics of imploding liners in magnetic flux compression experiments". *Journal of Physics D - Applied Physics*, vol.6, no.6, pp.661-676 (1973).
43. S. Minomura and H.G. Drickhamer, "Pressure induced phase transitions in Silicon, Germanium and some III-V compounds". *Journal of Physics and Chemistry of Solids*, vol.23, pp.451-456 (1962).
44. G.E. Duvall and R.A. Graham. "Phase transitions under shock-wave loading". *Review of Modern Physics*, vol. 49, no. 3, pp.525-579 (1977).
45. A.A. Barmin and A.B. Prishchenpenko. "Compression of a magnetic field in a single crystal by a strong converging ionising shock wave" in M. Cowan and R.B. Spielman (editors) *Megagauss magnetic field generation and pulsed power applications*, Nova Science Publisher, pp.35-40 (1994).
46. G. Schenk and J.G. Linhart. "Compression of magnetic fields by exploding foils" in W.G. Chace and H.K. Moore (editors) *Exploding wires*, vol.3, pp.223-230 (1964).

47. D.V. Keller and J.R. Penning Jr. "Exploding foils - the production of plane shock waves and the acceleration of thin flyer plates" in W.G. Chace and H.K. Moore (editors) *Exploding wires*, vol.2, pp.263-277 (1962).
48. A.H. Guenther, D.C. Wunsch and T.D. Soapes. "Acceleration of thin plates by exploding foil techniques" in W.G. Chace and H.K. Moore (editors) *Exploding wires*, vol.2, pp.279-298 (1962).
49. J.E. Osher, H.H. Chau, G. R. Gathers, R.S. Lee and R.C. Weingart. "Application of 100 kV electric gun for hypervelocity impact studies". *International Journal on Impact Engineering*, vol.5, pp.501-507 (1987).
50. J.E. Osher, G. Barnes, H.H. Chau, R.S. Lee, C. Lee and R.C. Weingart. "Operating characteristics and modelling of LLNL 100 kV electric gun". *IEEE Transactions on Plasma Science*, vol.17, pp.392-402 (1989).
51. J.E. Osher, R. Gathers, H.H. Chau, R.S. Lee G. Pomykal and R.C. Weingart. "Hypervelocity acceleration and impact experiments with the LLNL electric gun". *International Journal on Impact Engineering*, vol.10, pp.439-452 (1990).
52. R.S. Lee, J.E. Osher, H.H. Chau, G. Pomykal and R.D. Speer. "1 MJ electric gun facility at LLNL". *IEEE Transactions on Magnetics*, vol.29, no.1, pp.457-460 (1993).
53. R.S. Weingart, R.S. Lee, K. Jackson and N.L. Parker. "Acceleration of thin flyers by exploding metal foils: application to initiation studies". *Proceedings of the 6th International Symposium on Detonation*, Colorado, pp.653-663 (1976).
54. E. Hasman, M. Gvishi and Y. Carmel. "Measurement of shock initiation threshold of HNAB by flyer plate impact". *Propellants, Explosives, Pyrotechnics*, vol.11, pp.144-149 (1986).

-
55. M.A. Meyers. *Dynamic behaviour of materials*. Chapter 9 Explosive-material interactions, John Wiley and Son (1994).
 56. T.J. Tucker and P.L. Stanton. "Electrical Gurney energy: a new concept of modelling energy transference from electrically exploded conductors". *Sandia National Laboratory Report*, SAND-74-0244 (1975) unpublished.
 57. W.B. Thompson. *An introduction to plasma physics*, Addison Wesley (1962).
 58. M.A. Meyers. *Dynamic behaviour of materials*. Chapter 10 Detonation, John Wiley and Son (1994).
 59. A. Sakurai. "Blast wave theory" in M. Holt (editor) *Basic development in fluid dynamics*, vol.1, pp.309-375, Academic Press (1965).
 60. G.W. Anderson and F.W. Nielson. "Use of action integral in exploding wire studies" in W.G. Chase and H.K. Moore (editors) *Exploding wires*, vol.1, pp.97-102 (1959).
 61. S. Humphries Jr and C. Ekdahl. "Numerical models of pressure pulse generation by imploding metal liners". *IEEE Transactions on Plasma Sciences*, vol.24 no.6, pp.1334-1347 (1996).
 62. S.P. Lyon and J.D. Johnson. "SESAME: The Los Alamos National Laboratory equation-of-state database". *Los Alamos National Laboratory Report*, LA-UR-92-3407 (1992).
 63. T.J. Tucker and R.P. Toth. "A computer code for the prediction of the behaviour of electrical circuit containing exploding wires". *Sandia National Laboratory Report*, SAND-75-0042 (1975) unpublished.

-
64. N.F. Roderick, R.J. Kohn, W.F. McCullough, C.W. Beason, J.A. Lupo and J.D. Letterio. "Theoretical modelling of electromagnetically imploded plasma liners". *Laser and Particle Beams*, vol.1, no.2, pp.181-206 (1983).
 65. I.R. Lindemuth, J.H. Brownell, A.E. Greene, G.H. Nickel, T.A. Oliphant and D.L. Weiss. "A computational model of exploding metallic fuses for multi-megajoule switching". *Journal of Applied Physics*, vol.57, no.9, pp.4447-4460 (1985).
 66. B.M. Novac, A. Serban, I.R. Smith and H.R. Stewardson. "Simple and accurate estimation of the parameters of a fast discharge circuit". *International Journal of Electrical Engineer's Education*, vol.32, pp.83-84 (1995).
 67. A.L. Garcia. *Numerical methods for physics*, 2nd edition, Prentice Hall 2000.
 68. P. Lu, E. Naiman and W.E. Voreck. "Applications of fibre-optics to detonation events". *Proceedings of the 8th Symposium on Detonation*, pp.460-467 (1985).
 69. R.S. Caird, R.F. Benjamin, R.G. McQueen and D.J. Dickson. "Application of fibre-optic pins to explosive pulsed power Generators" in R.A. Greenwell (editor) *Fibre-Optic in Adverse Environment, Proceedings of SPIE*, vol.506, pp.122-126 (1984).
 70. R.F. Benjamin, F.J. Meyer and R.L. Maynard. "Microshell-tipped optical fibres as sensor of high pressure pulses in adverse environment" in R.A. Greenwell (editor) *Fibre-Optic in Adverse Environment, Proceedings of SPIE*, vol.506, pp.116-121 (1984).
 71. J. von Neumann and R.D. Richtmyer. "A method for the numerical calculation of hydrodynamic shocks". *Journal of Applied Physics*, vol.21, no.3, pp.232-237 (1950).

-
72. R.D. Richtmyer and K.W. Morton. *Difference method for initial-value problems*. 2nd edition, Interscience Publishers, New York (1967).
 73. R. Landshoff. "A numerical method for treating fluid flow in the presence of shocks". *Los Alamos Scientific Laboratory Technical Report, LA-1930* (1950).
 74. M.L. Wilkins. "Calculation of elastic-plastic flow" in B.J. Alder, S. Fernbach and M. Rosenberg (editors) *Methods in Computational Physics*, vol.3, pp.211-264 (1964).
 75. D. Potter. *Computational physics*, New York, Wiley-Interscience (1973).
 76. Y.B. Zeldovich and Y.P. Raizer. *Physics of shock waves and high-temperature hydrodynamic phenomena*, W.D. Hayes and R.F. Probstein (editors). Academic Press, New York (1966).
 77. M.A. Meyers. *Dynamic behaviour of materials*. Chapter 4 Shockwave, John Wiley and Son (1994).
 78. W. Hermann. "Constitutive equation for the dynamic compaction of ductile porous materials". *Journal of Applied Physics*, vol.40, no.6, pp.2490-2499 (1969).
 79. R.R. Boade. "Principal Hugoniot, second-shock Hugoniot, and release behaviour of pressed copper powder". *Journal of Applied Physics*, vol.41, no.11, pp.4542-4551 (1970).
 80. B.M. Butcher and C.H. Karnes. "Dynamic compaction of porous iron". *Journal of Applied Physics*, vol.40, no.7, pp.2967-2976 (1969).
 81. B.M. Butcher, M.M. Carroll and A.C. Holt. "Shock-wave compaction of porous aluminium". *Journal of Applied Physics*, vol.45, no.9, pp.3864-3875 (1974).

-
82. K. Kawakita and Y. Tsutsumi. "An empirical equation of state for powder compression". *Japanese Journal of Applied Physics*, vol.4, no.1, pp.56-63 (1965).
 83. K. Kawakita and K.H. Lüdde. "Some considerations on powder compression equations". *Powder Technology*, vol.4, pp.61-68 (1970).
 84. K. Kawakita and K.H. Lüdde. "On the application of the Heckel and Kawakita equations to powder compaction". *Powder Technology*, vol.43, pp.1-9 (1985).
 85. Y. Sano. "A continuum approach to dynamic compaction of metal powders". *The International Journal of Powder Metallurgy and Powder Technology*, vol.13, no.2, pp.81-98 (1977).
 86. N.W. Page and P.D. Killen. "Powder flow during dynamic and quasi-static compaction". *Powder Metallurgy*, vol.30, no.4, pp.233-239 (1987).
 87. N.W. Page and D. Raybould. "Dynamic powder compaction of some rapidly solidified crystalline and amorphous powders: compaction characteristics". *Material Science and Engineering A*, vol.118, pp.179-195 (1989).
 88. M.W. Petrie and N.W. Page. "An equation of state for shock loaded powders". *Journal of Applied Physics*, vol.69, no.6, pp.3517-3524 (1991).
 89. A.P. Mann, D.I. Pullin, M.N. Macrossan and N.W. Page. "Numerical modelling of dynamic powder compaction using the Kawakita equation of state". *Journal of Applied Physics*, vol.70, no.6, pp.3281-3290 (1991).
 90. N.W. Page and M.K. Warpenus. "Loading relations for metal powders pressed to high density". *Powder Technology*, vol.61, pp.87-94 (1990).

-
91. L. Boshoff-Mostert and H. J. Viljoen. "Comparative study of analytical methods for Hugoniot curves of porous materials". *Journal of Applied Physics*, vol.86, no.3, pp.1245-1254 (1999).
 92. D.J.K. Dijken and J. Th. De Hosson. "Shockwave equation of state of powder material". *Journal of Applied Physics*, vol.75, no.2, pp.809-813 (1994).
 93. D.J.K. Dijken and J. Th. De Hosson. "Shock wave velocity and shock pressure for low-density powders: A novel approach". *Applied Physics Letters*, vol.64, no.7, pp.933-935 (1994).
 94. D.J.K. Dijken and J. Th. De Hosson. "Thermodynamic model of the compaction of powder material by shock waves". *Journal of Applied Physics*, vol.75, no.1, pp.203-209 (1994).
 95. K.H. Oh and P.A. Persson. "Equation of state for extrapolation of high-pressure Hugoniot data". *Journal of Applied Physics*, vol.65, no.10, pp.3852-3856 (1989).
 96. K.H. Oh and P.A. Persson. "A constitutive model for shock Hugoniot of porous materials in the incomplete compaction regime". *Journal of Applied Physics*, vol.66, no.10, pp.4736-4742 (1989).
 97. G.A. Simon and H.H. Legner. "An analytical model for shock Hugoniot in porous materials". *Journal of Applied Physics*, vol.53, no.2, pp.943-947 (1982).
 98. Q. Wu and F. Jing. "Thermodynamic equation of state and application to Hugoniot predictions for porous materials". *Journal of Applied Physics*, vol.80, no.8, pp.4343-4349 (1996).
 99. S.P. Marsh. *Los Alamos shock wave data*, University of California, Berkeley (1980).

100. H. Almstrom, G. Bjarnholt, S.M. Goldberg, M.A. Liberman. "Numerical modelling of magnetic flux compression by cylindrical imploding ionizing shock waves". in V.K. Chernyshev, V.D. Selemir and L.N. Plyashkevich (editors) *Megagauss and megaampere pulse technology and applications*, pp.455-462 (1996).
101. L. Spitzer. *Physics of fully ionised gases*, Interscience (1956).
102. L. Spitzer and R.Härm. "Transport phenomena in a completely ionised gas". *Physical Review*, vol.89, no.5, pp.977- 981 (1953).
103. R.J. Zollweg and R.W. Liebermann. "Electrical conductivity of non-ideal plasmas". *Journal of Applied Physics*, vol.62, no.9, pp.3621-3627 (1987).
104. Y.T. Lee and R.M. More. "An electron conductivity model for dense plasma". *Physics of Fluids*, vol.27, no.5, pp.1273-1286 (1984).
105. V.B. Mintsev, V.E. Fortov and V.K. Gryaznov. "Electric conductivity of a high-temperature non-ideal plasma". *Soviet Physics, JETP*, vol.52, no.1, pp.59-63 (1980).
106. R.B. Mohanti and J.G. Gilligan. "Electrical conductivity and thermodynamic functions of weakly non-ideal plasma". *Journal of Applied Physics*, vol.68, no.10, pp.5044-5051 (1990).
107. D.J. Rose and M. Clark. *Plasmas and controlled fusion*. MIT Press (1961).
108. A.B. Amster, P.A. Kendall, L.J. Veilletter and B. Harrell. "Continuous oscillographic method for measuring the velocity and conductivity of stable and transient shocks in solid cast explosives". *Review of Scientific Instruments*, vol.31, no.2, pp.188-192 (1960).

109. F.C. Gibson, M.L. Bowser and C.M. Mason, "Method for the study of deflagration to detonation transition". *Review of Scientific Instruments*, vol.30, no.10, pp.916-919 (1959).
110. G.E. Ingram. "Application of charged coaxial cables to the measurement of projectile velocity and impact time in a compressed gas gun". *Review of Scientific Instruments*, vol.36, no.4, pp.458-460 (1965).
111. M.D. Mallory. "Propagation of shock waves in aluminium". *Journal of Applied Physics*, vol.26, no.5, pp.555-559 (1955).
112. G.R. Fowles. "Attenuation of the shock waves produced in a solid by flyer impact". *Journal of Applied Physics*, vol.31, no.4, pp.655-661 (1960).
113. J.O. Erkman and A.B. Christensen. "Attenuation of Shock Waves in Aluminium". *Journal of Applied Physics*, vol.36, no.13, pp.5395-5403 (1967).
114. A.L. Peratt and P. Koert. "Pulsed electromagnetic acceleration of exploded wire plasmas". *Journal of Applied Physics*, vol. 54, no. 11, pp.6292-6301 (1983).
115. J.D. Powell and J.H. Batteh. "Plasma dynamics of an arc-driven, electromagnetic, projectile accelerator". *Journal of Applied Physics*, vol.52, no.4, pp.2717-30 (1981).
116. R.E. Kidder. "Compression of magnetic field inside a hollow explosive-driven cylindrical conductor" in H. Knoepfel and F. Herlach (editors) *Megagauss magnetic field generation by explosives and related experiments*, EUR 2750c. Euratom, Brussels, pp.37-54 (1966).
117. R. Tipton. "Modeling flux compression generators with a 2D ALE code" in V.M. Titov and G.A. Shvetsov (Editors), *Megagauss fields and pulsed power systems*, pp.217-231, Nova Science Publishers (1990).

118. H. Knoepfel. *Pulsed high magnetic fields*. Appendix 4 Magnetohydrodynamic equations. North Holland Publishing Company, Amsterdam (1970).
119. F. Herlach. "Megagauss magnetic fields". *Reports on Progress in Physics*, vol.31, Part 1, pp.341-417 (1968).
120. V.G. Welsby. *The theory and design of inductance coils*. McDonald, London (1960).
121. H. Knoepfel. *Pulsed high magnetic fields*. Ch 2 Quasi-stationary magnetic fields. North Holland Publishing Company, Amsterdam (1970).
122. M.A. Weinstein. "Magnetic decay in a hollow circular cylinder". *Journal of Applied Physics*, vol.33, no.1, p.762 (1962).
123. F. Herlach. "A versatile epoxy casting technique for manufacturing magnetic probes". *Review of Scientific Instruments*, vol.40, no.6, pp.852-853 (1969).
124. H. Knoepfel. *Pulsed high magnetic fields*. Ch 11 Measurement of pulsed magnetic fields and currents. North Holland Publishing Company, Amsterdam (1970).
125. M.C. Volk, J.W. Lefforge and R Stetson. *Electrical encapsulation*. Reinhold Publishing Corp (1962).
126. D. Kind and H.Kärner. *High-voltage insulation technology*. Friedr. Vieweg and Sohn (1985).
127. R.F. Chisnell. "The motion of shock wave in a channel, with applications to cylindrical and spherical shock waves". *Journal of Fluid Mechanics*, vol.2, pp.286-298 (1957).

128. R.F. Chisnell. "An analytic description of converging shock waves". *Journal of Fluid Mechanics*. Vol.354, pp.357-375, (1998).
129. G.B. Whitham. "On the propagation of shock waves through regions of non-uniform area or flow". *Journal of Fluid Mechanics*, vol.4, pp.337-360 (1958).
130. J.S. Rinehart and J. Pearson. *Explosive working of metals*. Pergamon Press (1963).
131. B.L. Barthell, W.E. Anderson, V.M. Gomez, B.F. Henneke, J.E. Moore, G.A. Reeves, M.A. Salazar and J.D. Townsend. "Physical vapor deposited aluminium foils for high-energy density physics experiments". *Digest of Technical Papers. 10th IEEE International Pulsed Power Conference* (Cat. No.95CH35833), vol.2, pp.999-1004 (1995).
132. J.F. Leon, R.B. Spielman, J.R. Asay, C.A. Hall, W.A. Stygar and P. L'eplattennier. "Flux compression experiments on the Z accelerator". *Digest of Technical Papers. 12th IEEE International Pulsed Power Conference* (Cat. No.99CH36358), vol.1, pp.275-278 (1999).
133. T.W.L. Sanford, R.C. Mock, R.B. Spielman, D.L. Peterson, D. Mosher and N.F. Roderick. "Increased X-ray power generated from low-mass large-number aluminum-wire-array Z-pinch implosions". *Physics of Plasmas*, vol.5, no.10, pp.3737-3754 (1998).
134. L.M. Barker and R.E. Hollenbach. "Laser interferometer for measuring high velocities of any reflecting surface". *Journal of Applied Physics*, vol.43, no.11, pp.4669-4675 (1972).
135. F.J. Wessel, N.C. Wild, A. Fisher, H.U. Rahman, A. Ron and F.S. Felber. "Faraday rotation in a multimode optical fiber in a fast rise-time, high magnetic field". *Review of Scientific Instruments*, vol.57, no.9, pp.2246-2249 (1986).

1. H. Knoepfel. *Pulsed high magnetic fields*. North Holland Publishing Company, Amsterdam (1970).
2. W.R. Smythe. *Static and dynamic electricity*. Hemisphere Publishing Corp (3rd ed) (1989).
3. R. Courant and K.O. Friedrichs. *Supersonic flow and shock waves*. New York Springer Verlag (1976).
4. R. Kinslow (editor). *High-velocity impact phenomena*. Academic Press (1970).
5. M.A. Meyers. *Dynamic behaviour of materials*. John Wiley and Son (1994).
6. W.H. Press, B.P. Flannery, S.A. Teukolsky and W.T.Vetterling. *Numerical recipes. The art of scientific computing*. Cambridge University Press (1986).
7. The Mathworks, Inc. *The student edition of MATLAB. version 4 user's guide*. (1995).
8. P.W. Cooper and S.R. Kurowski. *Introduction to the technology of explosives*. Wiley VCH (1995).
9. P.W. Cooper. *Explosive technology*. Wiley VCH (1995).
10. L.L. Altgilbers, M.D.J. Brown, I. Grishnaev, B.M. Novac, I.R. Smith, I. Tkach and Y. Tkach. *Magnetocumulative generators*. Springer-Verlag (2000).

The work described in this thesis has resulted so far in the following publications

1. B.M. Novac, I.R. Smith, S.E. Goh, M.C. Enache, K. Gregory, P. Senior, R.J. Cliffe, R.A. Burke and H.R. Stewardson. "A novel flux compression/dynamic transformer technique for high-voltage pulse generation". *Digest of Technical Papers. 12th IEEE International Pulsed Power Conference* (Cat. No.99CH36358), vol.1, pp.343-346 (1999).
2. S.E. Goh, B.M. Novac, I.R. Smith, J.A. Porter and M.C. Enache. "Special-purpose high-voltage transformers". *Proceedings of 34th Universities Power Engineering Conference*, vol.1, pp.296-299 Leicester, UK (1999).
3. B.M. Novac, I.R. Smith and S.E. Goh. "An economic compact high voltage pulse generator". *Proceedings of IEE Symposium Pulsed Power 2000* (Digest No.00/053), pp 6/1-3. London, UK (2000).
4. S.E. Goh, B.M. Novac and I.R. Smith. "Dielectric-metallic phase transition in magnetic-flux compression experiments". *Proceedings of the IEE Symposium Pulsed Power 2000* (Digest No.00/053), pp 26/1-4. London, UK (2000).
5. B.M. Novac, I.R. Smith, S.E. Goh, P. Senior and H.R. Stewardson. "Fast pulse dynamic transformer". *Proceedings of the IEE Symposium Pulsed Power 2000* (Digest No.00/053), pp 27/1-4. London, UK (2000).
6. B.M. Novac, I.R. Smith, S.E. Goh, M.C. Enache, K. Gregory, P. Senior and H.R. Stewardson. "A novel flux compression/dynamic transformer technique for high-voltage pulse generation". *IEEE Transactions on Plasma Science*, vol.28, no.5, pp.1356-1361 (2000).

7. B.M. Novac, I.R. Smith, S.E. Goh, P. Senior and H.R. Stewardson. "Static and dynamic high-voltage pulse transformers". *Proceedings of the 13th International Conference on High-Power Particle beams (BEAMS 2000)*, pp.313-316, Nagaoka, Japan (2000).
8. B.M. Novac, I.R. Smith, S.E. Goh. "Monitoring the velocity of the insulator-metallic phase transition in aluminium powder under shock loading". *Journal of Physics D - Applied Physics*, vol.34, no.1, pp.174-176 (2001).
9. I.R. Smith, R.J. Cliffe, M.C. Enache, S.E. Goh, K. Gregory, H.M. Meese, B.M. Novac, P. Senior, R.D. Shah, P. Stevenson and H.R. Stewardson. "Pulsed Power Research at Loughborough University". *Presented at 13th IEEE International Pulsed Power Conference*, Las Vegas, USA (2001). To be published in the conference proceedings.

PHOTOGRAPHS OF SPIRAL RESISTANCE PROBE

FIGURE A-1 COATING OF SPIRAL PROBE WITH ALUMINIUM POWDER..... 297

FIGURE A-2 FILLING THE PVC HOLDER WITH ALUMINIUM POWDER..... 298

FIGURE A-3 BASE OF PVC HOLDER IS WIPED FREE OF POWDER..... 298

FIGURE A-4 DIELECTRIC BARREL IS GLUED TO THE BASE OF THE PVC HOLDER. 299

FIGURE A-5 SPIRAL PROBE IS MOUNTED ABOVE EXPLODING FOIL AND MYLAR FLYER.
..... 299

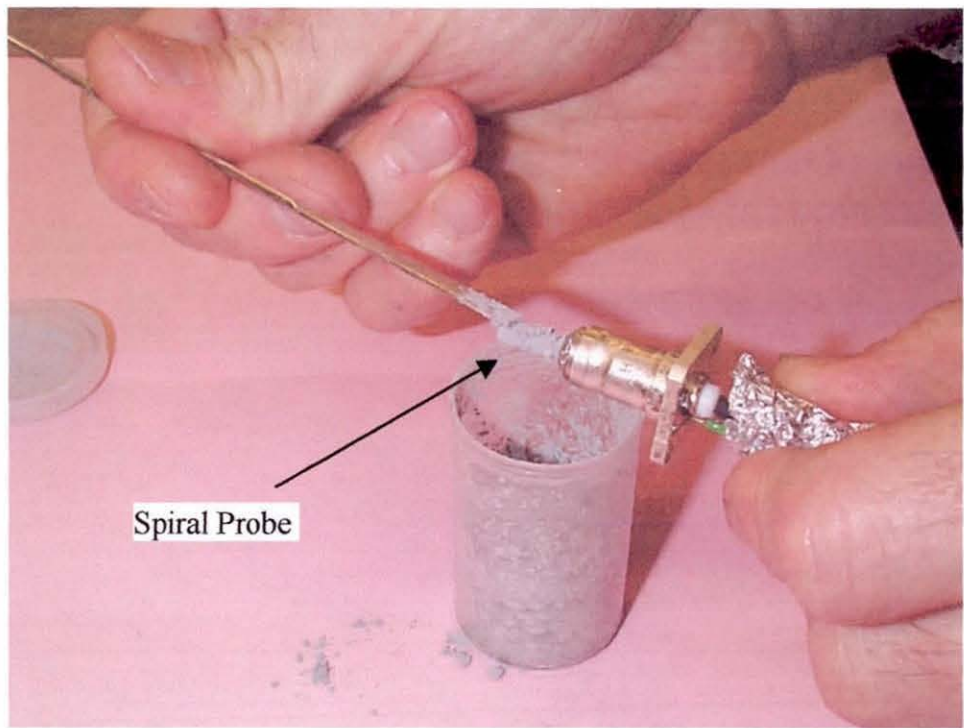


Figure A-1 Coating of spiral probe with aluminium powder.

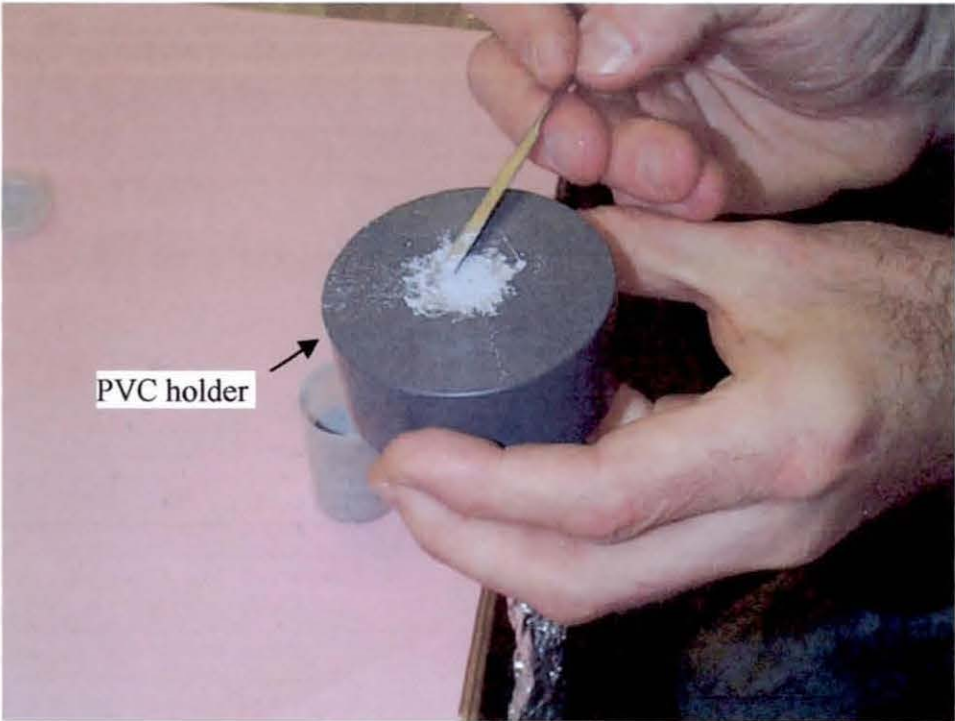


Figure A-2 Filling the PVC holder with aluminium powder.

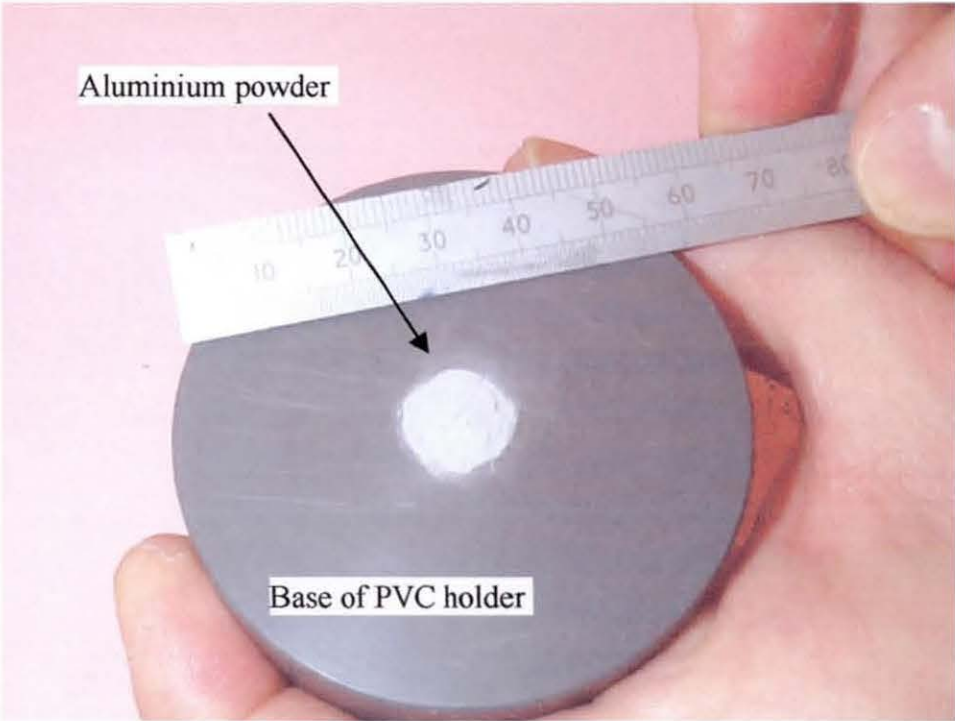


Figure A-3 Base of PVC holder is wiped free of powder.

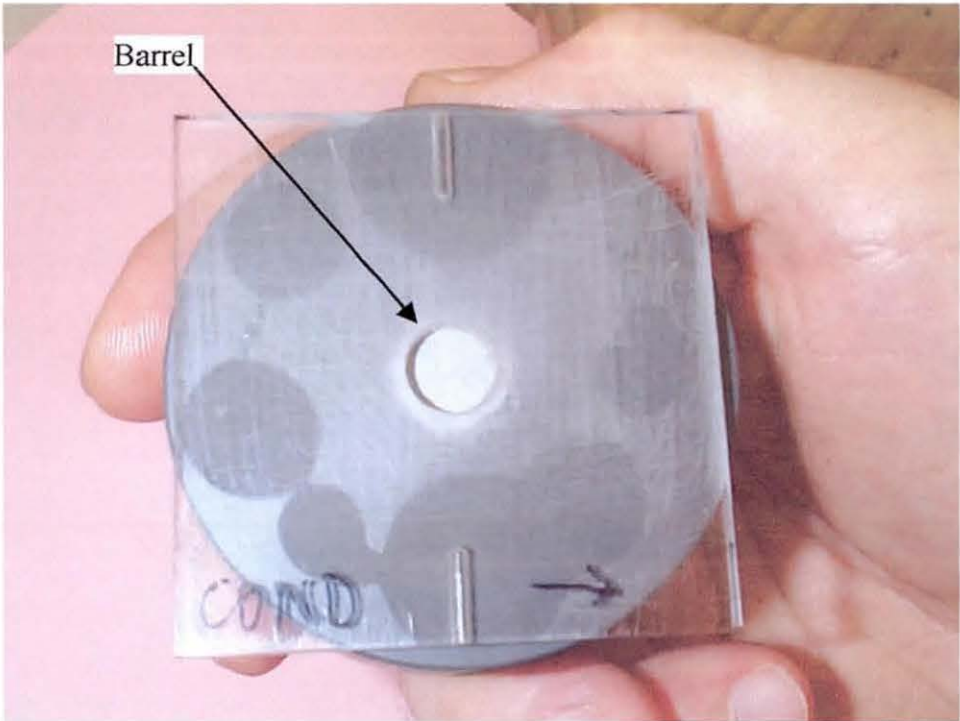


Figure A-4 Dielectric barrel is glued to the base of the PVC holder.

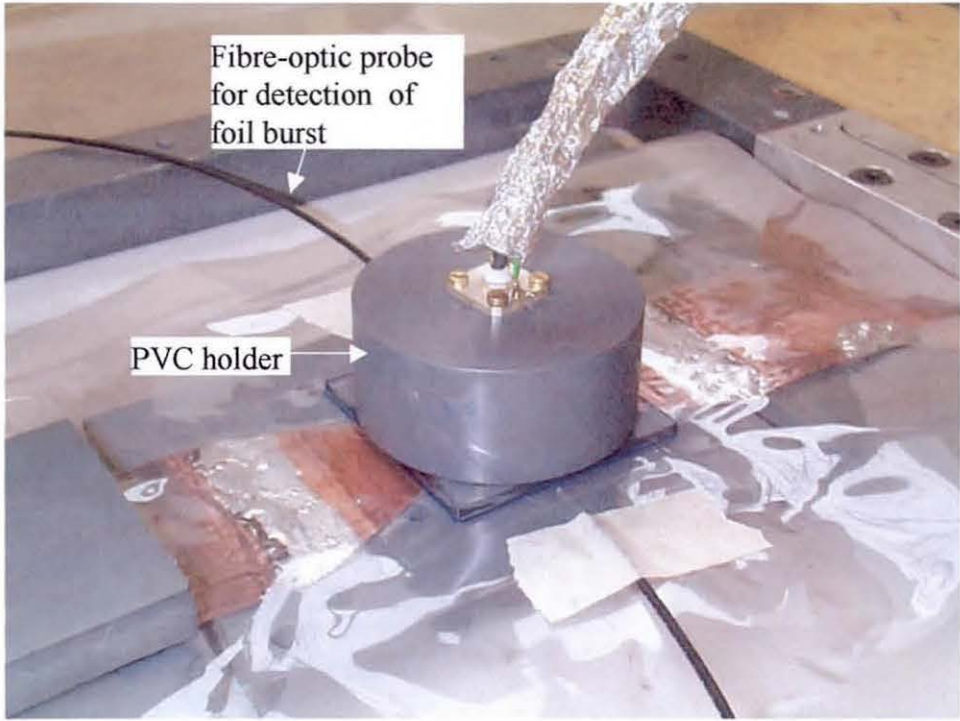


Figure A-5 Spiral probe is mounted above exploding foil and Mylar flyer.

PHOTOGRAPHS OF FIELD COIL CONSTRUCTION

FIGURE B-1 STEP – 1, SECURE WIRE TO PVC MANDREL TO START 300

FIGURE B-2 STEP – 2, EACH LAYER OF WINDING IS COATED WITH EPOXY. 301

FIGURE B-3 STEP – 3, SECURE COMPLETED WINDING WITH FIBRE CLOTH AND EPOXY
GLUE. 301

FIGURE B-4 STEP – 4, EPOXY CASTING IN PLASTIC CONTAINER..... 302

FIGURE B-5 STEP – 5, CONCRETE CASTING IN PVC CONTAINER. 302

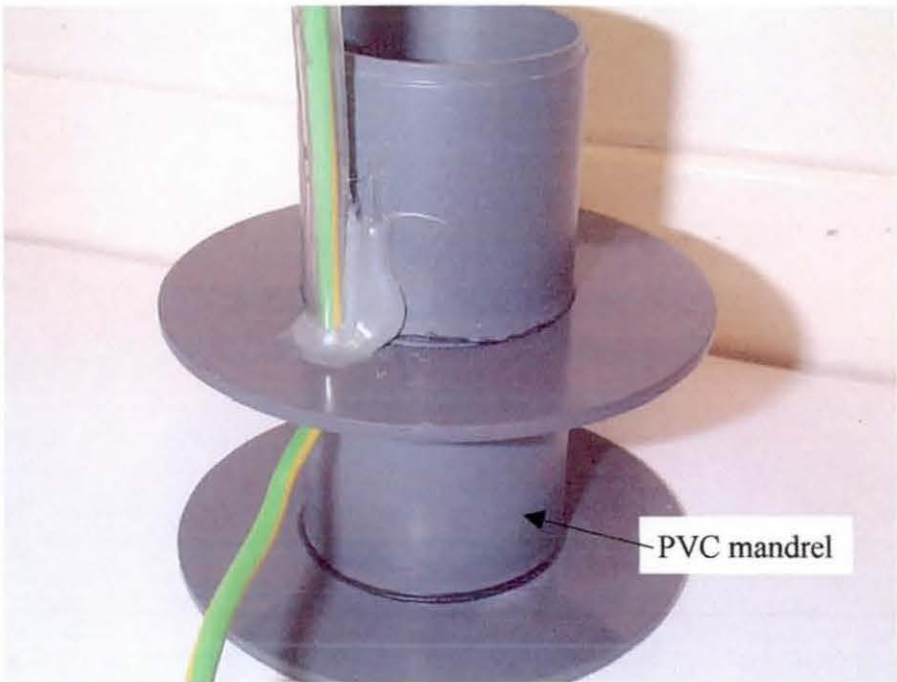


Figure B-1 Step – 1, Secure wire to PVC mandrel to start winding.

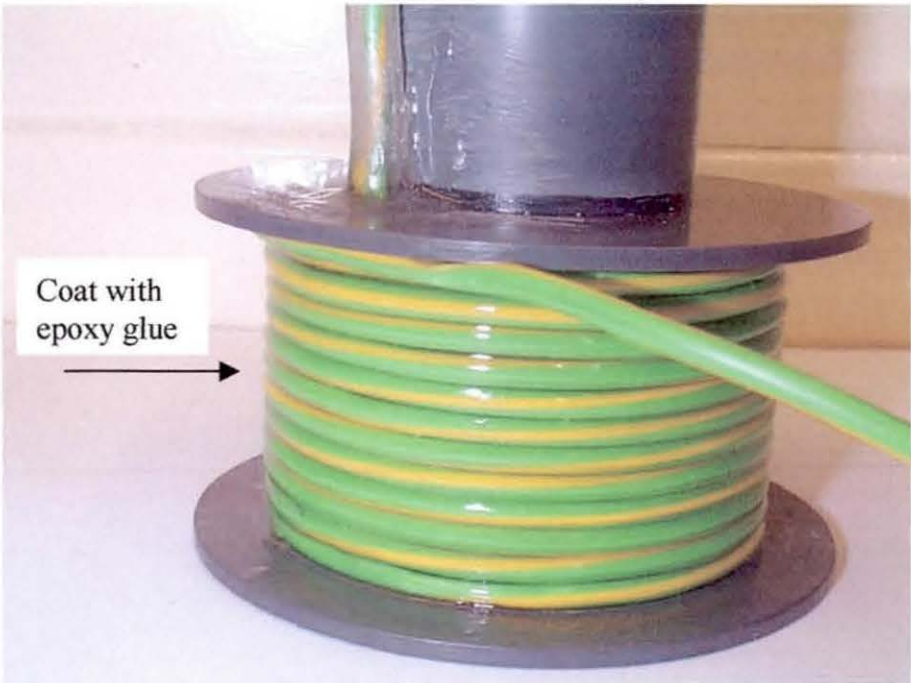


Figure B-2 Step – 2, Each layer of winding is coated with epoxy glue.



Figure B-3 Step – 3, Secure completed windings with fibre cloth and epoxy glue.

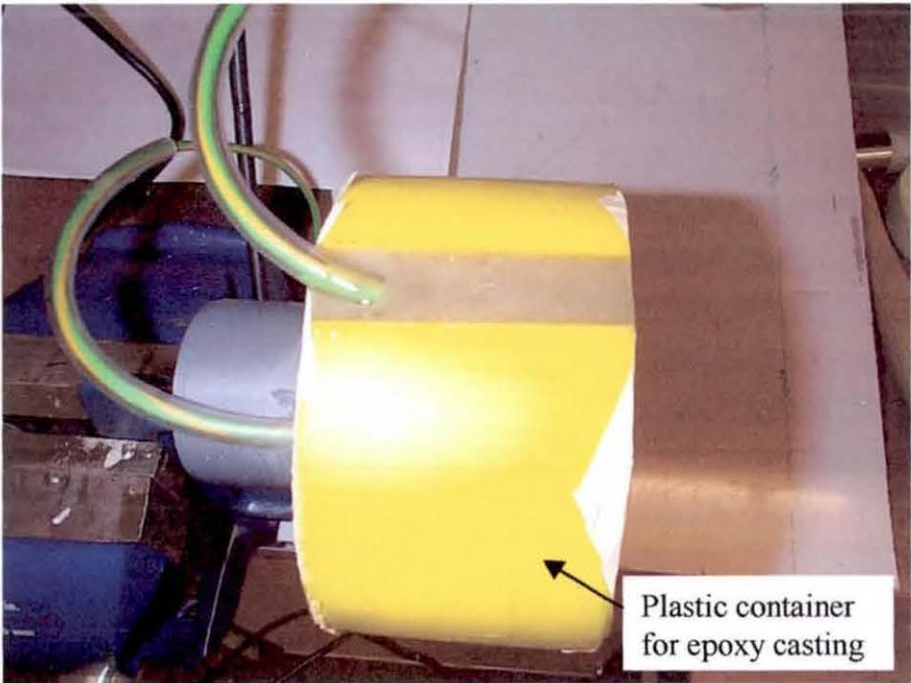


Figure B-4 Step – 4, Epoxy casting in plastic container.

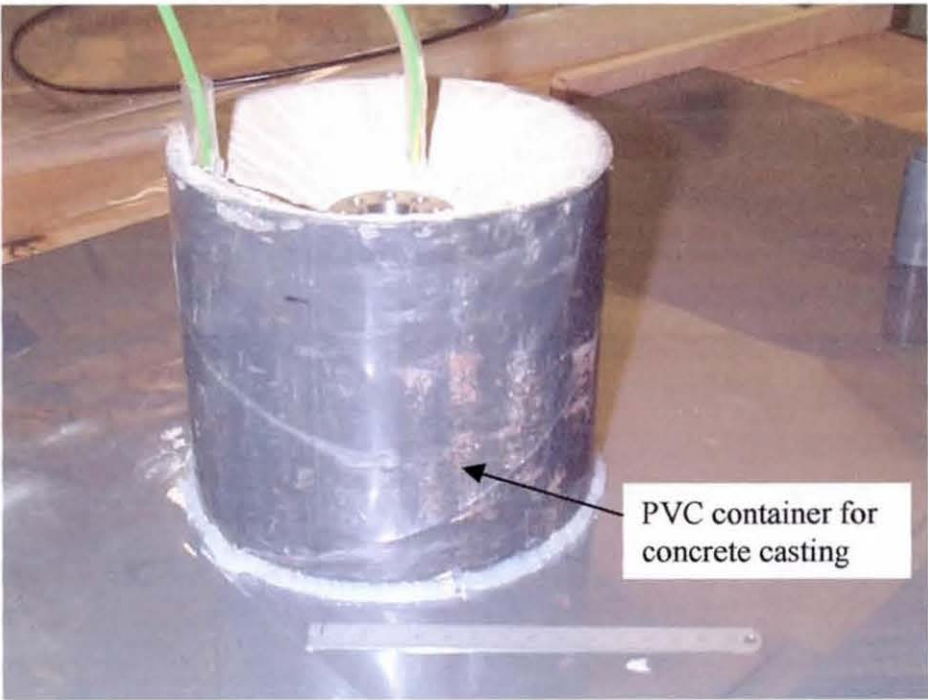


Figure B-5 Step – 5, Concrete casting in PVC container.

DRAWINGS AND PHOTOGRAPHS OF IMPLODER

FIGURE C-1	DRAWING OF CYLINDRICAL CURRENT CONDUCTOR AND END-PIECE.....	304
FIGURE C-2	CYLINDRICAL CURRENT CONDUCTOR AND END-PIECE.....	304
FIGURE C-3	DRAWING OF TOP PLATE OF TRANSMISSION LINE.....	305
FIGURE C-4	TOP PLATE OF TRANSMISSION LINE.....	305
FIGURE C-5	DRAWING OF POLYETHYLENE HIGH-VOLTAGE INSULATOR.....	306
FIGURE C-6	POLYETHYLENE HIGH-VOLTAGE INSULATOR.....	306
FIGURE C-7	DRAWING OF BASE PLATE OF TRASMISSION LINE.....	307
FIGURE C-8	BASE PLATE OF TRASMISSION LINE.....	307
FIGURE C-9	INDUCTIVE PROBE USED IN TEST NO. 137.	308
FIGURE C-10	ALUMINIUM POWDER ASSEMBLY USED IN TEST NO. 137.....	308
FIGURE C-11	STEP 1 - CONNECT BASE PLATE WITH TRANSMISSION LINE FROM CAPACITOR BANK.	309
FIGURE C-12	STEP 2 - LAY MYLAR FILM OVER BASE PLATE.....	309
FIGURE C-13	STEP 3 - ALIGN HIGH-VOLTAGE INSULATOR WITH BASE PLATE.	310
FIGURE C-14	STEP 4 - ALIGN TOP AND BASE PLATES OF TRANSMISSION LINE.....	310
FIGURE C-15	STEP 5 - SECURE TOP AND BASE PLATES OF TRANSMISSION LINE.	311
FIGURE C-16	STEP 6 - INSTALL POWDER ASSEMBLY INSIDE IMPLODER.	311
FIGURE C-17	STEP 7 - INSTALL INITIAL FIELD COIL OVER IMPLODER.....	312
FIGURE C-18	STEP 8 - INSTALL FOAM 'CATCHER' AND READY FOR FIRING.....	312

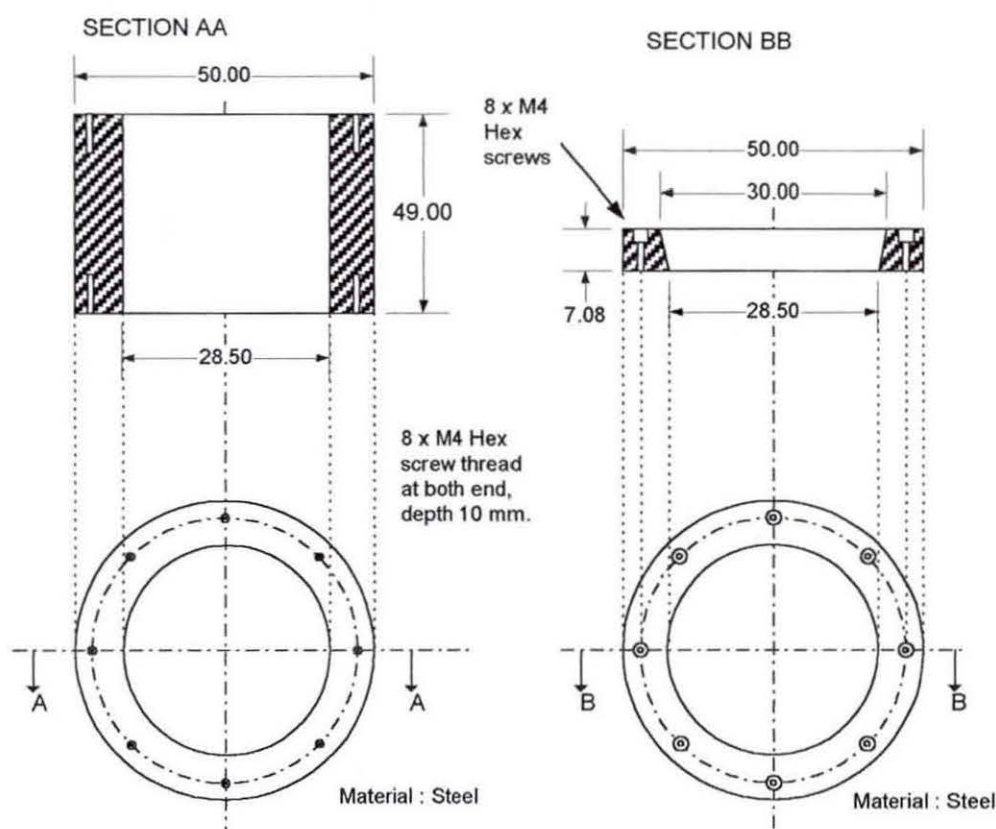


Figure C-1 Drawing of cylindrical current conductor and end-piece.

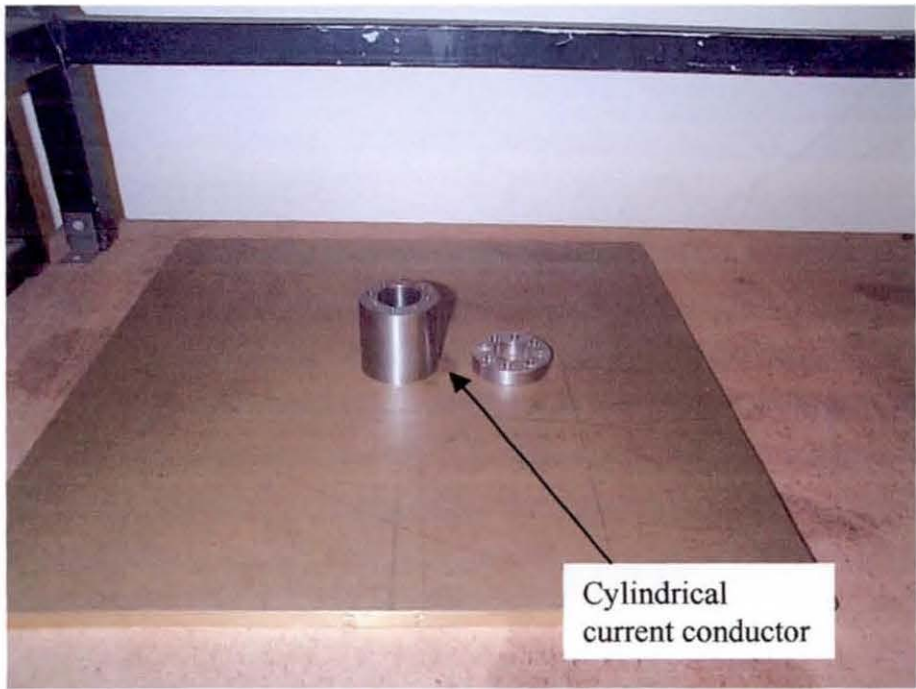


Figure C-2 Cylindrical current conductor and end-piece.

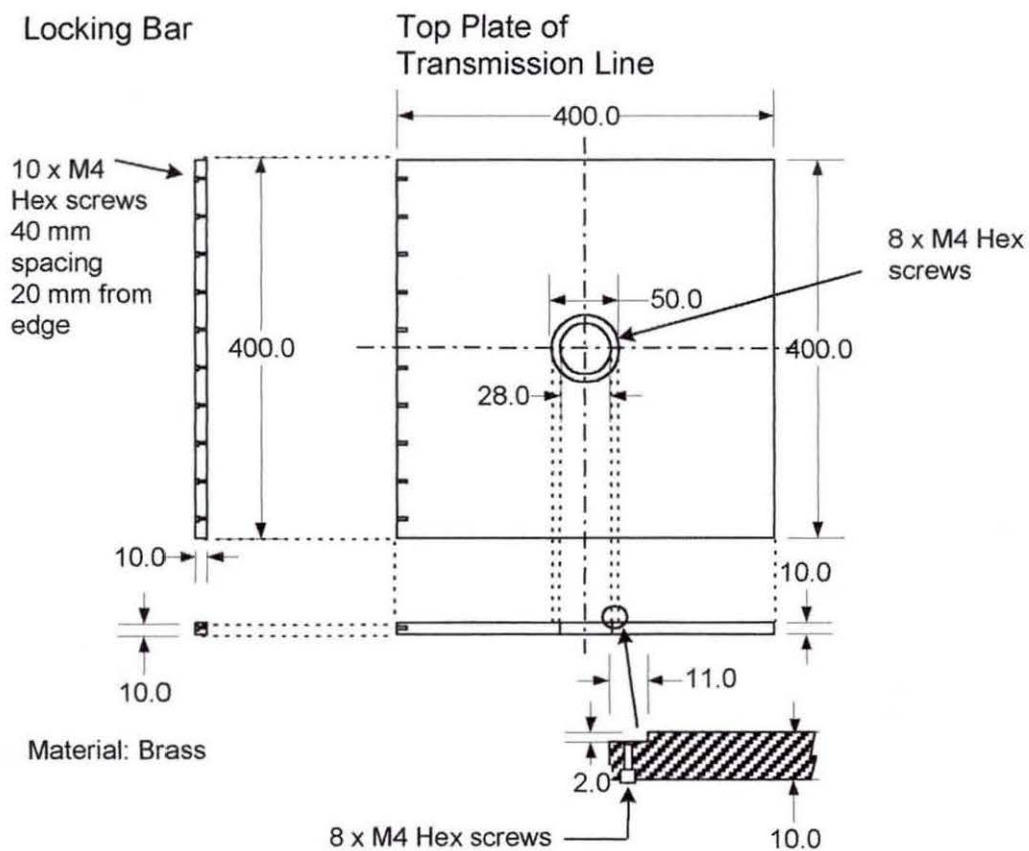


Figure C-3 Drawing of top plate of transmission line.

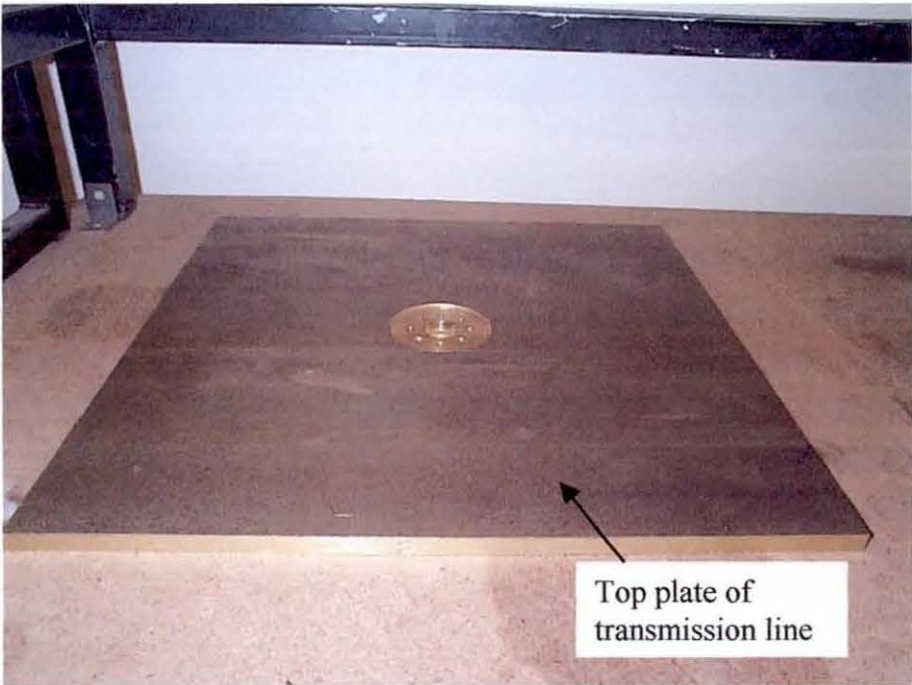


Figure C-4 Top plate of transmission line.

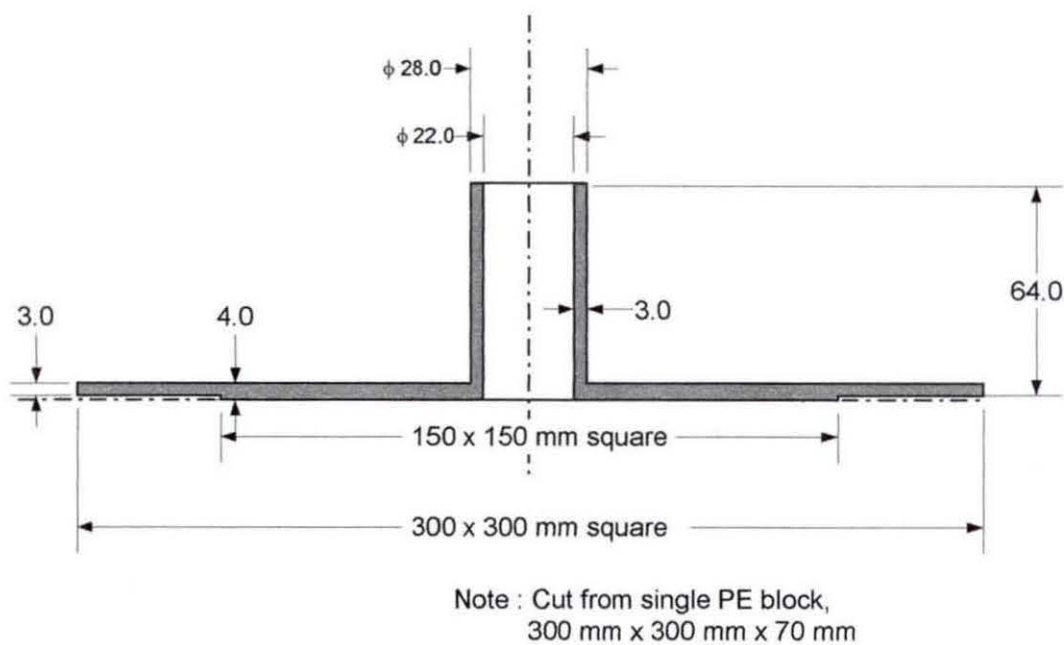


Figure C-5 Drawing of polyethylene high-voltage insulator.

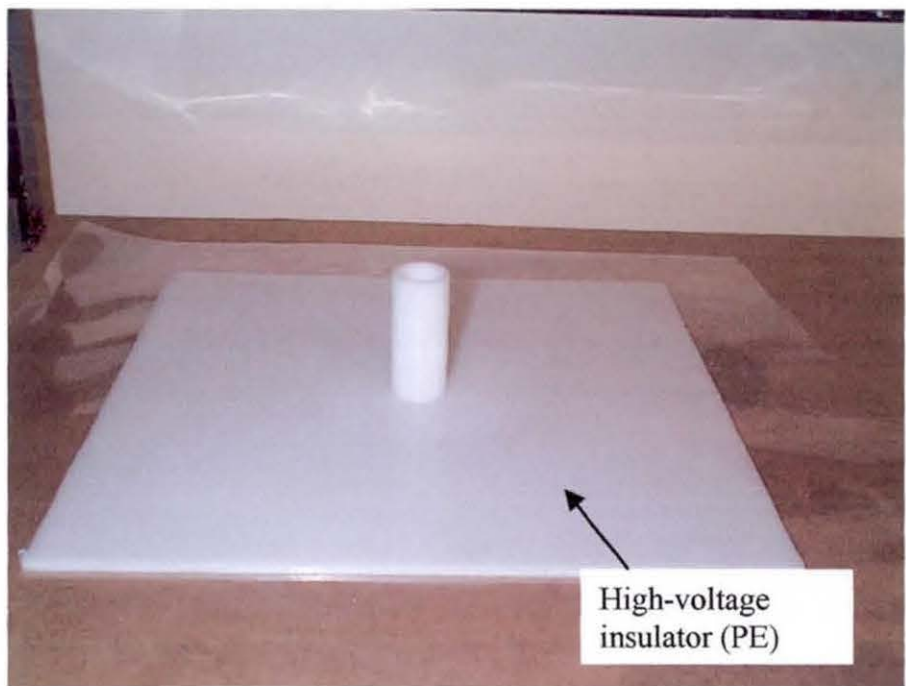


Figure C-6 Polyethylene high-voltage insulator.

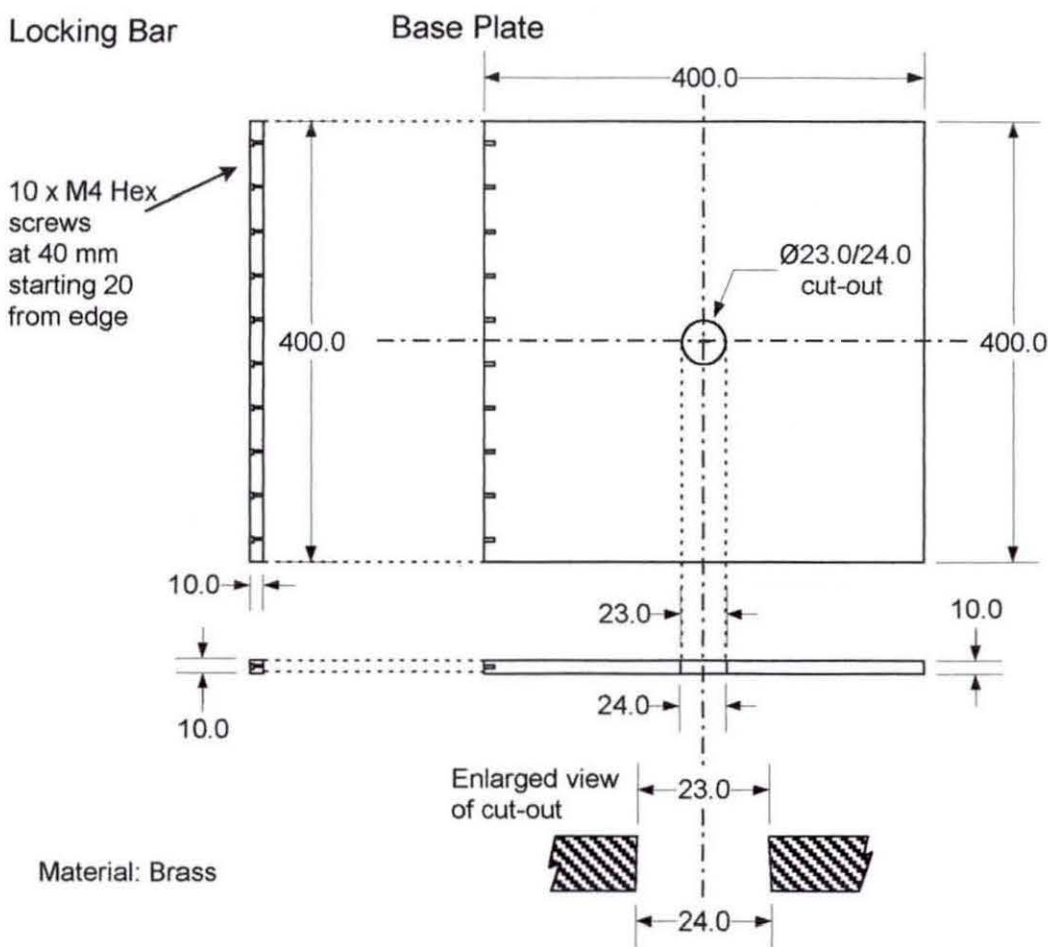


Figure C-7 Drawing of base plate of trasmission line.

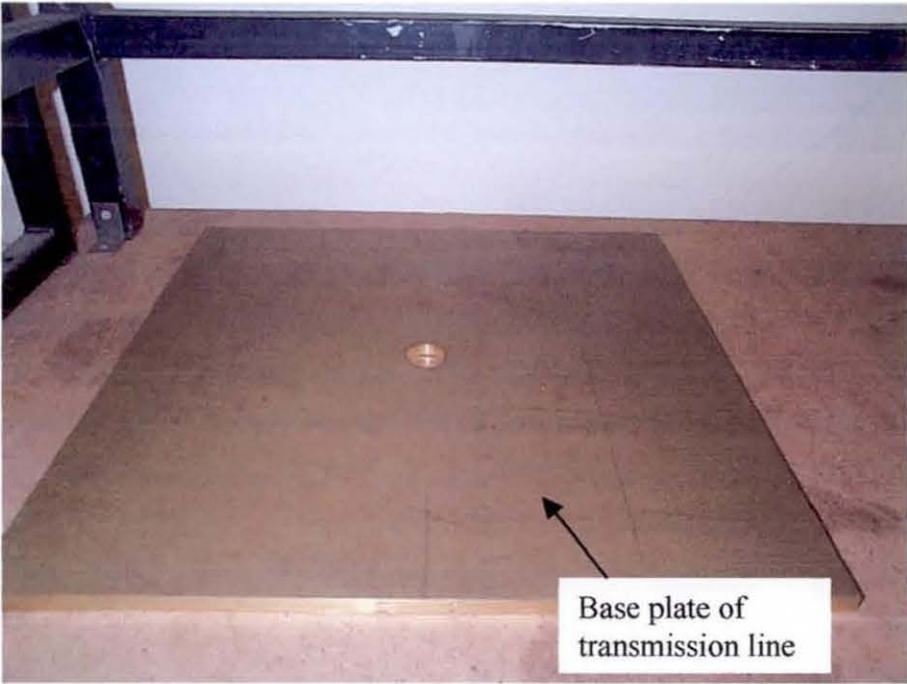


Figure C-8 Base plate of trasmission line.

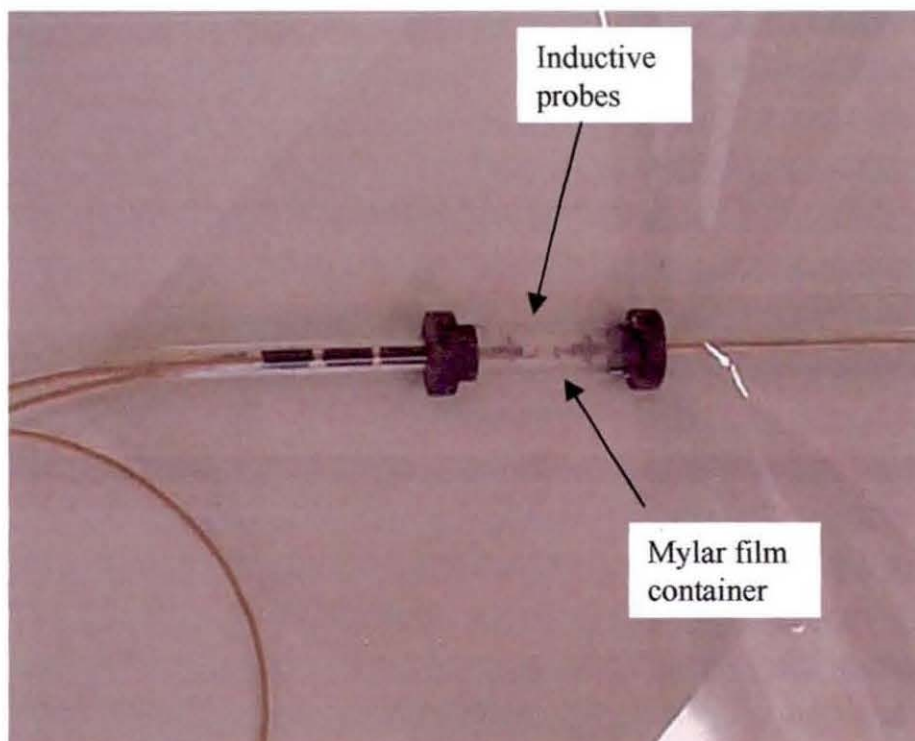


Figure C-9 Inductive probe used in test no. 137.

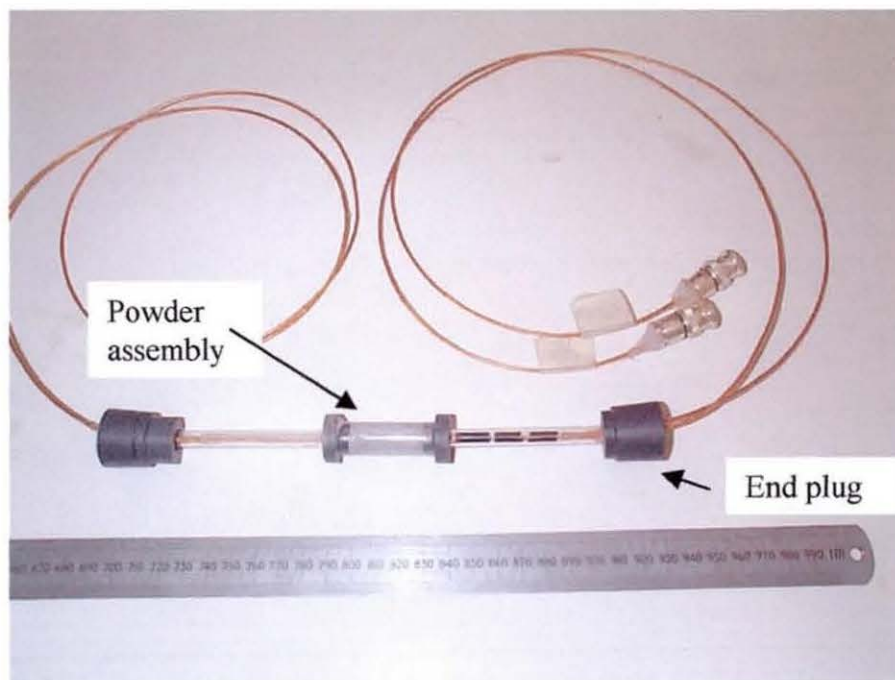


Figure C-10 Aluminium powder assembly used in test no. 137.

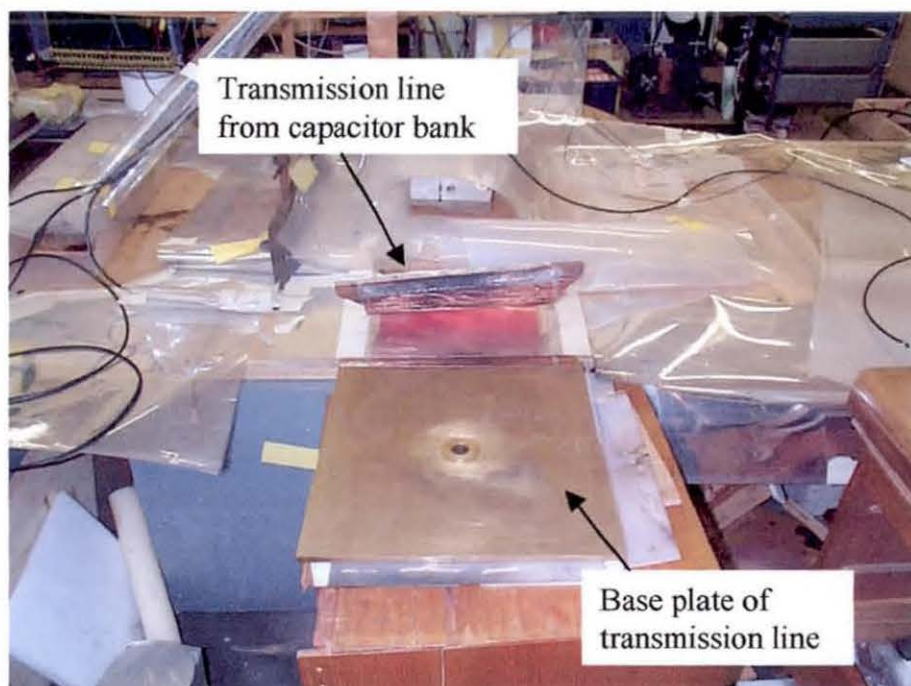


Figure C-11 Step 1 - Connect base plate with transmission line from capacitor bank.

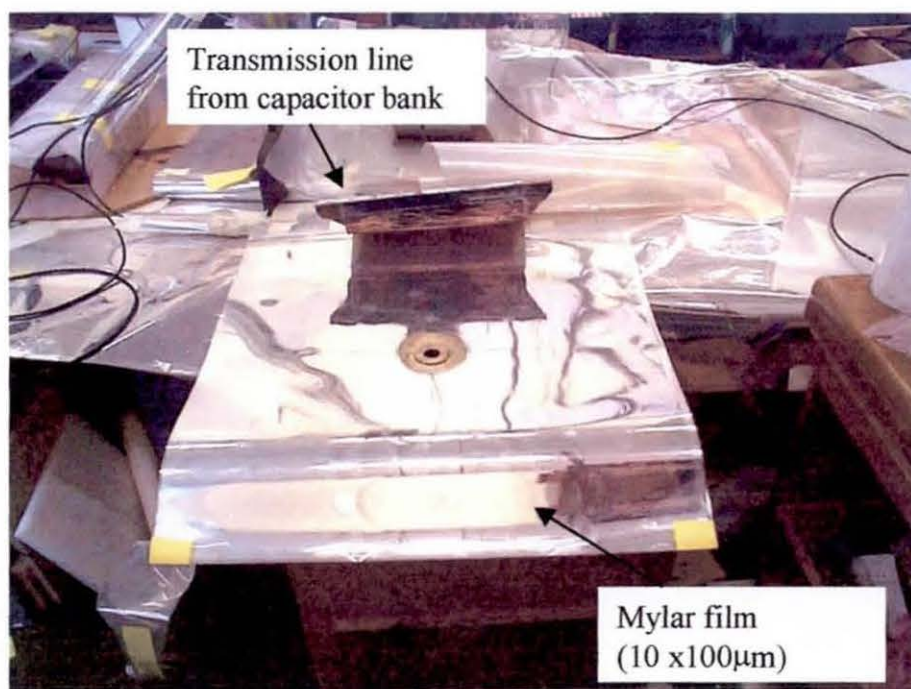


Figure C-12 Step 2 - Lay Mylar film over base plate.

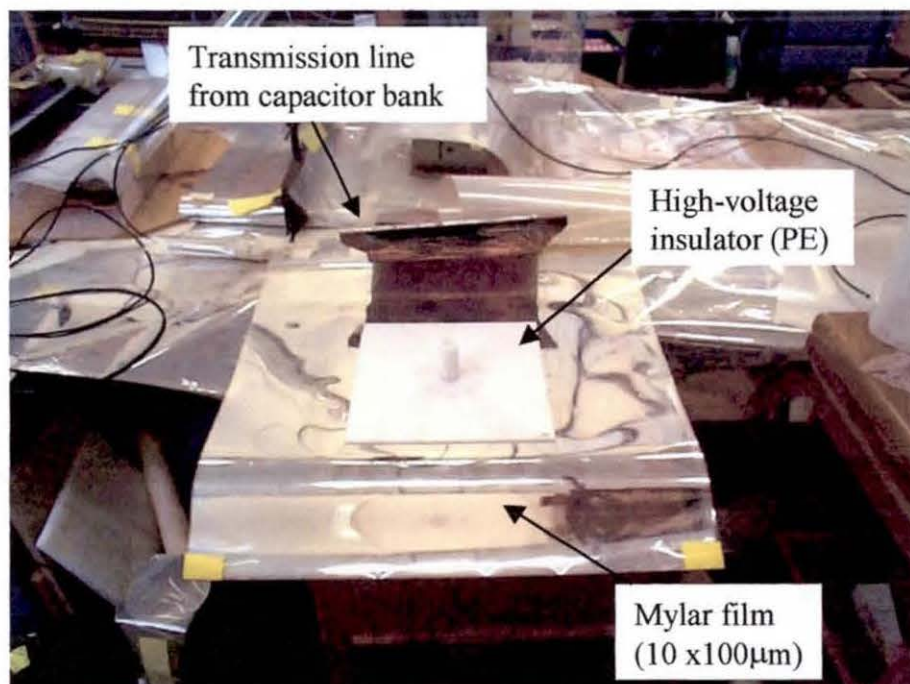


Figure C-13 Step 3 - Align high-voltage insulator with base plate.

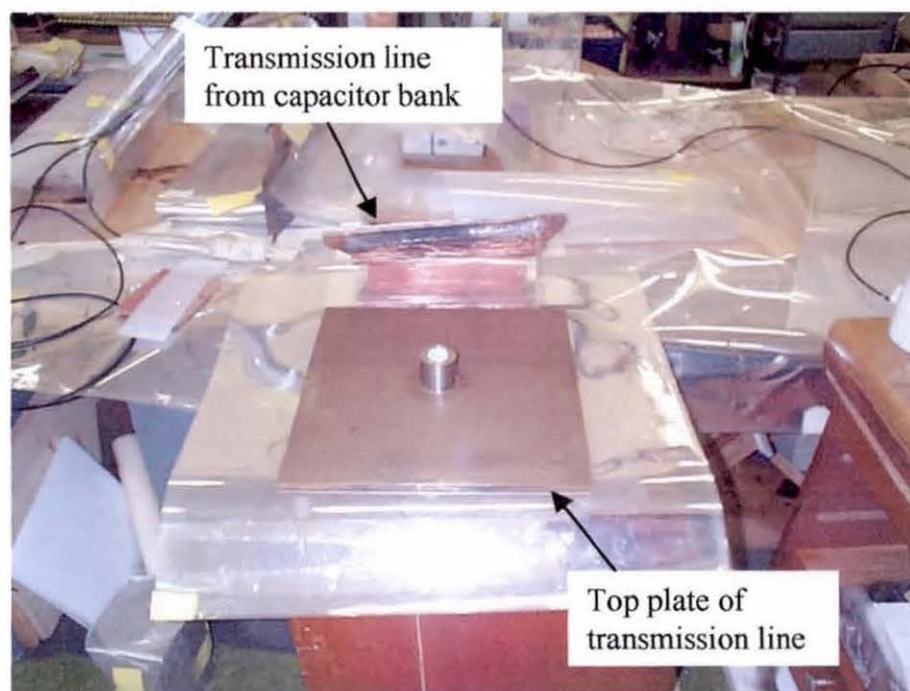


Figure C-14 Step 4 - Align top and base plates of transmission line.

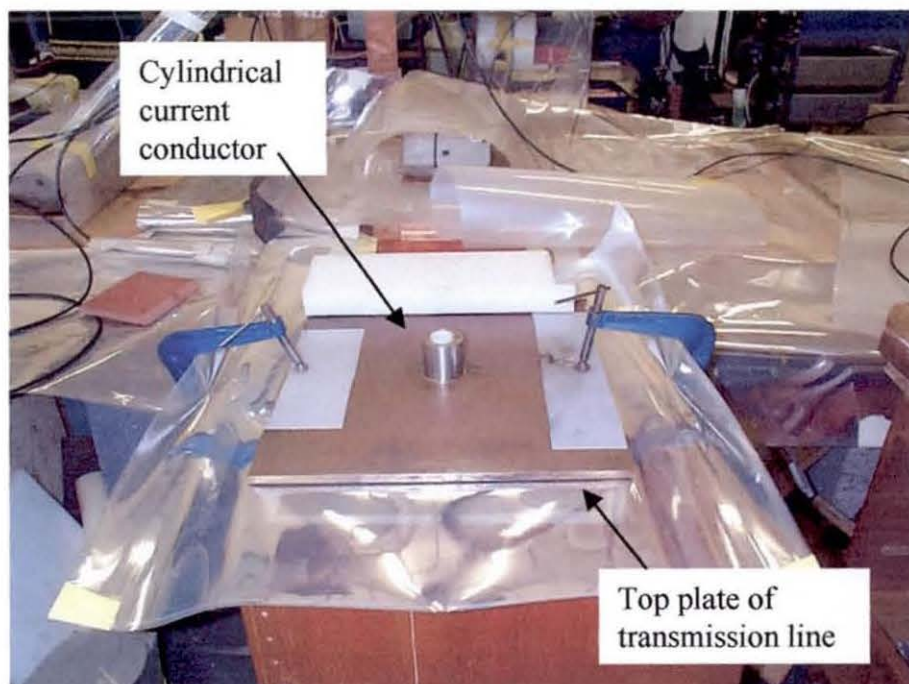


Figure C-15 Step 5 - Secure top and base plates of transmission line.

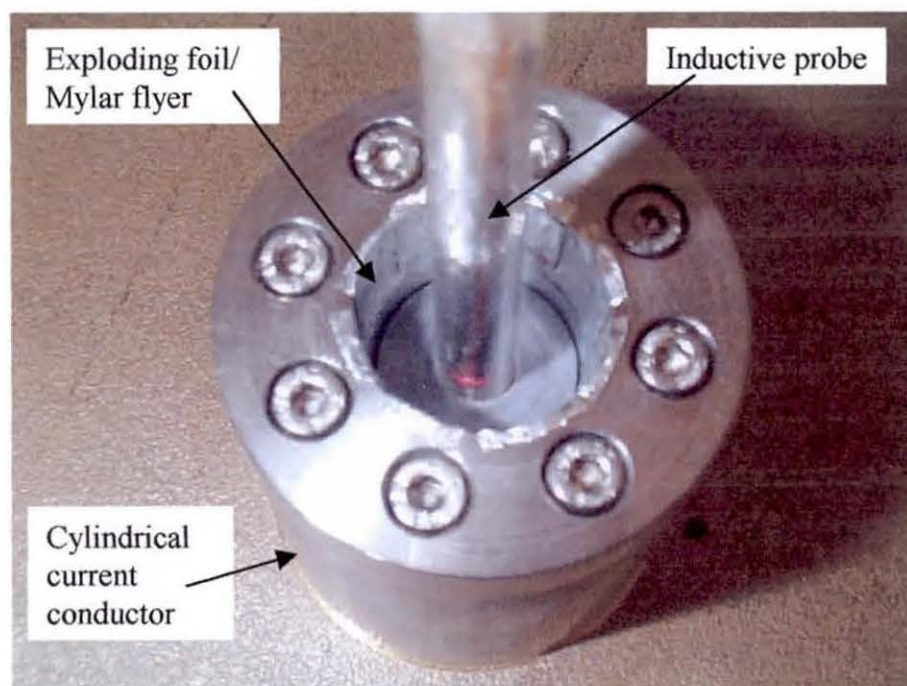


Figure C-16 Step 6 - Install powder assembly inside imploder.

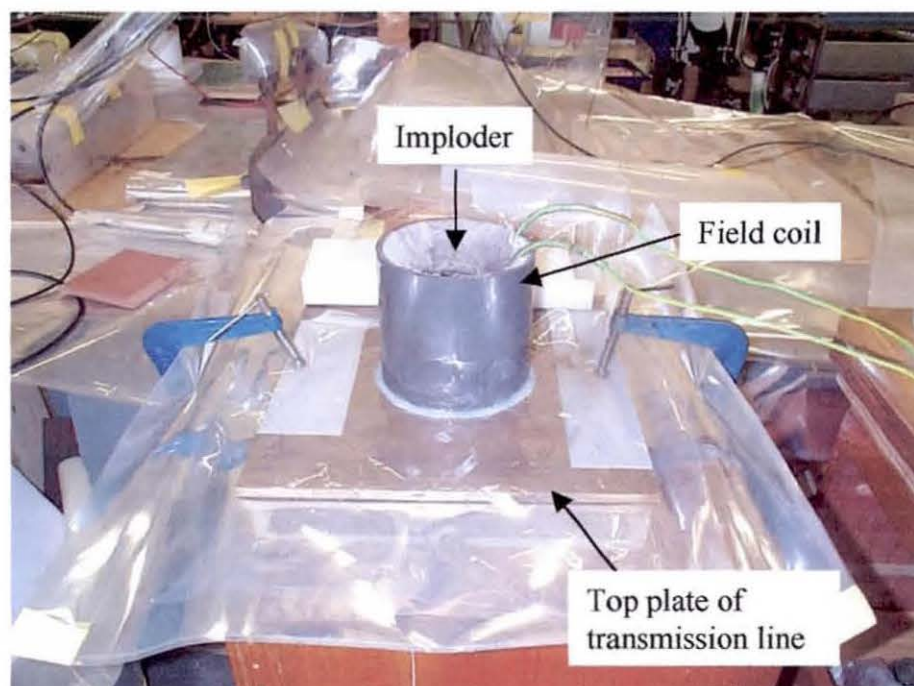


Figure C-17 Step 7 - Install initial field coil over imploder.

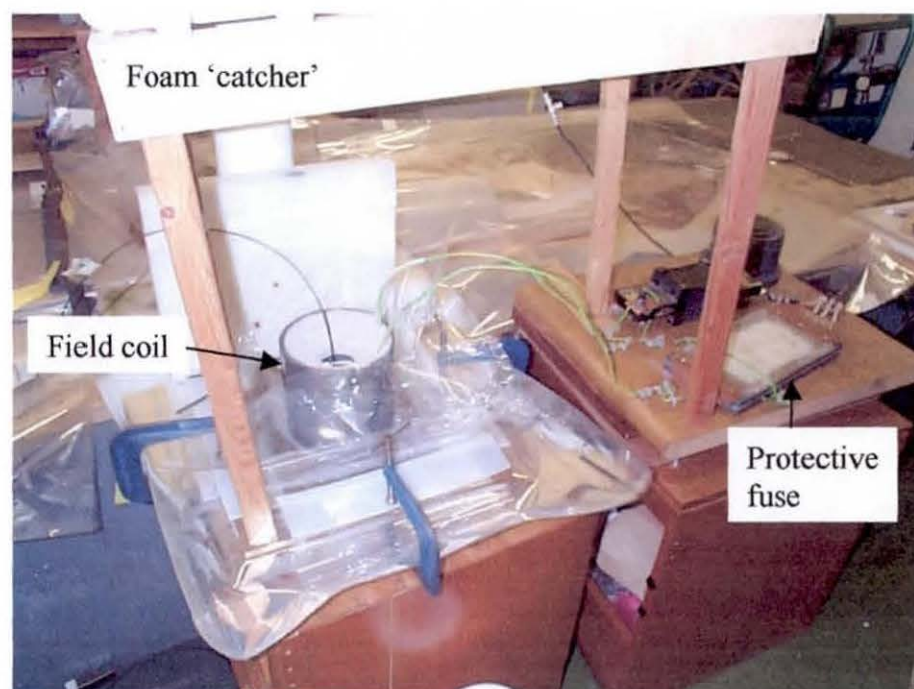


Figure C-18 Step 8 - Install foam 'catcher' and ready for firing.

FLAMMABILITY OF ALUMINIUM POWDER

The mechanism of combustion (or fire) and explosion for aluminium powder is very complex and some of the most important characteristics in regard to the ignition of aluminium powder are:

1. Lower flammable limit
2. Upper flammable limit
3. Minimum ignition temperature

The Lower Flammable Limit

The lower flammable limit is usually referred to as the minimum explosible concentration and is measured in grams per cubic metre of volume. It is generally associated with dust explosion, when finely divided combustible matter is dispersed into an atmosphere containing sufficient oxygen to permit combustion and a source of ignition of appropriate energy.

The minimum explosible concentration is the smallest amount of suspended dust that is capable of igniting and propagating a flame and it is affected by both particle size (see Table D-1) and moisture content. At dust concentration below the minimum value, where the particles are separated by relatively large distances, the heat liberated by the oxidisation of single particles is insufficient to ignite adjacent particles.

If a dust has a very small particle size, cohesive force may result in agglomerates having an effectively larger particle size, with a correspondingly smaller specific surface than the fine dust. A reduced explosion hazard will exist in these circumstances.

Table D-1. Effect of particle size reduction on the minimum explosible combustion of aluminium dust

Average particle size (μm)	Minimum explosible concentration g/m^3
20	30
35	25
40	35
90	45

Dust with particles larger than the critical dimension¹ of 500 μm will not explode.

The presence of moisture in dust is generally beneficial, since it tends to decrease the explosibility in two different, synergistic ways. Firstly, as the moisture content increases, the dust particles become more cohesive and produce agglomerates, which are more difficult to disperse. The dispersed agglomerates, having an effectively larger particle size than the dry dust, are more difficult to ignite and inhibit flame propagation. Secondly, any heat applied to a suspension of moist dust will first be required to vaporise the water and will therefore not be used in the combustion process.

It has been shown¹ that an increase in moisture content results in higher minimum ignition temperatures and gives increased value of minimum ignition energy and minimum explosible concentration.

The Upper Flammable Limit

Above the upper flammable limit, which is of the order $5\text{--}10 \text{ kg/m}^3$, the particles are so densely packed that ready access to the oxygen necessary for combustion is prevented, and flame propagation is quenched.

¹ Peter Field, *Handbook of Powder Technology, Volume 4 - Dust Explosions*. Elsevier Scientific Publishing Company, 1982

Minimum Ignition Temperature

The minimum ignition temperature of a dust explosion is the lowest temperature at which flame propagation occurs.

Explosion Parameters of Aluminium Powder/Dust

Table D-2 summarises the characteristics that are most important in the ignition of aluminium powder.

Table D-2 Explosion Parameters of Aluminium Powder/Dust²

Particle size	6 µm	flake	100 µm	1000 µm
Lower flammability limit or Minimum explosible concentration, g/m ³	30	45	n.d.	n.d.
Upper flammability limit, kg/m ³	5-10	5-10	5-10	5-10
Minimum ignition temperature, °C	420	610	n.d.	n.d.

n.d. = not determined.

² M. Jacobson, A.R. Cooper & J. Nagy. *Explosibility of metal powders*. US Bureau of Mines, R I 6316, Washington, 1964

EFFICIENCY OF THE DYNAMIC POWDER TRANSFORMER

The efficiency of the dynamic powder transformer is primarily determined by the foil explosion and flyer acceleration processes, which convert electrostatic energy stored in the capacitor bank into kinetic energy in the Mylar flyer.

Efficiency, η

The efficiency of the implosion process is defined as the ratio of the kinetic energy of the Mylar projectile at the point of impact with the aluminium powder to the energy initially stored in the capacitor bank. Figure E-1 shows the time variation of the energy stored in the capacitor bank, deposited in the foil and acquired by the Mylar flyer.

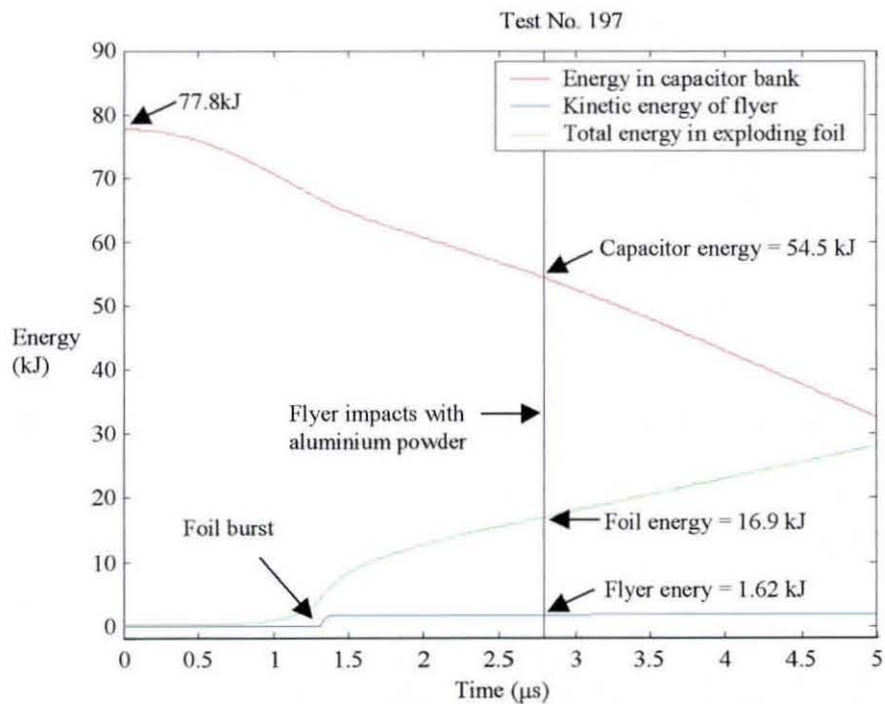


Figure E-1 Energy distribution for dynamic powder transformer in test no. 197

The energy initially stored in the capacitor bank was 77.8 kJ . At the time the Mylar flyer impacts with the aluminium powder, it has acquired a kinetic energy of 1.62 kJ , giving an efficiency of

$$\eta = \frac{1.62}{77.8} = 2.08\%$$

